Wave-Propagation Modeling and Inversion Using Frequency-Domain Integral Equation Methods

Christopher E. Strickland

A dissertation
submitted in partial fulfillment of the
requirements for the degree of

Doctor of Philosophy

University of Washington
2015

Reading Committee:
Robert I. Odom, Chair
Kenneth C. Creager
Randall J. LeVeque

Program Authorized to Offer Degree:
Earth and Space Sciences

Abstract

Wave-Propagation Modeling and Inversion Using Frequency-Domain Integral Equation Methods

Christopher E. Strickland

Chair of the Supervisory Committee:
Research Associate Professor, Robert I. Odom
Earth and Space Sciences

Full waveform inverse methods describe the full physics of wave propagation and can potentially overcome the limitations of ray theoretic methods. This work explores the use of integral equation based methods for simulation and inversion and illustrates their potential for computationally demanding problems. A frequency-domain integral equation approach to simulate wave-propagation in heterogeneous media and solve the inverse wave-scattering problem will be presented for elastic, acoustic, and electromagnetic systems. The method will be illustrated for georadar (ground- or ice-penetrating radar) applications and compared to results obtained using ray theoretic methods. In order to tackle the non-linearity of the problem, the inversion incorporates a broad range of frequencies to stabilize the solution. As with most non-linear inversion methods, a starting model that reasonably approximates the true model is critical to convergence of the algorithm. To improve the starting model, a variable reference inversion technique is developed that allows the background reference medium to vary for each source-receiver data pair and is less restrictive than using a single reference medium for the entire dataset. The reference medium can be assumed homogeneous (although different for each data point) to provide a computationally efficient, single-step, frequency-domain inversion approach

that incorporates finite frequency effects not captured by ray based methods. The inversion can then be iterated on to further refine the solution.

TABLE OF CONTENTS

LIST OF FIGURES

ACKNOWLEDGEMENTS

A great many have encouraged and mentored me through this long journey. First, I would like to thank my advisor Bob Odom; I don't think that I could have asked for a better person to guide me through this endeavor. I would also like to thank my committee members and several others at the UW who have helped me along the way: Ken Creager, Randy LeVeque, John Sahr, Paul Bodin, John Vidale, Heidi Houston, and John Booker. Being a non-traditional graduate student and working full-time has presented additional challenges that would have been difficult to overcome without support from several people at PNNL including Tim Johnson, Alain Bonneville, Mike Truex, Vince Vermeul, Charlotte Sullivan, Ray Clayton, Al Rohay, Fred Zhang, Chris Brown, Tyler Gilmore, and Mike Fayer. I would also like to acknowledge a number of friends and colleagues at other universities and national laboratories that I have worked with over the past several years: John Petersen, Roelof Versteeg, Bill Clement, Dimitris Ntarlagiannis, Lee Slater, Fred Day-Lewis, Bjorn Paulsson, Bob Hardage, Henk Keers, and Susan Hubbard. Finally, I thank my family for always being there and supporting me.

DEDICATION

“Where nothing, save the waves and I may hear our mutual murmurs sweep”
Lord Byron, The Isles of Greece

To my family

1 INTRODUCTION

Computationally efficient wave propagation simulation is important to a number of scientific fields including medical imaging, non-destructive testing, global seismic imaging, ocean acoustics, and near-surface geophysical investigations. Wave propagation modeling (the forward problem) is also central to the inverse scattering problem which seeks to determine the spatial distribution of the scattering media or source properties given a set of wave field observations.

Both the forward and inverse problems have been summarized by several researchers (Sheriff and Geldart 1982; Aki and Richards 2002; Tarantola 2004). Subsurface imaging has been performed for applications ranging from environmental monitoring to understanding global Earth structure. Models currently utilize millions of grid cells but will undoubtedly increase in size and complexity requiring numerical methods that efficiently scale with increasing model size and resolution.

Wave propagation modeling can be performed using a multitude of methods, however to make the problem easier to solve, approximations in the physics governing the problem are often employed. Geometric ray theory is one commonly used approximate method for describing wave-propagation in heterogeneous media primarily due it being computationally efficient to implement. Ray theory constitutes a high-frequency solution to the wave-equation and is valid when material heterogeneities and variations in wave amplitude are small over the scale of a wavelength (Kravstov and Orlov 1980). In ray theory, the measured travel-time or amplitude of the wave is sensitive only to the material properties along the geometrical ray path. Mathematically, this translates to a line integral along the ray-path from the signal source to the receiver. In many cases, the underlying assumptions are violated and ray theory may no longer accurately model wave-propagation. Application of ray theory to media that violate the validity criteria introduces several limitations. Low-velocities may not be correctly modeled, skewing the inverse solution toward higher velocities (Nolet 1987). Fine structure of the media smaller than the wavelengths of the propagating waves is also not accurately resolved due to its infinite-frequency approximation (Kravstov and Orlov 1980).

Realistic waves propagate at finite-frequencies and are often composed of a band of several frequencies components. Finite-frequency waves are sensitive to the material properties within a volume surrounding the ray path (Hagedoorn 1954; Woodward 1992; Snieder and Lomax 1996; Dahlen and Tromp 1998; Marquering et al. 1999; Nolet 2008). The sensitivity of the measured signal to changes to the material properties is termed the sensitivity, or Fréchet, kernel (Tarantola 1987) and can be calculated using various methods.

The sensitivity of the propagating wave to the spatial distribution of material properties is frequency dependent and the size of the sensitive volume increases with decreasing frequency. In general, the material properties themselves also show frequency dependence. For instance, even in simple linear media, the wave propagation and attenuation constants of an electromagnetic (EM) wave are both functions of the electrical permittivity, conductivity and frequency (Jackson 1999). This causes dispersion in EM waves where different frequencies propagate at different velocities. In addition, the relative contribution of permittivity and conductivity to the wave velocity is not constant and the frequency must be considered when using velocity measurements to infer either parameter.

In addition to approximate methods, wave-propagation modeling can be performed using numerical solutions to the full wave equation. Modeling of acoustic, elastic, and electromagnetic waves can be implemented using various methods including, finite-differences (Taflove and Brodwin 1975; Vidale and Clayton 1986; Graves 1996), spectral element (Tromp et al. 2005; Liu and Tromp 2006), finite elements (Marfurt 1984; Jin 1993), or integral equation solutions (Harrington 1968; Zwamborn et al. 1992; Bleszynsky et al. 1996; Fang et al. 2006). Numerical techniques simulate the full physics of wave propagation in heterogeneous media but generally have substantially higher computational requirements.

In contrast to finite-difference or finite element methods, the integral equation method produces a dense matrix. Using a direct method such as Gaussian elimination or LU decomposition to solve the matrix equation generally requires $O(N^3)$ operations and $O(N^2)$ in memory, where N is the number unknowns. For large scale problems using direct solvers would require very long computational run times. Iterative methods, such as conjugate gradient or other Krylov subspace methods, can often reduce the computational burden to $O(N^2)$. When the domain is uniformly discretized, the forward model matrix exhibits a Toeplitz form and can be readily recast as a circulant matrix. Circulant matrices have the useful property that their product

with a vector can be performed using a fast Fourier transform (FFT). When used in combination with an iterative method, the time required to solve the matrix equations can be reduced to O(NlogN) (Gan and Chew 1994; Fang et. al 2006). Compared to other numerical methods that exhibit $O(N^2)$ scaling, the computation savings can be substantial for large numbers of unknowns. The primary drawbacks to the FFT based fast solvers are that the number of grid points needs to be doubled in each dimension and that the grid block geometry is not as flexible as other methods (e.g. tetrahedral finite elements).

Each of the forward modeling methods provide a relationship between the modeled material properties and the simulated wave field data. Given a set of material properties the wave field can be calculated. The inverse problem aims to reverse this process and find the optimum set of model parameters that reproduces a collection of observed data. This optimization is commonly performed by linearizing the forward problem around an assumed model of the material properties.

The sensitivity kernel is specified by calculating changes to the simulated data due to small changes in the model parameters. In the limit as the change in a model parameter tends to zero, these are termed Fréchet derivatives (Tarantola 1987). The gradient of the forward model functional is the collection of Fréchet derivatives taken with respect to all combinations of model parameters and simulated data. This functional gradient can be explicitly specified as the sensitivity or Jacobian matrix to produce a linear system of equations which can be solved to determine the model parameters that fit the observed data. Various methods for solving linear systems can be employed such as direct, iterative, and gradient based methods. For gradient inversion approaches, an adjoint state method can be used to calculate the forward model gradient without explicitly determining the Fréchet derivatives (Chavent 1974; Plessix 2006). For large scale problems, adjoint state methods are computationally more efficient than direct methods since they do not need to explicitly calculate the Jacobian matrix. The main drawback is that the sensitivity of the inverse solution to errors cannot be easily determined.

The motivation for this work stems in part from a U.S. Department of Energy (USDOE) program investigating the use of geophysical methods to monitor near-surface environmental remediation technologies on the USDOE's Hanford nuclear reservation in southeast Washington State. Cross-borehole georadar, electrical resistivity and seismic methods were utilized to monitor hydraulic isolation technologies such as in situ drying (desiccation) of contaminated

sediments and surface infiltration barriers. Additional funding for this work was provided by the USDOE to develop subsurface monitoring technologies for carbon capture and storage (CCS) and geothermal energy applications. Two of the primary objectives of this work are to provide improved 3D imaging by incorporating finite-frequency effects, as well as separately estimating changes in the underlying material properties (e.g. electrical permittivity and conductivity). By doing so the ultimate goal is to better determine 3D changes in fluid saturation that occurs in response to fluid injection or extraction.

This work explores the use of integral equation based methods for wave propagation simulation and inversion and illustrates their potential for computationally demanding problems. A frequency-domain volume integral equation method to both simulate wave-propagation in heterogeneous media and solve the inverse wave-scattering problem is presented. A computationally efficient method is developed for elastic, acoustic, and electromagnetic systems. The volume integral equation method is used to simulate electromagnetic fields in 3D and the performance evaluated relative to other simulation methods. Frequency-domain full waveform inversion of simulated georadar data is then performed and compared to results derived using ray-theory. Rather than inverting for just EM velocity, I solve for the underlying material properties (e.g. electrical permittivity and conductivity). A broad range of frequencies in the data are utilized to both lessen the inherent non-linearity of the inverse problem (Pratt 1999; Meles 2010) and improve individual estimates of material properties that exhibit frequency dependent sensitivities. As with most non-linear inversion methods, a starting model that reasonably approximates the true model is critical to convergence of the algorithm. To improve the starting model, a variable reference inversion technique is developed that allows the background reference medium to vary for each source-receiver data pair and is less restrictive than using a single reference medium for the entire dataset. The reference medium can be assumed homogeneous (although different for each data point) to provide a computationally efficient, single-step, frequency-domain inversion approach that incorporates finite frequency effects not captured by ray based methods. The full waveform method can then be iterated on to refine the reconstructed image.

2 THEORETICAL DEVELOPMENT

In this section I will review the development of an integral equation solution to a general linear differential equation using a perturbation approach. I will then present a method for computing the forward model that exploits the circulant symmetry of the resulting equations. Circulant matrices arise from many physical systems, including wave propagation problems, and are a central component to fast solution algorithms. Next, I will discuss the data sensitivity matrix that also uses the symmetry of the resulting matrix to efficiently solve the inverse problem for some cases by efficiently calculating the inverse of the forward problem matrix. In the following chapters, the methods will be applied to electromagnetic and elastic wave propagation problems.

2.1 THE FORWARD PROBLEM

2.1.1 Green's Functions

Consider a general system governed by the linear differential operator, **L**, expressed in the frequency domain. Extension of the results can be adapted to the time domain using the Fourier transform and the following derivations therefore suppress the frequency dependence for brevity.

$$\mathbf{L}(\mathbf{r})\cdot\boldsymbol{\psi}(\mathbf{r})=\mathbf{s}(\mathbf{r});\qquad \mathbf{r}\in V \tag{2.1}$$

Where $\boldsymbol{\psi}$ corresponds to the solution, **r** the position vector, and **s** is a source function. The Fourier convention used here is that adopted by *Dahlen & Tromp 1998*, for any real function of time that is zero prior to t=0.

$$F(\omega)=\int_0^\infty f(t)e^{-i\omega t}\,dt \tag{2.2}$$

$$f(t)=\frac{1}{\pi}\mathrm{Re}\left[\int_0^\infty F(\omega)e^{i\omega t}\,d\omega\right] \tag{2.3}$$

$$F(-\omega)=F^*(\omega) \tag{2.4}$$

Equation (2.1) is applicable to any physical system governed by a scalar, vector, or tensor valued linear differential equation. The multiplication operator denotes either tensor contraction for vector and tensor cases or simple multiplication for scalars. In addition, linear boundary

conditions will be specified on the bounding surface ***S*** that can include internal surfaces. Homogeneous boundary conditions are specified when right-hand side of equation (2.5) is equal to zero.

$$\mathbf{B}(\mathbf{r})\cdot\boldsymbol{\psi}(\mathbf{r})=\mathbf{f}(\mathbf{r});\qquad \mathbf{r}\in S \tag{2.5}$$

Green's functions are important tools for solving inhomogeneous differential equations. The Green's function corresponds to the solution of a linear differential equation with a point source located at **r**' and that also satisfies the associated boundary conditions. For scalar sources, the Green's function is scalar valued but when both the source and solution are vectors, the Green's function is tensor valued.

$$\mathbf{L}(\mathbf{r})\cdot\mathbf{G}(\mathbf{r},\mathbf{r}')=\mathbf{I}\delta(\mathbf{r}-\mathbf{r}') \tag{2.6}$$

Green's functions can be used to obtain a solution due to a general source by linear superposition. The solution to the linear differential equation that first satisfies homogeneous boundary conditions can be determined using the Green's function as follows. First multiply both sides of equation (2.6) by the source term and integrate over a volume, V that contains the support of volume source term.

$$\mathbf{L}(\mathbf{r})\cdot\mathbf{G}(\mathbf{r},\mathbf{r}')\cdot\mathbf{s}(\mathbf{r}')=\mathbf{I}\cdot\delta(\mathbf{r}-\mathbf{r}')\cdot\mathbf{s}(\mathbf{r}') \tag{2.7}$$

$$\int_V \mathbf{L}(\mathbf{r})\cdot\mathbf{G}(\mathbf{r},\mathbf{r}')\cdot\mathbf{s}(\mathbf{r}')\,dV'=\int_V \mathbf{I}\cdot\delta(\mathbf{r}-\mathbf{r}')\cdot\mathbf{s}(\mathbf{r}')dV'=\mathbf{s}(\mathbf{r}) \tag{2.8}$$

The differential operator **L** acts only on the unprimed coordinates so that the order of operations can be exchanged with the integration. First, for homogeneous boundary conditions, the right-hand side of equation(2.7) can be simplified using the property of the Dirac delta function and the solution identified.

$$\mathbf{L}(\mathbf{r})\cdot\int_V \mathbf{G}(\mathbf{r},\mathbf{r})\cdot\mathbf{s}(\mathbf{r}')dV'=\mathbf{s}(\mathbf{r}) \tag{2.9}$$

$$\boldsymbol{\psi}(\mathbf{r})=\int_V \mathbf{G}(\mathbf{r},\mathbf{r}')\cdot\mathbf{s}(\mathbf{r}')\,dV' \tag{2.10}$$

When the boundary conditions are inhomogeneous, the Green's function is given by a linear combination of the Green's function that satisfies both the inhomogeneous differential equation and homogeneous boundary conditions designated by the subscript IH along with a second

function that satisfies the homogeneous differential equation and inhomogeneous boundary conditions designated by the subscript HI.

$$\mathbf{G}(\mathbf{r},\mathbf{r}') = \mathbf{G}_{IH}(\mathbf{r},\mathbf{r}') + \mathbf{G}_{HI}(\mathbf{r},\mathbf{r}') \tag{2.11}$$

$$\mathbf{L}(\mathbf{r}) \cdot \mathbf{G}_{IH}(\mathbf{r},\mathbf{r}') = \mathbf{I}\delta(\mathbf{r}-\mathbf{r}') \tag{2.12}$$

$$\mathbf{L}(\mathbf{r}) \cdot \mathbf{G}_{HI}(\mathbf{r},\mathbf{r}') = 0 \tag{2.13}$$

$$\mathbf{B}(\mathbf{r}) \cdot \mathbf{G}_{IH}(\mathbf{r},\mathbf{r}') = 0 \tag{2.14}$$

$$\mathbf{B}(\mathbf{r}) \cdot \mathbf{G}_{HI}(\mathbf{r},\mathbf{r}') = \mathbf{f}(\mathbf{r}) \tag{2.15}$$

$$\mathbf{L}(\mathbf{r}) \cdot \mathbf{G}(\mathbf{r},\mathbf{r}') = \mathbf{L}(\mathbf{r}) \cdot \left(\mathbf{G}_{IH}(\mathbf{r},\mathbf{r}') + \mathbf{G}_{HI}(\mathbf{r},\mathbf{r}')\right) = \mathbf{I}\delta(\mathbf{r}-\mathbf{r}') \tag{2.16}$$

$$\mathbf{B}(\mathbf{r}) \cdot \mathbf{G}(\mathbf{r},\mathbf{r}') = \mathbf{B}(\mathbf{r}) \cdot \left(\mathbf{G}_{IH}(\mathbf{r},\mathbf{r}') + \mathbf{G}_{HI}(\mathbf{r},\mathbf{r}')\right) = \mathbf{f}(\mathbf{r}) \tag{2.17}$$

The solution that satisfies both the inhomogeneous differential equation and the inhomogeneous boundary conditions can be obtained.

$$\boldsymbol{\psi}(\mathbf{r}) = \int_V \mathbf{G}_{IH}(\mathbf{r},\mathbf{r}') \cdot \mathbf{s}(\mathbf{r}')\, dV' + \int_V \mathbf{G}_{HI}(\mathbf{r},\mathbf{r}') \cdot \mathbf{s}(\mathbf{r}')\, dV' \tag{2.18}$$

Several methods for evaluating Green's functions exist; however analytic expressions can only be obtained for a few specialized cases. One case that will be used throughout this paper is the Green's function for the scalar Helmholtz equation in homogeneous media with radiation boundary conditions: the 3D whole-space scalar Green's function (Ward and Hohmann 1988).

$$g_b(r,r',\omega) = \frac{e^{-i\kappa_b|r-r'|}}{4\pi|r-r'|} \tag{2.19}$$

Tensor or dyadic whole-space Green's function derivations make use of the whole-space scalar Helmholtz equation Green's function. Green's functions for elastic and electromagnetic wave propagation applications will be utilized throughout this work.

2.1.2 Representation Theorem

Green's functions can be used to simplify a more complicated problem using a representation or uniqueness theorem that can be derived starting with two solutions to the differential equation corresponding to different source terms. Representation theorems of either the correlation or

convolution type are commonly used (Wapenaar and Fokkema 2006). The relationship between the source-solution pairs is known as a reciprocity theorem and if one solution is specified to be the Green's function then the relationship becomes a representation theorem.

$$\mathbf{L}(\mathbf{r})\cdot\boldsymbol{\psi}_1(\mathbf{r})=\mathbf{s}_1(\mathbf{r}) \tag{2.20}$$

$$\mathbf{L}(\mathbf{r})\cdot\boldsymbol{\psi}_2(\mathbf{r})=\mathbf{s}_2(\mathbf{r}) \tag{2.21}$$

A general convolution type reciprocity theorem for the linear operator defined in equations (2.20) and (2.21) will be derived. First, multiply equation (2.20) by $\boldsymbol{\psi}_2$ and equation (2.21) by $\boldsymbol{\psi}_1$ then subtract and integrate the resulting equation over the support volume V.

$$\begin{aligned}\int_V\left[\boldsymbol{\psi}_2^T(\mathbf{r})\cdot\mathbf{L}(\mathbf{r})\cdot\boldsymbol{\psi}_1(\mathbf{r})-\boldsymbol{\psi}_1^T(\mathbf{r})\cdot\mathbf{L}(\mathbf{r})\cdot\boldsymbol{\psi}_2(\mathbf{r})\right]dV\\ =\int_V\left[\boldsymbol{\psi}_2^T(\mathbf{r})\cdot\mathbf{s}_1(\mathbf{r})-\boldsymbol{\psi}_1^T(\mathbf{r})\cdot\mathbf{s}_2(\mathbf{r})\right]dV\end{aligned} \tag{2.22}$$

In many applications it is useful to convert the volume integrals into surface integrals over a surface bounding the volume including any internal cavities. Conversion from volume to surface integration illustrates the effects of the boundary conditions and can be used to simplify the reciprocal or representation theorem (Lanczos 1996). The adjoint operator $\mathbf{L}^\dagger$ is specified as the unique operator that satisfies the following extended or generalized Green's identity

$$\begin{aligned}\int_V\left[\boldsymbol{\psi}_2^T(\mathbf{r})\cdot\mathbf{L}(\mathbf{r})\cdot\boldsymbol{\psi}_1(\mathbf{r})-\boldsymbol{\psi}_1^T(\mathbf{r})\cdot\mathbf{L}^\dagger(\mathbf{r})\cdot\boldsymbol{\psi}_2(\mathbf{r})\right]dV\\ =\oint_S\left[\mathbf{Z}_{\mathbf{L}}\left(\boldsymbol{\psi}_1(\mathbf{r}),\boldsymbol{\psi}_2(\mathbf{r})\right)\right]\cdot\mathbf{n}dS\end{aligned} \tag{2.23}$$

The term on the right hand vanishes for a self adjoint operator and thus captures non-self adjoint aspects of the operator. A general operator can be decomposed as the sum of the complex conjugated adjoint operator and the remainder. The reciprocity theorem can then also be decomposed into volume and surface integral terms.

$$\mathbf{L}(\mathbf{r})=\mathbf{L}^\dagger(\mathbf{r})+\left(\mathbf{L}(\mathbf{r})-\mathbf{L}^\dagger(\mathbf{r})\right) \tag{2.24}$$

$$\begin{aligned}\int_V\left[\boldsymbol{\psi}_2^T(\mathbf{r})\cdot\mathbf{s}_1(\mathbf{r})-\boldsymbol{\psi}_1^T(\mathbf{r})\cdot\mathbf{s}_2(\mathbf{r})\right]dV\\ =\oint_S\left[\mathbf{Z}_{\mathbf{L}}\left(\boldsymbol{\psi}_1(\mathbf{r}),\boldsymbol{\psi}_2(\mathbf{r})\right)\right]\cdot\mathbf{n}dS-\int_V\left[\boldsymbol{\psi}_1^T(\mathbf{r})\cdot\left(\mathbf{L}(\mathbf{r})-\mathbf{L}^\dagger(\mathbf{r})\right)\cdot\boldsymbol{\psi}_2(\mathbf{r})\right]dV\end{aligned} \tag{2.25}$$

Green's tensors give the solutions to equations (2.20) and (2.21) corresponding to point sources at locations $\mathbf{r_1}$ and $\mathbf{r_2}$ and acting along the $\boldsymbol{p}$ and $\boldsymbol{q}$ directions respectively. Summation over repeated indices is used in the following.

$$L_{ij}(\mathbf{r})G_{jp}(\mathbf{r},\mathbf{r}_1)=\delta_{ip}\delta(\mathbf{r}-\mathbf{r}_1) \tag{2.26}$$

$$L_{ij}(\mathbf{r})G_{jq}(\mathbf{r},\mathbf{r}_2)=\delta_{iq}\delta(\mathbf{r}-\mathbf{r}_2) \tag{2.27}$$

When the second term on the right of equation (2.25) is equal to zero and the boundary conditions are such that the surface integral is also zero, equation (2.25) gives rise to reciprocity of the Green's function.

$$\begin{aligned}&\int_V\left[G_{qi}(\mathbf{r},\mathbf{r}_2)\,\delta_{ip}\delta(\mathbf{r}-\mathbf{r}_1)-G_{pi}(\mathbf{r},\mathbf{r}_2)\,\delta_{iq}\delta(\mathbf{r}-\mathbf{r}_1)\right]dV=0\\&G_{qp}(\mathbf{r}_2,\mathbf{r}_1)=G_{pq}(\mathbf{r}_1,\mathbf{r}_2)\\&\mathbf{G}(\mathbf{r}_2,\mathbf{r}_1)=\mathbf{G}^T(\mathbf{r}_1,\mathbf{r}_2)\end{aligned} \tag{2.28}$$

As an example of the simplification to the reciprocal theorem using equation(2.25), consider the scalar Helmholtz equation.

$$\nabla^2\phi_1(r,\omega)+\kappa^2(r,\omega)\phi_1(r,\omega)=s_1(r,\omega) \tag{2.29}$$

$$\nabla^2\phi_2(r,\omega)+\kappa^2(r,\omega)\phi_2(r,\omega)=s_2(r,\omega) \tag{2.30}$$

Substituting the operator corresponding to the Helmholtz equation into equation (2.22) gives

$$\begin{aligned}&\int_V\left[\phi_2(r,\omega)\nabla^2\phi_1(r,\omega)-\phi_1(r,\omega)\nabla^2\phi_2(r,\omega)\right]dV\\&\quad=\int_V\nabla\cdot\left[\phi_2(r,\omega)\nabla\phi_1(r,\omega)-\phi_1(r,\omega)\nabla\phi_2(r,\omega)\right]dV\\&\qquad=\int_S\mathbf{n}\cdot\left[\phi_2(r,\omega)\nabla\phi_1(r,\omega)-\phi_1(r,\omega)\nabla\phi_2(r,\omega)\right]dS\end{aligned} \tag{2.31}$$

$$\begin{aligned}&\int_S\mathbf{n}\cdot\left[\phi_2(r,\omega)\nabla\phi_1(r,\omega)-\phi_1(r,\omega)\nabla\phi_2(r,\omega)\right]dS\\&\quad=\int_V\left[s_1(r,\omega)\phi_2(r,\omega)-s_2(r,\omega)\phi_1(r,\omega)\right]dV\end{aligned} \tag{2.32}$$

Gauss' theorem has been used to transform the volume integrals into equivalent surface integral; potentials, ϕ, are scalar valued and gradients of the potentials are vector quantities. Equation (2.32) holds for any volume and the surface integral on the left hand side provides a

means to incorporate the effects of the boundary conditions at surface **S** on the solution. If both solutions satisfy the same homogeneous boundary conditions on the surface S then the surface integral vanishes. This can happen if either the solutions themselves or their gradients are zero on the surface. Also, if the integration volume is infinite and the solutions are constrained to be zero at infinity (radiation boundary conditions) then the surface integral once again vanishes.

If both source terms are point sources located at $\mathbf{r_1}$ and $\mathbf{r_2}$ and the associated Green's function or its gradient is zero on the bounding surface, then the Green's function satisfies homogeneous boundary conditions and reciprocity holds.

$$\begin{aligned} &\int_V \left[\delta(r-r_1) g_b(r,r_2,\omega)\right] dV = \int_V \left[\delta(r-r_2) g_b(r,r_1,\omega)\right] dV \\ &g_b(r_1,r_2,\omega) = g_b(r_2,r_1,\omega) \end{aligned} \tag{2.33}$$

Now if $\mathbf{s_2}$ is a concentrated point source, φ_2 is again the Green's function and equation (2.32) gives the integral solution for the φ_1, where $\mathbf{r_2}$ has been relabeled as **r'**.

$$\begin{aligned} \phi_1(r',\omega) = &\int_V s_1(r,\omega) g_b(r,r',\omega) dV \\ &- \int_S \mathbf{n} \cdot \left[g_b(r,r',\omega) \nabla \phi_1(r,\omega) - \phi_1(r,\omega) \nabla g_b(r,r',\omega) \right] dS \end{aligned} \tag{2.34}$$

Due to reciprocity of the Green's function; the primed and unprimed coordinates can be exchanged and equation (2.34) becomes

$$\begin{aligned} \phi_1(r,\omega) = &\int_V s_1(r',\omega) g_b(r,r',\omega) dV' \\ &- \int_S \mathbf{n} \cdot \left[g_b(r,r',\omega) \nabla \phi_1(r',\omega) - \phi_1(r',\omega) \nabla g_b(r,r',\omega) \right] dS' \end{aligned} \tag{2.35}$$

Once again Gauss' theorem has been used to transform the volume integrals into equivalent surface integral; potentials, ϕ, and Green function, g, are scalar valued and gradients are vector quantities. The integral solution derived using the representation theorem is the sum of volume and surface integral terms. The complete solution can then be interpreted as due to the sum of both volume and equivalent surface sources. The integration volume is arbitrary and while the Green's function has been constrained to satisfy homogeneous boundary conditions, the solution can have any value at the bounding surface. If, however the solution satisfies the same homogeneous boundary conditions with the Green's function, the surface integral vanishes. The

remainder of this paper will focus on whole-space problems using volume integral solutions to the wave equation that satisfy homogeneous boundary conditions.

2.1.3 Lippmann-Schwinger Equation

In this section, I will develop the equations describing the integral solution to the wave equation in heterogeneous media using a perturbation approach. First, decompose both the differential equation and boundary conditions operators into the sum of two linear operators.

$$\mathbf{L}(\mathbf{r}) = \mathbf{L}_0(\mathbf{r}) + \mathbf{P}_0(\mathbf{r}) \tag{2.36}$$

$$\mathbf{B}(\mathbf{r}) = \mathbf{B}_0(\mathbf{r}) + \boldsymbol{\beta}_0(\mathbf{r}) \tag{2.37}$$

The above decomposition is completely general and at this stage makes no assumptions as to the magnitude of one term relative to the other. The only requirement is that the sum be equal to the original operator. The numbered subscript is used for both terms in order to identify that each of the terms are linked to each other; if one term is changed the other term must then oppositely change to keep the sum the same. The naming convention that will be followed specifies $\mathbf{L_0}$, $\mathbf{P_0}$, $\boldsymbol{\psi}$, $\boldsymbol{\psi}_0$, $\mathbf{B}$ and $\boldsymbol{\beta_0}$ as the unperturbed operator, perturbation operator, perturbed solution, unperturbed solution, perturbed boundary conditions and boundary condition perturbation, respectively. Unless explicitly stated, both the boundary conditions and unperturbed boundary conditions will be homogeneous. The boundary condition perturbation can, however, be inhomogeneous. The unperturbed field is then a solution to the unperturbed equation.

$$\mathbf{L}_0(\mathbf{r}) \cdot \boldsymbol{\psi}_0(\mathbf{r}) = \mathbf{s}(\mathbf{r}); \quad \mathbf{r} \in V \tag{2.38}$$

$$\mathbf{B}_0(\mathbf{r}) \cdot \boldsymbol{\psi}_0(\mathbf{r}) = 0; \quad \mathbf{r} \in S \tag{2.39}$$

$$\boldsymbol{\psi}_0(\mathbf{r}) = \int_V \mathbf{G}_0(\mathbf{r}, \mathbf{r}'') \cdot \mathbf{s}(\mathbf{r}'')\, dV'' \tag{2.40}$$

The unperturbed Green's function, $\mathbf{G_0}$, satisfies the following equation.

$$\mathbf{L}_0(\mathbf{r}) \cdot \mathbf{G}_0(\mathbf{r}, \mathbf{r}') = \mathbf{I} \cdot \boldsymbol{\delta}(\mathbf{r} - \mathbf{r}') \tag{2.41}$$

$$\mathbf{B}_0(\mathbf{r}) \cdot \mathbf{G}_0(\mathbf{r}, \mathbf{r}') = 0; \quad \mathbf{r} \in S \tag{2.42}$$

Equation (2.6) can be re-written after substituting the operator decomposition from equations (2.36) and (2.37)

$$\left[\mathbf{L}_0(\mathbf{r})+\mathbf{P}_0(\mathbf{r})\right]\cdot\mathbf{G}(\mathbf{r},\mathbf{r}')=\mathbf{I}\cdot\boldsymbol{\delta}(\mathbf{r}-\mathbf{r}') \tag{2.43}$$

$$\mathbf{L}_0(\mathbf{r})\cdot\mathbf{G}(\mathbf{r},\mathbf{r}')=\mathbf{I}\cdot\boldsymbol{\delta}(\mathbf{r}-\mathbf{r}')-\mathbf{P}_0(\mathbf{r})\cdot\mathbf{G}(\mathbf{r},\mathbf{r}') \tag{2.44}$$

$$\mathbf{B}(\mathbf{r})=\left[\mathbf{B}_0(\mathbf{r})+\boldsymbol{\beta}_0(\mathbf{r})\right]\cdot\mathbf{G}(\mathbf{r},\mathbf{r}')=0$$

$$\mathbf{B}_0(\mathbf{r})\cdot\mathbf{G}(\mathbf{r},\mathbf{r}')=-\boldsymbol{\beta}_0(\mathbf{r})\cdot\mathbf{G}(\mathbf{r},\mathbf{r}') \tag{2.45}$$

The differential operator acting on the left hand side of equation (2.44) is same as the unperturbed Green's function equation; however equations (2.41) and (2.44) have different source terms. In addition, the boundary condition perturbation gives rise to an additional source term. By incorporating the right-hand side of equations (2.44) and (2.45) into (2.18) one obtains the relationship between the perturbed and unperturbed Green's functions and is known as the Lippmann-Schwinger equation (Rodberg & Thaler 1967; Dahlen et al. 2000; Sneider 2002; Fleury et al. 2010). The double-prime integration variable in the following has been used so as to avoid confusion with subsequent volume integrals.

$$\begin{aligned}\mathbf{G}(\mathbf{r},\mathbf{r}')=&\int_V\mathbf{G}_0(\mathbf{r},\mathbf{r}'')\cdot\mathbf{I}\cdot\boldsymbol{\delta}(\mathbf{r}-\mathbf{r}')\,dV''+\mathbf{G}_{HI}(\mathbf{r},\mathbf{r}')\\&-\int_V\mathbf{G}_0(\mathbf{r},\mathbf{r}'')\cdot\mathbf{P}_0(\mathbf{r}'')\cdot\mathbf{G}(\mathbf{r}'',\mathbf{r}')\,dV''\end{aligned} \tag{2.46}$$

$$\mathbf{G}(\mathbf{r},\mathbf{r}')=\mathbf{G}_0(\mathbf{r},\mathbf{r}')+\mathbf{G}_{HI}(\mathbf{r},\mathbf{r}')-\int_V\mathbf{G}_0(\mathbf{r},\mathbf{r}'')\cdot\mathbf{P}_0(\mathbf{r}'')\cdot\mathbf{G}(\mathbf{r}'',\mathbf{r}')\,dV'' \tag{2.47}$$

$$\mathbf{B}_0(\mathbf{r})\cdot\mathbf{G}_{HI}(\mathbf{r},\mathbf{r}')=-\boldsymbol{\beta}_0(\mathbf{r})\cdot\mathbf{G}(\mathbf{r},\mathbf{r}') \tag{2.48}$$

It is straight forward to show that equation (2.47) satisfies both the perturbed differential equation and the associated boundary conditions by substituting the result into equations (2.6) and (2.45). Making use of the Green's function reciprocity equation (2.47) can also be written as

$$\mathbf{G}(\mathbf{r},\mathbf{r}')=\mathbf{G}_0(\mathbf{r},\mathbf{r}')+\mathbf{G}_{HI}(\mathbf{r},\mathbf{r}')-\int_V\mathbf{G}_0^T(\mathbf{r}'',\mathbf{r})\cdot\mathbf{P}_0(\mathbf{r}'')\cdot\mathbf{G}(\mathbf{r}'',\mathbf{r}')\,dV'' \tag{2.49}$$

Unfortunately the perturbed Green's function appears on both sides of the equation and cannot be easily solved as presently formulated.

The integral solution to the general differential equation can also be obtained by substituting the Green's function into equation(2.10).

$$\boldsymbol{\psi}(\mathbf{r}) = \int_V \left[\mathbf{G}_0(\mathbf{r},\mathbf{r}') + \mathbf{G}_{HI}(\mathbf{r},\mathbf{r}') - \int_V \mathbf{G}_0(\mathbf{r},\mathbf{r}'') \cdot \mathbf{P}_0(\mathbf{r}'') \cdot \mathbf{G}(\mathbf{r}'',\mathbf{r}')\, dV'' \right] \cdot \mathbf{s}(\mathbf{r}')\, dV' \tag{2.50}$$

$$\begin{aligned} \boldsymbol{\psi}(\mathbf{r}) = & \int_V \mathbf{G}(\mathbf{r}'',\mathbf{r}') \cdot \mathbf{s}(\mathbf{r}') dV' + \int_V \mathbf{G}_{HI}(\mathbf{r}'',\mathbf{r}') \cdot \mathbf{s}(\mathbf{r}') dV' \\ & - \int_V \mathbf{G}_0(\mathbf{r},\mathbf{r}'') \cdot \mathbf{P}_0(\mathbf{r}'') \cdot \int_V \left[\mathbf{G}(\mathbf{r}'',\mathbf{r}') \cdot \mathbf{s}(\mathbf{r}') dV' \right] dV'' \end{aligned} \tag{2.51}$$

$$\begin{aligned} \boldsymbol{\psi}(\mathbf{r}) = & \int_V \mathbf{G}_0(\mathbf{r},\mathbf{r}') \cdot \mathbf{s}(\mathbf{r}')\, dV' + \int_V \mathbf{G}_{HI}(\mathbf{r}'',\mathbf{r}') \cdot \mathbf{s}(\mathbf{r}') dV' \\ & - \int_V \mathbf{G}_0(\mathbf{r},\mathbf{r}'') \cdot \mathbf{P}_0(\mathbf{r}'') \cdot \boldsymbol{\psi}(\mathbf{r}'')\, dV'' \end{aligned} \tag{2.52}$$

$$\begin{aligned} \boldsymbol{\psi}(\mathbf{r}) = & \boldsymbol{\psi}_0(\mathbf{r}) + \int_V \mathbf{G}_{HI}(\mathbf{r}'',\mathbf{r}') \cdot \mathbf{s}(\mathbf{r}') dV'' \\ & - \int_V \mathbf{G}_0(\mathbf{r},\mathbf{r}'') \cdot \mathbf{P}_0(\mathbf{r}'') \cdot \boldsymbol{\psi}(\mathbf{r}'')\, dV'' \end{aligned} \tag{2.53}$$

$$\begin{aligned} \boldsymbol{\psi}(\mathbf{r}) = & \boldsymbol{\psi}_0(\mathbf{r}) + \int_V \mathbf{G}_{HI}(\mathbf{r}'',\mathbf{r}') \cdot \mathbf{s}(\mathbf{r}') dV'' \\ & - \int_V \mathbf{G}_0^T(\mathbf{r}'',\mathbf{r}) \cdot \mathbf{P}_0(\mathbf{r}'') \cdot \boldsymbol{\psi}(\mathbf{r}'')\, dV'' \end{aligned} \tag{2.54}$$

When the boundary conditions are unperturbed, equations (2.47) and (2.53) simplify to the following:

$$\mathbf{G}(\mathbf{r},\mathbf{r}') = \mathbf{G}_0(\mathbf{r},\mathbf{r}') - \int_V \mathbf{G}_0(\mathbf{r},\mathbf{r}'') \cdot \mathbf{P}_0(\mathbf{r}'') \cdot \mathbf{G}(\mathbf{r}'',\mathbf{r}')\, dV'' \tag{2.55}$$

$$\boldsymbol{\psi}(\mathbf{r}) = \boldsymbol{\psi}_0(\mathbf{r}) - \int_V \mathbf{G}_0(\mathbf{r},\mathbf{r}'') \cdot \mathbf{P}_0(\mathbf{r}'') \cdot \boldsymbol{\psi}(\mathbf{r}'')\, dV'' \tag{2.56}$$

One commonly employed method for evaluating equation (2.56) is to assume that the perturbed Green's function present in the volume integral term is roughly equal to the unperturbed Green's function. This is termed the Born approximation and provides a means to calculate the perturbed Green's function using only the unperturbed Green's function and perturbation operator.

$$\boldsymbol{\psi}(\mathbf{r}) = \boldsymbol{\psi}_0(\mathbf{r}) - \int_V \mathbf{G}_0(\mathbf{r},\mathbf{r}'') \cdot \mathbf{P}_0(\mathbf{r}'') \cdot \boldsymbol{\psi}_0(\mathbf{r}'')\, dV'' \tag{2.57}$$

In the following sections, equation (2.47) will be discretized and reformulated to provide a computationally efficient means to compute the perturbed Green's function under specific conditions without requiring the use of the Born approximation.

2.1.4 Matrix Formulation

A general approach to approximate a continuous integral equation with a finite linear system is the method of weighted residuals. Consider the continuous integral equation

$$\mathbf{Lu} = \mathbf{f} \tag{2.58}$$

The solution is then approximated by a linear combination of N expansion functions $\mathbf{f}_n$

$$\mathbf{u} \simeq \hat{\mathbf{u}} = \sum_{n=1}^{N} a_n \mathbf{f}_n \tag{2.59}$$

The objective is to determine the expansion coefficients a_n such that the error between the numerical and exact solutions is minimized. To do this the numerical solution (2.59) is substituted into the integral equation (2.58) and the residual is given by

$$\mathbf{r} = \mathbf{L}\hat{\mathbf{u}} - \mathbf{f} \tag{2.60}$$

The residual is then discretized by forming inner products with M weighting functions $\mathbf{t}_m$ and the result is set equal to zero

$$\langle \mathbf{t}_m, \mathbf{r} \rangle = \left\langle \mathbf{t}_m, \mathbf{L}\left(\sum_{n=1}^{N} a_n \mathbf{f}_n \right) - \mathbf{f} \right\rangle = 0 \tag{2.61}$$

Due to the linearity of the integral operator **L**, equation (2.61) can be rearranged to obtain a system of M linear equations with N unknowns

$$\begin{aligned} &\left\langle \mathbf{t}_m, \mathbf{L}\left(\sum_{n=1}^{N} a_n \mathbf{f}_n \right) \right\rangle = \langle \mathbf{t}_m, \mathbf{f} \rangle \\ &\sum_{n=1}^{N} \langle \mathbf{t}_m, \mathbf{L}\mathbf{f}_n \rangle a_n = \langle \mathbf{t}_m, \mathbf{f} \rangle \end{aligned} \tag{2.62}$$

The left hand side of equation (2.62) is the product of a matrix with M rows and N columns and a column vector with N elements. The right hand side is simply a column vector with length M.

Basis functions that are commonly used include pulse, triangle, and mixed types. Various combinations of the expansion and testing basis function lead to different classes of numerical methods. Galerkin's method uses the same basis functions for both expansion and testing, least squares methods set the testing functions equal to the product of the linear operator and the expansion functions, and collocation methods use delta functions for the testing basis.

Turning now to the problem of solving (2.57) the integration volume will be divided into N cells that contain the support of the perturbation. An accurate solution requires that the largest dimension of the grid cell be much smaller than the wavelength of the solution at each cell (Ishimaru 1978). The final step is then to discretize the perturbation, as well as both the unperturbed and perturbed Green's functions to produce a system of equations that can be used to numerically calculate the total solution.

The perturbation operator will be assumed constant in each grid cell and the elements of the Green's function matrix are determined using the method of weighted residuals using equation (2.62). For instance using the collocation methods with pulse expansions functions, the Green's function at location $\boldsymbol{r_j}$ due to a point source at $\boldsymbol{r_s}$ is given by the following

$$\mathbf{G}(\mathbf{r}_j,\mathbf{r}_s)=\mathbf{G}_0(\mathbf{r}_j,\mathbf{r}_s)-\sum_i^N\left[\int_V \mathbf{G}_0(\mathbf{r}_j,\mathbf{r}_i)\,dV_i\right]\cdot\mathbf{P}_0(\mathbf{r}_i)\cdot\mathbf{G}(\mathbf{r}_i,\mathbf{r}_s) \tag{2.63}$$

Equation (2.63) can now be cast in matrix form where the perturbation, $\boldsymbol{P}$, is a matrix containing the discrete grid point perturbation operator. The elements in matrix $\boldsymbol{G}$ are the integrals of the tensor Green's function for each of N grid cells within the perturbed media volume. The dot operator will also be used for matrix multiplication in the following equations.

$$\mathbf{G}_{ij}=\mathbf{G}(\mathbf{r}_i,\mathbf{r}_j) \tag{2.64}$$

$$\mathbf{G}=\mathbf{G}_0-\mathbf{G}_0\cdot\mathbf{P}_0\cdot\mathbf{G} \tag{2.65}$$

$$\mathbf{A}\cdot\mathbf{G}=\mathbf{b};\quad \mathbf{A}=\left[\mathbf{I}+\mathbf{G}_0\cdot\mathbf{P}_0\right],\ \mathbf{b}=\mathbf{G}_0 \tag{2.66}$$

The matrix $\boldsymbol{G_0}$ is N by N, and fully populated which for large N would make the system of equations in (2.66) computationally difficult to solve. For tensor or vector cases in 3 dimensions, each element of $\boldsymbol{G_0}$ is actually a sub matrix that contains the 3 by 3 elements of the integrated Green's tensor.

The matrix formulation for equation (2.53) can be obtained in a similar fashion

$$\mathbf{G}\cdot\mathbf{s}=\mathbf{G}_0\cdot\mathbf{s}-\mathbf{G}_0\cdot\mathbf{P}_0\cdot\mathbf{G}\cdot\mathbf{s} \tag{2.67}$$

$$\boldsymbol{\psi}=\boldsymbol{\psi}_0-\mathbf{G}_0\cdot\mathbf{P}_0\cdot\boldsymbol{\psi} \tag{2.68}$$

$$\mathbf{A}\cdot\boldsymbol{\psi}=\mathbf{c};\quad \mathbf{A}=\left[\mathbf{I}+\mathbf{G}_0\cdot\mathbf{P}_0\right],\ \mathbf{c}=\boldsymbol{\psi}_0 \tag{2.69}$$

2.2 TOEPLITZ AND CIRCULANT MATRICES

For all the wave propagation problems studied in this paper, under certain conditions the Green's function and the corresponding matrix exhibit a particular symmetry that can make the problem computationally more tractable. Specifically, if the background media is chosen to be homogeneous and uniformly discretized, the Green's function matrix can be constructed so that it exhibits a block Toeplitz form, that is the block elements for each diagonal from left to right are constant.

$$\mathbf{G}=\begin{pmatrix} \mathbf{G}_{r_0} & \mathbf{G}_{r_1} & \mathbf{G}_{r_2} & \cdots & \mathbf{G}_{r(n-1)} \\ \mathbf{G}_{r_{-1}} & \mathbf{G}_{r_0} & \mathbf{G}_{r_1} & \cdots & \mathbf{G}_{r(n-2)} \\ \mathbf{G}_{r_{-2}} & \mathbf{G}_{r_{-1}} & \mathbf{G}_{r_0} & \cdots & \mathbf{G}_{r(n-3)} \\ \vdots & \vdots & \vdots & \ddots & \vdots \\ \mathbf{G}_{r_{(1-n)}} & \mathbf{G}_{r_{(2-n)}} & \mathbf{G}_{r_{(3-n)}} & \cdots & \mathbf{G}_{r_0} \end{pmatrix} \tag{2.70}$$

A Toeplitz matrix can also be easily transformed into a block circulant matrix by doubling each spatial grid dimension.

$$\mathbf{G}=\begin{pmatrix} \mathbf{G}_{r_0} & \mathbf{G}_{r_1} & \mathbf{G}_{r_2} & \cdots & \mathbf{G}_{r_{(n-1)}} & \mathbf{G}_{r_{(1-n)}} & \cdots & \mathbf{G}_{r_{-2}} & \mathbf{G}_{r_{-1}} \\ \mathbf{G}_{r_{-1}} & \mathbf{G}_{r_0} & \mathbf{G}_{r_1} & \cdots & \mathbf{G}_{r_{(n-2)}} & \mathbf{G}_{r_{(n-1)}} & \cdots & \mathbf{G}_{r_{-3}} & \mathbf{G}_{r_{-2}} \\ \mathbf{G}_{r_{-2}} & \mathbf{G}_{r_{-1}} & \mathbf{G}_{r_0} & \ddots & \mathbf{G}_{r_{(n-3)}} & \mathbf{G}_{r_{(n-2)}} & \cdots & \mathbf{G}_{r_{-4}} & \mathbf{G}_{r_{-3}} \\ \vdots & \vdots & \vdots & \ddots & \ddots & \vdots & \vdots & \vdots & \vdots \\ \vdots & \vdots & \vdots & \vdots & \ddots & \ddots & \vdots & \vdots & \vdots \\ \vdots & \vdots & \vdots & \vdots & \vdots & \ddots & \ddots & \vdots & \vdots \\ \vdots & \vdots & \vdots & \vdots & \vdots & \vdots & \ddots & \ddots & \vdots \\ \mathbf{G}_{r_2} & \mathbf{G}_{r_3} & \mathbf{G}_{r_4} & \cdots & \mathbf{G}_{r_{(2-n)}} & \mathbf{G}_{r_{(3-n)}} & \cdots & \mathbf{G}_{r_0} & \mathbf{G}_{r_1} \\ \mathbf{G}_{r_1} & \mathbf{G}_{r_2} & \mathbf{G}_{r_3} & \cdots & \mathbf{G}_{r_{(1-n)}} & \mathbf{G}_{r_{(2-n)}} & \cdots & \mathbf{G}_{r_{-1}} & \mathbf{G}_{r_0} \end{pmatrix} \tag{2.71}$$

Circulant matrices possess a number of useful properties. First, one can see from (2.71) that each row in the matrix is equal to the row above that has been right circular shifted by one element. The consequence is that multiplication with a vector is simply a convolution operator, *. The circulant matrix and vector product can be efficiently performed using the fast Fourier transform, FFT, accelerating the process of solving systems of equations that contain circulant matrices (Davis 1979; Golub and Van Loan 2013). The matrix-vector product can be calculated by taking the discrete FFT, $\boldsymbol{F_n}$, of the vector $\boldsymbol{x}$ and the first column of the Circulant matrix $\boldsymbol{g}$, multiplying the transformed vectors element wise, and finally taking the inverse FFT. In this way the number of operations for each matrix-vector product can be reduced from $O(N^2)$ to O(NlogN).

$$\mathbf{G}\cdot\mathbf{x}=\mathbf{g}*\mathbf{x}=\mathbf{F}_n^{-1}\cdot\left[\left(\mathbf{F}_n\cdot\mathbf{g}\right)\cdot\left(\mathbf{F}_n\cdot\mathbf{x}\right)\right] \tag{2.72}$$

In addition, the FFT can also be used to diagonalize a circulant matrix providing a means to rapidly calculate the singular value decomposition (SVD) or pseudo-inverse of the matrix (Golub and Van Loan 2013).

$$\mathbf{G}=\mathbf{V}_n^{\otimes}\cdot\left(\mathbf{S}\right)\cdot\mathbf{V}_n \tag{2.73}$$

$$\mathbf{S}=diag\left(\mathbf{F}_n\cdot\mathbf{g}\right) \tag{2.74}$$

$$\mathbf{V}_n^{\otimes}=\sqrt{n}\mathbf{F}_n^{-1} \tag{2.75}$$

$$\mathbf{V}_n=\frac{1}{\sqrt{n}}\mathbf{F}_n \tag{2.76}$$

$$\mathbf{G}^{-1}=\mathbf{F}_n\cdot\left(\mathbf{S}^{-1}\right)\cdot\mathbf{F}_n^{-1} \tag{2.77}$$

While all simple circulant matrices (those with 1 by 1 blocks) can be diagonalized in this way, it is not possible to do so for all types of block circulant (BC) matrices. Generally, block circulant matrices can be inverted when each of the block elements has a well-defined inverse. For instance, the SVD can be performed for two types of block circulant matrices: block circulant with circulant blocks (BCCB) and circulant block diagonal (CBD) matrices. In a BCCB matrix, both the matrix itself and the blocks are circulant. A CBD has non-zero circulant blocks only along the diagonal. The inverse (or pseudo-inverse) of this matrix is simply another CBD

matrix with the inverses of the individual block matrices now on the diagonal. In both cases, the blocks are also circulant and therefore the inverse can be computed from equation(2.77).

$$\mathbf{CBD} = \begin{pmatrix} \mathbf{C}_1 & 0 & 0 & \cdots & 0 \\ 0 & \mathbf{C}_2 & 0 & \cdots & 0 \\ 0 & 0 & \mathbf{C}_3 & \cdots & 0 \\ \vdots & \vdots & \vdots & \ddots & \vdots \\ 0 & 0 & 0 & \cdots & \mathbf{C}_M \end{pmatrix} \tag{2.78}$$

$$\mathbf{CBD}^{-1} = \begin{pmatrix} \mathbf{C}_1^{-1} & 0 & 0 & \cdots & 0 \\ 0 & \mathbf{C}_2^{-1} & 0 & \cdots & 0 \\ 0 & 0 & \mathbf{C}_3^{-1} & \cdots & 0 \\ \vdots & \vdots & \vdots & \ddots & \vdots \\ 0 & 0 & 0 & \cdots & \mathbf{C}_M^{-1} \end{pmatrix} \tag{2.79}$$

In addition to the matrix inverses, iterative methods can be used to solve the system of equations. Iterative matrix solvers search the solution space by iteratively generating a sequence of solutions using matrix-vector and possibly vector-matrix transpose products. A number of Krylov subspace methods (e.g. bi-conjugate gradient or transpose free quasi-minimum residual) also have the useful property that requires only the matrix-vector product. Thus when combined with the efficiency of the FFT based circulant matrix-vector product, the computational burden reduces to O(NlogN) operations required to solve the system of equation. This method can be applied to efficiently simulate and invert acoustic, elastic, and electromagnetic wave propagation problems.

2.3 THE INVERSE PROBLEM

The inverse problem seeks to find the physical parameters, **m**, which results in the best fit between modeled, $\mathbf{d}_{\text{ref}}$, and observed data, $\mathbf{d}_{\text{obs}}$. The misfit or error can be represented by a functional that depends on state variables determined from the state equations, $\mathbf{d}_{\text{obs}} = \mathbf{L}(\mathbf{m})$, defining the problem that is of interest. The state equations (the forward problem) describe the physics of the problem and depend on the set of model parameters. The best fit solution to the inverse problem corresponds then to the minimization of this functional, and in general depends non-linearly on both the state variables and the model parameters. The inversion schemes

presented here will attempt to minimize the L2 norm of the difference between the simulated reference media wavefields, $\mathbf{d}_{ref} = \boldsymbol{\psi}^{ref}$, and the true wavefields, $\mathbf{d}_{obs} = \boldsymbol{\psi}^{obs}$, observed at a set of receivers and due to a collection of source locations.

$$S(\mathbf{m}) = \frac{1}{2}\sum_{s,r}\left[\boldsymbol{\psi}_s^{obs}(\mathbf{r}_r) - \boldsymbol{\psi}_s^{ref}(\mathbf{r}_r)\right]^T \cdot \left[\boldsymbol{\psi}_s^{obs}(\mathbf{r}_r) - \boldsymbol{\psi}_s^{ref}(\mathbf{r}_r)\right] \tag{2.80}$$

Minimization of the misfit generally proceeds by linearizing the functional, **L**(**m**), about some reference state, $\mathbf{m}_0$. To do this the gradient of the functional is needed, that is the change in the functional with respect to both the state variables (wavefield solutions to the forward problem) and model parameters. Since the forward model solution also depends on the model parameters, the functional gradient also depends on the derivatives of the state variables with respect to model parameters. These derivatives are called Fréchet derivatives (after Maurice Fréchet who studied problems using derivatives taken with respect to functions). The set of Fréchet derivatives taken with respect to each model parameter can be assembled into the Jacobian or sensitivity matrix and represents the linearization of the forward problem about the reference model parameters.

A brute force method for computing the sensitivity matrix would require a forward simulation for each model parameter and would therefore be very computationally expensive. In this section, I will discuss methods for efficiently minimizing the misfit and solving the inverse problem.

2.3.1 Scattering Integral Method

Given the Green's function for a reference medium, the solution due to an arbitrary source and at any location can be determined. The perturbation operator can also be related to the solution perturbation using the Green's function for the reference state in a scattering integral approach (Zhao et al. 2005; Chen et al. 2007; Chen et al. 2011).

$$\boldsymbol{\psi}^{obs}(\mathbf{r})_s - \boldsymbol{\psi}^{ref}(\mathbf{r})_s = \delta\boldsymbol{\psi} = \int_V \mathbf{G}_{ref}(\mathbf{r},\mathbf{r}') \cdot \delta\mathbf{P}(\mathbf{r}') \cdot \boldsymbol{\psi}^{obs}(\mathbf{r}')_s \, dV' \tag{2.81}$$

$$\delta\mathbf{P}(\mathbf{r}) = \mathbf{L}^{obs}(\mathbf{r}) - \mathbf{L}^{ref}(\mathbf{r}) \tag{2.82}$$

Equation (2.81) is exact regardless of the chosen reference state. In the limit as the perturbation goes to zero, the observed solution approaches the reference solution equation (2.81) can be reformulated as

$$\delta\boldsymbol{\psi}(\mathbf{r})_s = \int_V \mathbf{G}_{ref}(\mathbf{r},\mathbf{r}')\cdot\delta\mathbf{P}(\mathbf{r}')\cdot\boldsymbol{\psi}^{ref}(\mathbf{r}')_s\, dV' \tag{2.83}$$

Alternatively, both the solution corresponding to the reference medium and the observed solution can also be represented using the integral equation approach. It will be assumed that the unperturbed Green's function is common to both the modeled and observed solutions. Since the perturbation is simply the sum of the unperturbed and perturbed Green's function, this can be done without introducing additional restrictions. The subscript ***s*** is used to note that the solutions correspond to a particular source. The reference solution can be expressed as

$$\boldsymbol{\psi}^{ref}(\mathbf{r})_s = \int_V \mathbf{G}^{ref}(\mathbf{r},\mathbf{r}')\cdot\mathbf{s}^{ref}(\mathbf{r}')\, dV'$$

$$\boldsymbol{\psi}^{ref}(\mathbf{r})_s = \boldsymbol{\psi}_0^{ref}(\mathbf{r})_s - \int_V \mathbf{G}_0^s(\mathbf{r},\mathbf{r}')\cdot\mathbf{P}_s^{ref}(\mathbf{r}')\cdot\boldsymbol{\psi}^{ref}(\mathbf{r}')_s\, dV' \tag{2.84}$$

$$\boldsymbol{\psi}_0^{ref}(\mathbf{r})_s = \int_V \mathbf{G}_0^s(\mathbf{r},\mathbf{r}')\cdot\mathbf{s}^{ref}(\mathbf{r}')\, dV' \tag{2.85}$$

And the observed solution is similarly given by

$$\boldsymbol{\psi}^{obs}(\mathbf{r})_s = \int_V \mathbf{G}^{obs}(\mathbf{r},\mathbf{r}')\cdot\mathbf{s}^{obs}(\mathbf{r}')\, dV'$$

$$\boldsymbol{\psi}^{obs}(\mathbf{r})_s = \boldsymbol{\psi}_0^{obs}(\mathbf{r})_s - \int_V \mathbf{G}_0^s(\mathbf{r},\mathbf{r}')\cdot\mathbf{P}_s^{obs}(\mathbf{r}')\cdot\boldsymbol{\psi}^{obs}(\mathbf{r}')_s\, dV' \tag{2.86}$$

$$\boldsymbol{\psi}_0^{obs}(\mathbf{r})_s = \int_V \mathbf{G}_0^s(\mathbf{r},\mathbf{r}')\cdot\mathbf{s}^{obs}(\mathbf{r}')\, dV' \tag{2.87}$$

The above are also exact expressions for the reference and observed solutions; the respective Green's functions have simply been re-written using a different reference state. The source terms have been allowed to differ between the reference and observed solutions so that, in addition to the media perturbation, the source term perturbation can be estimated. Initially, it will be assumed that the source term is known and is the same for both the reference and observed solutions.

$$\boldsymbol{\psi}_0^{obs}(\mathbf{r})_s - \boldsymbol{\psi}_0^{ref}(\mathbf{r})_s = \int_V \mathbf{G}_0^s(\mathbf{r},\mathbf{r}')\cdot\left[\mathbf{s}^{obs}(\mathbf{r}') - \mathbf{s}^{ref}(\mathbf{r}')\right] dV' = 0 \tag{2.88}$$

The difference between the observed and modeled solutions can then be calculated as

$$\delta\boldsymbol{\psi}(\mathbf{r})_s = \boldsymbol{\psi}^{obs}(\mathbf{r})_s - \boldsymbol{\psi}^{ref}(\mathbf{r})_s \tag{2.89}$$

$$\delta\boldsymbol{\psi}(\mathbf{r})_s = \left[\int_V \mathbf{G}_0^s(\mathbf{r},\mathbf{r}') \cdot \mathbf{P}_s^{ref}(\mathbf{r}') \cdot \boldsymbol{\psi}^{ref}(\mathbf{r}')_s \, dV' - \int_V \mathbf{G}_0^s(\mathbf{r},\mathbf{r}') \cdot \mathbf{P}_s^{obs}(\mathbf{r}') \cdot \boldsymbol{\psi}^{obs}(\mathbf{r}')_s \, dV' \right] \tag{2.90}$$

$$\delta\boldsymbol{\psi}(\mathbf{r})_s = \int_V \mathbf{G}_0^s(\mathbf{r},\mathbf{r}') \cdot \left[\mathbf{P}_s^{ref}(\mathbf{r}') \cdot \boldsymbol{\psi}^{ref}(\mathbf{r}')_s - \mathbf{P}_s^{obs}(\mathbf{r}') \cdot \boldsymbol{\psi}^{obs}(\mathbf{r}')_s \right] dV' \tag{2.91}$$

$$\begin{aligned} \delta\boldsymbol{\psi}(\mathbf{r})_s = & \int_V \mathbf{G}_0^s(\mathbf{r},\mathbf{r}') \cdot \left[\mathbf{P}_s^{ref}(\mathbf{r}') \cdot \boldsymbol{\psi}^{ref}(\mathbf{r}')_s \right] dV' \\ & - \int_V \mathbf{G}_0^s(\mathbf{r},\mathbf{r}') \cdot \left[\mathbf{P}_s^{obs}(\mathbf{r}') \cdot \left(\boldsymbol{\psi}^{ref}(\mathbf{r}')_s + \delta\boldsymbol{\psi}(\mathbf{r}')_s \right) \right] dV' \end{aligned} \tag{2.92}$$

Equation (2.92) can be further simplified by substituting the difference in the unknown observed perturbation and the modeled perturbation operators. Due to the assumption that the unperturbed Green's function is the same for both observed and modeled solutions, the perturbation difference is independent of the chosen unperturbed system.

$$\mathbf{P}_0^{obs}(\mathbf{r}) - \mathbf{P}_0^{ref}(\mathbf{r}) = \mathbf{L}^{obs}(\mathbf{r}) - \mathbf{L}^{ref}(\mathbf{r}) = \delta\mathbf{P}(\mathbf{r}) \tag{2.93}$$

$$\begin{aligned} \delta\boldsymbol{\psi}(\mathbf{r})_s = & -\int_V \mathbf{G}_0^s(\mathbf{r},\mathbf{r}') \cdot \left[\mathbf{P}_s^{obs}(\mathbf{r}') \cdot \delta\boldsymbol{\psi}(\mathbf{r}')_s \right] dV' \\ & - \int_V \mathbf{G}_0^s(\mathbf{r},\mathbf{r}') \cdot \left[\left(\mathbf{P}_s^{obs}(\mathbf{r}') - \mathbf{P}_s^{ref}(\mathbf{r}') \right) \cdot \boldsymbol{\psi}^{ref}(\mathbf{r}')_s \right] dV' \end{aligned} \tag{2.94}$$

$$\begin{aligned} \delta\boldsymbol{\psi}(\mathbf{r})_s = & -\int_V \mathbf{G}_0^s(\mathbf{r},\mathbf{r}') \cdot \mathbf{P}_s^{ref}(\mathbf{r}') \cdot \delta\boldsymbol{\psi}(\mathbf{r}')_s \, dV' \\ & - \int_V \mathbf{G}_0^s(\mathbf{r},\mathbf{r}') \cdot \delta\mathbf{P}(\mathbf{r}') \cdot \boldsymbol{\psi}^{ref}(\mathbf{r}')_s \, dV' \\ & - \int_V \mathbf{G}_0^s(\mathbf{r},\mathbf{r}') \cdot \delta\mathbf{P}(\mathbf{r}') \cdot \delta\boldsymbol{\psi}(\mathbf{r}')_s \, dV' \end{aligned} \tag{2.95}$$

The last term on the right of (2.95) contains the product of $\delta\mathbf{P}$ and $\delta\boldsymbol{\psi}$. For small changes in both the perturbation operator and solution, the last term will be small compared to the remaining terms so that, to first order equation, (2.95) can be written as

$$\begin{aligned}\delta\boldsymbol{\psi}(\mathbf{r})_s &= -\int_V \mathbf{G}_0^s(\mathbf{r},\mathbf{r}')\cdot\mathbf{P}_s^{ref}(\mathbf{r}')\cdot\delta\boldsymbol{\psi}(\mathbf{r}')_s\,dV' \\ &\quad -\int_V \mathbf{G}_0^s(\mathbf{r},\mathbf{r}')\cdot\delta\mathbf{P}(\mathbf{r}')\cdot\boldsymbol{\psi}^{ref}(\mathbf{r}')_s\,dV'\end{aligned} \tag{2.96}$$

In a typical experimental dataset, one utilizes a collection of source and received signal measurement positions. In the above equations, the solution or change in the solution are given for a single source and at all spatial locations. Equation (2.96) for multiple sources and receivers can be written in matrix form and rearranged.

$$\delta\boldsymbol{\psi} = -\mathbf{G}_0\cdot\mathbf{P}^{ref}\cdot\delta\boldsymbol{\psi} - \mathbf{G}_0\cdot\delta\mathbf{P}\cdot\boldsymbol{\psi}^{ref} \tag{2.97}$$

$$\delta\boldsymbol{\psi} + \mathbf{G}_0\cdot\mathbf{P}^{ref}\cdot\delta\boldsymbol{\psi} = -\mathbf{G}_0\cdot\delta\mathbf{P}\cdot\boldsymbol{\psi}^{ref} \tag{2.98}$$

$$\left(\mathbf{I} + \mathbf{G}_0\cdot\mathbf{P}^{ref}\right)\cdot\delta\boldsymbol{\psi} = -\mathbf{G}_0\cdot\delta\mathbf{P}\cdot\boldsymbol{\psi}^{ref} \tag{2.99}$$

$$\mathbf{G}_0\cdot\delta\mathbf{P}\cdot\boldsymbol{\psi}^{ref} = -\left(\mathbf{I} + \mathbf{G}_0\cdot\mathbf{P}^{ref}\right)\cdot\delta\boldsymbol{\psi} \tag{2.100}$$

$$\mathbf{G}_0 = \begin{pmatrix} \mathbf{G}_0^1 & 0 & 0 & \cdots & 0 \\ 0 & \mathbf{G}_0^2 & 0 & \cdots & 0 \\ 0 & 0 & \mathbf{G}_0^3 & \cdots & 0 \\ \vdots & \vdots & \vdots & \ddots & \vdots \\ 0 & 0 & 0 & \cdots & \mathbf{G}_0^s \end{pmatrix}$$

$$\mathbf{P}^{ref} = \begin{pmatrix} \mathbf{P}_1^{ref} & 0 & 0 & \cdots & 0 \\ 0 & \mathbf{P}_2^{ref} & 0 & \cdots & 0 \\ 0 & 0 & \mathbf{P}_3^{ref} & \cdots & 0 \\ \vdots & \vdots & \vdots & \ddots & \vdots \\ 0 & 0 & 0 & \cdots & \mathbf{P}_s^{ref} \end{pmatrix}$$

$$\mathbf{P}^{obs} = \begin{pmatrix} \mathbf{P}_1^{obs} & 0 & 0 & \cdots & 0 \\ 0 & \mathbf{P}_2^{obs} & 0 & \cdots & 0 \\ 0 & 0 & \mathbf{P}_3^{obs} & \cdots & 0 \\ \vdots & \vdots & \vdots & \ddots & \vdots \\ 0 & 0 & 0 & \cdots & \mathbf{P}_s^{obs} \end{pmatrix}$$

$$\delta\mathbf{P} = \mathbf{P}^{obs} - \mathbf{P}^{ref} = \begin{pmatrix} \delta\mathbf{P}_1 & 0 & 0 & \cdots & 0 \\ 0 & \delta\mathbf{P}_2 & 0 & \cdots & 0 \\ 0 & 0 & \delta\mathbf{P}_3 & \cdots & 0 \\ \vdots & \vdots & \vdots & \ddots & \vdots \\ 0 & 0 & 0 & \cdots & \delta\mathbf{P}_s \end{pmatrix}$$

$$\boldsymbol{\psi}^{ref} = \begin{pmatrix} \boldsymbol{\psi}_1^{ref} \\ \boldsymbol{\psi}_2^{ref} \\ \boldsymbol{\psi}_3^{ref} \\ \vdots \\ \boldsymbol{\psi}_s^{ref} \end{pmatrix}; \qquad \delta\boldsymbol{\psi} = \begin{pmatrix} \delta\boldsymbol{\psi}_1 \\ \delta\boldsymbol{\psi}_2 \\ \delta\boldsymbol{\psi}_3 \\ \vdots \\ \delta\boldsymbol{\psi}_s \end{pmatrix}$$

The perturbation is the desired quantity from the inversion and typically represents the spatial heterogeneity in the system that we wish to determine. For the wave propagation problems studied here, the perturbation operator can be factored into the product of a simple diagonal matrix containing the material properties (i.e. velocity, density, or electrical permittivity) at each location and another linear differential operator. This differential operator acts on the solution to produce an associated field quantity (such as traction for elastic problems), $\boldsymbol{\Phi}^{ref}$. In order to solve the inverse problem, equation (2.100) will be rewritten.

$$\mathbf{G}_0 \cdot \boldsymbol{\Phi}^{ref} \cdot \delta\mathbf{M} = -\left(\mathbf{I} + \mathbf{G}_0 \cdot \mathbf{P}_0^{ref}\right) \cdot \delta\boldsymbol{\psi} \tag{2.101}$$

$$\delta\mathbf{P} \cdot \boldsymbol{\psi}^{ref} = \mathbf{D} \cdot \begin{pmatrix} \delta\mathbf{m}_1 & 0 & 0 & \cdots & 0 \\ 0 & \delta\mathbf{m}_2 & 0 & \cdots & 0 \\ 0 & 0 & \delta\mathbf{m}_3 & \cdots & 0 \\ \vdots & \vdots & \vdots & \ddots & \vdots \\ 0 & 0 & 0 & \cdots & \delta\mathbf{m}_s \end{pmatrix} \begin{pmatrix} \boldsymbol{\psi}_1^{ref} \\ \boldsymbol{\psi}_2^{ref} \\ \boldsymbol{\psi}_3^{ref} \\ \vdots \\ \boldsymbol{\psi}_s^{ref} \end{pmatrix}$$

$$\delta\mathbf{P} \cdot \boldsymbol{\psi}^{ref} = \mathbf{D} \cdot \begin{pmatrix} \boldsymbol{\psi}_1^{ref} & 0 & 0 & \cdots & 0 \\ 0 & \boldsymbol{\psi}_2^{ref} & 0 & \cdots & 0 \\ 0 & 0 & \boldsymbol{\psi}_3^{ref} & \cdots & 0 \\ \vdots & \vdots & \vdots & \ddots & \vdots \\ 0 & 0 & 0 & \cdots & \boldsymbol{\psi}_s^{ref} \end{pmatrix} \begin{pmatrix} \delta\mathbf{m}_1 \\ \delta\mathbf{m}_2 \\ \delta\mathbf{m}_3 \\ \vdots \\ \delta\mathbf{m}_s \end{pmatrix} = \mathbf{D} \cdot \boldsymbol{\Psi}^{ref} \cdot \delta\mathbf{M}$$

$$\delta\mathbf{P}\cdot\boldsymbol{\psi}^{ref}=\mathbf{D}\cdot\boldsymbol{\Psi}^{ref}\cdot\delta\mathbf{M}=\boldsymbol{\Phi}^{ref}\cdot\delta\mathbf{M} \tag{2.102}$$

To this point, the media perturbations and Green's functions have been allowed to vary for individual sources. For any practical tomography problem the true medium properties, however, are the same for all sources and this can be incorporated in two distinct ways. First, all of the reference media can be assumed the same for all sources and the same can be assumed for the observed media. The media perturbation is then the same for all sources.

$$\mathbf{m}_1^{obs}=\mathbf{m}_2^{obs}=\mathbf{m}_3^{obs}=\mathbf{m}_s^{obs}$$
$$\mathbf{m}_1^{ref}=\mathbf{m}_2^{ref}=\mathbf{m}_3^{ref}=\mathbf{m}_s^{ref}$$
$$\delta\mathbf{m}_1=\delta\mathbf{m}_2=\delta\mathbf{m}_3=\delta\mathbf{m}_s$$

$$\delta\mathbf{M}=\begin{pmatrix}\delta\mathbf{m}\\ \delta\mathbf{m}\\ \delta\mathbf{m}\\ \vdots\\ \delta\mathbf{m}\end{pmatrix}=\begin{pmatrix}\mathbf{I}\\ \mathbf{I}\\ \mathbf{I}\\ \vdots\\ \mathbf{I}\end{pmatrix}\cdot\delta\mathbf{m}=\mathbf{I}_s\cdot\delta\mathbf{m} \tag{2.103}$$

Substituting this result into equation (2.102) and solving for the media perturbation gives

$$\mathbf{A}\cdot\delta\mathbf{m}=\mathbf{b}$$
$$\mathbf{A}=\mathbf{G}_0\cdot\boldsymbol{\Phi}^{ref}\cdot\mathbf{I}_s \tag{2.104}$$
$$\mathbf{b}=-\left(\mathbf{I}+\mathbf{G}_0\cdot\mathbf{P}_0^{ref}\right)\cdot\delta\boldsymbol{\psi}$$

$$\delta\mathbf{m}=\mathbf{A}^{-1}\cdot\mathbf{b}=-\mathbf{I}_s^{-1}\cdot\left(\boldsymbol{\Phi}^{ref}\right)^{-1}\cdot\left(\mathbf{G}_0^{-1}+\mathbf{P}_0^{ref}\right)\cdot\delta\boldsymbol{\psi} \tag{2.105}$$

It was assumed earlier that the observed and reference source terms were the same and therefore their difference vanished. When the source term is allowed to change, the equations above become

$$\mathbf{b}=-\left(\mathbf{I}+\mathbf{G}_0\cdot\mathbf{P}_0^{ref}\right)\cdot\delta\boldsymbol{\psi}+\mathbf{G}_0\delta\mathbf{s} \tag{2.106}$$

$$\delta\mathbf{m}=\mathbf{A}^{-1}\cdot\mathbf{b}=-\mathbf{I}_s^{-1}\cdot\left(\boldsymbol{\Phi}^{ref}\right)^{-1}\cdot\left[\left(\mathbf{G}_0^{-1}+\mathbf{P}_0^{ref}\right)\cdot\delta\boldsymbol{\psi}-\delta\mathbf{s}\right] \tag{2.107}$$

The second approach for incorporating the reference media is to allow the reference conditions to change for each source and receiver location which is termed here as the variable

reference method. In this case the reference media is not the same for each source location and (2.103) then becomes

$$\mathbf{m}_1^{ref} \neq \mathbf{m}_2^{ref} \neq \mathbf{m}_3^{ref} \neq \mathbf{m}_s^{ref}$$

$$\delta\mathbf{M} = \begin{pmatrix} \mathbf{m}^{obs} \\ \mathbf{m}^{obs} \\ \mathbf{m}^{obs} \\ \vdots \\ \mathbf{m}^{obs} \end{pmatrix} - \begin{pmatrix} \mathbf{m}_1^{ref} \\ \mathbf{m}_2^{ref} \\ \mathbf{m}_3^{ref} \\ \vdots \\ \mathbf{m}_s^{ref} \end{pmatrix} = \begin{pmatrix} \mathbf{I} \\ \mathbf{I} \\ \mathbf{I} \\ \vdots \\ \mathbf{I} \end{pmatrix} \cdot \mathbf{m}^{obs} - \mathbf{m}^{ref} = \mathbf{I}_s \cdot \mathbf{m}^{obs} - \mathbf{m}^{ref} \tag{2.108}$$

The forward and inverse solutions are also given below. One notable difference in equation (2.110) is that the inverse solution is now solving for the model parameters rather than the model parameter changes.

$$\begin{aligned} &\mathbf{A} \cdot \mathbf{m}^{obs} = \mathbf{b} \\ &\mathbf{A} = \mathbf{G}_0 \cdot \boldsymbol{\Phi}^{ref} \cdot \mathbf{I}_s \\ &\mathbf{b} = -\left(\mathbf{I} + \mathbf{G}_0 \cdot \mathbf{P}_0^{ref}\right) \cdot \delta\boldsymbol{\psi} + \mathbf{G}_0\mathbf{s} + \mathbf{G}_0\mathbf{m}^{ref} \end{aligned} \tag{2.109}$$

$$\mathbf{m}^{obs} = \mathbf{A}^{-1} \cdot \mathbf{b} = -\mathbf{I}_s^{-1} \cdot \left[\left(\boldsymbol{\Phi}^{ref}\right)^{-1} \cdot \left[\left(\mathbf{G}_0^{-1} + \mathbf{P}_0^{ref}\right) \cdot \delta\boldsymbol{\psi} - \delta\mathbf{s} \right] - \mathbf{m}^{ref} \right] \tag{2.110}$$

The matrix inverses (or pseudo-inverses) in (2.105) and (2.110) are typically difficult to compute, however $\boldsymbol{\Phi}^{\text{ref}}$ is a diagonal matrix whose elements are the modeled wave field or associated wave field obtained from the previous iteration, $\mathbf{I_s}$ has a simple left inverse, and matrix $\mathbf{G_0}$ is block circulant. For some problems (e.g. acoustic wave propagation) the matrix $\mathbf{G_0}$ is a simple circulant; in this case the pseudo-inverse and SVD can be rapidly computed using the FFT providing a means to compute the inverse solution in O(NlogN) operations. Regularization can be performed by truncation of the singular values obtained from the SVD of the Green's function matrix.

In general, the inverse of the Green's function matrix cannot be easily computed, however the matrix may still have a block circulant form. In this case linear iterative solvers can also be used to solve (2.101) for the desired perturbation at each step in the inversion in O(NlogN) operations.

3 THREE-DIMENSIONAL FRÉCHET SENSITIVITY KERNELS FOR ELECTROMAGNETIC WAVE PROPAGATION

C.E. Strickland, T.C. Johnson, and R.I. Odom
Submitted to: Geophysical Journal International, October 21st, 2014

Summary

Electromagnetic imaging methods are useful tools for monitoring subsurface changes in pore-fluid content and the associated changes in electrical permittivity and conductivity. The most common method for georadar tomography uses a high frequency ray-theoretic approximation that is valid when material variations are sufficiently small relative to the wavelength of the propagating wave. Georadar methods, however, often utilize electromagnetic waves that propagate within heterogeneous media at frequencies where ray theory may not be applicable. In this paper we describe EM wave propagation 3-D Fréchet sensitivity kernels that capture the data sensitivity to material perturbations for a given source-receiver combination. Various data functional types are formulated that consider all three components of the electric wavefield and incorporate near-, intermediate-, and far-field contributions. We show that EM waves exhibit substantial variations for different relative source-receiver component orientations. The 3-D sensitivities also illustrate out-of-plane effects that are not captured in 2-D sensitivity kernels and can influence results obtained using 2-D inversion methods to image structures that are in reality 3-D.

3.1 INTRODUCTION

Electromagnetic (EM) methods such as magnetotellurics, controlled source electromagnetics, and georadar have been widely used for subsurface imaging in near-surface environments (Wilt et al. 1995; Peterson 2001; Binley et al. 2002; Zhdanov 2002). EM waves are employed to investigate properties of the earth and have similar aspects to seismic theory for elastic wave propagation. In this paper we will focus on high-frequency (MHz) EM signals typical of georadar methods.

Solutions to wave propagation problems depend on model parameters (e.g. wave velocity or slowness) that define the material structures through which the wave propagates. Waveform data can be represented as functionals of the model parameters which are themselves functions of position within the support volume of the model.

An important aspect of such systems is how a change in model parameters affects the observed data. Data types are generally non-linear functionals of the model parameters but can be linearized to provide a relationship between small model parameter changes and the corresponding data changes. The data change can then be expressed as a volume integral whose integrand is the product of the change in model parameters and the associated data sensitivity kernel, K_D. The data sensitivity kernels are Fréchet derivatives of the data functional taken with respect to each model parameter and evaluated around a reference model.

$$\delta D = \int_V K_D(\mathbf{r}) \cdot \delta m(\mathbf{r})\, d^3\mathbf{r} \tag{3.1}$$

Inverse problems seek to determine the unknown model parameters from the measured data obtained using a finite set of source and receiver combinations. In many cases the data is a non-linear functional of the model parameters; unique solutions to the inverse problem often do not exist and are obtained using an optimization process to determine the best fit to the data. Both global search (e.g. Monte Carlo, simulated annealing) and local optimization methods can be used to solve the inverse problem (Tarantola 2004). Local methods linearize the problem using an initial set of model parameters and the gradient or Jacobian matrix. Gradient-based methods are commonly used for georadar inversion (Ernst et al. 2007; Meles et al. 2012) and avoid the computational cost involved with calculating and storing the Jacobian matrix; the disadvantage is that the Jacobian matrix in not available for formal model resolution analysis. The Jacobian or sensitivity matrix is determined from the set of Fréchet derivatives which are defined as

derivatives of a particular data point with respect to the model parameters (Tarantola 2004, Plessix 2006). Fréchet sensitivity kernels correspond to the rows of the Jacobian matrix for each data point and play a central role in the tomographic inverse problem, mapping perturbations in model parameters to the resulting change in the data. The objective is to solve this linearized relationship for a change in model parameters using a dataset of observations, update the starting model, and finally iterate this process to ultimately produce a final optimal estimate of the model parameters.

Waveform data functionals can be defined in a variety of ways and lead to different sensitivity kernels. In each case, data functionals depend on both the observed and modeled wave-field solutions. Common data types include simple wave-field residuals (Ernst et al. 2007; Meles et al. 2010), in addition to cross-correlation based travel-times and amplitudes and their generalizations to frequency dependent quantities (Gee & Jordan 1992; Chen et al. 2007).

Approximations in the modeled physics must often be employed to make the problem computationally practical, but can also introduce errors and artefacts in the inversion. Ray theory is often used to model wave-propagation in heterogeneous media. Ray theory constitutes an approximate, high-frequency solution to the wave-equation that is valid when material heterogeneities and variations in wave amplitude are small over the scale of a wavelength (Kravtsov and Orlov 1980). Specifically, the spatial variations in the media must be much larger than both the wavelength of the propagating waves and the width of the first Fresnel zone. The ray-theoretic sensitivities of the wavefield data are non-zero only for the material properties along the geometrical ray path so that structures not located directly on the ray-path from the source to the receiver have no effect on the measurement.

Waves often propagate within heterogeneous media at frequencies where ray theory is not applicable. Finite-frequency waves are sensitive to the three-dimensional structure surrounding both the source and where the wave is measured. Intuitively, the media directly between the source of the wave and where the signal is received should have the greatest effect on the measurement. Also, structure that is located far from both the source and receiver would be expected to exhibit little effect on the measured signal. In order to quantitatively determine media properties from wave propagation measurements, the wavefield sensitivity to 3-D model structure must first be known.

The main contribution to the sensitivity kernel typically occurs within a region surrounding the geometric ray-path and is termed the first Fresnel volume or just the Fresnel volume. The Fresnel volume is often defined as the region where constructive interference occurs between primary and scattered waves. The Fresnel volume contains the set of points contributing scattered energy that is delayed relative to the fastest travel-time by less than a fractional period of the wave (Kravstov and Orlov 1980; Vasco et al. 1995; Červený 2001). In homogeneous media such constant delay-time surfaces bounding the first Fresnel volume take the shape of an ellipsoid with the source and receiver at the loci and the width proportional to the wavelength. In heterogeneous media, the shape of the Fresnel volume is more complex and can be determined using dynamic ray tracing (Červený and Soares 1992; Tian et al. 2007) or finite-difference solutions to the eikonal equation (Ammon and Vidale 1993; Watanabe et al. 1999).

In general, the sensitivity is not constrained to just the first Fresnel volume but extends throughout the entire volume. The model-data sensitivity mapping can be performed using empirical relationships (Watanabe et al. 1999; Day-Lewis et al. 2002), by making use of approximate solutions to the wave-equation (Yomogida 1992; Snieder and Lomax 1996; Marquering et al. 1999; Dahlen et al. 2000; Hung et al. 2000; Johnson et al. 2005; Jocker et al. 2006; Buursink et al. 2008) or using full-wave equation methods (Tromp et al. 2005; Zhao et al. 2005; Meles et al. 2010).

Finite-frequency sensitivity kernels and their application to inverse problems have been studied by many researchers over the past several years particularly in the seismic community. In principal, incorporating finite frequency effects can provide higher resolution imaging results. The full 3D sensitivity kernels have been calculated using full-wave equation approaches for seismic applications, (Tromp et al. 2005; Zhao et al. 2005; Zhang and Shen 2008), EM induction problems in both the frequency domain (Tølbøll and Christensen 2007) and time domain (Hördt 1998; Christensen 2014), as well as direct current electrical resistivity (Barker 1979; Dahlin and Zhou 2004).

A number of data functional types can be defined and produce diverse sensitivities. For instance, the sensitivity kernels for different combinations of source and receiver orientations can be substantial (Shen et al. 2008) and effects due to near-, intermediate-, and far-field contributions can all lead to different sensitivity kernels. Also, cross-correlation based travel-time and amplitude sensitivity kernels can be used to incorporate finite-frequency effects (Luo &

Schuster 1991; Marquering et al. 1999) and provide high signal-to-noise data functionals by integrating the waveform data within a finite time window to produce a single scalar value. In addition to integrated data types, a great deal of information can be extracted from the wavefield at discreet time increments providing supplementary constraints on the inverse solution (Nolet 1987).

In this paper we provide details on 3-D Fréchet sensitivity kernels for EM wave propagation problems. We begin by developing the underlying electromagnetic theory starting from Maxwell's equations. Next, we define expressions for several data functionals and derive exact expressions for their Fréchet sensitivity kernels. Then, examples will be given in both the frequency and time domains for various source and receiver orientations and data functionals calculated for both homogeneous and heterogeneous background media. Finally, properties of the EM sensitivity kernels and their effects on observed data will be discussed. Similar to seismic waves, EM waves show substantial variations for different relative source-receiver component orientations. The 3-D sensitivities also illustrate out-of-plane effects that are not captured in 2-D sensitivity kernels and can influence results obtained using 2-D inversion methods to image structures that are in reality 3-D.

3.2 THEORETICAL DEVELOPMENT

In this section we will first briefly review Maxwell's equations that govern EM wave propagation. Then we develop solutions using scattering theory for the both the background electric wavefield in the reference media and the electric wavefield perturbation due to a small change in the model parameters.

3.2.1 Electromagnetic Wave Equations

In the frequency domain Maxwell's equations are given by

$$\nabla \times \mathbf{E}(\mathbf{r},\omega) = -i\omega\mathbf{B}(\mathbf{r},\omega) \tag{3.2}$$

$$\nabla \times \mathbf{H}(\mathbf{r},\omega) = \mathbf{J}(\mathbf{r},\omega) + i\omega\mathbf{D}(\mathbf{r},\omega) + \mathbf{I}_0(\mathbf{r},\omega) \tag{3.3}$$

$$\nabla \bullet \left[\mathbf{D}(\mathbf{r},\omega)\right] = \rho \tag{3.4}$$

$$\nabla \bullet \left[\mathbf{B}(\mathbf{r},\omega)\right] = 0 \tag{3.5}$$

with the constitutive relationships for linear media

$$\mathbf{J}(\mathbf{r},\omega)=\sigma(\mathbf{r})\mathbf{E}(\mathbf{r},\omega) \tag{3.6}$$

$$\mathbf{D}(\mathbf{r},\omega)=\varepsilon(\mathbf{r})\mathbf{E}(\mathbf{r},\omega) \tag{3.7}$$

$$\mathbf{B}(\mathbf{r},\omega)=\mu(\mathbf{r})\mathbf{H}(\mathbf{r},\omega) \tag{3.8}$$

In the above equations, **E** is the electric field, **H** is the magnetic field, **J** is the current density, **D** is the electric flux density, **B** is the magnetic flux density, ε is the electrical permittivity, σ is the electrical conductivity, μ is the magnetic permeability, and **r** is the position vector. An external electric current source $\mathbf{I_0}$ has been included in equation 3. We will also assume that the magnetic permeability is equal to that of free space which is often a reasonable assumption for many typical earth materials.

Substituting equation (3.8) into (3.2) and taking the curl of both sides gives

$$\nabla\times\nabla\times\mathbf{E}(\mathbf{r},\omega)=-i\omega\mu_0\nabla\times\mathbf{H}(\mathbf{r},\omega) \tag{3.9}$$

Next, substitute equation (3.3) into (3.9) and use $\mathbf{S}(\mathbf{r},\omega)=-i\omega\mu\mathbf{I}_0(\mathbf{r},\omega)$ (a modified source term proportional to the time derivative of the external electric current source) to obtain

$$\nabla\times\nabla\times\mathbf{E}(\mathbf{r},\omega)-\kappa^2(\mathbf{r},\omega)\mathbf{E}(\mathbf{r},\omega)=\mathbf{S}(\mathbf{r},\omega) \tag{3.10}$$

$$\kappa^2(\mathbf{r},\omega)=-i\omega\mu_0\left[\sigma(\mathbf{r})+i\omega\varepsilon(\mathbf{r})\right]$$

$$\kappa(\mathbf{r},\omega)=\sqrt{-i\omega\mu_0\left[\sigma(\mathbf{r})+i\omega\varepsilon(\mathbf{r})\right]} \tag{3.11}$$

Equation (3.10) is the EM vector wave equation for the electric field with the solution given by

$$\mathbf{E}(\mathbf{r},\omega)=\int \boldsymbol{G}\ (\mathbf{r},\mathbf{r}',\omega)\cdot\mathbf{S}(\mathbf{r}',\omega)\,d^3\mathbf{r}' \tag{3.12}$$

When the both the source and the wavefield are vectors, the Green's function in (3.12) is a tensor. Assuming the media is homogeneous and that the electric wavefield $\mathbf{E}(\mathbf{r},\omega)\to 0$ *as* $\mathbf{r}\to 0$, the 3D whole-space tensor Green's function can be written in Cartesian coordinates as

$$G_{pq}=i\omega\mu_0\left(\delta_{pq}+\frac{1}{\kappa^2}\frac{\partial^2}{\partial x_p\partial x_q}\right)g(\mathbf{r},\mathbf{r}',\omega) \tag{3.13}$$

$$G_{pq} = (C_{NF} + C_{IF})\left(\delta_{pq} - \frac{3x_p x_q}{\left(|\mathbf{r}-\mathbf{r}'|\right)^2} \right) + C_{FF}\left(\delta_{pq} - \frac{x_p x_q}{\left(|\mathbf{r}-\mathbf{r}'|\right)^2} \right) \tag{3.14}$$

$$x_p = \left(r_p - r_p'\right);\ p,q = 1,\ 2,\ or\ 3 (x,\ y,\ or\ z)$$

$$g(\mathbf{r},\mathbf{r}',\omega) = \frac{1}{4\pi}\left[\frac{e^{-i\kappa|\mathbf{r}-\mathbf{r}'|}}{|\mathbf{r}-\mathbf{r}'|} \right] \tag{3.15}$$

$$C_{NF} = \frac{i\omega\mu_0}{4\pi\kappa}\left[\frac{-1}{\kappa\ |\mathbf{r}-\mathbf{r}'|^3} \right] e^{-i\kappa|\mathbf{r}-\mathbf{r}'|}$$

$$C_{IF} = \frac{i\omega\mu_0}{4\pi\kappa}\left[\frac{1}{i\,|\mathbf{r}-\mathbf{r}'|^2} \right] e^{-i\kappa|\mathbf{r}-\mathbf{r}'|} \tag{3.16}$$

$$C_{FF} = \frac{i\omega\mu_0}{4\pi\kappa}\left[\frac{\kappa}{|\mathbf{r}-\mathbf{r}'|} \right] e^{-i\kappa|\mathbf{r}-\mathbf{r}'|}$$

Where the coefficients in (3.16) correspond to the near-, intermediate-, and far-field terms, the prime denotes the source position, and r_p specifies the p^{th} component of the position vector.

3.2.2 Scattering Integral Solution

The scattering integral solution begins by decomposing the EM material properties into background and perturbation components. The decomposition is completely arbitrary; however, the background reference medium is often chosen to simplify the problem. At this point, no assumptions need to be made as to the magnitude of the material perturbation relative to the background.

$$\sigma(\mathbf{r}) = \sigma_b(\mathbf{r}) + \delta\sigma(\mathbf{r}) \tag{3.17}$$

$$\varepsilon(\mathbf{r}) = \varepsilon_b(\mathbf{r}) + \delta\varepsilon(\mathbf{r}) \tag{3.18}$$

$$\kappa^2(\mathbf{r},\omega) = \kappa_b^2(\mathbf{r},\omega) + \delta\kappa^2(\mathbf{r},\omega)$$

$$\kappa_b^2(\mathbf{r},\omega) = -i\omega\mu_0\left[\sigma_b(\mathbf{r}) + i\omega\varepsilon_b(\mathbf{r})\right] \tag{3.19}$$

$$\kappa_b(\mathbf{r},\omega) = \sqrt{-i\omega\mu_0\left[\sigma_b(\mathbf{r}) + i\omega\varepsilon_b(\mathbf{r})\right]}$$

Where the subscript, b, specifies the background media and the remaining terms give the material perturbations. Substituting equations (3.17) through (3.19) into (3.10) gives

$$\nabla\times\nabla\times\mathbf{E}(\mathbf{r},\omega)-\kappa_b^2(\mathbf{r},\omega)\mathbf{E}(\mathbf{r},\omega)=\mathbf{S}(\mathbf{r},\omega)+\delta\kappa^2(\mathbf{r},\omega)\mathbf{E}(\mathbf{r},\omega) \tag{3.20}$$

Georadar acquisition geometries often utilize a single receiver component that is oriented in the same direction as the transmitting antenna. One way to lessen the difficulty in solving equation (3.20) is to neglect components not aligned with the antenna orientations, reducing the problem to a scalar wave equation (Johnson et al. 2005, Buursink et al. 2008). In effect, the polarizations of the electric wavefield perturbations that scatter from material perturbations are assumed to have the same orientation as the background wavefield. A somewhat similar simplification has been employed in seismic problems that make a paraxial ray approximation to reduce the computational burden and neglect directivity effects in the wavefield perturbation (Dahlen et. al. 2000). We also note that for both cases near- and intermediate-field terms do not contribute to the solution.

One of the objectives of this dissertation is to investigate the EM sensitivity kernels for the individual vector wavefield components incorporating near-, intermediate-, and far-field contributions. To do this, the full vector wave equation will be used to compute the background wavefield and wavefield perturbation.

The integral solution to equation (3.20) for the electric wavefield is given as

$$\begin{aligned}\mathbf{E}(\mathbf{r},\omega)&=\int_V \boldsymbol{G}_b(\mathbf{r},\mathbf{r}',\omega)\cdot\left(\mathbf{S}(\mathbf{r}',\omega)+\delta\kappa^2(\mathbf{r},\omega)\mathbf{E}(\mathbf{r}',\omega)\right)d^3\mathbf{r}'\\ \mathbf{E}(\mathbf{r},\omega)&=\mathbf{E}_b(\mathbf{r},\omega)+\int_V \boldsymbol{G}_b(\mathbf{r},\mathbf{r}',\omega)\cdot\mathbf{E}(\mathbf{r}',\omega)\delta\kappa^2(\mathbf{r}',\omega)\,d^3\mathbf{r}'\end{aligned} \tag{3.21}$$

We can subtract the background wavefield from both sides to determine the wavefield perturbation and is given by the integral solution due to an equivalent current source that is simply the product of the material perturbation and the total electric wavefield.

$$\delta\mathbf{E}(\mathbf{r},\omega)=\int_V \mathbf{G}_b(\mathbf{r},\mathbf{r}',\omega)\cdot\mathbf{E}(\mathbf{r}',\omega)\delta\kappa^2(\mathbf{r}',\omega)d^3\mathbf{r}' \tag{3.22}$$

To determine the data sensitivity, we need to quantify the data change for a small incremental change in the model parameters. In the limit as the material perturbation goes to zero, the total wavefield approaches the background wavefield. To obtain the wavefield perturbation due to a small model perturbation in equation (3.22), we now make the Born

approximation and replace the total wavefield in the integral with the background wavefield (Ishimaru 1978).

$$\delta\mathbf{E}(\mathbf{r},\omega) = \int_V \boldsymbol{G}_b(\mathbf{r},\mathbf{r}',\omega)\cdot\mathbf{E}_b(\mathbf{r}',\omega)\,\delta\kappa^2(\mathbf{r}',\omega)d^3\mathbf{r}' \tag{3.23}$$

In order to numerically evaluate equation(3.23), we discretize both the material perturbation and the background wavefield into N cube shaped grid elements, assuming they are constant within the volume each grid cell, v_n, and centered at $\mathbf{r}_n$. This assumption requires that the dimensions of v_n be much smaller than the wavelength of the field (Ishimaru 1978).

$$\begin{aligned}
&\delta\kappa^2(\mathbf{r},\omega) = \sum_{n=1}^{N}\delta\kappa^2(\mathbf{r}_n,\omega)\Gamma_n(\mathbf{r}) \\
&\mathbf{E}(\mathbf{r},\omega) = \sum_{n=1}^{N}\mathbf{E}(\mathbf{r}_n,\omega)\Gamma_n(\mathbf{r}) \\
&\Gamma_n(\mathbf{r})\begin{cases}1, \mathbf{r}\in v_n\\ 0, \mathbf{r}\notin v_n\end{cases}
\end{aligned} \tag{3.24}$$

Using the discretization in equation (3.24), the wavefield perturbation integral solution (3.23) at each receiver location becomes

$$\delta\mathbf{E}(\mathbf{r}_r,\omega) = \sum_n\left[\int_{v_n}\boldsymbol{G}_b(\mathbf{r}_r,\mathbf{r}',\omega)d^3\mathbf{r}'\right]\cdot\mathbf{E}_b(\mathbf{r}_n,\omega)\delta\kappa^2(\mathbf{r}_n,\omega) \tag{3.25}$$

In equation (3.25), the center of each grid element is located at $\mathbf{r}_n$, the receiver location is at $\mathbf{r}_r$, and $\mathbf{r}'$ is a dummy integration variable. Care must be taken in evaluating the integral of the Green's function due to the singularity at the source location at $\mathbf{r}_r = \mathbf{r}'$. Fortunately, methods exist to evaluate the integral (Chew 1990) for various volume shapes. For the homogeneous media case, the principal volume method (van Bladel, 1961) is used with cube shaped grid volume elements to integrate the singularity in the Green's function integral, $\hat{\boldsymbol{G}}$. The integration for volume elements located outside the source region can also be analytically evaluated and the results for both the singular and non-singular cases are given by the following

$$\hat{G}_{pq} = i\omega\mu_0 \frac{\delta_{pq}}{3\kappa_b^2}\left[2\left(1-i\kappa_b a\right)e^{i\kappa_b a}-3\right]; \qquad \mathbf{r}_r = \mathbf{r}'$$

$$\hat{G}_{pq} = \frac{4\pi a}{3\kappa_b^2}\left[\frac{\sin(\kappa_b a)}{\kappa_b a}-\cos(\kappa_b a)\right]G_{pq}; \qquad \mathbf{r}_r \neq \mathbf{r}' \tag{3.26}$$

$$a = \left(\frac{3}{4\pi}\right)^{\frac{1}{3}} s; \quad s = cube\,side\,length$$

In the heterogeneous background media case, to compute the value of the Fréchet sensitivity kernels within each grid element, we need $\mathbf{E}_b(\mathbf{r}_n,\omega)$, $\delta\kappa^2(\mathbf{r}_n)$ and the Green's function at $\mathbf{r}_r$, due to a source at each grid element, $\mathbf{r}_n$. Calculating the Green's tensor for a source at each grid point would be computationally cost prohibitive, however the reciprocity (Chew 1990) of the Green's tensor, $\mathbf{G}_b(\mathbf{r}_r,\mathbf{r}_n,\omega) = \mathbf{G}_b^T(\mathbf{r}_n,\mathbf{r}_r,\omega)$, can be exploited to reduce the number of required simulations to just those centered on the receiver locations (Chen et al. 2007). The Green's tensor can be obtained by simulating the fields that result from (x-,y-, and z-directed) sources at each of the frequencies of interest and located at the receiver position, **r**. The integral in equation (3.25), can then be evaluated by assuming that the simulated Green's function is constant in each grid volume and can then be pulled out of the integral. To compute the electric fields and Green's functions for the heterogeneous case we used a finite-difference time domain code, XFdtd (REMCOM ©, State College PA) with a cell size of approximately 0.04 m in all coordinate directions. The fields are subsequently transformed into the frequency domain prior to computing the wavefield perturbation in equation (3.25).

3.3 DATA FUNCTIONALS

For this paper, we consider two frequency-domain and three time-domain data functionals, $D_{ij}(\mathbf{r}_r,\mathbf{r}_s)$. Each type depends on the ith component of both the background and observed wavefields measured at location $\mathbf{r}_r$, and that are generated by a particular source applied at $\mathbf{r}_s$ along direction j. For all of the data functional types, the background wavefield is calculated using (3.12) and the wavefield perturbation using equation (3.25). Time-domain data functionals are obtained from frequency-domain quantities using the Fourier transform in (3.27). In addition

to the data functional itself, we also require the Fréchet derivative of the data functional taken with respect to the calculated background wavefield, which we term the data perturbation, $\delta D_{in}(\mathbf{r}_r, \mathbf{r}_s)$.

We will assume that all time-domain wavefields are real valued and vanish prior to t=0. The Fourier convention that we use is

$$F\left[e(t)\right] = E(\omega) = \int_{-\infty}^{\infty} e(t)e^{-i\omega t}dt = \int_{0}^{\infty} e(t)e^{-i\omega t}dt \tag{3.27}$$

$$F^{-1}\left[E(\omega)\right] = e(t) = \frac{1}{2\pi}\int_{-\infty}^{\infty} E(\omega)e^{i\omega t}d\omega = \frac{1}{\pi}\Re e\int_{0}^{\infty} E(\omega)e^{i\omega t}d\omega \tag{3.28}$$

In equation (3.28) the symmetry relation $E(-\omega) = E^{*}(\omega)$ has been used to reduce the integration limits for the inverse Fourier transform.

The first three and perhaps the simplest data functionals are the waveform residuals and are calculated as the difference between the observed and calculated background electric fields. The two frequency-domain types correspond to the real components of the wavefield residual data functional and data perturbation

$$D_{ij}^{\mathrm{R}}(\mathbf{r}_r, \mathbf{r}_s, \omega_m) = \Re e\left[E^i(\mathbf{r}_r, \omega_m)_{s^j} - E_b^i(\mathbf{r}_r, \omega_m)_{s^j}\right] \tag{3.29}$$

$$\delta D_{ij}^{\mathrm{R}}(\mathbf{r}_r, \mathbf{r}_s, \omega_m) = \Re e\left[\delta E^i(\mathbf{r}_r, \omega_m)_{s^j}\right] \tag{3.30}$$

and the imaginary components

$$D_{ij}^{I}(\mathbf{r}_r, \mathbf{r}_s, \omega_m) = Im\left[E^i(\mathbf{r}_r, \omega_m)_{s^j} - E_b^i(\mathbf{r}_r, \omega_m)_{s^j}\right] \tag{3.31}$$

$$\delta D_{ij}^{I}(\mathbf{r}_r, \mathbf{r}_s, \omega_m) = Im\left[\delta E^i(\mathbf{r}_r, \omega_m)_{s^j}\right] \tag{3.32}$$

The third is also a waveform residual but is now specified using the time-domain observed $e^i(\mathbf{r}_r, t_m)_{s^j}$ and background $e_b^i(\mathbf{r}_r, t_m)_{s^j}$ electric fields measured at time t_m.

$$D_{ij}^{T}(\mathbf{r}_r, \mathbf{r}_s, \omega_m) = e^i(\mathbf{r}_r, t_m)_{s^j} - e_b^i(\mathbf{r}_r, t_m)_{s^j} \tag{3.33}$$

$$\delta D_{ij}^{T}(\mathbf{r}_r, \mathbf{r}_s, \omega_m) = \delta e^i(\mathbf{r}_r, t_m)_{s^j} \tag{3.34}$$

The time-domain wavefield perturbation $\delta\mathbf{e}^i(\mathbf{r}_r, t)_{s^j}$ and electric field can be expressed by inverse Fourier transforming from the frequency domain.

$$e^i(\mathbf{r}_r,t)_{s^j} = \frac{1}{\pi}\Re e\int_0^\infty E_b^j(\mathbf{r}',\omega)_{s^j} e^{i\omega t} d\omega \tag{3.35}$$

$$\delta e^i(\mathbf{r}_r,t)_{s^j} = \frac{\Re e}{\pi}\int_0^\infty\int_V \sum_j G_{ij}(\mathbf{r}_r,\mathbf{r}',\omega)\cdot E_b^j(\mathbf{r}',\omega)_{s^j}\delta\kappa^2(\mathbf{r}',\omega)e^{i\omega t} d^3\mathbf{r}' d\omega \tag{3.36}$$

The fourth type of data functional specifies the travel-time shift of a portion of the wavefield by maximizing the cross-correlation between the observed and the calculated background wavefields over a time window t_{m0} to t_{m1}(Dahlen et al. 2000).

$$D_{ij}^{TT}(\mathbf{r}_r,\mathbf{r}_s,t_{m0},t_{m1}) = \Delta t \rightarrow \max\left[\int_{t_{m0}}^{t_{m1}} e^i(\mathbf{r}_r,t)_{s^j}\cdot e_b^i(\mathbf{r}_r,t-\Delta t)_{s^j} dt\right] \tag{3.37}$$

We can expand the travel-time data perturbation in a Taylor series and retain first order terms to give

$$\delta D_{ij}^{TT}(\mathbf{r}_r,\mathbf{r}_s,t_{m0},t_{m1}) = \frac{\int_{t_{m0}}^{t_{m1}} \frac{\partial e_b^i}{\partial t}(\mathbf{r}_r,t)_{s^j}\,\delta e^i(\mathbf{r}_r,t)_{s^j} dt}{\int_{t_{m0}}^{t_{m1}} \frac{\partial^2 e_b^i}{\partial t^2}(\mathbf{r}_r,t)_{s^j}\, e_b^i(\mathbf{r}_r,t)_{s^j} dt} \tag{3.38}$$

For the fifth and final data functional, we first calculate the observed wavefield and background wavefield amplitudes as root-mean-squared (RMS) averages over a time window t_{m0} to t_{m1}.

$$A_{ij}(\mathbf{r}_r,\mathbf{r}_s,t_{m0},t_{m1}) = \left[\frac{1}{(t_{m1}-t_{m0})}\int_{t_{m0}}^{t_{m1}}\left(e^i(\mathbf{r}_r,t)_s\right)^2 dt\right]^{\frac{1}{2}} \tag{3.39}$$

$$\tilde{A}_{ij}(\mathbf{r}_r,\mathbf{r}_s,t_{m0},t_{m1}) = \left[\frac{1}{(t_{m1}-t_{m0})}\int_{t_{m0}}^{t_{m1}}\left(e_b^i(\mathbf{r}_r,t)_{s^j}\right)^2 dt\right]^{\frac{1}{2}} \tag{3.40}$$

For small wavefield perturbations the RMS amplitude and amplitude perturbation can be written as:

$$\begin{aligned} A_{ij}(\mathbf{r}_r,\mathbf{r}_s,t_{m0},t_{m1}) &= \tilde{A}_{ij}(\mathbf{r}_r,\mathbf{r}_s,t_{m0},t_{m1}) + \delta A_{ij}(\mathbf{r}_r,\mathbf{r}_s,t_{m0},t_{m1}) \\ &= \left[\frac{1}{(t_{m1}-t_{m0})}\int_{t_{m0}}^{t_{m1}}\left(e_b^i(\mathbf{r}_r,t)_{s^j} + \delta e^i(\mathbf{r}_r,t)_{s^j}\right)^2 dt\right]^{\frac{1}{2}} \end{aligned} \tag{3.41}$$

$$\delta A_{ij}(\mathbf{r}_r,\mathbf{r}_s,t_{m0},t_{m1}) \approx \tilde{A}_{ij}(\mathbf{r}_r,\mathbf{r}_s,t_{m0},t_{m1}) \left[\frac{\int_{t_{m0}}^{t_{m1}} e_b^i(\mathbf{r}_r,t)_{s^j}\, \delta e^i(\mathbf{r}_r,t)_{s^j}\, dt}{\int_{t_{m0}}^{t_{m1}} e_b^i(\mathbf{r}_r,t)_{s^j}\, e_b^i(\mathbf{r}_r,t)_{s^j}\, dt} \right] \tag{3.42}$$

The data functional is then defined as the natural logarithm of the ratio of observed and background RMS amplitudes.

$$D_{ij}^A(\mathbf{r}_r,\mathbf{r}_s,t_{m0},t_{m1}) = \ln\left(\frac{A_{ij}(\mathbf{r}_r,\mathbf{r}_s,t_{m0},t_{m1})}{\tilde{A}_{ij}(\mathbf{r}_r,\mathbf{r}_s,t_{m0},t_{m1})} \right) \tag{3.43}$$

Similar to (3.38), the RMS amplitude data perturbation can be derived by expanding (3.43), retaining terms up to first order, and substituting (3.42).

$$D_{ij}^A(\mathbf{r}_r,\mathbf{r}_s,t_{m0},t_{m1}) = \ln\left(\frac{\tilde{A}_{ij}+\delta A_{ij}}{\tilde{A}_{ij}} \right) = \ln\left(1+\frac{\delta A_{ij}}{\tilde{A}_{ij}} \right) \approx \frac{\delta A_{ij}}{\tilde{A}_{ij}} \tag{3.44}$$

$$\begin{aligned} D_{ij}^A(\mathbf{r}_r,\mathbf{r}_s,t_{m0},t_{m1}) &= \tilde{D}_{ij}^A(\mathbf{r}_r,\mathbf{r}_s,t_{m0},t_{m1}) + \delta D_{ij}^A(\mathbf{r}_r,\mathbf{r}_s,t_{m0},t_{m1}) \\ &= \ln\left(\frac{\tilde{A}_{ij}(\mathbf{r}_r,\mathbf{r}_s,t_{m0},t_{m1})}{\tilde{A}_{ij}(\mathbf{r}_r,\mathbf{r}_s,t_{m0},t_{m1})} \right) + \delta D_{ij}^A(\mathbf{r}_r,\mathbf{r}_s,t_{m0},t_{m1}) \\ &= \delta D_{ij}^A(\mathbf{r}_r,\mathbf{r}_s,t_{m0},t_{m1}) \end{aligned} \tag{3.45}$$

$$\delta D_{ij}^A(\mathbf{r}_r,\mathbf{r}_s,t_{m0},t_{m1}) = \frac{\int_{t_{m0}}^{t_{m1}} e_b^i(\mathbf{r}_r,t)_s\, \delta e^i(\mathbf{r}_r,t)_s\, dt}{\int_{t_{m0}}^{t_{m1}} \left[e_b^i(\mathbf{r}_r,t)_s \right]^2 dt} \tag{3.46}$$

3.4 Electromagnetic Data Sensitivity Kernels

Each of the EM data functionals defined in the previous section depends on both the electrical conductivity and the electrical permittivity structure within the support volume. The EM sensitivity kernels corresponding to each data functional and model parameter type can be obtained by substituting the wavefield perturbation into the associated data perturbation and finally comparing with equation (3.1).

Starting with the frequency-domain data functional types, we substitute equation (3.25) into equation (3.30) to give the sensitivity kernels for the real component of the data

$$\delta D_{ij}^{R}(\mathbf{r}_r,\mathbf{r}_s,\omega_m) = \int_V K_{ij}^{R_\varepsilon}(\mathbf{r}_r,\mathbf{r}_s,\omega_m)\varepsilon(\mathbf{r}')d^3\mathbf{r}' + \int_V K_{ij}^{R_\sigma}(\mathbf{r}_r,\mathbf{r}_s,\omega_m)\sigma(\mathbf{r}')d^3\mathbf{r}' \tag{3.47}$$

$$K_{ij}^{R_\varepsilon}(\mathbf{r}_r,\mathbf{r}_s,\omega_m) = \Re e\left[\omega^2\mu_0\sum_j G_{ij}(\mathbf{r}_r,\mathbf{r}',\omega_n)\cdot E_b^j(\mathbf{r}',\omega_n)_{s^j}\right] \tag{3.48}$$

$$K_{ij}^{R_\sigma}(\mathbf{r}_r,\mathbf{r}_s,\omega_m) = \Re e\left[-i\omega\mu_0\sum_j G_{ij}(\mathbf{r}_r,\mathbf{r}',\omega_n)\cdot E_b^j(\mathbf{r}',\omega_n)_{s^j}\right] \tag{3.49}$$

The imaginary component sensitivity kernels are calculated by substituting equation (3.25) into (3.32)

$$\delta D_{ij}^{I}(\mathbf{r}_r,\mathbf{r}_s,\omega_m) = \int_V K_{ij}^{I_\varepsilon}(\mathbf{r}_r,\mathbf{r}_s,\omega_m)\varepsilon(\mathbf{r}')d^3\mathbf{r}' + \int_V K_{ij}^{I_\sigma}(\mathbf{r}_r,\mathbf{r}_s,\omega_m)\sigma(\mathbf{r}')d^3\mathbf{r}' \tag{3.50}$$

$$K_{ij}^{I_\varepsilon}(\mathbf{r}_r,\mathbf{r}_s,\omega_m) = Im\left[\omega^2\mu_0\sum_j G_{ij}(\mathbf{r}_r,\mathbf{r}',\omega_n)\cdot E_b^j(\mathbf{r}',\omega_n)_{s^j}\right] \tag{3.51}$$

$$K_{ij}^{I_\sigma}(\mathbf{r}_r,\mathbf{r}_s,\omega_m) = Im\left[-i\omega\mu_0\sum_j G_{ij}(\mathbf{r}_r,\mathbf{r}',\omega_n)\cdot E_b^j(\mathbf{r}',\omega_n)_{s^j}\right] \tag{3.52}$$

Time-domain sensitivity kernels can be determined by substituting equation (3.35) into the corresponding data perturbation. The sensitivity kernels for the discrete time wavefield residual data functional are given by

$$\delta D_{ij}^{T}(\mathbf{r}_r,\mathbf{r}_s,t_m) = \int_V K_{T_{in}^{sr}}^{\varepsilon}(t_n)\varepsilon(\mathbf{r}')d^3r' + \int_V K_{T_{in}^{sr}}^{\sigma}(t_n)\sigma(\mathbf{r}')d^3r' \tag{3.53}$$

$$K_{ij}^{T_\varepsilon}(\mathbf{r}_r,\mathbf{r}_s,t_m) = \frac{\Re e}{\pi}\int_0^\infty \omega^2\mu_0\sum_j G_{ij}(\mathbf{r}_r,\mathbf{r}',\omega_n)E_b^j(\mathbf{r}',\omega_n)_{s^j}e^{i\omega t}d\omega\Big|_{t_m} \tag{3.54}$$

$$K_{ij}^{T_\sigma}(\mathbf{r}_r,\mathbf{r}_s,t_m) = \frac{\Re e}{\pi}\int_0^\infty -i\omega\mu_0\sum_j G_{ij}(\mathbf{r}_r,\mathbf{r}',\omega_n)E_b^j(\mathbf{r}',\omega_n)_{s^j}e^{i\omega t}d\omega\Big|_{t_m} \tag{3.55}$$

Finally, the travel-time sensitivity kernels can be obtained from equation (3.38)

$$K_{ij}^{TT_\varepsilon}(\mathbf{r}_r,\mathbf{r}_s,t_{m0},t_{m1}) = C_{TT}\int_{t_{m0}}^{t_{m1}} \frac{\partial e_b^i}{\partial t}(\mathbf{r}_r,t)_{s^j} K_{ij}^{T_\varepsilon}(\mathbf{r}_r,\mathbf{r}_s,t)dt \tag{3.56}$$

$$K_{ij}^{TT_\sigma}(\mathbf{r}_r,\mathbf{r}_s,t_{m0},t_{m1}) = C_{TT}\int_{t_{m0}}^{t_{m1}} \frac{\partial e_b^i}{\partial t}(\mathbf{r}_r,t)_{s^j} K_{ij}^{T_\sigma}(\mathbf{r}_r,\mathbf{r}_s,t)dt \tag{3.57}$$

$$C_{TT} = \frac{1}{\int_{t_{m0}}^{t_{m1}} \frac{\partial^2 e_b^i}{\partial t^2}(\mathbf{r}_r,t)_s e_b^i(\mathbf{r}_r,t)_{s^j}\,dt} \tag{3.58}$$

and the RMS amplitude sensitivity kernels can be obtained from equation (3.46)

$$K_{ij}^{A_\varepsilon}(\mathbf{r}_r,\mathbf{r}_s,t_{m0},t_{m1}) = C_A\int_{t_{m0}}^{t_{m1}} e_b^i(\mathbf{r}_r,t)_{s^j} K_{ij}^{A_\varepsilon}(\mathbf{r}_r,\mathbf{r}_s,t)dt \tag{3.59}$$

$$K_{ij}^{A_\sigma}(\mathbf{r}_r,\mathbf{r}_s,t_{m0},t_{m1}) = C_A\int_{t_{m0}}^{t_{m1}} e_b^i(\mathbf{r}_r,t)_{s^j} K_{ij}^{A_\sigma}(\mathbf{r}_r,\mathbf{r}_s,t)dt \tag{3.60}$$

$$C_A = \frac{1}{\int_{t_{m0}}^{t_{m1}} \left[e_b^i(\mathbf{r}_r,t)_{s^j} \right]^2 dt} \tag{3.61}$$

Examining equations (3.56) through (3.61), the cross correlation based travel-time and RMS amplitude sensitivity kernels are simply weighted averages of the time-domain sensitivity kernels in (3.54) and (3.55) over the time window from t_{m0} to t_{m1} with weights proportional to either the background wavefield or its time derivative.

3.5 Results and Discussion

The 3-D EM sensitivity kernels for both homogeneous and heterogeneous media will be shown below to illustrate several fundamental aspects. First, sensitivities will be expressed in the frequency-domain at three representative frequencies. Time-domain expressions will then be shown at several time steps starting with the time just prior to the onset of first arriving energy at the receiver. Finally, sensitivity kernels for cross-correlation based travel-time and RMS amplitude data functionals will be discussed. All of the EM sensitivity kernels have been normalized by the average amplitude of the Z directed source and receiver.

Two source-receiver geometries will be used: 1) the receiver is first positioned perpendicular to the direction of the applied current source and then 2) the receiver is repositioned at a higher angle from the plane perpendicular to the source direction. A cross-section through the XZ (y=0 m) plane is shown in figure 1 for the first source-receiver geometry, the source (black arrow) is located at x =2 m, y =5 m, & z =5 m and applied in the z direction; the receiver is located at x =8 m, y =5 m, & z =5 m and all three components (red arrows) will be compared. The modelled volume is a cube with 10 m sides. The homogeneous model has $\varepsilon = 7.5\varepsilon_0$ ($\varepsilon_0 = 8.854 \times 10^{-12}$ F/m) and $\sigma = 0.01$ S/m. The heterogeneous model employs the same background media as the homogeneous case along with an additional homogenous cube anomaly ($\varepsilon = 15\varepsilon_0$ ($\varepsilon_0 = 8.854 \times 10^{-12}$ F/m) and $\sigma = 0.1$ S/m) with 1 m sides and centered at x=y=z=0 m (figure 2).

We begin with the sensitivity kernels for the homogeneous case. The frequency-domain Fréchet sensitivity kernels for electrical permittivity shown in figure 2 at frequencies of 50, 100, and 200 MHz (columns 1, 2, and 3 respectively) and along two cross sections: one in the XZ plane at y =0 (rows 1 and 3) and the second in the YZ plane at x =0 m (rows 2 and 4). Both the source and receiver are oriented in the Z direction and are positioned at the same depth level, z =5 m. The conductivity sensitivity kernels show similar behavior and will not be shown for brevity. The upper two rows give the real component sensitivity kernels and the lower two are for the imaginary component. Sensitivities exhibit a general ellipsoidal shape that increases with decreasing frequency, consistent with the shape of the corresponding Fresnel volume. Larger magnitudes are evident near both the source and receiver locations and are the result of near- and intermediate-field contributions. The hollow cigar shaped kernels similar to those observed for seismic waves (Marquering et al. 1999; Hung et al. 2000; Tromp et al. 2005) can also be seen for some but not for all frequencies. The shape of the frequency-domain sensitivity kernels will change depending on both the frequency and distance between the source and receiver, similar to those for acoustic waves (Woodward 1992). At each location in the volume, the sensitivity kernels are the tensor-vector product of the Green's tensor centered on the receiver and the electric field generated at the source location. Each quantity exhibits a sinusoidal variation and can constructively or destructively interfere depending on the wavelength and separation.

The imaginary component Fréchet sensitivity kernels corresponding to receiver orientations in the X and Y directions are shown in figures 3 and 4 respectively. In both cases, it is interesting

to see that zero amplitude nodal planes are present. For a Z directed source and X directed receiver, the amplitude of the sensitivity kernel is zero for z =5 m. Likewise, a Y directed receiver has nodal planes at both z =5 m and y =5 m. All of the sensitivity kernels are constructed as products of the Green's tensor and the background wavefield. At locations where either the Green's tensor or background wavefield vanishes, so too does the sensitivity kernel. From equation (3.14) the off-diagonal components of the Green's function produce the field components that are orthogonal to the source direction and are zero if the source and receiver locations are the same. This explains why the nodal planes exist for receiver orientations that are not aligned with the source.

Next, we describe the sensitivity kernels at discrete times for the various source and receiver geometries. A Ricker wavelet with its maximum amplitude at t =100 ns has been used for the source time function and is shown along with its first derivative in figure 5 which has been included to illustrate signal modification by the iω coefficient in the near-, intermediate-, and far field terms of equation (3.16). Cross sections of the sensitivity kernels in the XZ plane are shown in figure 6 and the YZ plane in figure 7 and the source and receiver are both located at the z =5 m depth level and oriented in the Z direction. The first time shown (upper left) is prior to the arrival of any appreciable energy at the receiver, the second time (upper middle) occurs near the onset of the initially arriving energy, with subsequent times (descending to the right and then down) selected to capture the entire received signal. The electric field at the receiver locations are shown in the lowermost plot with the selected times designated by crosses at t =130, 146, 148, 150, 160, 170, 180, 190, and 200 ns.

Prior to the onset of energy arriving at the receiver, the sensitivity is everywhere effectively zero as would be expected due to causality. As the wavelet begins to arrive at the receiver, the sensitivity increases between the source and receiver and is roughly symmetric about the YZ plane. The shape is approximately cylindrical and could be considered the finite-frequency extension of the ray-theoretic straight line Fermat kernel. Near-field effects are also clearly evident but are of opposite sign to the portion between the source and receiver. As time proceeds, the ellipsoidal envelope of the sensitivity grows similar to the constant-time boundary of the Fresnel volume. One interesting aspect is that the sensitivity in the XZ plane is smaller than for out-of-plane locations (figure 7), particularly for late times, and can affect data interpretation for various survey layouts. For instance in a cross-borehole survey utilizing Z component receivers,

the late-time data would actually be more sensitive to out-of-plane anomalies than for those within the imaging plane.

We now turn to the discrete time kernels for a Z directed source and X directed receiver (figures 8 and 9). The source and receiver are both located at the z =5 m depth level and for this case the x component of the background field at the receiver (and all points in the z =5 m plane) will be zero (blue line in lower plot). This is simply due to the x-component radiation pattern of the Green's tensor. The sensitivity kernel is non-zero except for points on the z =5 m plane and indicates that anomalies located off the z =5 m plane can scatter energy that arrives at the receiver. Near-field effects are also seen but have a somewhat different character showing a larger contribution at the receiver than near the source. We also note that the sensitivity kernel is anti-symmetric across the z =5 m plane. Anomalies that are symmetric across the z = 5 m plane contribute equal but opposite sensitivities from each side of the plane and will then produce no net effect on the data. In contrast to the Z directed source and receiver, the X directed receiver has its maximum sensitivity in the XZ imaging plane.

The sensitivity kernels for a Z directed source and Y directed receiver both positioned at z =5 m is shown in figure 10. Similar to the receiver orientation in the X direction, the Y direction has a nodal plane at z =5 m but also shows a second nodal plane at x =0. Again this can be explained by the interference between the radiation patterns of the Green's tensors centered on the source and receiver. In contrast to the Z directed receiver, the Y component possesses a different sensitivity for points not on the x =5 m and z =5 m planes. In addition, the Y directed receiver has its maximum sensitivity at 45 degrees off of the XZ imaging plane. Such differences in the sensitivity patterns may be exploited to better constrain 3D inversion estimates for anomalies located both on and off the imaging planes.

The final discrete time kernel also uses a Z directed source and X directed receiver but now repositions the receiver to be at a higher angle (figures 11 and 12). In this case the sensitivity kernel is a composite of the kernels described above for the level Z-Z (source-receiver) orientations and the Z-X orientation since both source and receiver are angled in the XZ plane relative to the source-receiver separation. The Z-X sensitivity is approximately one half the magnitude for the Z-Z case and the composite of the two is then dominated by the Z-Z sensitivity. The high angle Z-X sensitivity kernel is similar to the level Z-Z case; however, the sensitivity is reduced above the source and to the left of the receiver indicative of the Z-X

contribution. Meles et al. (2012) constructed 2D discrete time EM sensitivity kernels that show similar patterns to the Z-Z and Z-X cases illustrated here; however out of plane sensitivity features were not captured due to the 2D implementation.

We now describe the cross-correlation based travel-time and RMS amplitude sensitivity kernels. The source and receiver are both in the Z direction. From equations (3.56) through (3.61), the sensitivity kernels are weighted averages of the discrete time kernels with weights proportional to the wave field at the receiver or its time derivatives. Since the x and y background wavefield components at the receiver are zero for the level case, so are the travel-time and RMS amplitude sensitivity kernels. The travel-time sensitivity kernels for permittivity and conductivity perturbations are shown in figure 13 and the corresponding amplitude sensitivity kernels shown in figure 14 for the level geometry. The high angle cases are then shown in figures 15 and 16. For both the permittivity and conductivity perturbations, the level and high angle cases are very similar. The general ellipsoidal shape and larger sensitivity magnitudes near the source and receiver are observed similar to the other sensitivity kernels described above. Also, some of the kernels (figures 14 and 16 upper left panel) have zero sensitivity on the line connecting the source and receiver and is similar to the hollow cigar or "banana-doughnut" shape seen for 3-D seismic wave velocity sensitivity kernels (Marquering et al. 1999). Here we are concerned with sensitivities for electrical permittivity and conductivity rather than velocity. For EM waves, velocity is a non-linear function of the electrical permittivity and conductivity so cannot be easily compared to EM velocity or amplitude sensitivity kernels by other researchers (Johnson et al 2005; Buursink et al. 2008); however, their general characteristics show many similarities.

Finally, the sensitivity kernels for the heterogeneous case are described. A cube anomaly with 1 m sides and having an electrical permittivity and conductivity that are two times and ten times those of the background media was used to provide a reasonable contrast. Figure 17 shows the frequency-domain, imaginary component of the permittivity sensitivity kernels for a Z-directed source and both Z-directed and X-directed receivers. The discrete time-domain permittivity sensitivity kernels are shown in in figures 18 and 19 for a Z-directed receiver, an X-directed receiver in figures 20 and 21, and finally the Y-directed receiver is shown in figure 22. All of the sensitivity kernels for the heterogeneous case are similar in character to the homogeneous case; however the region corresponding to the location of the anomaly consistently

exhibits a reduced level of sensitivity. Also, the sensitivity kernels with a Z-directed source and receiver appeared to show the largest differences compared to the homogeneous case. This is likely due to the fact that the X-directed and Y-directed receiver orientations have low sensitivities at the location of the anomaly and so exhibit little sensitivity changes between the homogeneous and heterogeneous cases.

3.6 CONCLUSIONS

We have presented 3-D Fréchet EM sensitivity kernels for several types of data functionals. Fréchet sensitivity kernels play a central role in the tomographic inverse methods and it is important to understand their characteristics and how they may impact the inversion. Often only a single component of the measured signal is used; however, incorporating other components can help to better constrain the inversion. We have described the EM sensitivity kernels for all three components of the electric wavefield and illustrated their differences and similarities. In addition, discrete time sensitivities can be used for full-waveform inverse methods and illustrate important aspects present in both homogeneous and heterogeneous media. Finally, EM cross-correlation travel-time and RMS amplitude sensitivity kernels can be used to incorporate finite frequency effects and have characteristics similar to those for seismic wave propagation problems.

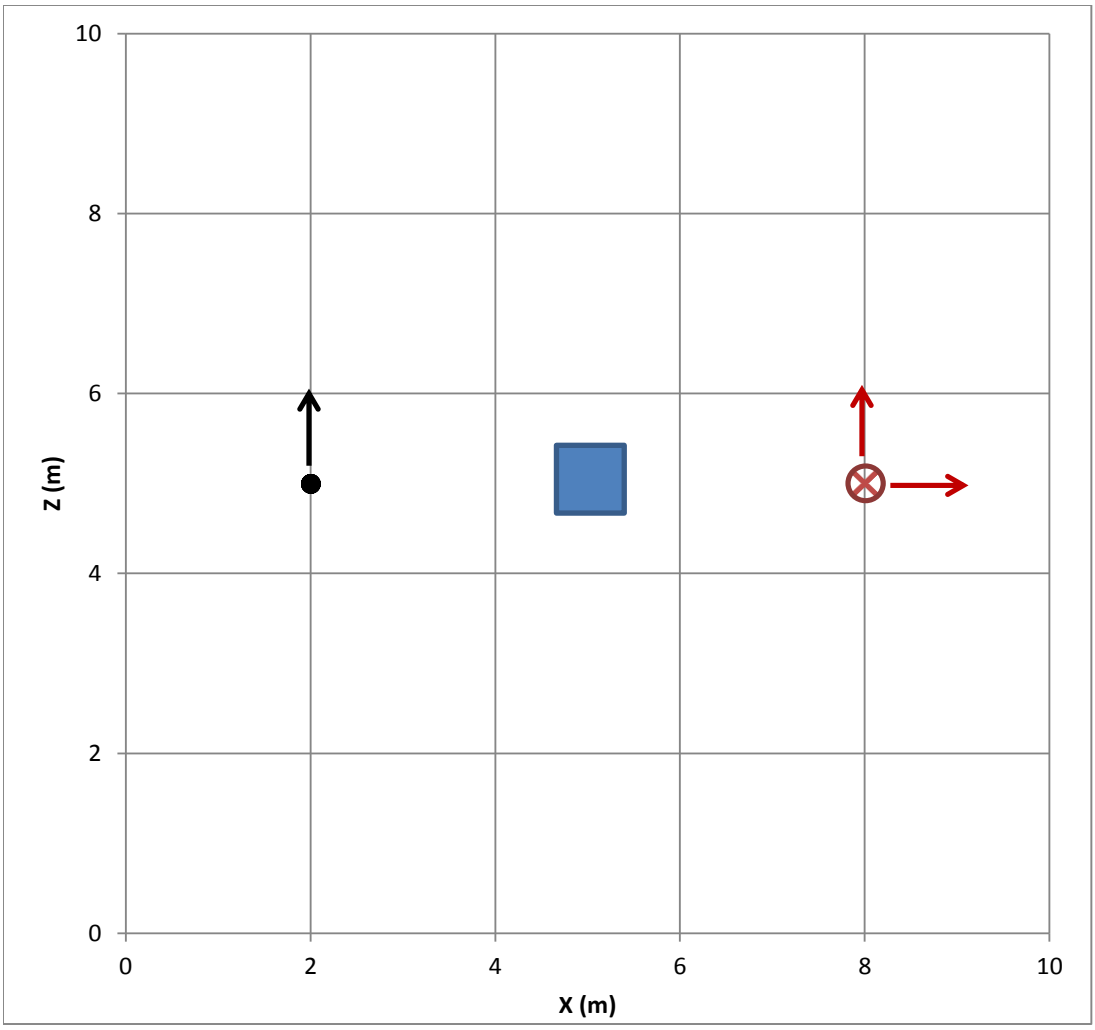

Figure 3.1 Source-receiver geometry and anomaly used in the heterogeneous case

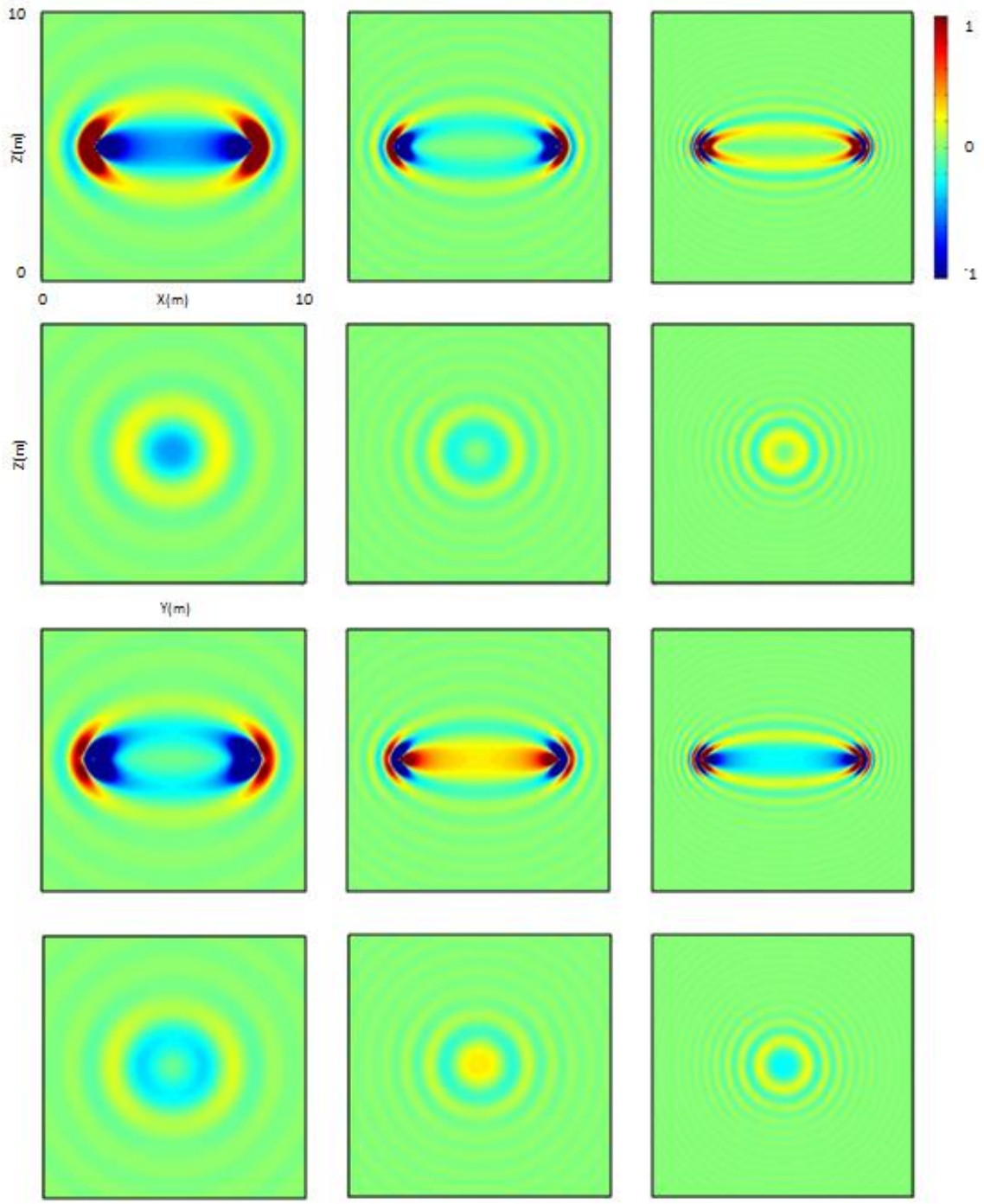

Figure 3.2 Homogeneous background medium, frequency-domain permittivity sensitivity kernels in the XZ, y=0 m (first and third rows) and YZ, x=0 m (second and fourth rows) planes: imaginary (upper two rows) and real (lower two rows) components for three frequencies. Columns 1, 2, and 3 correspond to frequencies of 50, 100, and 200 MHz respectively. Level source-receiver geometry, source is in the Z-direction and receiver is also in the Z-direction.

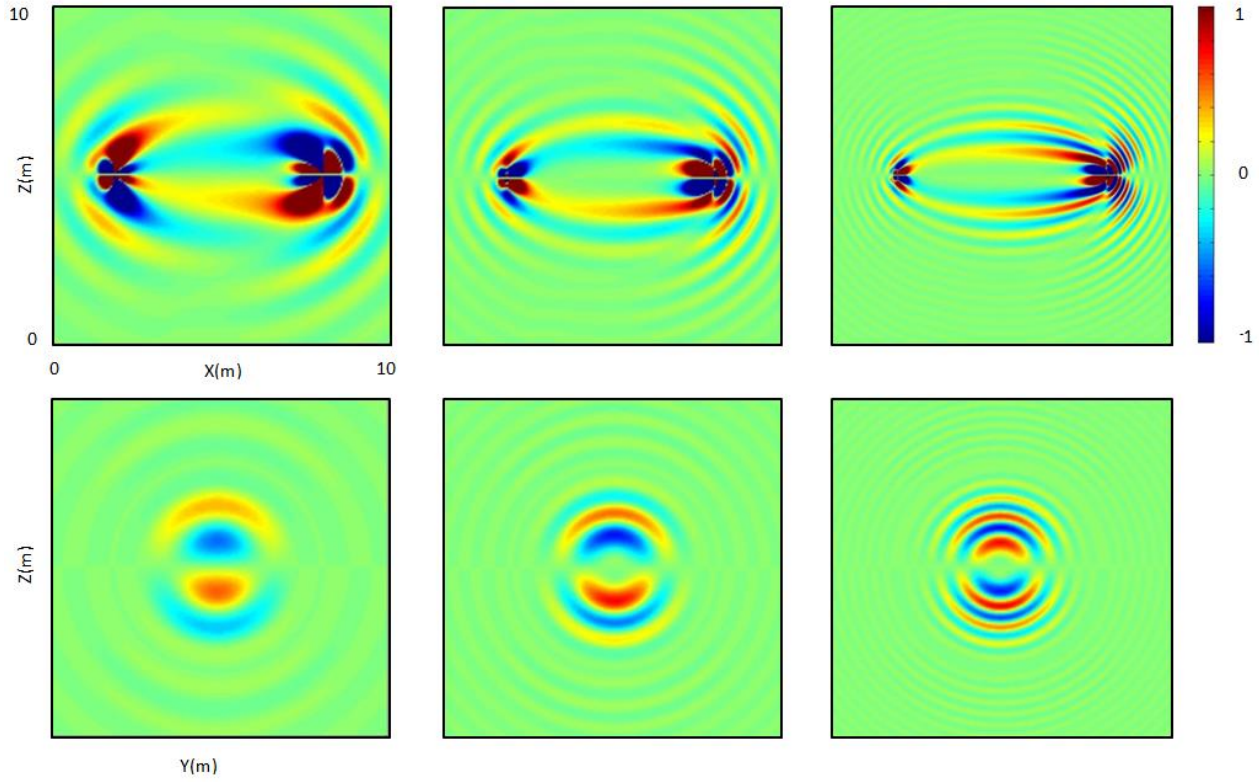

Figure 3.3 Homogeneous background medium, frequency-domain imaginary component of the permittivity sensitivity kernels in the XZ, y=0 m (top) and YZ, x=0 m (bottom) planes. Columns 1, 2, and 3 correspond to frequencies of 50, 100, and 200 MHz respectively. Level source-receiver geometry, source is in the Z-direction and receiver is in the Y-direction.

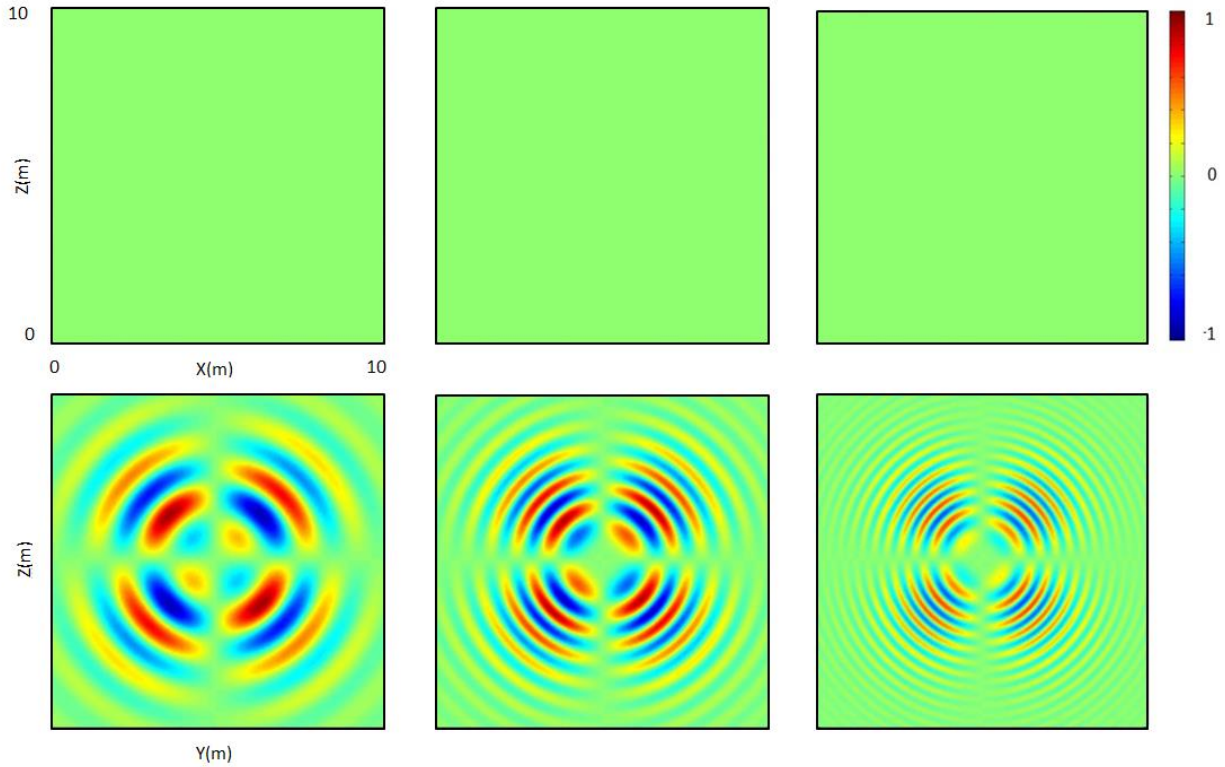

Figure 3.4 Homogeneous background medium, frequency-domain imaginary component of the permittivity sensitivity kernels in the XZ, y=0 m (top) and YZ, x=0 m (bottom) planes. Columns 1, 2, and 3 correspond to frequencies of 50, 100, and 200 MHz respectively. Level source-receiver geometry, source is in the Z-direction and receiver is in the Y-direction.

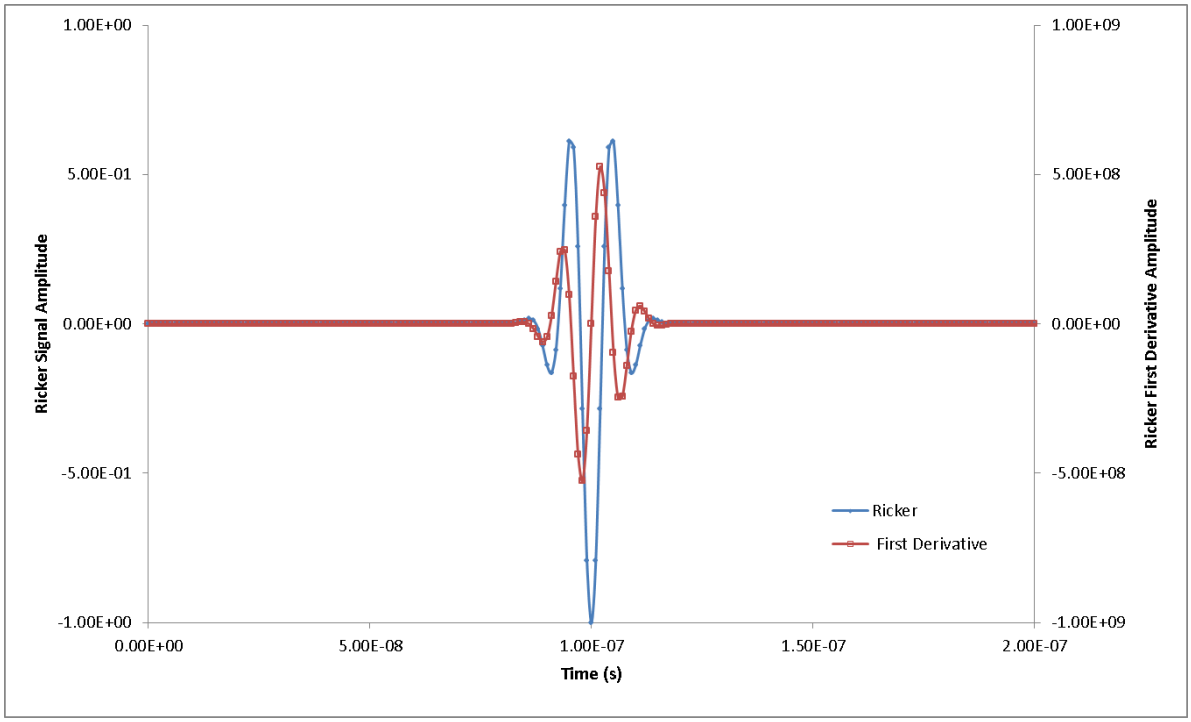

Figure 3.5 Ricker wavelet used for the source time function (blue) and its first time derivative (red).

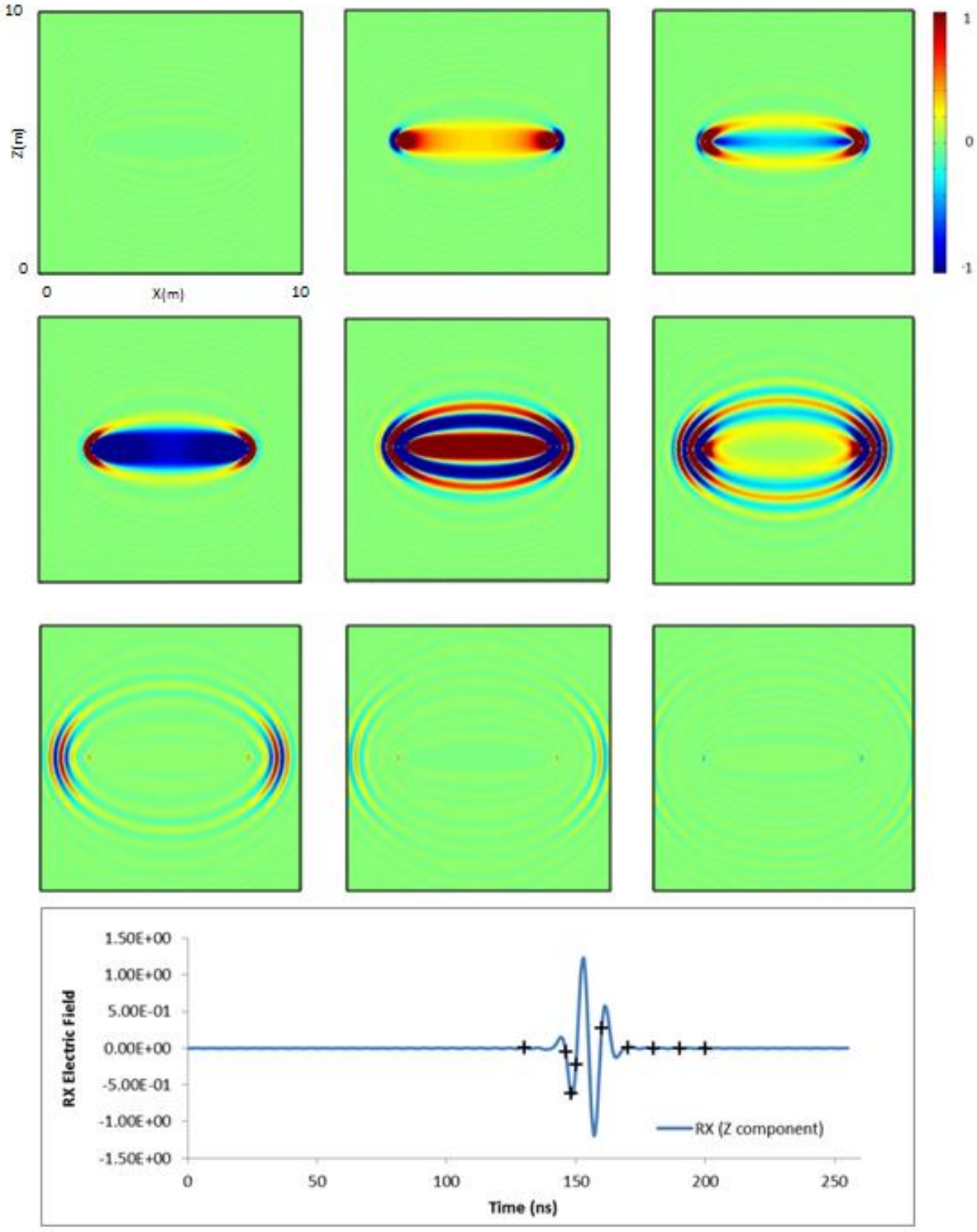

Figure 3.6 Cross-section through XZ plane (Y=0): homogeneous background medium, permittivity Fréchet sensitivity kernels at discrete times indicated by crosses for a level, Z directed transmitter and Z directed receiver geometry. Z-component of the electric field at the receiver is shown in the lower plot.

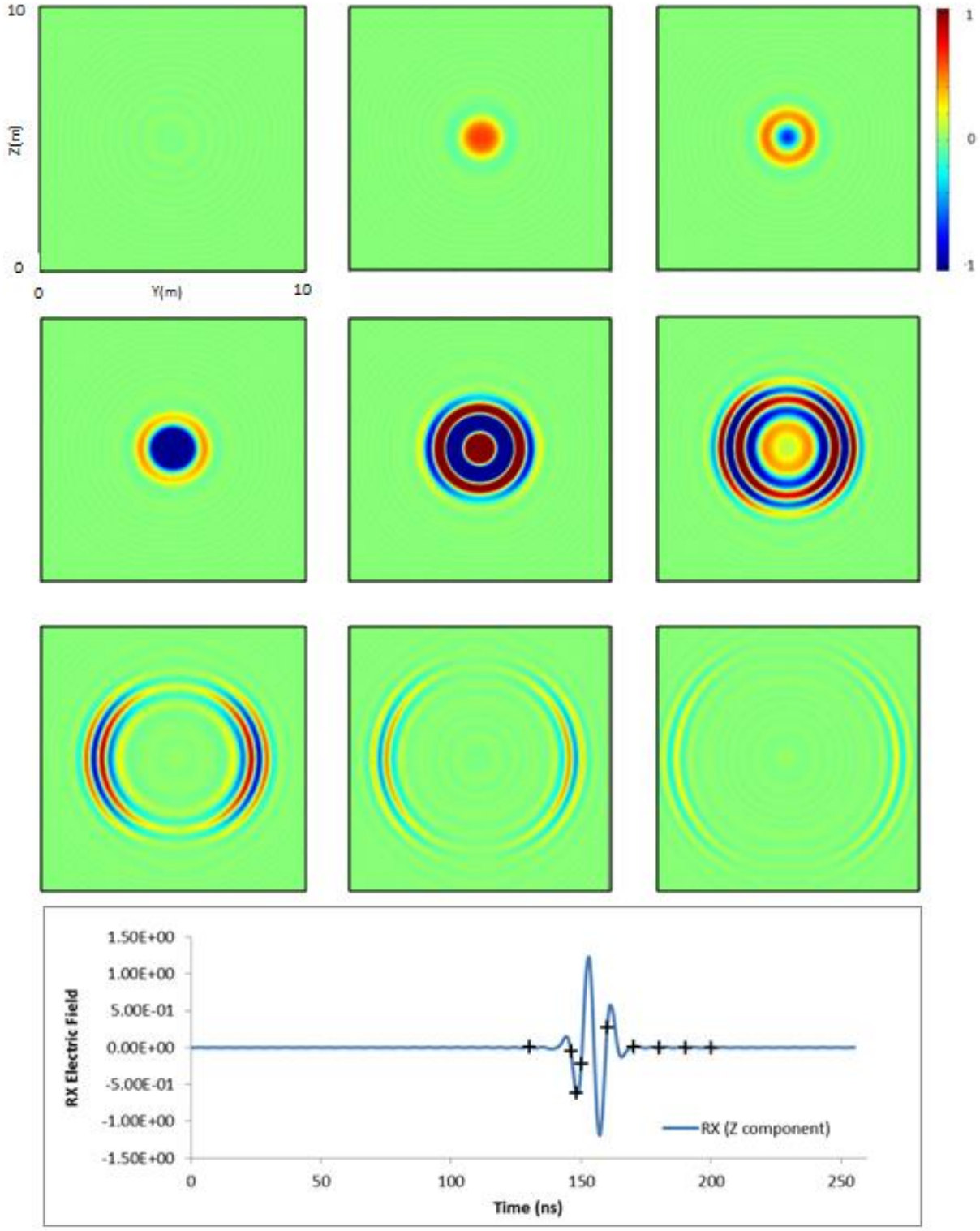

Figure 3.7 Cross-section through YZ plane (X=0): homogeneous background medium, permittivity Fréchet sensitivity kernels at discrete times indicated by crosses for a level, Z directed transmitter and Z directed receiver geometry. Z-component of the electric field at the receiver is shown in the lower plot.

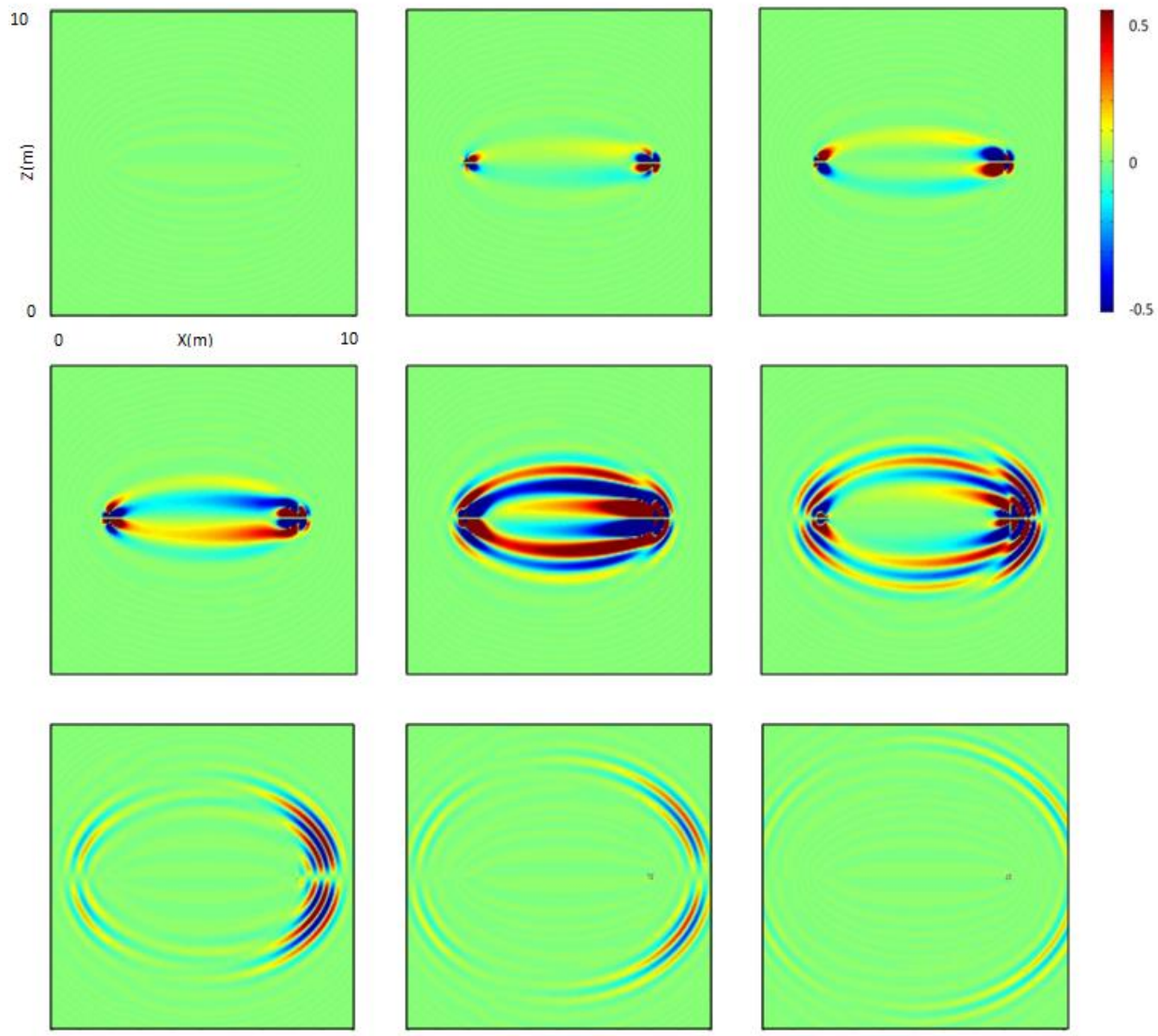

Figure 3.8 Cross-section through XZ plane (Y=0): homogeneous background medium, permittivity Fréchet sensitivity kernels at discrete times for a level, Z-directed transmitter and X-directed receiver geometry.

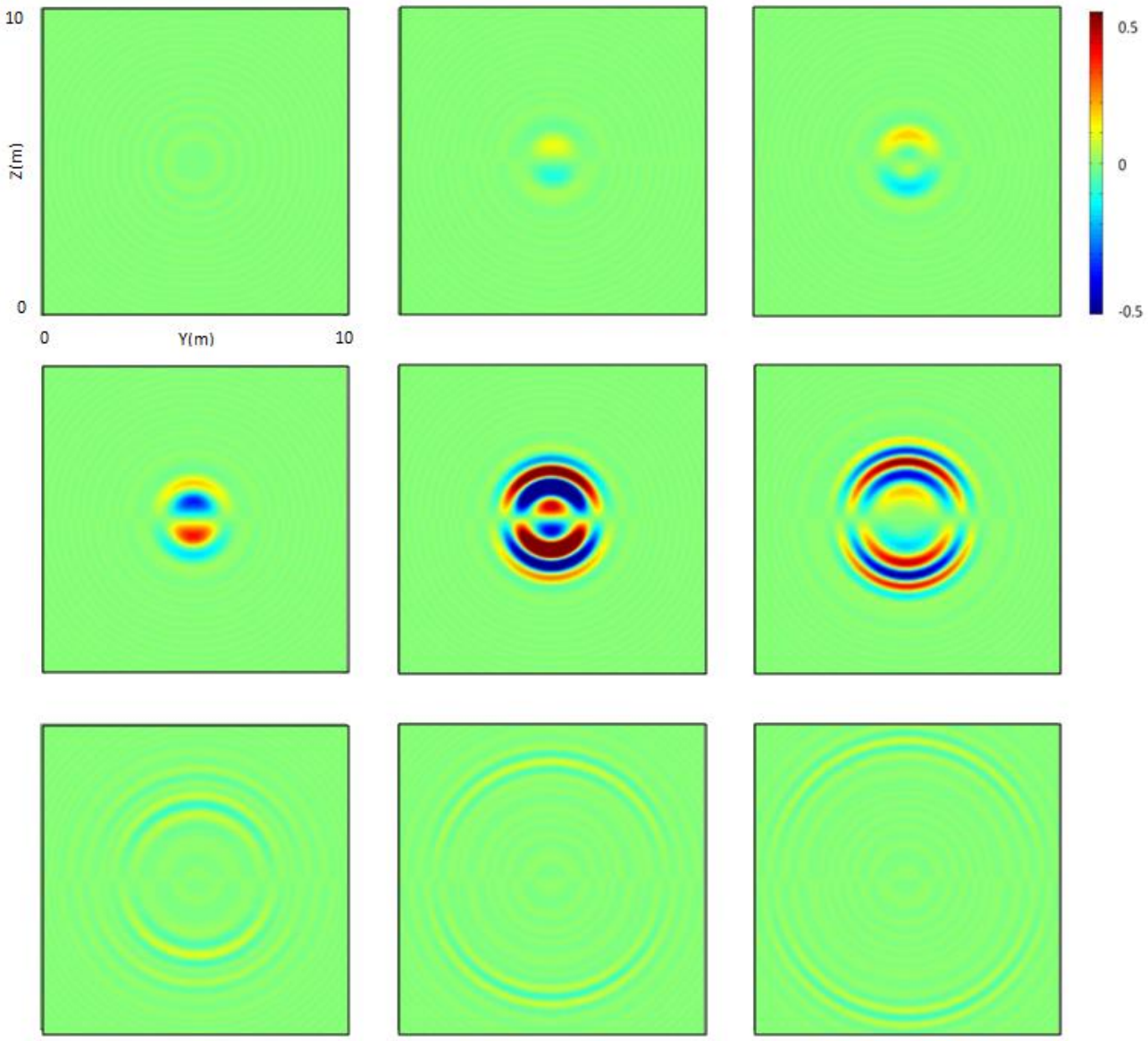

Figure 3.9 Cross-section through YZ plane (X=0): homogeneous background medium, permittivity Fréchet sensitivity kernels at discrete times for a level, Z-directed transmitter and X-directed receiver geometry.

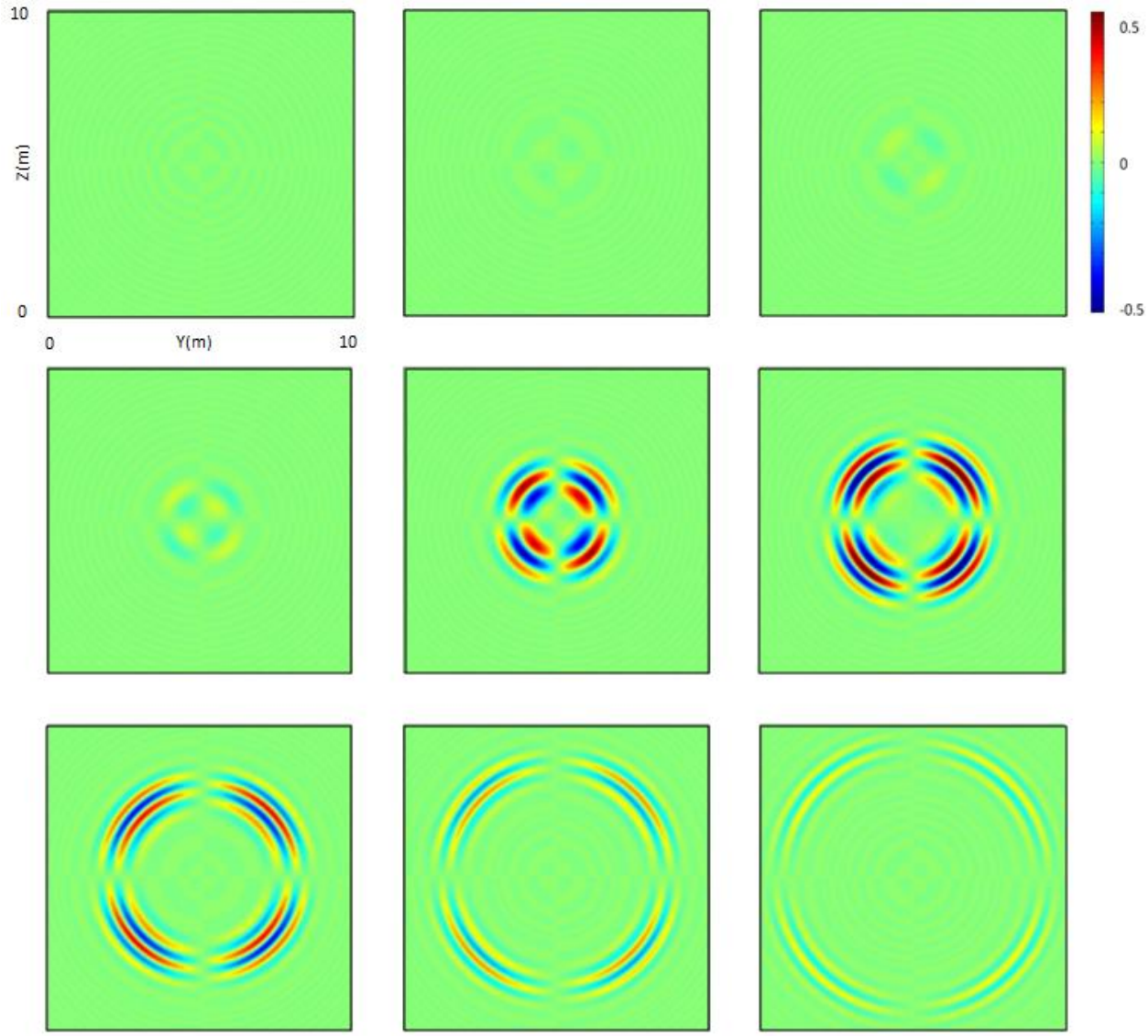

Figure 3.10 Cross-section through YZ plane (X=0): homogeneous background medium, permittivity Fréchet sensitivity kernels at discrete times for a level, Z-directed transmitter and Y-directed receiver geometry.

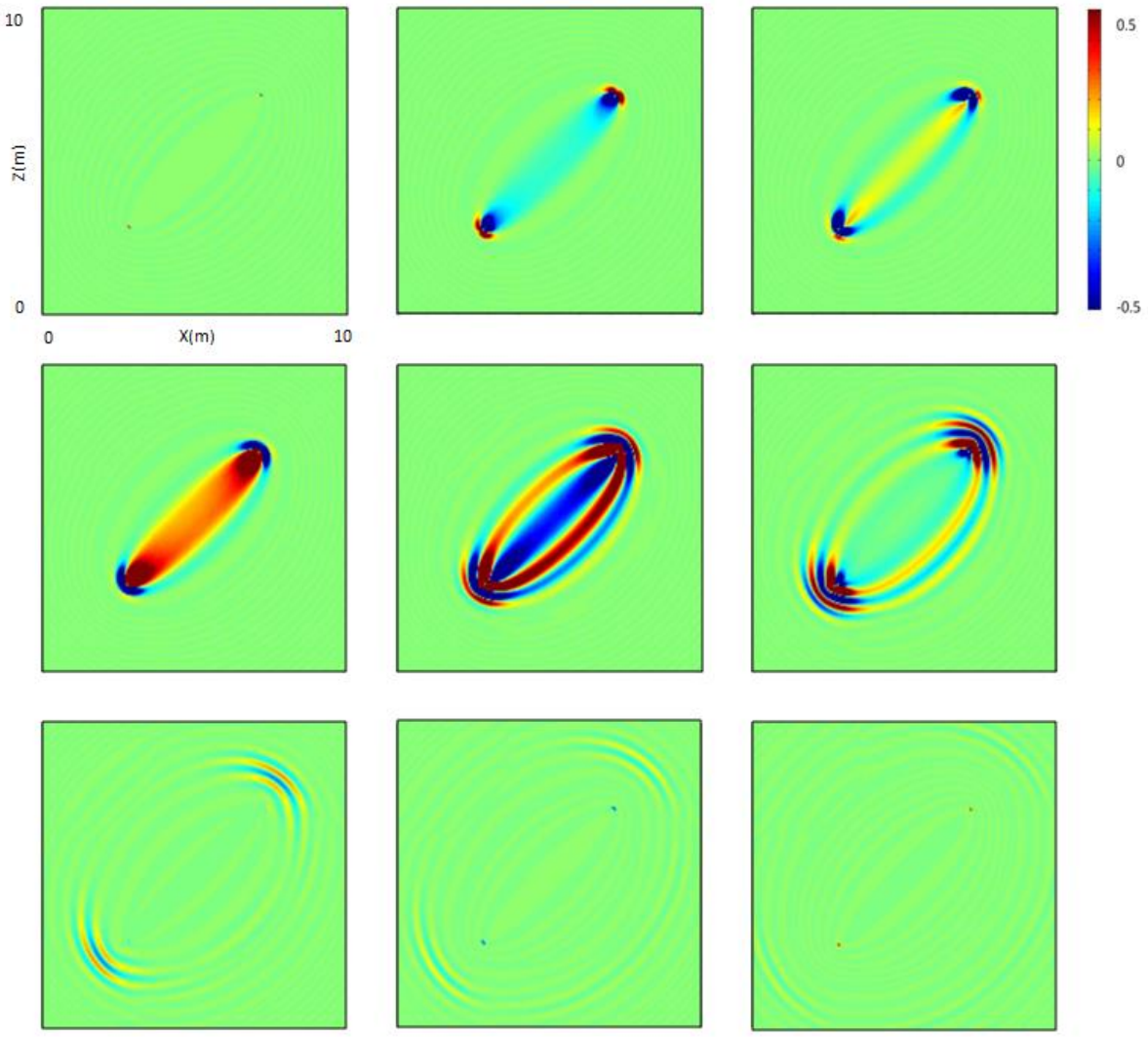

Figure 3.11 Cross-section through XZ plane (Y=0): homogeneous background medium, permittivity Fréchet sensitivity kernels at discrete times for an angled, Z-directed transmitter and X-directed receiver geometry.

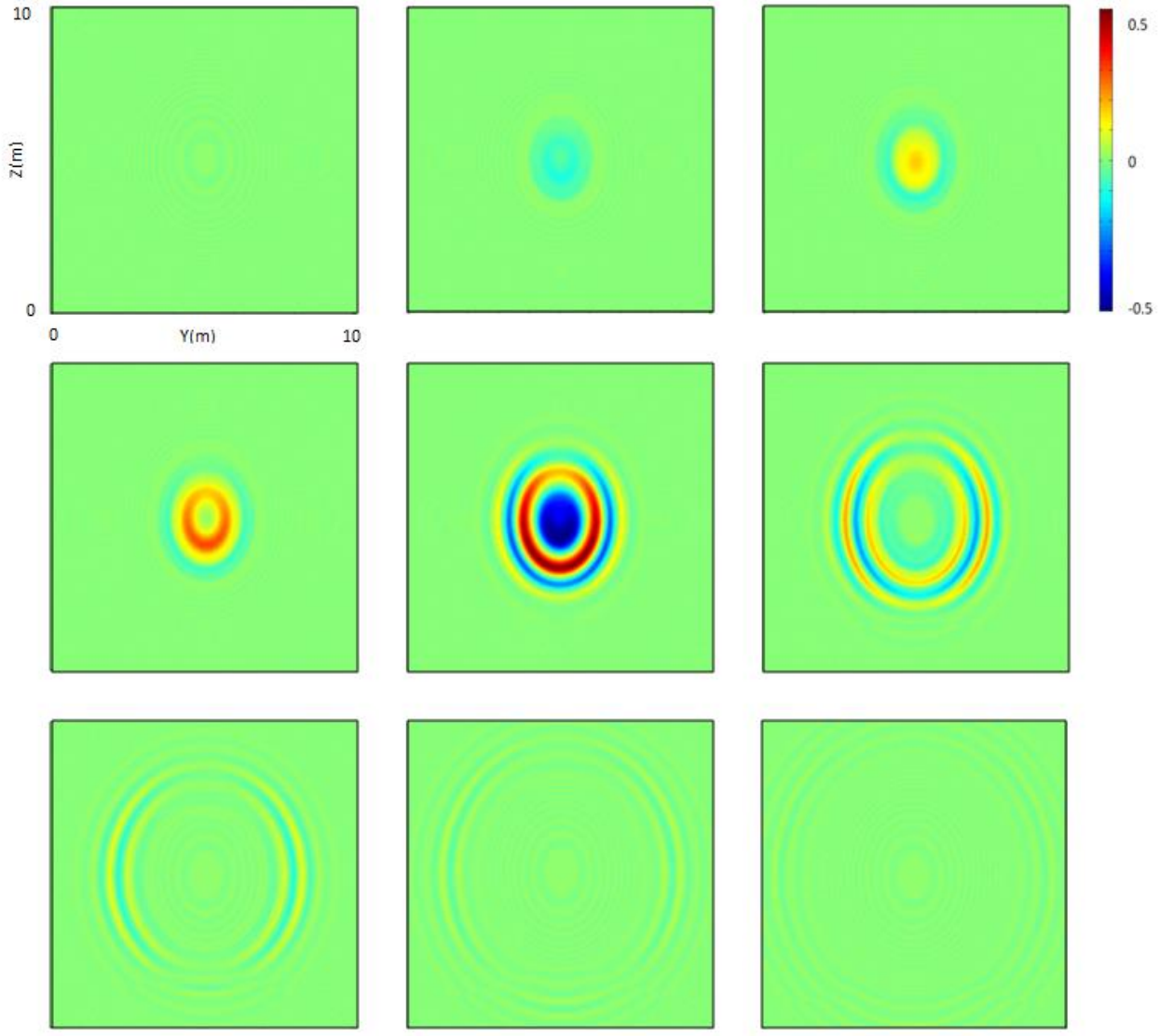

Figure 3.12 Cross-section through XZ plane (Y=0): homogeneous background medium, permittivity Fréchet sensitivity kernels at discrete times for an angled, Z-directed transmitter and X-directed receiver geometry.

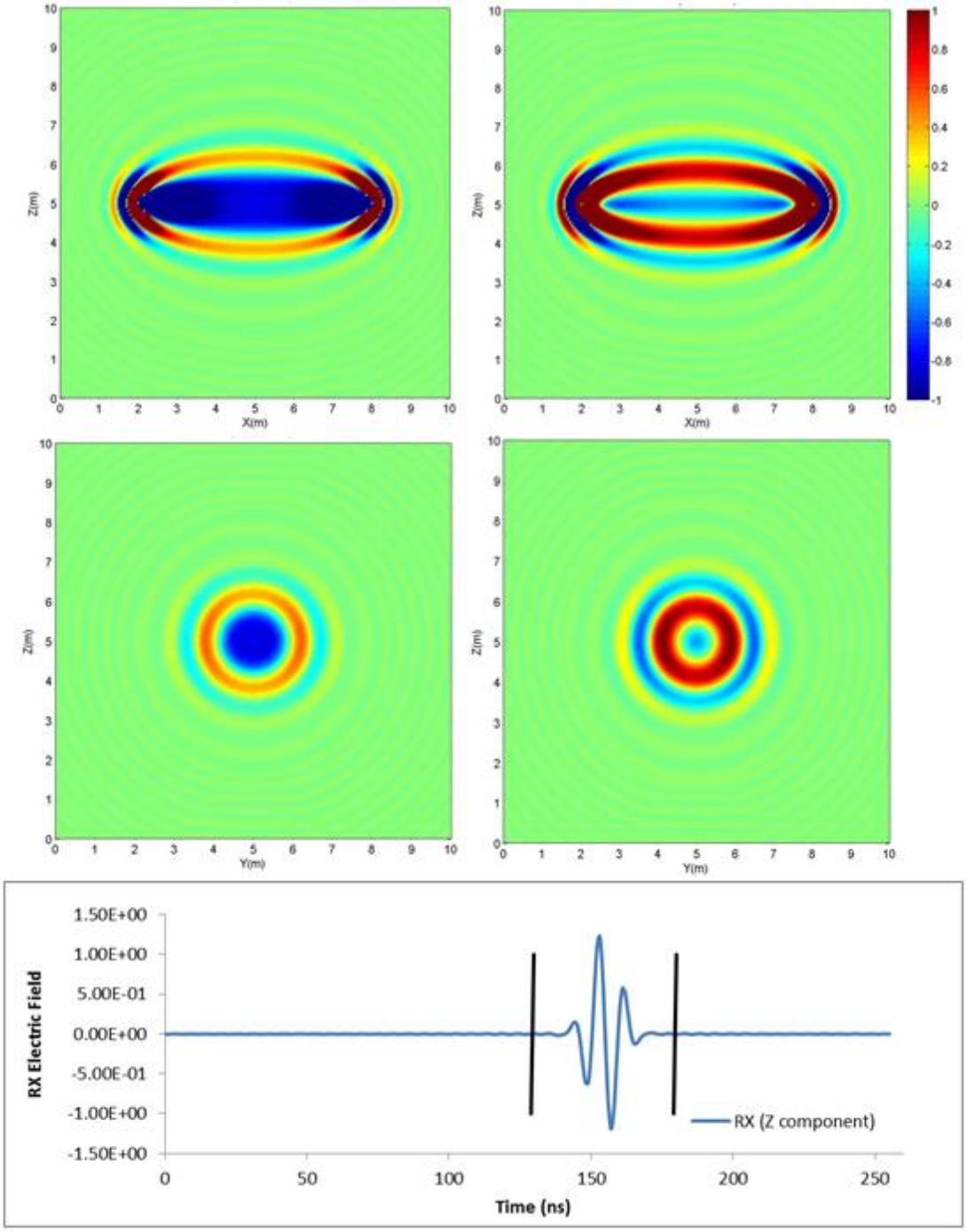

Figure 3.13 Cross-section through XZ (upper) and YZ (lower): homogeneous background medium, travel-time permittivity (left) and conductivity (right) Fréchet sensitivity kernels for a level, Z-directed transmitter and Z-directed receiver geometry. Vertical lines denote the time integration window.

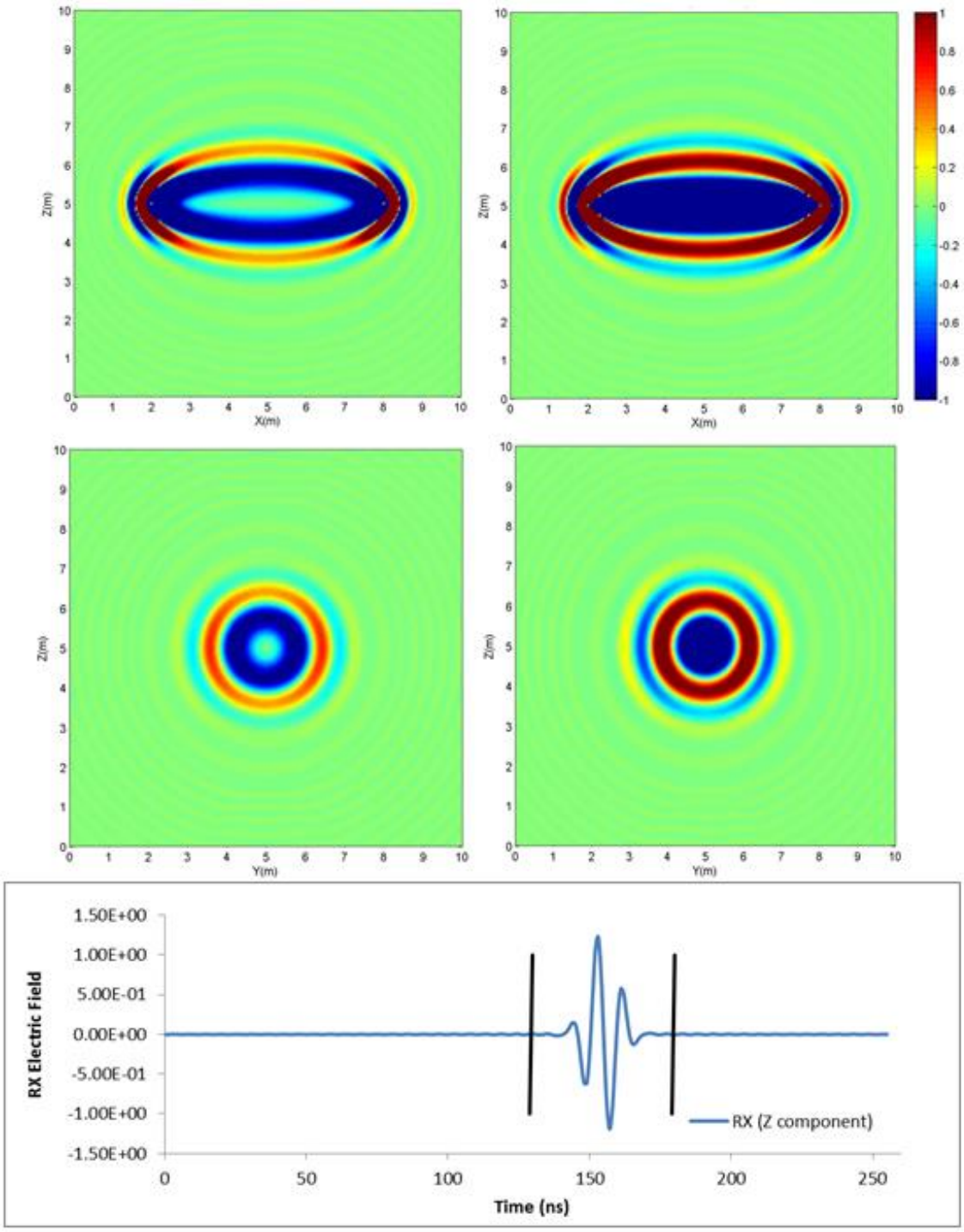

Figure 3.14 Cross-section through XZ (upper) and YZ (lower): homogeneous background medium, RMS amplitude permittivity (left) and conductivity (right) Fréchet sensitivity kernels for an angled, Z-directed transmitter and Z-directed receiver geometry. Vertical lines denote the time integration window.

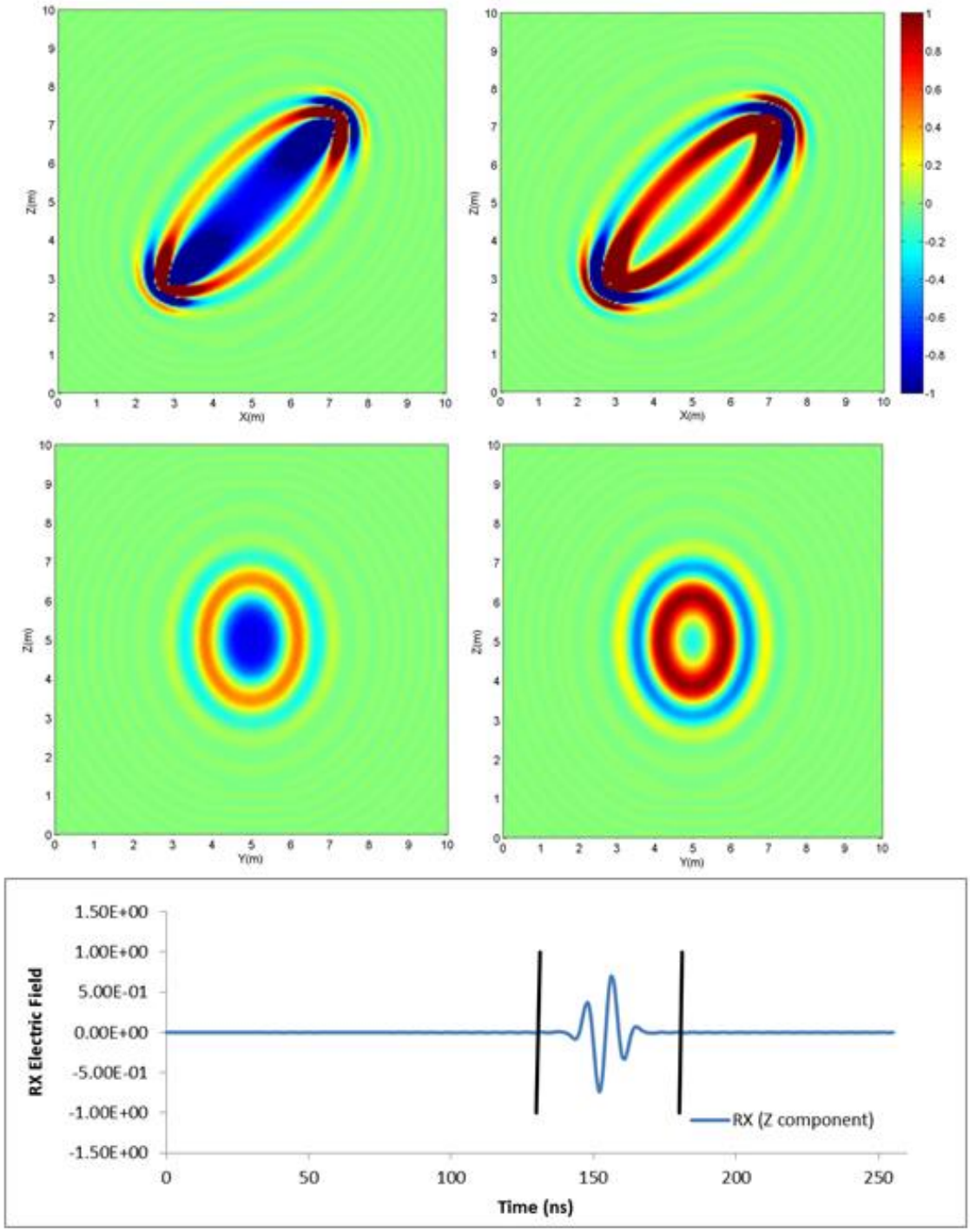

Figure 3.15 Cross-section through XZ (upper) and YZ (lower): homogeneous background medium travel-time permittivity (left) and conductivity (right) Fréchet sensitivity kernels for a level, Z-directed transmitter and Z-directed receiver geometry. Vertical lines denote the time integration window.

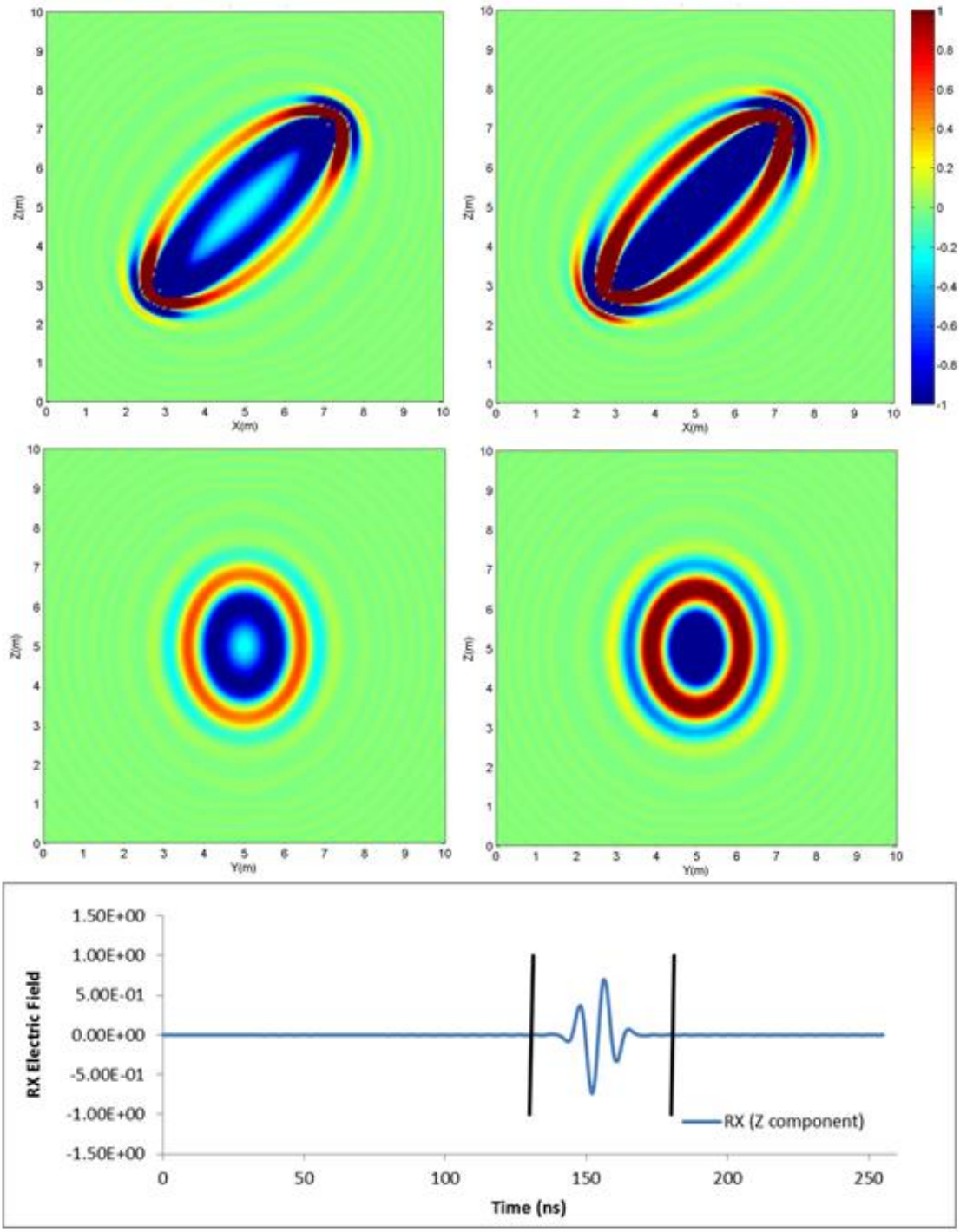

Figure 3.16 Cross-section through XZ (upper) and YZ (lower): homogeneous background medium RMS amplitude permittivity (left) and conductivity (right) Fréchet sensitivity kernels for an angled, Z-directed transmitter and Z-directed receiver geometry. Vertical lines denote the time integration window.

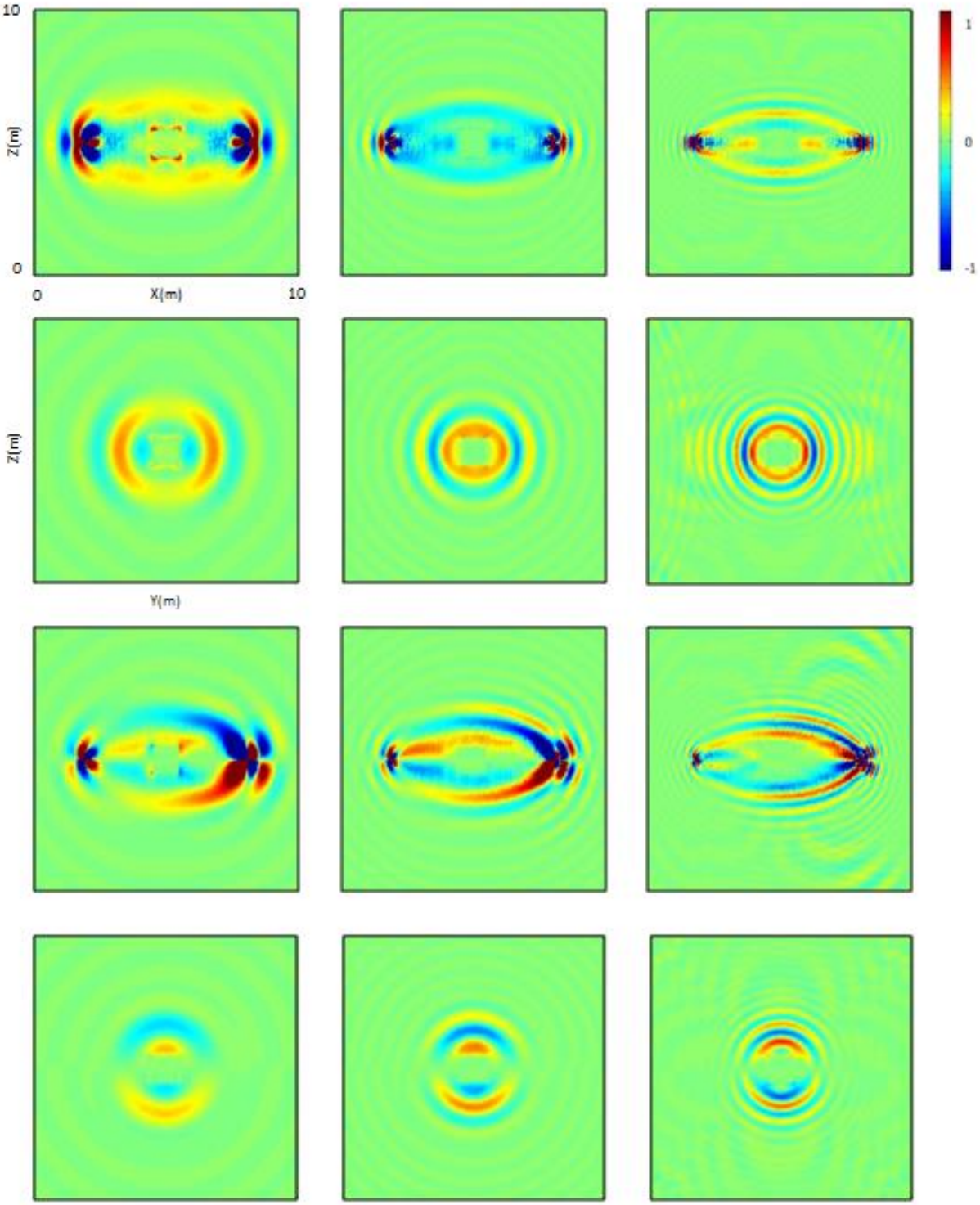

Figure 3.17 Heterogeneous background medium, frequency-domain permittivity sensitivity kernels in the XZ, y=0 m (first and third rows) and YZ, x=0 m (second and fourth rows) planes: imaginary (upper two rows) components for three frequencies. Columns 1, 2, and 3 correspond to frequencies of 50, 100, and 200 MHz respectively. Source is in the z-direction, receiver is in the z-direction (upper two rows), and in the x-direction (lower two rows).

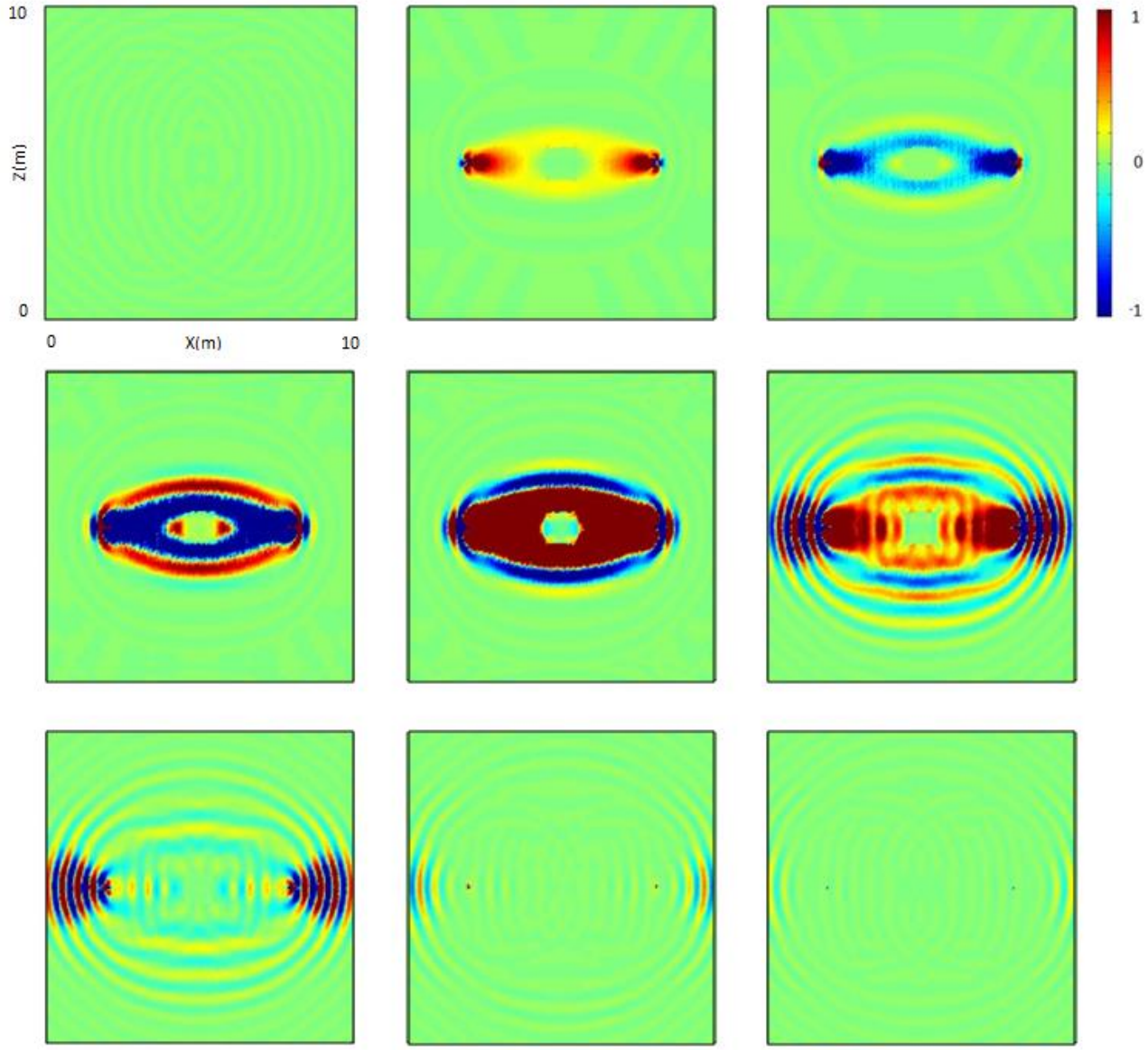

Figure 3.18 Cross-section through XZ plane (Y=0): heterogeneous background medium, permittivity Fréchet sensitivity kernels at discrete times for level, Z-directed transmitter and Z-directed receiver geometry.

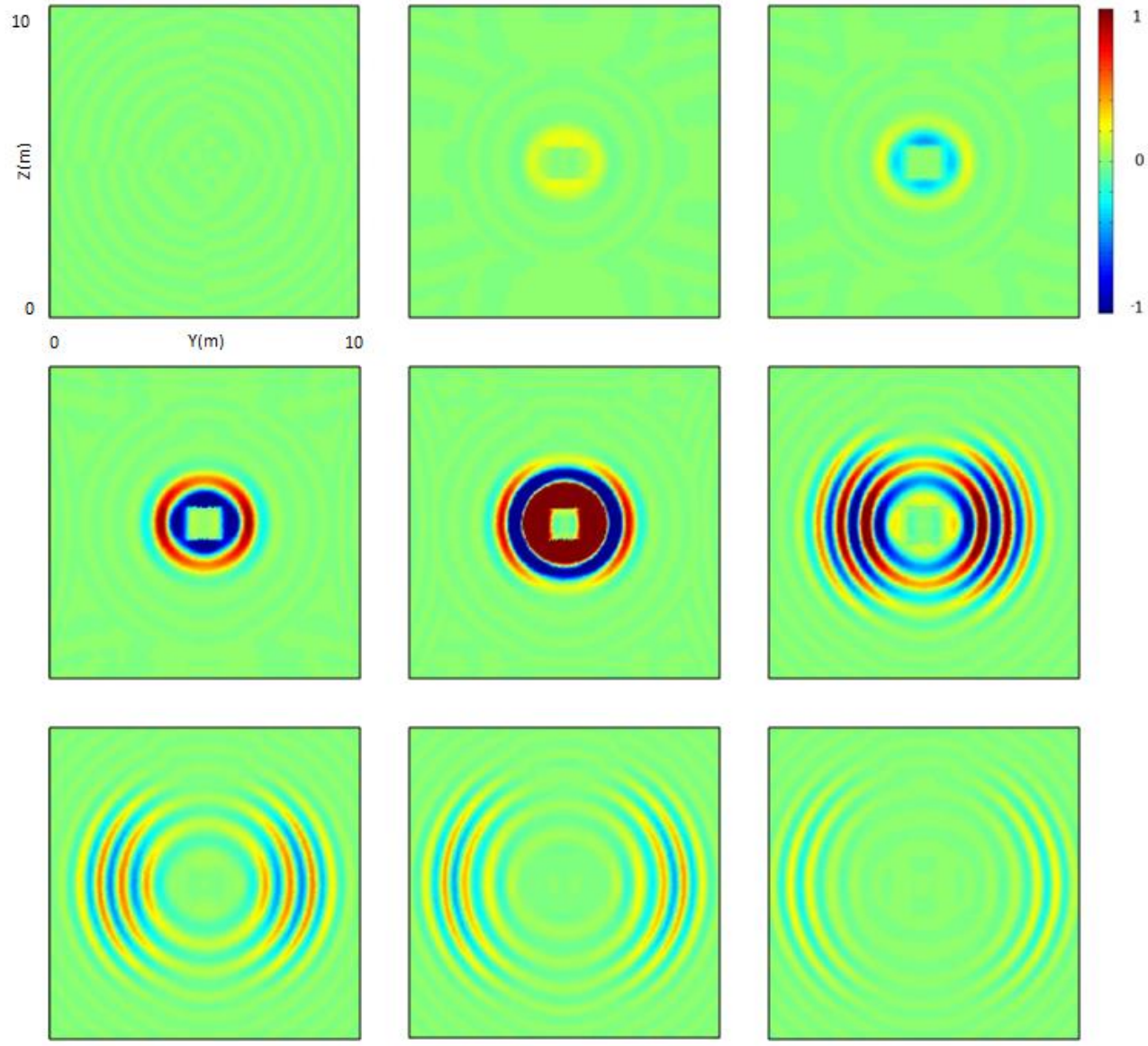

Figure 3.19 Cross-section through YZ plane (X=0): heterogeneous background medium, permittivity Fréchet sensitivity kernels at discrete times for level, Z-directed transmitter and Z-directed receiver geometry.

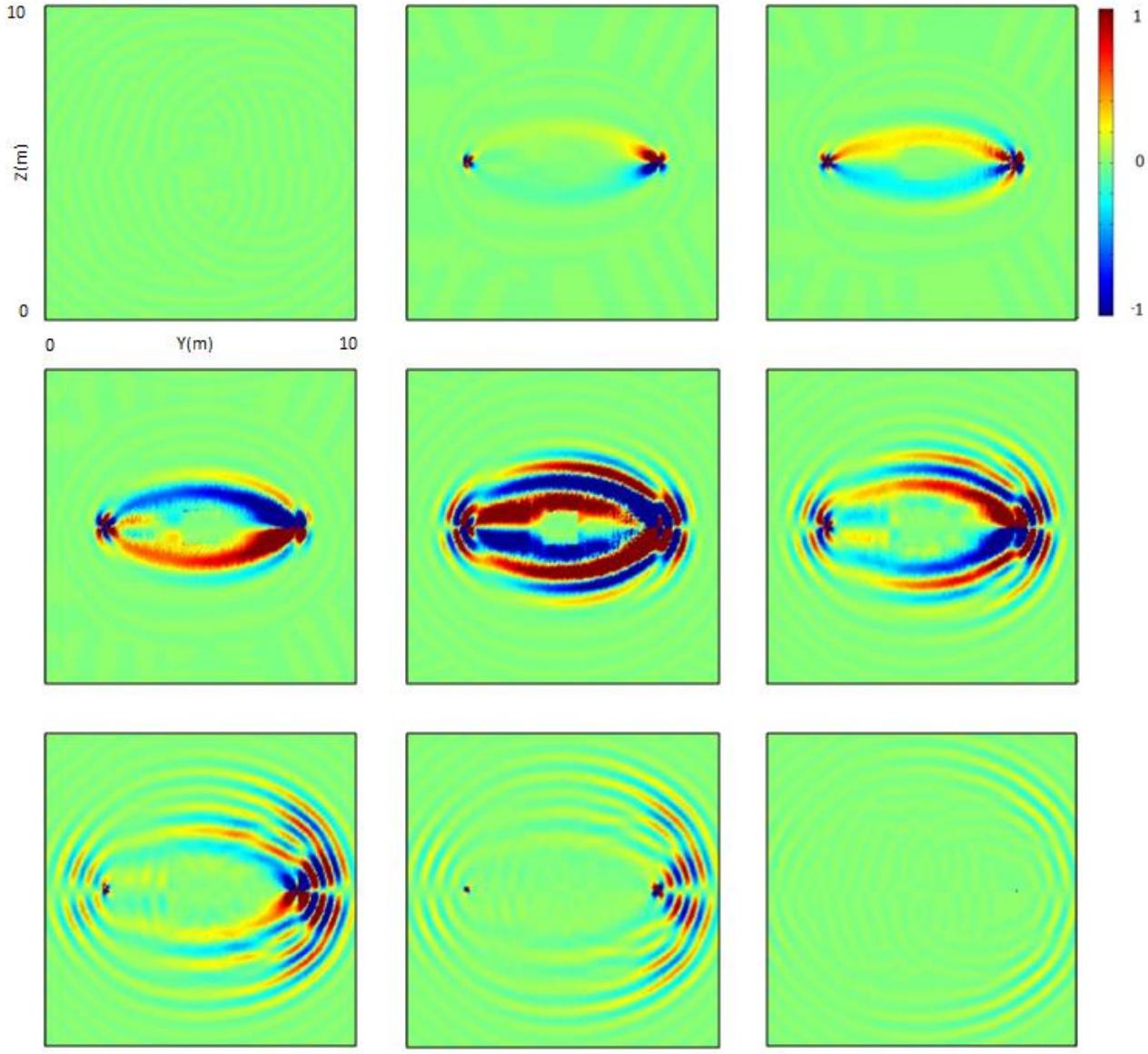

Figure 3.20 Cross-section through XZ plane (Y=0): heterogeneous background medium, permittivity Fréchet sensitivity kernels at discrete times for level, Z-directed transmitter and X-directed receiver geometry.

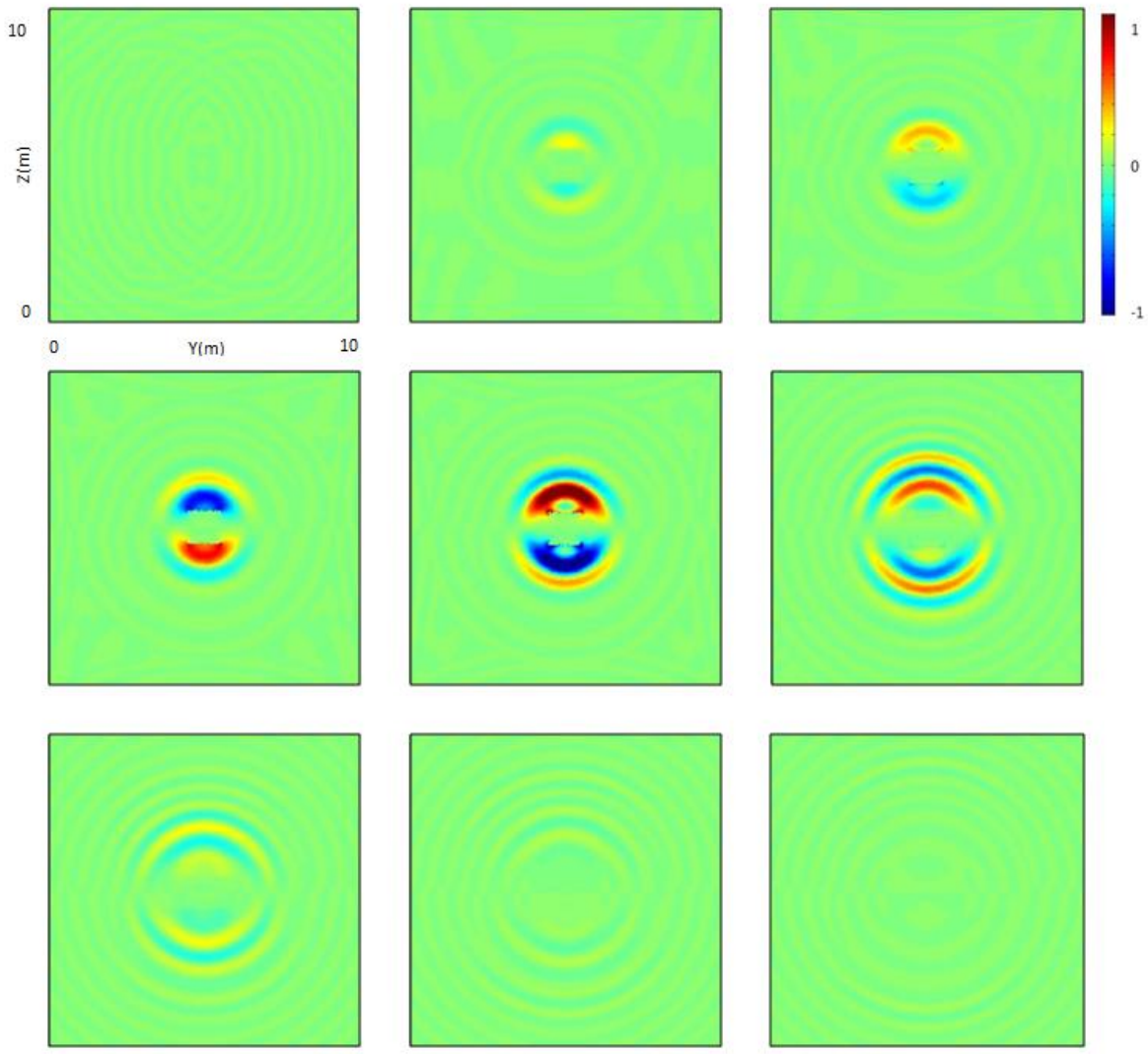

Figure 3.21 Cross-section through YZ plane (X=0): heterogeneous background medium, permittivity Fréchet sensitivity kernels at discrete times for level, Z-directed transmitter and X-directed receiver geometry.

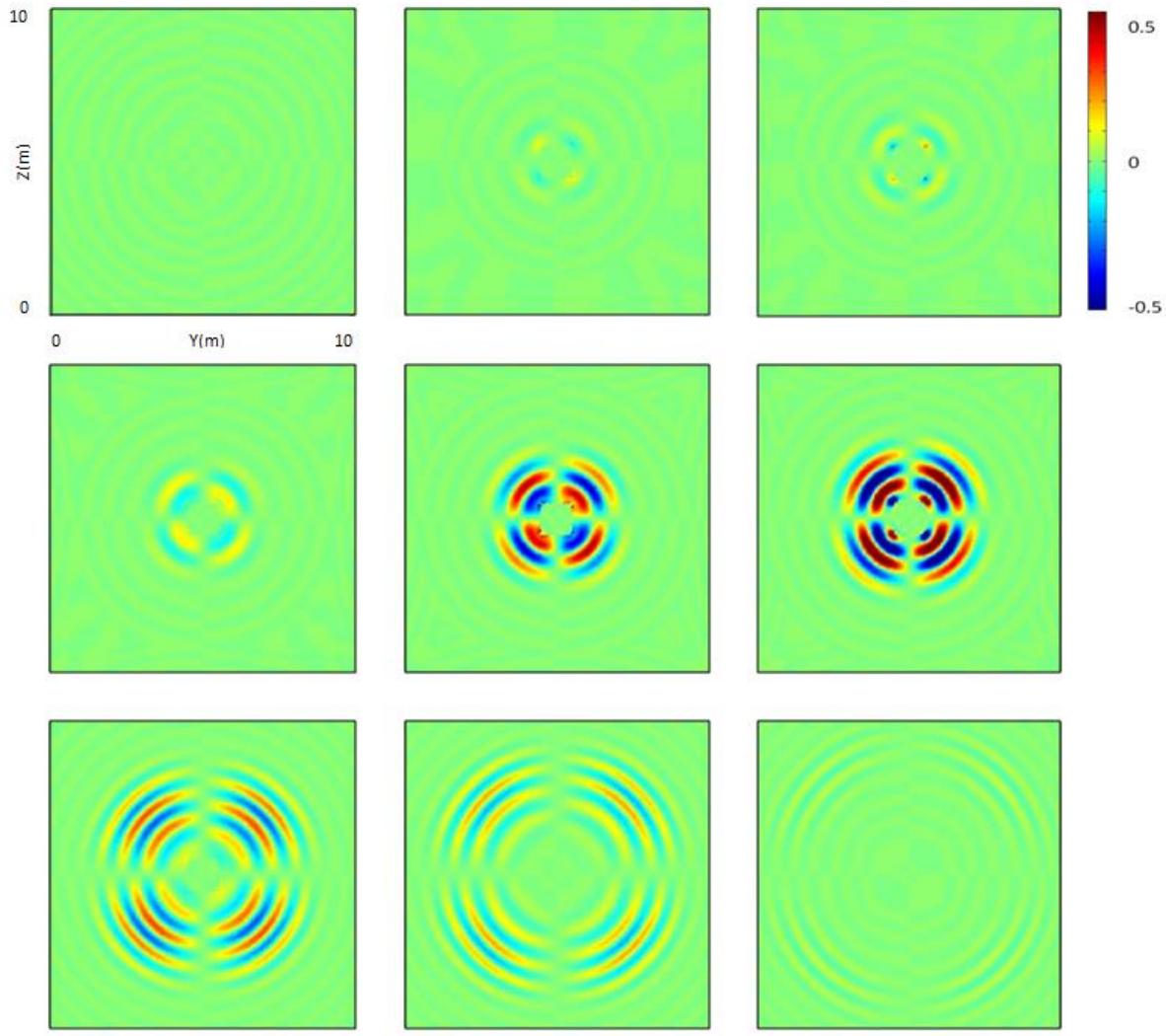

Figure 3.22 Cross-section through YZ plane (X=0): heterogeneous background medium, permittivity Fréchet sensitivity kernels at discrete times for level, Z-directed transmitter and Y-directed receiver geometry.

4 ELECTROMAGNETIC INTEGRAL EQUATION FORWARD MODELING

A number of methods have been developed to solve electromagnetic problems and include analytical techniques applied to simple geometries, asymptotic methods such as Wentzel-Kramers-Brillouin-Jeffreys (WKBJ) or ray-theoretic approximations, and modern numerical methods applicable to problems involving arbitrary structures and sources. The governing electromagnetic equations can be formulated in both differential and integral forms and numerical methods have been developed to solve each type. Finite-differences and finite-element (FEM) methods are common approaches for discretizing and solving the resulting differential equations. The differential equations can also be transformed into an equivalent integral equation and provides an alternative framework for developing numerical solutions to electromagnetic problems.

Finite-difference methods discretize the underlying partial differential equations by approximating the derivatives of a continuous function using values of the function at discrete sample points. Problems can be formulated in either the time-domain (FDTD) or frequency-domain (FDFD) using finite-differences and both cases produce sparse matrices; however different numerical approaches are used to solve the resulting equations. FDFD solve the resulting linear system using standard algorithms for sparse matrices and are generally more difficult than FDTD problems. FDTD problems are solved explicitly by stepping from the initial state through time. FDTD is a robust and accurate method that can handle problems involving complex structures and wide bandwidth signals.

Maxwell's equations describing electromagnetic fields can also be formulated as an integral equation involving the corresponding Green's function. Inhomogeneities can be in the form of an irregular but homogeneous body that can be dealt with using surface integral equations and lessens the computational burden due to the reduced dimensionality of the problem. When the media is inhomogeneous throughout the support volume, volume integral equation (VIE) methods must be employed and are generally more difficult to solve.

Both finite differences and volume integral methods will be described and compared. For electromagnetic problems with electrical sizes (the number of wavelengths in the domain for the highest frequency of interest) that are moderate, the FDTD method has been shown to be

accurate and computationally efficient. A fundamental issue is that numerical dispersion errors for the FDTD solution accumulate over time and can reach unacceptable levels for large structures. Fast volume integral equation solution algorithms have been developed that efficiently scale with the number of unknowns, do not produce accumulating dispersion errors, and can provide an alternative approach for solving large electrical problems.

4.1 FINITE DIFFERENCE TIME-DOMAIN METHOD

FDTD numerical dispersion errors accumulate as EM disturbance propagates through the grid. In order to keep the cumulative errors at a constant threshold, finer cell discretization is required as the domain size increases. In lossless media the general form of the numerical dispersion relation for the full-vector-field FDTD Yee algorithm in three-dimensions (Taflove and Hagness 2005) is given by

$$\left[\frac{\sin\left(\frac{\omega\Delta t}{2}\right)}{c\Delta t}\right]^2=\left[\frac{\sin\left(\frac{\tilde{\kappa}_x\Delta t}{2}\right)}{\Delta x}\right]^2+\left[\frac{\sin\left(\frac{\tilde{\kappa}_y\Delta t}{2}\right)}{\Delta y}\right]^2+\left[\frac{\sin\left(\frac{\tilde{\kappa}_z\Delta t}{2}\right)}{\Delta z}\right]^2 \tag{4.1}$$

Where c is the EM velocity, $\tilde{\kappa}_i$ is the numerical propagation constant in the ith direction, ω is the angular frequency of the propagating wave, and Δx, Δy, and Δz are the grid discretization lengths. In contrast, the true dispersion relation is

$$\left(\frac{\omega}{c}\right)^2=\left(k_x\right)^2+\left(k_y\right)^2+\left(k_z\right)^2 \tag{4.2}$$

Where κ_i is the true propagation constant in the ith direction. Equation (4.1) can be simplified by assuming the discretization is the same in all directions (cubic cells) and that the wave propagates along one of the cell edge directions

$$\left[\frac{\sin\left(\frac{\omega\Delta t}{2}\right)}{c\Delta t}\right]=\left[\frac{\sin\left(\frac{\tilde{\kappa}\,\Delta t}{2}\right)}{\Delta}\right] \tag{4.3}$$

The grid sampling density $N_\lambda = \lambda/\Delta$ where λ is the wavelength of the highest frequency field component and the Courant stability factor $S = c\Delta t/\Delta$ can be substituted into equation (4.3) and rearranged

$$\frac{1}{S}\sin\left(\frac{\pi S}{N_\lambda}\right) = \sin\left(\frac{\tilde{\kappa}\,\Delta t}{2}\right) \tag{4.4}$$

Equation (4.4) can now be readily solved to give the numerical propagation constant

$$\tilde{\kappa} = \frac{2}{\Delta}\sin^{-1}\left[\frac{1}{S}\sin\left(\frac{\pi S}{N_\lambda}\right)\right] \tag{4.5}$$

This result is leads to two fundamental aspects of any FDTD solution. First, in order for the solution to remain stable the numerical propagation constant must be real valued. This can be accomplished by properly specifying the Courant stability factor. The second aspect relates to the numerical phase velocity

$$\tilde{v}_p = \frac{\omega}{\tilde{\kappa}} = c\left(\frac{\pi}{N_\lambda \sin^{-1}\left[\frac{1}{S}\sin\left(\frac{\pi S}{N_\lambda}\right)\right]}\right) \tag{4.6}$$

Equation (4.6) shows that the numerical phase velocity is always less than the true phase velocity and approaches the true value as N_λ becomes very large. In any FDTD problem N_λ and S are fixed and determine both the spatial and temporal discretization. The grid sampling density is typically determined by specifying an upper bound on the phase velocity error for the highest frequency. For lower frequencies this leads to numerical phase velocities that are more accurate but gives rise to numerical dispersion that is not present in the true solution. Individual frequency components propagate at different phase velocities through the FDTD grid and the total phase error accumulates as the size of the computational domain increases. In order to maintain a constant total phase error in the solution, the grid sampling density must increase as the domain size increases.

FDTD is an explicit method and the time required to solve the finite difference equations is proportional to the product of the number of grid cells and the number of time steps

$$T_{FDTD} \sim N_{GRID} \cdot N_T \tag{4.7}$$

The number of grid cells and time steps are determined from the lengths of the individual spatial (L_x, L_y, and L_z) and temporal domains (L_t) and their discretization (Δx, Δy, Δz, and Δt)

$$N_{GRID} = N_x \cdot N_y \cdot N_z = \frac{L_x}{\Delta x} \cdot \frac{L_y}{\Delta y} \cdot \frac{L_z}{\Delta z} \tag{4.8}$$

$$N_T = \frac{L_T}{\Delta t} \tag{4.9}$$

Finally, the time step is determined from the Courant stability factor, the maximum phase velocity, and minimum spatial discretization

$$\Delta t = \frac{S \cdot \min(\Delta x, \Delta y, \Delta z)}{v_p^{\max}} = \frac{S \cdot \Delta_{\min}}{v_p^{\max}} \tag{4.10}$$

As described earlier, the spatial discretization is given as a fraction of the minimum wavelength that exists in the simulation. The fraction is specified as the inverse of the grid sampling density and was shown to be proportional to the size of the spatial domain.

$$N_\lambda \sim L_{\max} \tag{4.11}$$

Assuming for the moment that the spatial domain is equal in x, y and z (a cube), substitution of this relationship into equation (4.8) gives

$$\Delta \sim \frac{\lambda_{\min}}{L_{\max}} \tag{4.12}$$

$$N_{GRID} \sim \frac{L_x^2 \cdot L_y^2 \cdot L_z^2}{\lambda_{\min}^3} = \frac{V^2}{\lambda_{\min}^3} \tag{4.13}$$

Equation (4.12) can also be substituted into (4.10) and the total computation time to solve the FDTD problem is

$$T_{FDTD} \sim N_{GRID} \cdot \frac{V^{\frac{1}{3}} L_T v_p^{\max}}{S \lambda_{\min}} = \frac{V^{\frac{7}{3}} L_T v_p^{\max}}{S \lambda_{\min}^4} \tag{4.14}$$

Rather than increasing proportional to the product of the number of time steps and the volume of the modeled domain, the computational costs actually scale as $O(N^{7/3})$. This can be

considered as a worst case scenario due to the assumption of a cubic domain. If the domain is electrically large in only one dimension the computational burden scales as $O(N^{5/3})$, and in two dimensions as $O(N^2)$. This is a direct result of the requirement that the grid sampling density must increase with the electrical size (i.e. the number of wavelengths across the model domain) of the modeled domain in order to maintain a fixed total phase error in the simulation.

4.2 VOLUME INTEGRAL EQUATION METHOD

The volumetric integral equation method is also known as the method of moments (MoM) when applied to electromagnetic problems. VIE transforms the electromagnetic boundary-value problem into a matrix equation that can be numerically solved.

In contrast to finite-difference or finite element methods, the integral equation method produces a fully populated matrix. The FDTD sparse matrices can be explicitly solved by time-stepping from the initial state, however the resulting VIE matrices must be solved using either direct methods, such as Gaussian elimination, or iterative methods. Using a direct method such as Gaussian elimination or LU decomposition to solve the matrix equation generally requires $O(N^3)$ operations and $O(N^3)$ in memory, where N is the number unknowns. For large scale problems using direct solvers would require very long computational run times. Iterative methods, such as conjugate gradient or other Krylov subspace methods, can often reduce the computational burden to $O(N^2)$. When the domain is uniformly discretized, the forward model matrix can be structured as a circulant matrix. Circulant matrices have the useful property that their product with a vector can be performed using a fast Fourier transform (FFT). When used in combination with an iterative method, the time required to solve the matrix equations can be reduced to O(NlogN) (Gan and Chew 1994; Fang et. al 2006). Compared to other numerical methods that exhibit power law scaling, the computation savings can be substantial. The primary drawbacks to the FFT based fast solvers are that the number of grid points needs to be doubled in each dimension and that the grid block geometry is not as flexible as other methods (e.g. tetrahedral finite elements). In principle, fast solvers can also be combined with other methods (FEM, FDTD, FDFD) to provide both computational efficiency and grid flexibility.

Integral equation techniques require the calculation of a Green's function for an assumed background model and for electromagnetic problems is in general tensor valued. The background

can be arbitrarily chosen but in practice is selected to make the problem computational efficient to solve.

4.2.1 Electromagnetic Integral Equations

The integral equations for the electric and magnetic field are given by

$$\mathbf{E}(\mathbf{r},\omega) = \mathbf{E}_b(\mathbf{r},\omega) + \int_V \boldsymbol{G}_b^E(\mathbf{r},\mathbf{r}',\omega)\cdot\mathbf{E}(\mathbf{r}',\omega)\delta\kappa^2(\mathbf{r}',\omega)\,dv \tag{4.15}$$

$$\mathbf{H}(\mathbf{r},\omega) = \mathbf{H}_b(\mathbf{r},\omega) + \int_V \boldsymbol{G}_b^H(\mathbf{r},\mathbf{r}',\omega)\cdot\mathbf{H}(\mathbf{r}',\omega)\delta\kappa^2(\mathbf{r}',\omega)\,dv \tag{4.16}$$

$$\kappa^2(\mathbf{r},\omega) = -i\omega\mu_0\left[\sigma(\mathbf{r}) + i\omega\varepsilon(\mathbf{r})\right] \tag{4.17}$$

Where **E**, **H**, and κ are the respective electric field, magnetic field, and propagation constant in the modeled domain, $\mathbf{E}_b$, $\mathbf{H}_b$ and κ_b correspond to the fields and propagation constant in an assumed background media, and the media perturbation $\delta\kappa = \kappa - \kappa_b$. The electric field whole-space Green's function in homogeneous media is given by

$$\mathbf{G}_b^E = i\omega\mu_0\left(\mathbf{I} + \frac{1}{\kappa_b^2}\nabla\nabla\right)g(\mathbf{r},\mathbf{r}',\omega) \tag{4.18}$$

$$g(\mathbf{r},\mathbf{r}',\omega) = \frac{1}{4\pi}\left[\frac{e^{-i\kappa_b|\mathbf{r}-\mathbf{r}'|}}{|\mathbf{r}-\mathbf{r}'|}\right] \tag{4.19}$$

$$G_{pq} = (C_{NF} + C_{IF})\left(\frac{3x_p x_q}{\left(|\mathbf{r}-\mathbf{r}'|\right)^2} - \delta_{pq}\right) + C_{FF}\left(\frac{x_p x_q}{\left(|\mathbf{r}-\mathbf{r}'|\right)^2} - \delta_{pq}\right) \tag{4.20}$$

$$x_p = \left(r_p - r_p'\right);\ p,q = 1,\ 2,\ or\ 3\,(x,\ y,\ or\ z)$$

$$C_{NF} = \frac{i\omega\mu_0}{4\pi\kappa_b}\left[\frac{1}{\kappa_b\,|\mathbf{r}-\mathbf{r}'|^3}\right]e^{-i\kappa_b|\mathbf{r}-\mathbf{r}'|}$$

$$C_{IF} = \frac{i\omega\mu_0}{4\pi\kappa_b}\left[\frac{-1}{i\,|\mathbf{r}-\mathbf{r}'|^2}\right]e^{-i\kappa_b|\mathbf{r}-\mathbf{r}'|} \tag{4.21}$$

$$C_{FF} = \frac{i\omega\mu_0}{4\pi\kappa_b}\left[\frac{-\kappa_b}{|\mathbf{r}-\mathbf{r}'|}\right]e^{-i\kappa_b|\mathbf{r}-\mathbf{r}'|}$$

Where the prime denotes the source position and r_p specifies the p^{th} component of the position vector. The magnetic field Green's function can be calculated from the electric field Green's function

$$\mathbf{G}_b^H = \frac{1}{i\omega\mu}\nabla\times\mathbf{G}_b^E \tag{4.22}$$

4.2.2 Numerical Implementation

The electric field integral equation (4.15) is solved using the method of weighted residuals. Pulse basis functions are used for the electric field and the media perturbation in this work. Higher accuracy basis function can also be readily incorporated and lead to better convergence for problems with large material contrasts (Jin, 2002). Equation (4.15) can then be written as

$$\mathbf{E}(\mathbf{r},\omega) = \mathbf{E}_b(\mathbf{r},\omega) + \sum_n \left[\int_{v_n} \boldsymbol{G}_b(\mathbf{r},\mathbf{r}_n^{'},\omega) dv' \right] \cdot \mathbf{E}(\mathbf{r}_n^{'},\omega)\delta\kappa^2(\mathbf{r}_n^{'},\omega) \tag{4.23}$$

The Green's function possesses a singularity for grid cells within the source region. The principal volume method (van Bladel, 1961) is used to evaluate the integral of the Green's function (Chew 1990) and can be applied to various volume shapes. The Green's function integral, $\hat{\boldsymbol{G}}$ for cubic volume elements located both within and outside the source region can be analytically evaluated and the results for both are given by the following

$$\hat{G}_{pq} = i\omega\mu_0 \frac{\delta_{pq}}{3\kappa_b^2}\left[2\left(1-i\kappa_b\right)e^{i\kappa_b a}-3\right]; \qquad \mathbf{r}=\mathbf{r}'$$

$$\hat{G}_{pq} = \frac{4\pi\alpha}{3\kappa_b^2}\left[\frac{\sin(\kappa_b a)}{\kappa_b a}-\cos(\kappa_b a)\right]G_{pq}; \qquad \mathbf{r}\neq\mathbf{r}' \tag{4.24}$$

$$a = \left(\frac{3}{4\pi}\right)^{\frac{1}{3}} s; \quad s = cube\,side\,length$$

The Green's function integral (4.24) will be substituted into equation (4.23) then rearranged and written in matrix form

$$\begin{aligned}
&\mathbf{A}\boldsymbol{\psi} = \boldsymbol{\psi}_b \\
&\mathbf{A} = \left[\mathbf{I} - \hat{\mathbf{G}}\boldsymbol{\delta\kappa}\right] \\
&\boldsymbol{\psi} = \mathbf{E}(\mathbf{r}, \omega) \\
&\boldsymbol{\psi}_b = \mathbf{E}_b(\mathbf{r}, \omega)
\end{aligned} \tag{4.25}$$

The modeled and background electric fields are vectors with length N (number of grid cell), media perturbation matrix is diagonal and N by N, and the Green's function integral matrix is N by N and fully populated. When the grid is uniformly discretized, the Green's function integral matrix can be cast in circulant form by doubling the grid in each coordinate direction. By doing so matrix-vector multiplication only requires the the first column of the matrix and can be performed using the FFT. Using a transpose-free iterative method to solve the system of equations can be performed in O(NlogN) operations and O(N) in memory.

4.2.3 Results

Figures 4.1 and 4.2 show the model used to validate the VIE approach which consists of a 1.25 m by 1.25 m by 0.5 m rectangular anomaly with $\varepsilon_r = 7$ and $\sigma = 0.01$ S/m embedded within a homogeneous media with $\varepsilon_r = 3$ and $\sigma = 0.001$ S/m. The grid is 5m by 5m by 2m and has been discretized into 0.05 m cubic elements in the VIE method. Grid elements in the FDTD method are more finely discretized near material discontinuities. The FDTD simulations were performed using XFdtd (REMCOM Inc.) with a 10 layer perfectly matched layer (PML) surrounding the model boundary. A 50 MHz Ricker wavelet input current source signal is shown in Figure 4.3 and has been implemented somewhat differently in the FDTD and VIE methods. A 1Amp soft current source with a length of 10cm was used in the FDTD simulation and a 1Amp Hertzian dipole was used for the VIE method. The location of the source along with three receiver locations that will be used to compare the FDTD and VIE solutions is shown in Figure 4.1.

The z-component of the electric field signals at the three receiver locations obtained with the VIE method are shown in Figure 4.4. Comparisons of the electric field (z-component) using the VIE and FDTD methods are also shown at the receiver locations (Figure 4.5) and using a cross-section (Figure 4.6) through the XY plane at x=0. Some differences are evident particularly in the cross-section images and are likely due to the somewhat different source implementations and differences in the colors used for plotting each method. In general, the VIE results compare

favorably to those from the FDTD method with differences less than 5 percent at all points in the model.

The VIE method used 512 individual frequencies, however 34 frequencies contributed to 99.9 percent of the total energy in the signal. To investigate the use of fewer frequencies, a set of VIE solutions were obtained using subsets of the complete set of frequencies. The solutions obtained using the reduced set of frequencies compared well with the full solution except that a small amplitude high frequency signal is present at all times for the reduced frequency subset solution.

In addition to comparing the VIE and FDTD electric field solutions, the execution times for each method were evaluated. The execution times required for the VIE method is shown in Figure 4.7. The number of grid cells varied from a few hundred to just under half a million and the VIE method showed O(NlogN) scaling as expected. It is also interesting to compare the VIE and FDTD methods as the size of the domain increases. The FDTD method was assumed to scale $O(V^2)$ as derived in the previous section and a range of coefficients were selected to bound the actual scaling and were based on a limited number of FDTD simulations. Depending on the actual FDTD scaling coefficient, Figure 4.8 shows that the efficiency of VIE can approach and surpass the FDTD method as the electrical size becomes large.

The ultimate goal of forward simulation for geophysical problems is to provide input to an inversion algorithm. While here we are comparing time-domain results with FDTD, the native implementation for the VIE method is in the frequency-domain. The VIE method can be seamlessly incorporated into a frequency-domain inversion scheme to more effectively deal with the inherent non-linearity present in full waveform inverse problem (Pratt et al. 1999; Meles et al. 2012). Any inversion will require a full forward simulation using a source at each location used in the actual geophysical survey. To speed the calculation, the problem is typically parallelized by simultaneously running forward simulations at all the required source positions. In the frequency-domain the problem can be further parallelized by running each frequency at each source location simultaneously. By only simulating and inverting frequencies that significantly contribute to the total energy in the signal, then additional computational saving can be realized.

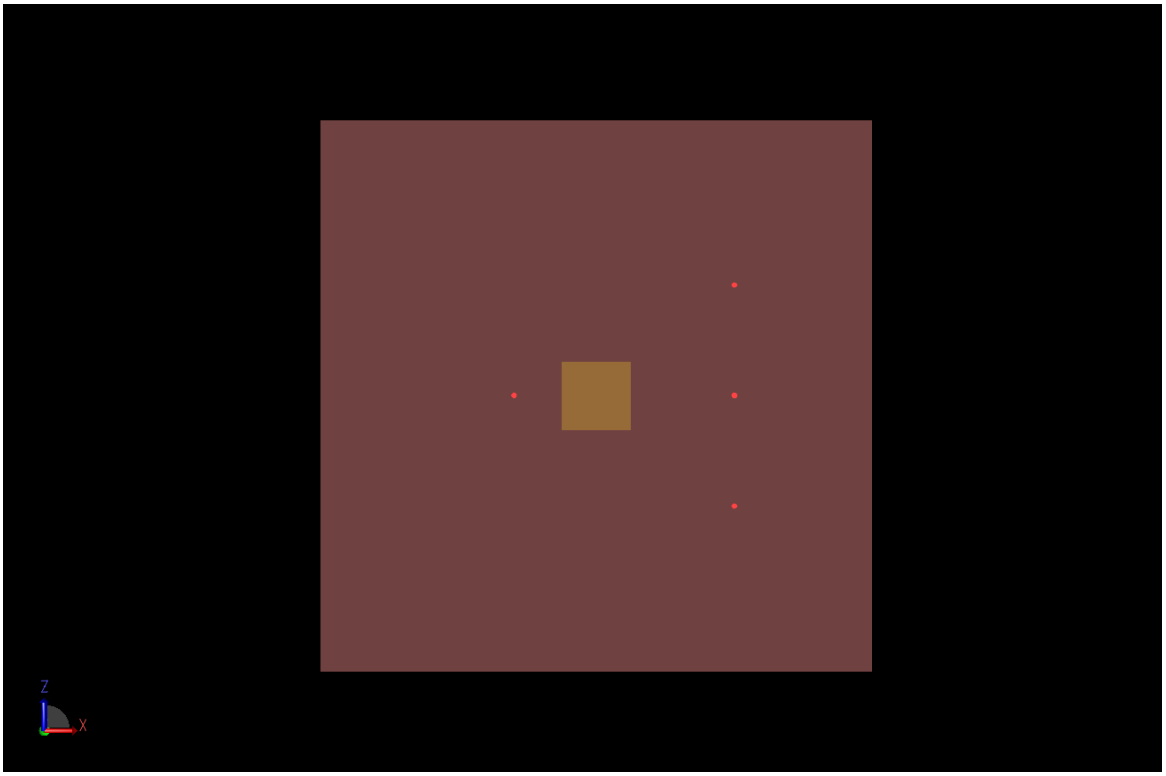

Figure 4.1 Model used for both VIE and FDTD simulations. Source is located on the left of the anomaly and three receiver locations are shown on the right of the anomaly.

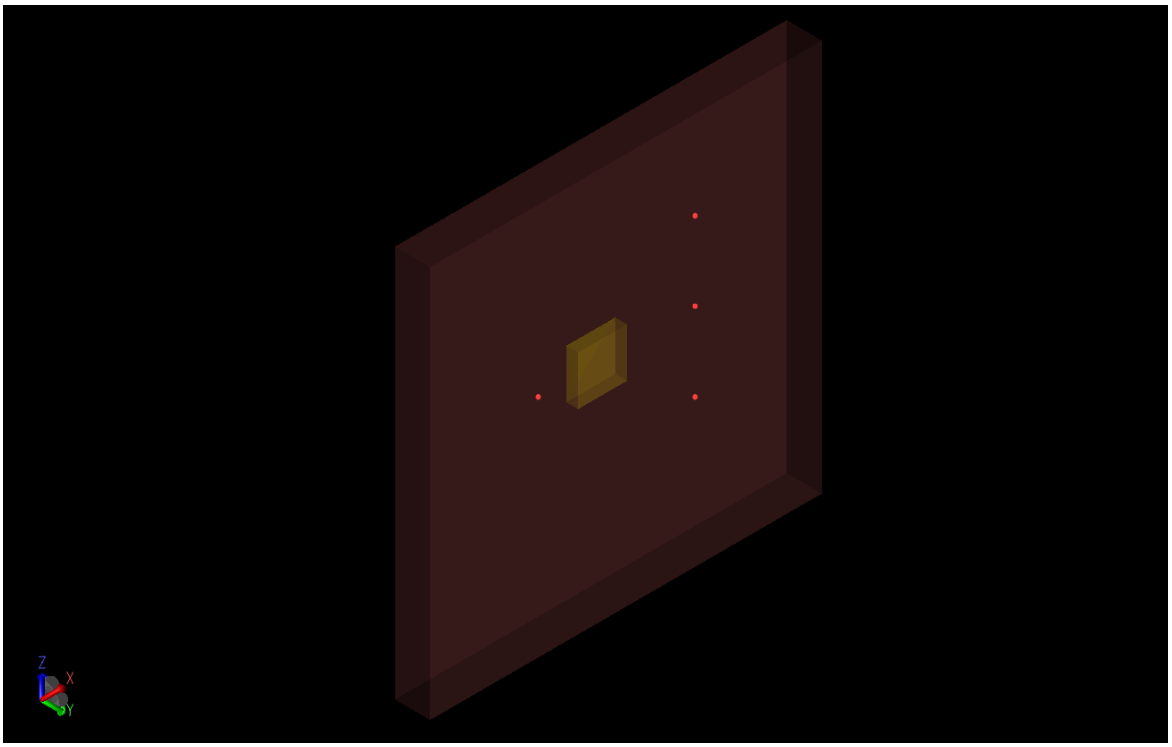

Figure 4.2 Angled perspective of the model used for both VIE and FDTD simulations. Source is located on the left of the anomaly and three receiver locations are shown on the right of the anomaly.

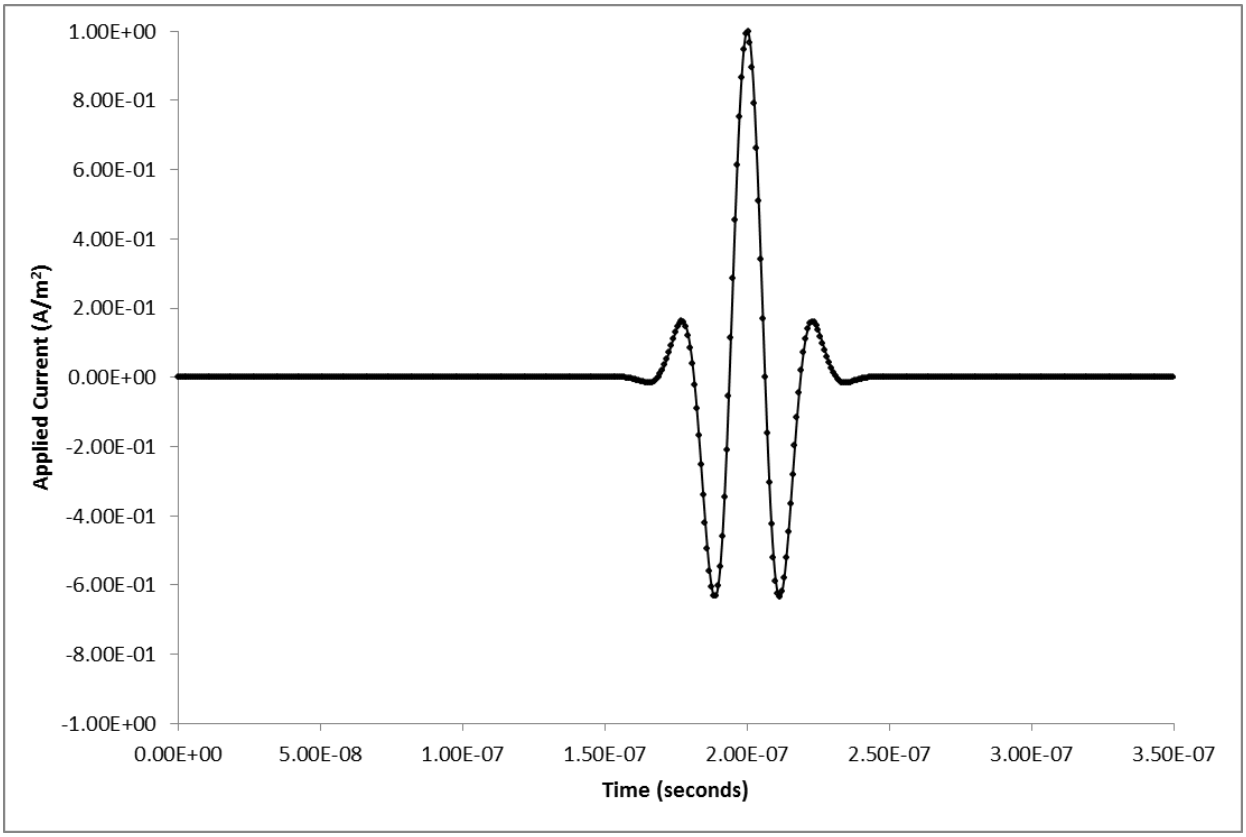

Figure 4.3 Source time function used for both FDTD and VIE simulations.

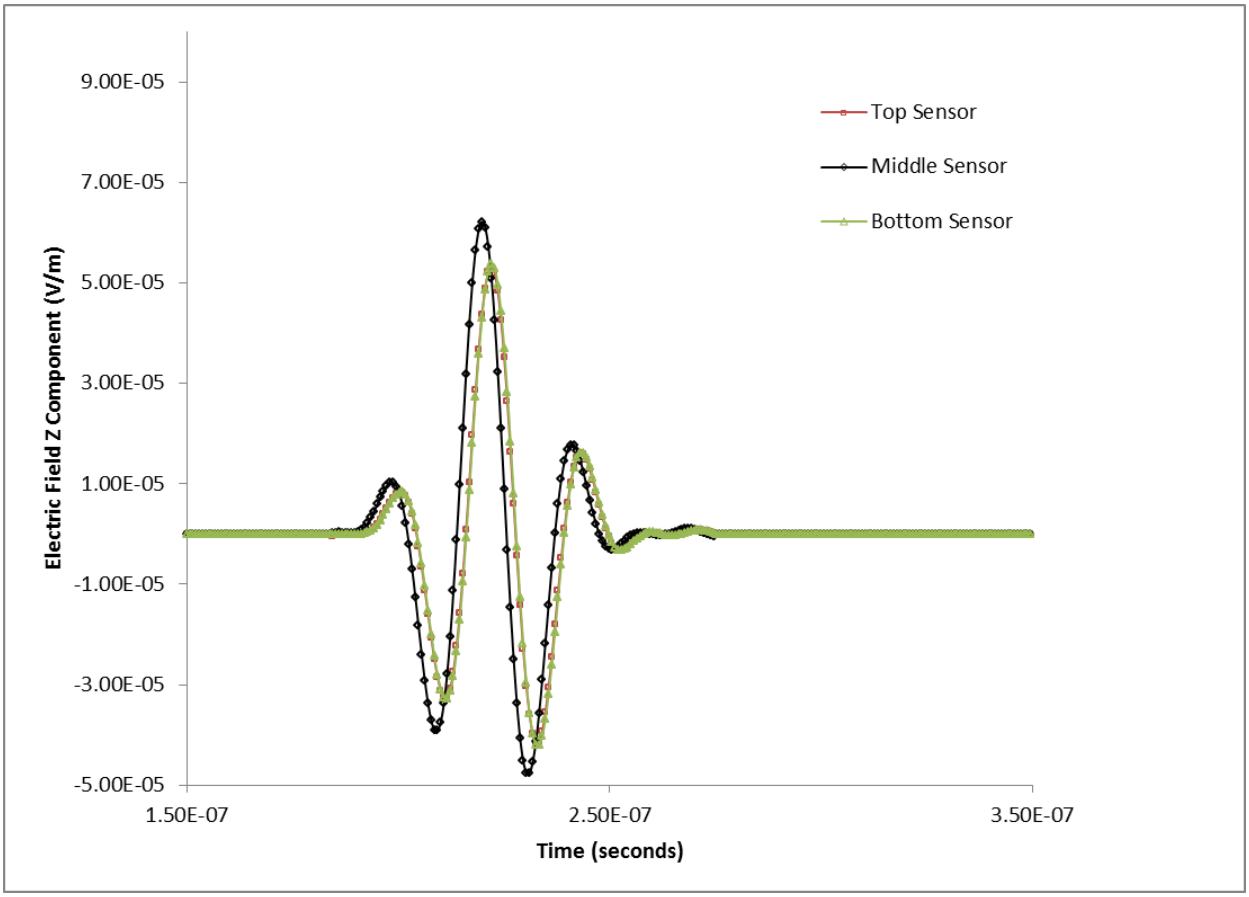

Figure 4.4 VIE electric field solution at three receiver locations.

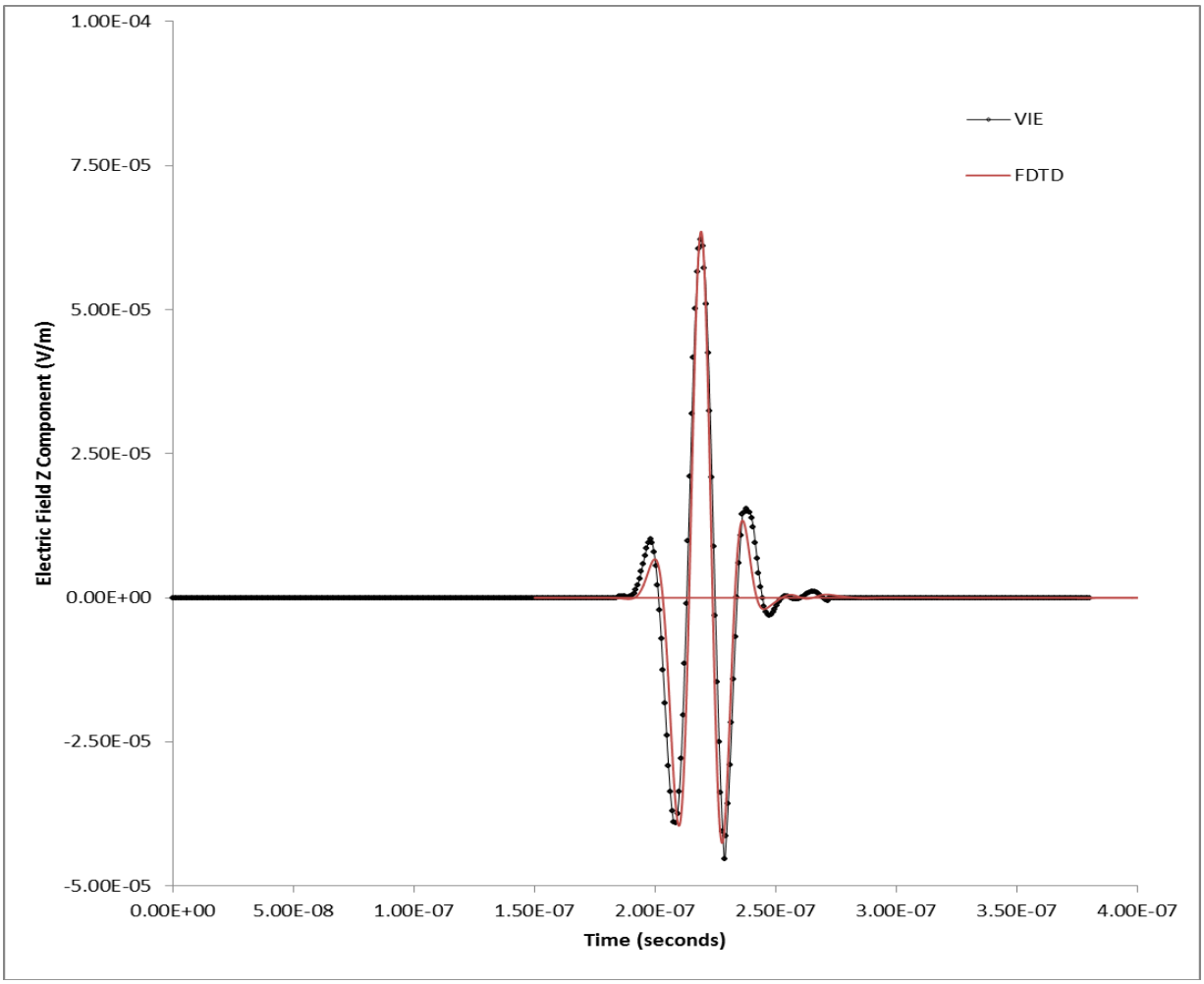

Figure 4.5 Electric field comparisons between FDTD and VIE methods at central receiver location.

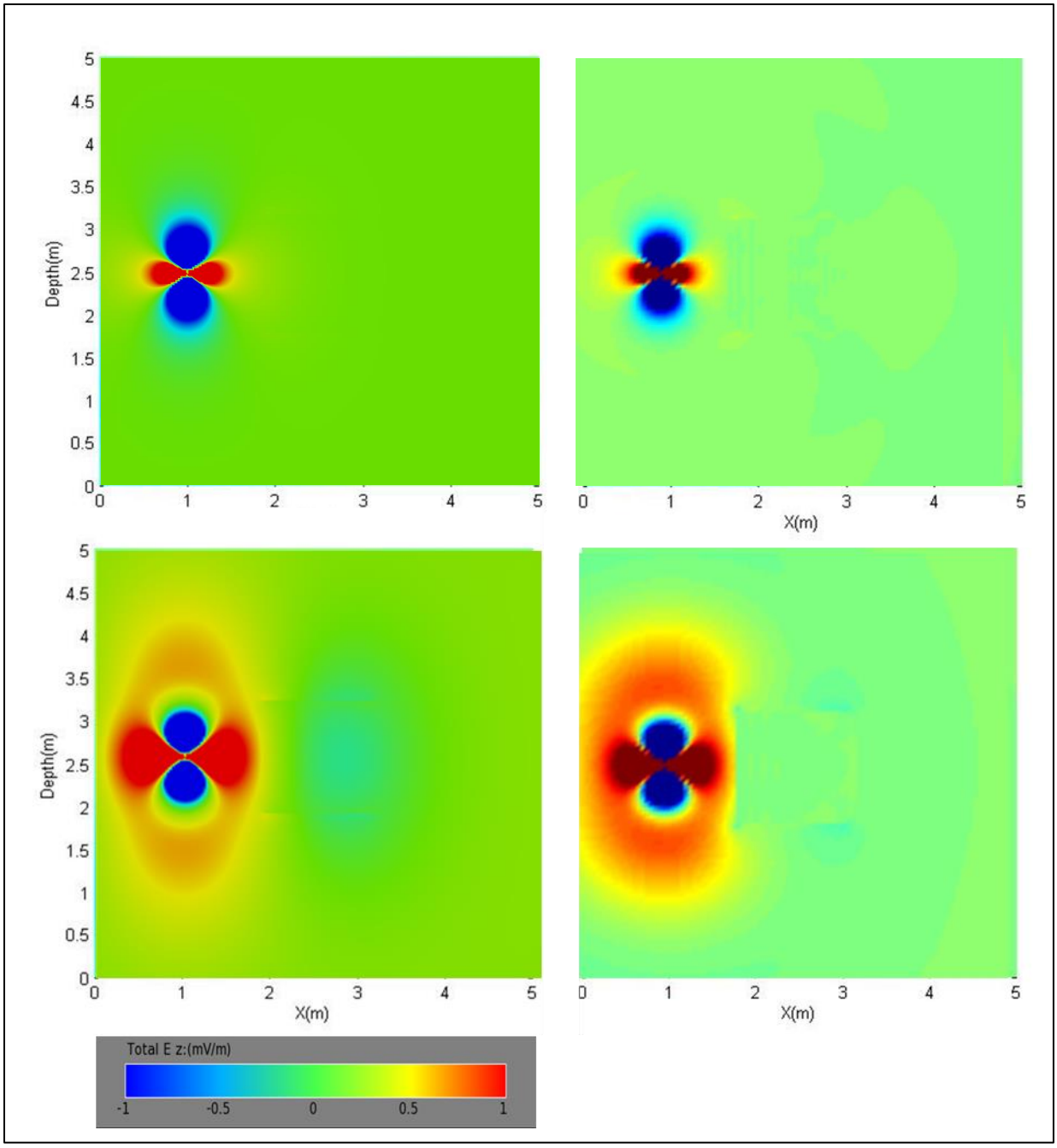

Figure 4.6 Electric field results for both VIE (right column) and FDTD (left column) methods at two times (upper and lower rows).

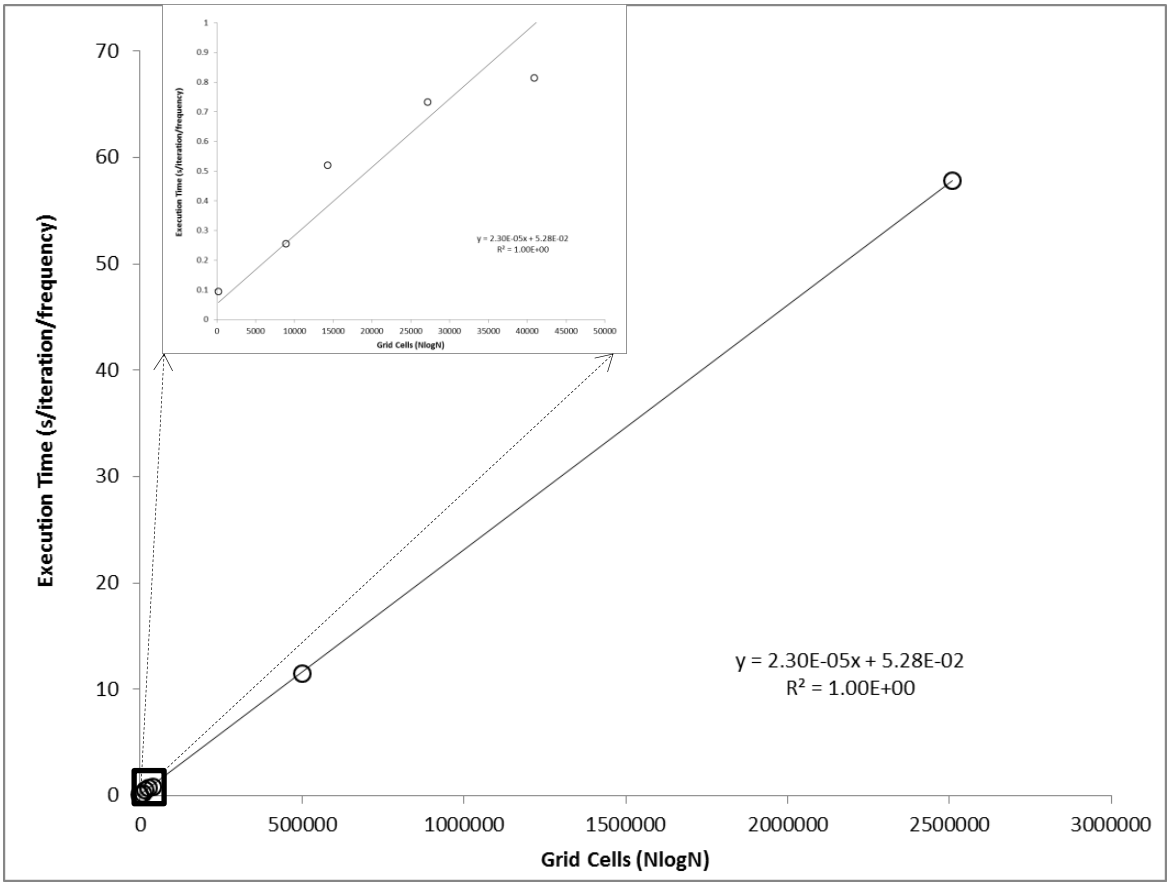

Figure 4.7 Execution time required using the VIE method.

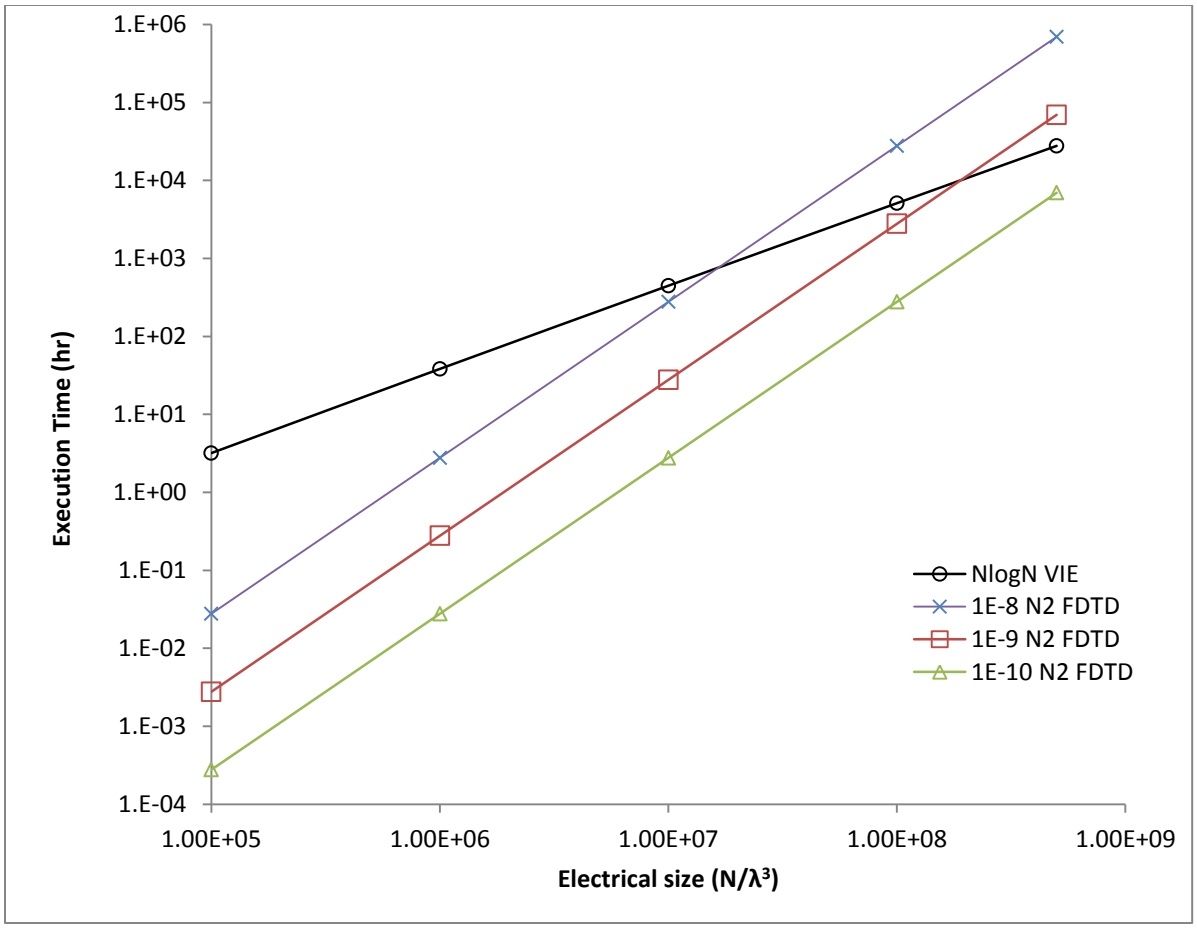

Figure 4.8 Comparison of execution times for VIE and the FDTD method using an assumed V^2 scaling dependence.

5 FREQUENCY-DOMAIN GEORADAR INVERSION

Georadar has been widely used for subsurface imaging in near-surface environments (Peterson 2001; Binley et al. 2002). Georadar makes use of high frequency (MHz) electromagnetic (EM) waves to determine (image) the spatial distributions of EM properties (electrical permittivity and conductivity) within the Earth using geophysical inversion methods. The technique can be implemented using EM sources and receivers that are both positioned at the surface to delineate the geometry of subsurface structures due to contrasts in material properties (e.g. reflectivity). In addition to surface methods, cross-borehole and surface-borehole methods can be used to image both the EM properties and property contrasts of the medium between the boreholes and surface.

Geophysical inverse problems seek to determine an unknown set of model parameters (e.g. EM properties) from data obtained using a finite set of source-receiver combinations along with simulations of the acquired data using the relevant physics of the problem (the forward problem). Unique solutions to the inverse problem often do not exist and a variety of optimization methods can be used to determine a solution that best fits the observed data (Tarantola 2004). Local methods linearize the inverse problem using the sensitivity matrix (also known as the gradient or Jacobian matrix) evaluated for an assumed set of model parameters. Gradient-based local optimization methods are commonly used for full waveform georadar inversion (Ernst et al. 2007; Meles et al. 2012) and can avoid the computational costs involved with calculating and storing the Jacobian matrix; however, the Jacobian matrix is not available for formal model resolution analysis. Regardless of the optimization method used, the objective of the inversion is to solve this linearized relationship for a change in model parameters using the dataset of observations, update the starting model, and finally iterate this process to produce a final optimal estimate of the model parameters.

Forward models used in georadar inversions are most commonly based on ray theory. Ray theory constitutes an approximate, high-frequency solution to the wave-equation that is valid when spatial variations in the media through which the wave propagates are sufficiently smooth. Specifically, media variations must be much larger than both the wavelength of the propagating waves and the width of the first Fresnel zone (Kravstov and Orlov 1980). Application of ray theory to media introduces several limitations associated with the high-frequency approximation,

the limited angular coverage of subsurface structures, and the reduced number of signal attributes available to constrain the inversion. Low-velocities may not be correctly modeled, skewing the inverse solution toward higher velocities (Nolet 1987) and fine structures smaller than the wavelengths of the propagating waves are not accurately resolved due to its infinite-frequency approximation (Kravstov and Orlov 1980).

Wave-propagation modeling can also be performed using various numerical solution methods (FDTD, FDFD, FEM, VIE) to the full EM wave equation (Taflove and Brodwin 1975; Marfurt 1984; Zwamborn et al. 1992; Jin 1993; Bleszynsky et al. 1996; Fang et al. 2006). Numerical techniques simulate the full physics of wave propagation in heterogeneous media but have substantially higher computational requirements. To improve the limited resolution of ray-based approaches, numerical full-wave equation methods can be incorporated in the inversion. Full-waveform inversion methods can yield substantially higher spatial resolution compared to ray-based methods.

Realistic waves propagate at finite-frequencies and in general, the EM material properties themselves are frequency dependent. Wave phase velocities and attenuation constants are each functions of the electrical permittivity, conductivity, and frequency (Jackson, 1999). This causes dispersion in EM waves where different frequencies propagate and attenuate at different frequencies. In addition, the relative contribution of permittivity and conductivity to both the wave velocity and attenuation vary with frequency, complicating interpretation in the time-domain. Due to the limiting high-frequency approximation, ray-based methods are unable to capture frequency dependent effects and in situations where such effects are significant (such as in media with large electrical conductivities), full EM wave equation inversion methods must be used.

Full-wave form inversion makes use of the entire received signal, and more accurately captures the physical description of wave propagation. Surface reflectivity based georadar inversion methods often implement wavefield migration algorithms common in seismic exploration (van der Kruk et al., 2003; Yilmaz, 2001). Such migration methods utilize the entire recorded waveform but are unable to recover volumetric material properties. Cross-borehole and surface-borehole methods typically utilize just the direct arriving travel-time and amplitude portions of the received signal for ray-based tomographic imaging. Full-waveform inversions can

also be implemented that make use of the entire signal and have been shown to provide sub-wavelength imaging resolution.

Kuroda et al. (2007) first demonstrated a full-waveform cross-borehole georadar inversion method to image electrical permittivity. Ernst et al. (2007) used a cascaded inversion approach to determine both electrical permittivity and conductivity in an alternating fashion. Meles et al. (2010) then developed an improved method that simultaneously inverted for both parameters and incorporated both transverse electric (TE) and transverse magnetic (TM) modes of EM wave propagation to allow for inversion of both surface-borehole and cross-borehole data. All of the above approaches used a 2D FDTD solution to Maxwell's equations.

Full-waveform geophysical inversion problems generally require the use of non-linear optimization techniques. The non-linearity of the problem has been attributed to multiple scattering associated with differences between the true model parameters and those of the assumed model (Mora, 1987). Scattering not only depends on the differences in model parameters but on the frequency of the propagating wave. The non-linearity can be addressed by starting the inversion using low frequencies, which are less sensitive to smaller features, and progressively include higher frequencies to improve resolution. This approach can be implemented in the frequency-domain by performing the inversions on subsets of frequencies using the output model from the previous lower frequency set as input to the next inversion step (Pratt et al. 1998; Bing and Greenhalgh, 2003). A combined frequency-time-domain approach can also be used whereby the time domain data are bandwidth filtered by first including only low frequencies and subsequently adding higher frequencies as the inversion proceeds (Meles et al. 2010). The non-linearity can also be lessened by constraining the starting model so that it is reasonable close to the true model using the results of ray-based inversion methods; however, this approach can often fail for models with complex structures (Meles et al. 2010).

In this chapter I outline a frequency-domain, full-waveform georadar inversion approach. Rather than using the results of ray-based methods for constraining the initial model parameters, I have developed a method that allows the assumed background media to vary for each source-receiver pair used in the inversion. This is in contrast to methods that make the more restrictive assumption that the background is the same for all source-receiver combinations. In many cross-borehole environments ray-paths have been shown to be approximately straight (Peterson, 2001), with the implication that the media can thus be modeled as approximately homogeneous for each

source-receiver combination. The new method also assumes that the media influencing the measurement (between source and receiver) can be approximated as homogeneous for each source-receiver pair (but different for each measurement pair), however, wave propagation modeling is performed using a finite-frequency approach. Analytic solutions to Maxwell's equations are used for efficient computation and describe the frequency dependent effects not captured by ray-based methods. Data are inverted in the frequency-domain and can be used for imaging highly-conductive/dispersive materials. The method can then be continued to provide an iterative, nonlinear, 3D full-waveform inversion of georadar data in the frequency-domain.

5.1 FORWARD PROBLEM

In the frequency domain Maxwell's equations can be written in compact form as follows:

$$\begin{bmatrix} i\omega\varepsilon(\mathbf{r})-\sigma(\mathbf{r}) & \nabla\times \\ \nabla\times & -i\omega\mu \end{bmatrix}\begin{bmatrix} \mathbf{E}(\mathbf{r},\omega) \\ \mathbf{H}(\mathbf{r},\omega) \end{bmatrix}=\begin{bmatrix} -i\omega\mathbf{I}_0(\mathbf{r},\omega) \\ \mathbf{0} \end{bmatrix} \tag{5.1}$$

In the above equations, **E** is the electric field, **H** is the magnetic field, ε is the electrical permittivity, σ is the electrical conductivity, μ is the magnetic permeability, and **r** is the position vector. An external electric current source $\mathbf{I_0}$ has been included in equation 3. We will also assume that the magnetic permeability is equal to that of free space which is often a reasonable assumption for many typical earth materials.

I will also use $\mathbf{S}(\mathbf{r},\omega)=-i\omega\mu_0\mathbf{I}_0(\mathbf{r},\omega)$ (a modified source term proportional to the time derivative of the external electric current source) and combine the electrical parameters

$$\begin{aligned} \kappa^2(\mathbf{r},\omega) &= -i\omega\mu_0\left[\sigma(\mathbf{r})+i\omega\varepsilon(\mathbf{r})\right] \\ \kappa(\mathbf{r},\omega) &= \sqrt{-i\omega\mu_0\left[\sigma(\mathbf{r})+i\omega\varepsilon(\mathbf{r})\right]} \end{aligned} \tag{5.2}$$

Georadar applications typically utilize sensors that detect the electric field and the integral solution for the electric field is given by

$$\mathbf{E}(\mathbf{r},\omega)=\int \boldsymbol{G}\,(\mathbf{r},\mathbf{r}',\omega)\cdot\mathbf{S}(\mathbf{r}',\omega)\,d^3\mathbf{r}' \tag{5.3}$$

In general, the source and the wavefield are vectors and the electric field Green's function in (5.3) is tensor valued. Also, once the electric field is known the magnetic field can be obtained using the relationship: $\mathbf{H}(\mathbf{r},\omega) = \frac{1}{i\omega}\nabla\times\mathbf{E}(\mathbf{r},\omega)$.

5.2 INVERSE PROBLEM

Various approaches have been developed to solve the inverse problem (Aki & Richards, 1980; Menke, 1984; Parker, 1994; Tarantola, 2004; Aster, Borchers & Thurber, 2005). In this section I will describe some commonly used methods along with the approach implemented in this work.

The elements involved in most inverse problems are the data, **d**, and a physical model, **f**, that depends upon a set of model parameters, **m**. The basic premise is that the data and model parameters are related through the physical model (or just model), **f**(**d**,**m**)=**0**. The objective of inverse theory is to solve (the solution may not exist or be non-unique) this relationship for the model parameters given a set of data observed from particular experiment.

Generally, the physical model depends on both the data and the model parameters; however in many situations the data can be separated from the physical model

$$\mathbf{f}(\mathbf{d},\mathbf{m}) = \mathbf{d} - \mathbf{g}(\mathbf{m}) = 0 \qquad (5.4)$$

In equation (5.4) the physical model, **g**(**m**), has been recast in explicit form as a function (or functional when **m** is itself a function of spatial position, **m**(**r**)) of the model parameters but now no longer depends on the data. Inverse problems can be further divided into two general classes: linear and non-linear.

5.2.1 Linear Inverse Problem

Linear inverse problems are those where the physical model depends linearly on the model parameters, **g**(**m**) = **Gm**. Numerous applications in the physical sciences can be modeled as linear problems. For linear problems, equation (5.4) becomes

$$\mathbf{d} = \mathbf{G}\mathbf{m} \qquad (5.5)$$

When both the data and model parameters are continuous functions of space (and often time or frequency), the physical model corresponds to the following integral equation

$$d(\mathbf{r}) = \int G(\mathbf{r}', \mathbf{r}) m(\mathbf{r}') d\mathbf{r}' \tag{5.6}$$

More often data are collected at discrete locations and times

$$d(\mathbf{r}_i) = d_i = \int G(\mathbf{r}', \mathbf{r}_i) m(\mathbf{r}') d\mathbf{r}' \tag{5.7}$$

Finally, the model parameters may also be discrete and equation (5.5) is cast as a linear system of equations

$$d_i = \sum_j G(\mathbf{r}_j, \mathbf{r}_i) m(\mathbf{r}_j) = \sum_j G_{ij} m_j \tag{5.8}$$

The solution to the inverse problem (**m**) for nearly every problem of interest is non-unique. In this case, one attempts to choose a model that in some sense provides the "best" fit to the observed data so that the predicted data, $\mathbf{d}^{est} = \mathbf{G}\mathbf{m}^{est}$, is as close as possible to the observed data, $\mathbf{d}^{true} = \mathbf{G}\mathbf{m}^{true}$ or equivalently, that the length of their difference, or the error $e_i = d_i^{est} - d_i^{true}$, is as small as possible (Menke, 1984; Aster, Borchers, & Thurber, 2005). The most commonly used measures of length or norms are Lebesgue measures denoted by L_n:

$$L_1 = \|\mathbf{e}\|_1 = \left[\sum_i |e_i|^1 \right]^{\frac{1}{1}} \tag{5.9}$$

$$L_2 = \|\mathbf{e}\|_2 = \left[\sum_i |e_i|^2 \right]^{\frac{1}{2}} \tag{5.10}$$

$$\vdots$$

$$L_n = \|\mathbf{e}\|_n = \left[\sum_i |e_i|^n \right]^{\frac{1}{n}} \tag{5.11}$$

An important aspect of the various norms is the weight that the largest element contributes to total; the higher norms give increasingly larger weigh to the largest misfit elements and are more sensitive to data outliers. When the data errors are univariant (each with unit standard deviation) and follow a Gaussian distribution, minimizing the L_2 norm of the misfit is the proper choice to recover the model parameters from the inversion. The model parameters that minimize the L_2 norm also minimize the square of the L_2

$$E = \left(\|\mathbf{e}\|_2 \right)^2 = \mathbf{e}^T \mathbf{e} = (\mathbf{d} - \mathbf{G}\mathbf{m}^{est})^T (\mathbf{d} - \mathbf{G}\mathbf{m}^{est}) \tag{5.12}$$

More commonly, the standard deviations vary for the individual data point and the least squares misfit criterion, the chi-squared statistic, for M measurements and N model parameters is given by

$$\chi^2(\mathbf{m}) = \sum_{i=1}^{M} \left[\frac{\left| \sum_{j=1}^{N} G_{ij} m_j - d_i \right|^2}{\sigma_i^2} \right] \tag{5.13}$$

To incorporate the data standard deviations into the inverse solution, the system of equations (5.8) can be rescaled and the minimum of (5.13) found by taking the derivative with respect to the model parameters and setting equal to zero, which gives the normal equations to solve the least-squares problem

$$\begin{aligned} \mathbf{C}_d^{-1/2} &= diag\left(1/\sigma_1 , 1/\sigma_2 , ..., 1/\sigma_m \right) \\ \mathbf{G}_w &= \mathbf{C}_d^{-1/2}\mathbf{G} \\ \mathbf{d}_w &= \mathbf{C}_d^{-1/2}\mathbf{d} \end{aligned} \tag{5.14}$$

$$\mathbf{G}_w^T \mathbf{G}_w \mathbf{m}^{est} = \mathbf{G}_w^T \mathbf{d}_w \tag{5.15}$$

The weights in equation are assembled in the covariance matrix, $\mathbf{C}_d$, which implicitly assume that the individual data elements are independent with variances σ^2. In addition to the data covariance, the model covariance, $\mathbf{C}_m$, can be calculated from

$$\mathbf{C}_m = \left(\mathbf{G}_w^T \mathbf{G}_w \right)^{-1} = \left(\mathbf{G}^T \mathbf{C}_d \mathbf{G} \right)^{-1} \tag{5.16}$$

The model covariance is generally not diagonal and indicates that, unlike the data, the model parameters are correlated. Also, since the chi-squared statistic is a function of the random data measurement errors, it too is a random variable with a χ^2 distribution and v = M-N degrees of freedom (Draper & Smith, 1998). Under the assumption used here, the chi-squared statistic approaches the degrees of freedom as v becomes large with a standard deviation of $(2v)^{1/2}$. Thus for large v, the true model would be expected in the interval $\chi^2 = v \pm (2v)^{1/2}$.

Finally, as noted earlier higher order norms give increasing weight to outliers in the data. When this occurs, it is advantageous to use the smallest power norm possible. The L_1 norm solution will be less sensitive to data outliers than the least-squares solution. One approach to deal with data outliers is to plot the distribution and simply remove those with large errors. A

more elegant method would be to instead apply a weighting function that down-weights the data that show large misfits, compute a new solution, calculate the new data misfit, and repeat the process until the solution converges. This is termed the iteratively re-weighted least squares method and (assuming convergence occurs) can be used to generate the L_1 norm inverse solution.

5.2.2 Non-linear Inverse Problem

Problems where the physical model depends non-linearly on the model parameters are inherently more difficult to solve and to answer fundamental questions related to uniqueness than for linear problems. Inverse solutions can be obtained using global optimization methods that search the parameter space using a large number of realizations (calculating synthetic data assuming a particular set of model parameters = forward modeling). For problems with large numbers of model parameters, global methods can require so many forward model runs such that they are computationally impractical.

Local optimization methods are often used to solve large inverse problems by linearizing the physical model about a set of assumed reference model parameters; the process then iteratively updates the model parameters with the goal of converging to the optimal solution. In the following sections, I will extend the previous description of the linear inverse problem to the non-linear case and describe several common solution methods.

5.2.3 Data and Misfit Functionals

For wave propagation problems presented here, data functionals $D\left(\psi_i^s(\mathbf{r}_r,\mathbf{m}^{true}),\psi_i^s(\mathbf{r}_r,\mathbf{m}^{ref})\right)$ will be used that measure the misfit between the observed (true) and reference wavefields, $\boldsymbol{\psi}^s(\mathbf{r}_r,\mathbf{m}^{true})$ and $\boldsymbol{\psi}^s(\mathbf{r}_r,\mathbf{m}^{ref})$ which themselves depend on the corresponding set of true and reference model parameters respectively. The data functional depends on the ith component of both the reference and observed wavefields measured at location $\mathbf{r}_r$, and that are generated by a particular source s. In addition to the data functional itself, we also require the Fréchet derivative of the data functional taken with respect to the model parameters, $\delta D\left(\psi_i^s(\mathbf{r}_r,\mathbf{m}^{ref})\right)$. Many types of data functionals can be defined (Strickland et al., 2015); however, one of the simplest data functionals for waveform inversion is the scaled

wavefield residual for data point indexed by m corresponding to the i[th] component of the wavefield measured at location $\mathbf{r}_r$, generated by source s, and assuming reference model parameters $\mathbf{m}^{ref}$. The wavefield data will also be specified in the frequency-domain and the misfit functional will then include a range of frequencies, f, to be used in the inversion

$$D_m = \frac{\psi_i^s(\mathbf{r}_r, \mathbf{m}^{ref}, \omega_f) - \psi_i^s(\mathbf{r}_r, \mathbf{m}^{true}, \omega_f)}{\sigma_{srif}} = \frac{\psi_m(\mathbf{m}^{ref}) - \psi_m(\mathbf{m}^{true})}{\sigma_m} \tag{5.17}$$

The corresponding data perturbation will also be required and will be defined using the wavefield Fréchet derivative, $\frac{\delta\psi_m}{\delta m_n}$

$$\delta D_{mn} = \frac{1}{\sigma_{srif}} \frac{\delta\psi_i^s(\mathbf{r}_r, \mathbf{m}^{ref}, \omega_f)}{\delta m_n^{ref}} = \frac{1}{\sigma_m} \frac{\delta\psi_m}{\delta m_n} \tag{5.18}$$

The objective is to minimize the misfit functional which, for the least-squares case, is the sum of the squared wavefield residuals normalized by their respective standard deviations (chi-squared).

$$\begin{aligned} \chi^2(\mathbf{m}, \mathbf{m}^{ref}) &= \frac{1}{2} \sum_{s=1}^{N_s} \sum_{r=1}^{N_r} \sum_{i=1}^{3} \left[\frac{\psi_i^s(\mathbf{r}_r, \mathbf{m}, \omega_f) - \psi_i^s(\mathbf{r}_r, \mathbf{m}^{ref}, \omega_f)}{\sigma_{srif}} \right]^2 \\ &= \frac{1}{2} \sum_{m=1}^{M} \left[D_m \right]^2 \end{aligned} \tag{5.19}$$

Also, expand the misfit functional to second order in the model perturbation, ($\mathbf{m}$-$\mathbf{m}^{ref}$)

$$\begin{aligned} \chi^2(\mathbf{m}, \mathbf{m}^{ref}) \approx \chi^2(\mathbf{m}^{ref}, \mathbf{m}^{ref}) &+ \nabla\chi^2(\mathbf{m}^{ref})(\mathbf{m} - \mathbf{m}^{ref})^T \\ &+ \frac{1}{2}(\mathbf{m} - \mathbf{m}^{ref})\mathbf{H}(\mathbf{m}^{ref})(\mathbf{m} - \mathbf{m}^{ref})^T \end{aligned} \tag{5.20}$$

$$\nabla\chi^2(\mathbf{m}^{ref}) = \mathbf{J}(\mathbf{m}^{ref})^T \mathbf{D}(\mathbf{m}^{ref}) \tag{5.21}$$

$$\mathbf{D}(\mathbf{m}^{ref}) = \begin{bmatrix} D_1 \\ \vdots \\ D_m \end{bmatrix} \tag{5.22}$$

$$\mathbf{J}(\mathbf{m}^{ref}) = \begin{bmatrix} \delta D_{11} \cdots \delta D_{1n} \\ \vdots \quad \ddots \quad \vdots \\ \delta D_{m1} \cdots \delta D_{mn} \end{bmatrix} = \mathbf{C}_d^{-1/2} \begin{bmatrix} \frac{\delta \psi_1}{\delta m_1} \cdots \frac{\delta \psi_1}{\delta m_n} \\ \vdots \quad \ddots \quad \vdots \\ \frac{\delta \psi_m}{\delta m_1} \cdots \frac{\delta \psi_m}{\delta m_n} \end{bmatrix} \tag{5.23}$$

$$\begin{aligned} \mathbf{H}(\mathbf{m}^{ref}) &= \mathbf{J}(\mathbf{m}^{ref})^T \mathbf{J}(\mathbf{m}^{ref}) + \left(\nabla \mathbf{J}(\mathbf{m}^{ref})\right)^T \mathbf{D}(\mathbf{m}^{ref}) \\ &\approx \mathbf{J}(\mathbf{m}^{ref})^T \mathbf{J}(\mathbf{m}^{ref}) \end{aligned} \tag{5.24}$$

Using the linearization in (5.20), various linear solution methods can be recursively employed to find the model parameters that minimize the misfit functional. The matrices in equation (5.20) can be calculated using two approaches: the scattering integral, and adjoint-wavefield methods.

5.2.4 Scattering-Integral

Following the derivation in section 3.2, the scattering integral solution begins by decomposing the EM material properties into background and perturbation components.

$$\sigma(\mathbf{r}) = \sigma_b(\mathbf{r}) + \delta\sigma(\mathbf{r}) \tag{5.25}$$

$$\varepsilon(\mathbf{r}) = \varepsilon_b(\mathbf{r}) + \delta\varepsilon(\mathbf{r}) \tag{5.26}$$

$$\kappa^2(\mathbf{r},\omega) = \kappa_b^2(\mathbf{r},\omega) + \delta\kappa^2(\mathbf{r},\omega) \tag{5.27}$$

Where the subscript, b, specifies the reference or background media and the remaining terms give the material perturbations. Using the notation for EM wavefields, $\boldsymbol{\psi}(\mathbf{r},\omega_f) = \mathbf{E}(\mathbf{r},\omega)$ Maxwell's equations can then be written as

$$\nabla \times \nabla \times \mathbf{E}(\mathbf{r},\omega) - \kappa_b^2(\mathbf{r},\omega)\mathbf{E}(\mathbf{r},\omega) = \mathbf{S}(\mathbf{r},\omega) + \delta\kappa^2(\mathbf{r},\omega)\mathbf{E}(\mathbf{r},\omega) \tag{5.28}$$

The integral solution to equation (5.28) for the electric wavefield is given as

$$\begin{aligned} \mathbf{E}(\mathbf{r},\omega) &= \int_V \boldsymbol{G}_b(\mathbf{r},\mathbf{r}',\omega) \cdot \left(\mathbf{S}(\mathbf{r}',\omega) + \delta\kappa^2(\mathbf{r},\omega)\mathbf{E}(\mathbf{r}',\omega)\right) d^3\mathbf{r}' \\ \mathbf{E}(\mathbf{r},\omega) &= \mathbf{E}_b(\mathbf{r},\omega) + \int_V \boldsymbol{G}_b(\mathbf{r},\mathbf{r}',\omega) \cdot \mathbf{E}(\mathbf{r}',\omega)\delta\kappa^2(\mathbf{r}',\omega)\, d^3\mathbf{r}' \end{aligned} \tag{5.29}$$

We can subtract the background wavefield from both sides to determine the wavefield perturbation and can be obtained from the integral solution due to an equivalent current source given by the product of the material perturbation and the total electric wavefield.

$$\Delta\mathbf{E}(\mathbf{r},\omega) = \int_V \mathbf{G}_b(\mathbf{r},\mathbf{r}',\omega)\cdot\mathbf{E}(\mathbf{r}',\omega)\delta\kappa^2(\mathbf{r}',\omega)d^3\mathbf{r}' \tag{5.30}$$

To determine the electric wavefield Fréchet derivative, we need to quantify the data change for a small incremental change in the model parameters. In the limit as the material perturbation goes to zero, the total wavefield approaches the background wavefield

$$\delta\mathbf{E}(\mathbf{r},\omega) = -i\omega\mu_0\int_V \boldsymbol{G}_b(\mathbf{r},\mathbf{r}',\omega)\cdot\mathbf{E}_b(\mathbf{r}',\omega)\left[\delta\sigma(\mathbf{r}')+i\omega\delta\varepsilon(\mathbf{r}')\right]d^3\mathbf{r}' \tag{5.31}$$

$$\delta\mathbf{E}(\mathbf{r}_i,\omega) = \sum_j\left[\frac{\delta\mathbf{E}(\mathbf{r}_i,\omega)}{\delta\sigma(\mathbf{r}_j)}\delta\sigma(\mathbf{r}_j)+\frac{\delta\mathbf{E}(\mathbf{r}_i,\omega)}{\delta\varepsilon(\mathbf{r}_j)}\delta\varepsilon(\mathbf{r}_j)\right] \tag{5.32}$$

$$\frac{\delta\mathbf{E}(\mathbf{r}_i,\omega)}{\delta\sigma(\mathbf{r}_j)} = -i\omega\mu_0\int_{V_j}\boldsymbol{G}_b^T(\mathbf{r}',\mathbf{r}_i,\omega)\cdot\mathbf{E}_b(\mathbf{r}',\omega)d^3\mathbf{r}' \tag{5.33}$$

$$\frac{\delta\mathbf{E}(\mathbf{r}_i,\omega)}{\delta\varepsilon(\mathbf{r}_j)} = \omega^2\mu_0\int_{V_j}\boldsymbol{G}_b^T(\mathbf{r}',\mathbf{r}_i,\omega)\cdot\mathbf{E}_b(\mathbf{r}',\omega)d^3\mathbf{r}' \tag{5.34}$$

The background electric wavefield can be calculated from a forward simulation using the reference model parameters (electrical permittivity and conductivity). In equations (5.33) and (5.34) the reciprocity of the Green's function, $\mathbf{G}_b(\mathbf{r}_n,\mathbf{r}',\omega) = \mathbf{G}_b^T(\mathbf{r}_n,\mathbf{r}',\omega)$ has been used to simplify the required calculations. In the scattering integral method the Green's functions are computed from three forward simulations using sources located at each of the receiver positions and aligned with principal coordinate directions. The Fréchet derivatives, $\delta E_n/\delta m_m$, then can be efficiently computed by spatially convolving the Green's function with the calculated background electric field. The Jacobian, **J** and Hessian, **H** matrices can then be calculated by substituting equations (5.33), (5.34), and (5.22) into (5.23) and (5.24).

5.2.5 Adjoint Wavefield

An alternative method for efficient computation of the gradient of the misfit function is the adjoint state or adjoint wavefield method. The Fréchet derivatives, $\delta E_i/\delta m_j$, can be substituted into equations (5.21) and (5.23). So far the data have been assumed to be real valued. When the

data are complex, the inner product defining the norm of the residual vector must be modified as the product of the conjugate transpose of the residual vector with itself, $\left(\|\mathbf{e}\|_2\right)^2 = \mathbf{e}^H\mathbf{e}$. Without any loss of generality the data can be assumed univariant, $\mathbf{C}_d^{-1/2} = \mathbf{I}$, and the gradient of the misfit functional written in operator notation as

$$\nabla\chi^2(\mathbf{m}^{ref}) = \begin{bmatrix} \nabla\chi_\varepsilon^2(\mathbf{m}^{ref}) \\ \nabla\chi_\sigma^2(\mathbf{m}^{ref}) \end{bmatrix} = \begin{bmatrix} -i\omega\mu_0\mathbf{E}_b^H\boldsymbol{G}_b^H \\ \omega^2\mu_0\mathbf{E}_b^H\boldsymbol{G}_b^H \end{bmatrix}\mathbf{D}(\mathbf{m}^{ref}) \tag{5.35}$$

The conjugate transpose of the Green's operator corresponds to the adjoint of the EM forward model operator and acts on the data residuals to produce the gradient of the misfit functional. In the time domain, the adjoint operator propagates the EM wavefield in reverse time and for lossless media is identical to the forward EM operator (i.e. self-adjoint). When the electrical conductivity is non-zero, the adjoint operator causes the back propagated residual to grow exponentially and can potentially create numerical instability in the computed adjoint wavefield.

The gradient of the misfit functional can be obtained by forming the inner product of the background electric field and the back propagated residuals for each source. Using the adjoint state method the gradient of the misfit can be calculated without directly computing or storing the Jacobian matrix.

5.2.6 Steepest Descent

In the steepest-descent method, second order and higher terms are neglected in the series expansion of the misfit functional.

$$\chi^2(\mathbf{m},\mathbf{m}^{ref}) \approx \chi^2(\mathbf{m}^{ref},\mathbf{m}^{ref}) + \nabla\chi^2(\mathbf{m}^{ref})(\mathbf{m}-\mathbf{m}^{ref})^T \tag{5.36}$$

It is clear from (5.36) that the misfit can be reduced by simply moving along the model parameter perturbation vector aligned in the down-gradient direction. The optimal step length taken along this direction can be determined by performing a line search; that is by evaluating the misfit functional at several points along the down-gradient direction and interpolating to find the one that minimizes the misfit. The steepest-descent method provides slow but certain convergence to the local minimum of the misfit functional.

5.2.7 Gauss-Newton and Damped Least-Squares

The misfit functional can also be minimized by retaining second order terms in the series expansion. When the Hessian matrix is approximated by neglecting the second term in equation (5.24), the minimum of the misfit functional can be obtained using the Gauss-Newton method

$$\begin{aligned} &\mathbf{J}(\mathbf{m}^{ref})^T \mathbf{J}(\mathbf{m}^{ref})\Delta\mathbf{m} = \mathbf{J}(\mathbf{m}^{ref})^T \mathbf{D}(\mathbf{m}^{ref}) \\ &\Delta\mathbf{m} = (\mathbf{m} - \mathbf{m}^{ref}) \end{aligned} \tag{5.37}$$

The matrix on the left-hand side is symmetric and positive semi-definite and can be solved using direct or iterative solvers. If the matrix is singular, the method can fail and to mitigate this possibility the damped least-squares method can be used. This method augments the matrix in the Gauss-Newton method with a second term that stabilizes or regularizes the solution

$$\left[\mathbf{J}(\mathbf{m}^{ref})^T \mathbf{J}(\mathbf{m}^{ref}) + \mathbf{L}(\mathbf{m}^{ref})\right]\Delta\mathbf{m} = \mathbf{J}(\mathbf{m}^{ref})^T \mathbf{D}(\mathbf{m}^{ref}) \tag{5.38}$$

Several different forms for the regularization matrix L can be used, but the simplest is a scalar multiple of the identity matrix and is termed the Levenberg-Marquardt method

$$\left[\mathbf{J}(\mathbf{m}^{ref})^T \mathbf{J}(\mathbf{m}^{ref}) + \beta\mathbf{I}\right]\Delta\mathbf{m} = \mathbf{J}(\mathbf{m}^{ref})^T \mathbf{D}(\mathbf{m}^{ref}) \tag{5.39}$$

The scalar coefficient β is strictly positive and can be adjusted to accelerate convergence of the method. Positivity ensures that the matrix is non-singular, symmetric and positive definite. Direct methods using matrix factorization can then be used to solve the system; however, for large systems the computational requirements can be quite high and iterative solvers must be used.

5.2.8 Iterative Solvers

Iterative methods solve a linear system of equations, **Ax** = **b**, by generating a sequence of solutions, x_m, that recursively converges to the optimal solution. The first iterative solvers (i.e. Jacobi, Gauss-Seidel, and Successive Over-Relaxation) are relaxation methods that recursively modify an approximate solution until convergence. The modifications are termed relaxation steps and attempt to remove components of the residual or error vector and are implemented by factoring the original matrix into diagonal, lower-, and upper- triangular matrices. Another important class of iterative methods for solving linear systems is Krylov subspace methods.

Krylov subspace methods approximate the solution from: $x_m = \mathbf{x}_0 + K_m(\mathbf{A}, \mathbf{r}_0) = \mathbf{x}_0 + span\left\{\mathbf{r}_0, \mathbf{A}^2\mathbf{r}_0, ..., \mathbf{A}^{m-1}\mathbf{r}_0\right\}$, where x_0 corresponds to the initially chosen solution, and the residual $\mathbf{r}_0 = \mathbf{b}\text{-}\mathbf{A}\mathbf{x}_0$. The Krylov subspace, K_m, contains all vectors, $\mathbf{x} = p(\mathbf{A})\mathbf{r}_0$, where $p(\mathbf{A})$ is a polynomial of degree less than or equal to m-1. A number of Krylov subpace iterative methods have been developed that use a diagonalization or bidiagonalization process and include conjugate gradients, generalized minimum residual, bi-conjugate gradients, and several others. In this work I will focus on the LSQR algorithm (Paige and Saunders, 1982) that applies the conjugate gradient method to the normal equations, $\mathbf{A}^T\mathbf{A}\mathbf{x} = \mathbf{A}^T\mathbf{b}$, to provide a least squares solution to an overdetermined inverse problem. When the problem is under determined the method returns the damped least squares solution with minimum length |x|.

The solution to the normal equations that result from the Gauss-Newton method in equation (5.37) is simply the least squares solution to

$$\begin{aligned} &\mathbf{J}(\mathbf{m}^{ref})\Delta\mathbf{m} = \mathbf{D}(\mathbf{m}^{ref}) \\ &\mathbf{J}_{ref}\Delta\mathbf{m} = \mathbf{D}_{ref} \end{aligned} \tag{5.40}$$

The LSQR algorithm can then be applied to this linear system to provide the least squares solution to the problem.

5.2.9 Singular Value Decomposition

Another useful method for analyzing and solving least squares problems is the singular value decomposition (SVD). In some cases the linear system, $\mathbf{A}\mathbf{x} = \mathbf{b}$, can be solved by finding the matrix inverse $\mathbf{A}^{-1}$ such that $\mathbf{x} = \mathbf{A}^{-1}\mathbf{b}$. Generally the inverse of the matrix does not exist; however, it can be shown that every matrix has an SVD (Golub & Van Loan, 2013) that produces a generalized inverse, $\mathbf{A}^{\dagger}$. The SVD of an M by N matrix is given by

$$\mathbf{A} = \mathbf{U}\mathbf{S}\mathbf{V}^T \tag{5.41}$$

Where **U** is an M by M orthogonal matrix, **S** is an M by N diagonal matrix with nonnegative elements termed singular values, and **V** is an N by N orthogonal matrix. For the inverse problems discussed here, the columns of **U** are unit basis vectors spanning the data space, and the columns of **V** are basis vectors spanning the model space. The singular values are typically arranged in

decreasing order and some may be zero. If there are P nonzero singular values, the matrix **S** can be written as

$$\mathbf{S}=\begin{pmatrix}\mathbf{S}_P & \mathbf{0}\\ \mathbf{0} & \mathbf{0}\end{pmatrix} \tag{5.42}$$

The last M – P and N – P columns of **U** and **V** respectively are multiplied by the zeros in **S** and do not contribute to the solution. The matrices can then be reduced to include only the first P columns (denoted by the subscript P) and the SVD can be simplified as

$$\mathbf{A}=\mathbf{U}_P\mathbf{S}_P\mathbf{V}_P^T \tag{5.43}$$

The SVD can be used to compute the generalized inverse which can be shown to provide a least squares solution, $\mathbf{x}_\dagger$, to the linear system

$$\begin{aligned}\mathbf{x}_\dagger &= \mathbf{A}^\dagger\,\mathbf{b}\\ \mathbf{A}^\dagger &= \mathbf{V}_P\mathbf{S}_P^{-1}\mathbf{U}_P^T\end{aligned} \tag{5.44}$$

In equation (5.44) the inverse of the matrix **S** can be readily computed by taking the reciprocal of each of the diagonal elements in the matrix. While all the diagonal elements of **S** are positive, some may be very small and can lead to large errors in $\mathbf{S}^{-1}$. One way to deal with this problem is to simply set to zero the elements in $\mathbf{S}^{-1}$ corresponding to singular values less than some small threshold. In this way the number of singular values and basis functions that are used to reconstruct the solution has been truncated but leads to improved numerical stability.

5.3 IMPLEMENTATION

In this section a frequency domain, full waveform inversion approach will be outlined and compared to ray based inversion. In each case the inverse solution has been obtained using the Gauss-Newton method and the SVD of the Jacobian or sensitivity matrix, **J**; regularization is accomplished only by truncating the singular values used in the inversion. One of the goals here is to quantitatively show how the frequency domain full waveform sensitivity kernels, J_{FD}, capture the physics of the problem better than ray theoretic sensitivity kernels, J_S, and ultimately result in improved imaging. The scattering integral method is used to compute the elements of the full waveform sensitivity kernels which when discretized comprise the rows of the Jacobian

matrix. Ray theoretic travel time sensitivity kernels for the mth data point (observed travel time) are defined as

$$t_M = \sum_{j=1}^{N} J_M^S(\mathbf{r}_j)s(\mathbf{r}_j) = \sum_{j=1}^{N} J_{Mj}^S s_j$$
$$J_{Mj}^S = |\Delta \mathbf{r}_{Mj}|_2 \tag{5.45}$$

Where s_j corresponds to the slowness (reciprocal of velocity) at location $\mathbf{r}_j$, and the ray theoretic sensitivity kernel, J_{Mj}^S, is defined as the length of the mth ray that passes through location $\mathbf{r}_j$, For many subsurface environments, ray-paths are approximately straight (Peterson, 2001) which will be assumed here for the ray based inversions.

The computational domain consists of two anomalies embedded in a homogeneous medium with electrical permittivity, $\varepsilon = 7.5\varepsilon_0$, ($\varepsilon_0 = 8.854 \times 10^{-12}$) and electrical conductivity, $\sigma = 0.01$ S/m (Figure 5.1). The upper anomaly has $\varepsilon = 15\varepsilon_0$, and electrical conductivity, $\sigma = 0.1$ S/m and is 1m by 1m by 1m centered at x = 0m, y = 0m, and z =1m. The lower anomaly has $\varepsilon = 10\varepsilon_0$, and electrical conductivity, $\sigma = 0.1$ S/m and is 1m by 1m by 3m centered at x = 0m, y = 0m, and z = -1.5m. In Figure 5.1, transmitting antenna locations are designated by red x shaped markers and the locations where the electric field is measured are marked with open black circles. The full domain includes the complete set of transmitter and source locations and cannot be easily solved without parallelization. To reduce the computational needs, only the receiver positions in the y = 0m plane will be utilized generating M source-receiver pairs (Figure 5.2). The inversion will also be constrained so that the model parameters (electrical permittivity and conductivity) will be constrained to vary only in the x- and z-direction which allows the domain to be reduced to 10m by 1m by 10m. The elements of the Jacobian matrix are then calculated using the scattering integral method and the electrical field computed using the volume integral equation EM simulator described in chapter 4. The 3-D forward model computational domain is now 10m by 1m by 10m and discretized into 0.1m cubical element. The Jacobian elements are integrated along the y-direction to produce two M by N Jacobian matrices and two N element vectors for the permittivity and conductivity model parameters and each frequency corresponding to equations (5.34) and (5.33) respectively. This results in an inversion domain that is discretized into 0.1m by 0.1m by 1m grid elements. The Jacobian matrices for a single frequency ω_f are given by

$$\delta\mathbf{E}(\mathbf{r}_i,\omega_f)=\sum_{j=1}^{N}\left[\frac{\delta\mathbf{E}(\mathbf{r}_i,\omega_f)}{\delta\sigma(\mathbf{r}_j)}\delta\sigma(\mathbf{r}_j)+\frac{\delta\mathbf{E}(\mathbf{r}_i,\omega_f)}{\delta\varepsilon(\mathbf{r}_j)}\delta\varepsilon(\mathbf{r}_j)\right]$$

$$\delta\mathbf{E}(\mathbf{r}_i,\omega_f)=\sum_{j=1}^{N}\left[J_{ijf}^{\sigma}\delta\sigma_j+J_{ijf}^{\varepsilon}\delta\varepsilon_j\right] \tag{5.46}$$

$$\delta\mathbf{E}_f=\left[\mathbf{J}_f^{\sigma}\delta\boldsymbol{\sigma}+\mathbf{J}^{\varepsilon}\delta\boldsymbol{\varepsilon}_f\right]=\left[\mathbf{J}_f^{\sigma}+\mathbf{J}_f^{\varepsilon}\right]\begin{bmatrix}\delta\boldsymbol{\sigma}\\ \delta\boldsymbol{\varepsilon}\end{bmatrix}$$

The frequency domain inversion scheme utilizes both the real and imaginary components of the measured electric field in addition to several frequencies over the 30-180 MHz band. The inverse problem can then be modified as

$$\begin{aligned}\mathrm{Re}\left(\delta\mathbf{E}_f\right)&=\left[\mathrm{Re}\left(\mathbf{J}_f^{\sigma}\right)\ \mathrm{Re}\left(\mathbf{J}_f^{\varepsilon}\right)\right]\begin{bmatrix}\delta\boldsymbol{\sigma}\\ \delta\boldsymbol{\varepsilon}\end{bmatrix}\\ \mathrm{Im}\left(\delta\mathbf{E}_f\right)&=\left[\mathrm{Im}\left(\mathbf{J}_f^{\sigma}\right)\ \mathrm{Im}\left(\mathbf{J}_f^{\varepsilon}\right)\right]\begin{bmatrix}\delta\boldsymbol{\sigma}\\ \delta\boldsymbol{\varepsilon}\end{bmatrix}\end{aligned} \tag{5.47}$$

$$\delta\mathbf{d}_f=\mathbf{C}_d^{-\frac{1}{2}}\begin{bmatrix}\mathrm{Re}\left(\delta\mathbf{E}_f\right)\\ \mathrm{Im}\left(\delta\mathbf{E}_f\right)\end{bmatrix}=\mathbf{C}_d^{-\frac{1}{2}}\begin{bmatrix}\mathrm{Re}\left(\mathbf{J}_f^{\sigma}\right)\ \mathrm{Re}\left(\mathbf{J}_f^{\varepsilon}\right)\\ \mathrm{Im}\left(\mathbf{J}_f^{\sigma}\right)\ \mathrm{Im}\left(\mathbf{J}_f^{\varepsilon}\right)\end{bmatrix}\begin{bmatrix}\delta\boldsymbol{\sigma}\\ \delta\boldsymbol{\varepsilon}\end{bmatrix}=\mathbf{J}_f\delta\mathbf{m}$$

$$\delta\mathbf{d}=\begin{bmatrix}\delta\mathbf{d}_1\\ \delta\mathbf{d}_2\\ \vdots\\ \delta\mathbf{d}_f\end{bmatrix}=\begin{bmatrix}\mathbf{J}_1\\ \mathbf{J}_2\\ \vdots\\ \mathbf{J}_f\end{bmatrix}=\mathbf{J}_{FD}\delta\mathbf{m} \tag{5.48}$$

A shifted Ricker wavelet is used for the current source term in equation (3.10) to simulate the electric field for each transmission location. The power spectrum of the source signal is shown in Figure 5.3 and 99.9% of the energy occurs between 30 MHz and 180 MHz frequencies. Figure 5.2 also shows the ray coverage pattern for rays emanating from a single transmitter location and being measured at several receiver locations and is termed a fan. The corresponding electric field at each of the receiver locations is depicted in Figure 5.4 along with travel-time (filled circles) and maximum amplitude (open circles) picks used in the ray based inversions.

An important aspect of wave propagation imaging is the sensitivity of the data to model parameters and for ray based inversions this can be investigated by examining the ray coverage or ray density (Figure 5.5). At positions in the domain where many rays pass through, one would

expect that the model parameters (slowness) are likely to be better resolved than where fewer rays intersect. The ray density specifies the cumulative sensitivity (sum of all rays divided by the number of data) for all the ray lengths in a given grid volume and provides a semi-quantitative measure of the data-model parameter sensitivity. Similarly the cumulative sensitivity can be used to describe the model parameter sensitivity for full waveform inversion and can been used as a surrogate for the true model parameter resolution (Meles et. al 2012). The full waveform cumulative sensitivity is shown in Figure 5.6 corresponding to a 100 MHz signal for a single fan (upper plot) and three transmitter fans (lower plot). From Figure 5.6, large sensitivities are apparent near the source and receiver centers and reflect the near-field contributions from the EM Green's functions. The assumption that Green's function and the electric field are constant in each cell leads to large errors near the center of the source and receiver in equations (5.33) and (5.34). The large sensitivity near the source and receiver can greatly influence the estimated model parameters and can be addressed in a number of ways. Here the sensitivity is simply set to zero within a small radius (0.02m) around the source and receiver location for each source-receiver pair. Doing so does not mean that the sensitivity is zero at the source and receiver locations since the sensitivity due to other source-receiver combinations contribute at those locations. Figure 5.7 illustrates the change in cumulative sensitivity due to this modification; the upper plot shows the original sensitivity for all the 100 MHz data and the lower plot utilizes the zeroed sensitivity at each source/receiver center. The sensitivities also depend on frequency, as well as the reference model parameters. The reference model parameters used in the Green's function can be assumed the same for all source-receiver data points; however this restriction is not necessary and in the case of homogeneous reference media can be relaxed without any additional computational burden. In this dissertation this has been used and by doing so some of the heterogeneity is incorporated into the initial iteration of the inversion.

Other key aspects of the inversion are the singular values, chi-squared values, and model basis functions that are used to reconstruct the model parameters. The model basis functions for the ray based (Figure 5.8) and 100 MHz frequency domain inversions (Figure 5.9) have very different characteristics. The ray based model basis function show a characteristic "X" pattern while the corresponding full waveform model basis functions are less localized. In both cases the model bases begin to show large spatial variations associated with smaller singular values. The singular value plots (Figure 5.10) for the ray based (upper plot) and full waveform (lower plot)

cases are also somewhat different. The ray based singular values initially decrease quite rapidly while those for the full waveform case show a more gradual change throughout most of the range. The chi-squared values (equation(5.19)) have also been calculated for various models obtained by assuming different truncation indices in the inversion. A plot of the chi-squared value versus truncation index for ray based and full waveform methods are shown in Figure 5.11 and Figure 5.12 respectively. As mentioned previously, the chi-squared value is expected to be close to the number of degrees of freedom for the most likely solution. The full waveform method attains this value using fewer model basis functions (smaller truncation index) than the ray based inversion as shown by the open circles on each plot.

Finally, the model parameters estimated using both ray theory and full waveform methods are compared. Both methods make use of all the data and the full waveform utilizes 25 frequencies in the 30-180 MHz band. Cross sections of the true models are shown Figure 5.13 for electrical permittivity (upper left) and conductivity (upper right). The ray based recovered electrical permittivity is shown in the lower right plot which shows that the general features of the true model have been recovered, however much of the details have been lost. The full waveform recovered models are shown in Figure 5.14 and illustrate the improvements in electrical permittivity (upper plot) and electrical conductivity (lower plot) resolution compared to the ray based results. While SVD can be used for the simplified geometry here, larger scale problems with millions of model parameters will require the use of iterative methods and parallelization. In addition to the SVD solution, the method here was adapted to use an iterative solver in the inversion. At each iteration of the inversion, a reference model is assumed and an estimate of the model parameters is solved for using the LSQR algorithm. The inversion begins by using just the 30 MHz data and progressively includes additional frequencies in steps until all frequencies in the band have been included. For the case considered here the final solution obtained with the iterative solver is very similar to the solution estimated with SVD.

5.4 CONCLUSIONS

A 3-D frequency domain full waveform inversion method has been developed for georadar applications. While the method has been demonstrated for a simplified geometry, the results show that full waveform inversion has the potential to provide much higher resolution images compared to ray based methods.

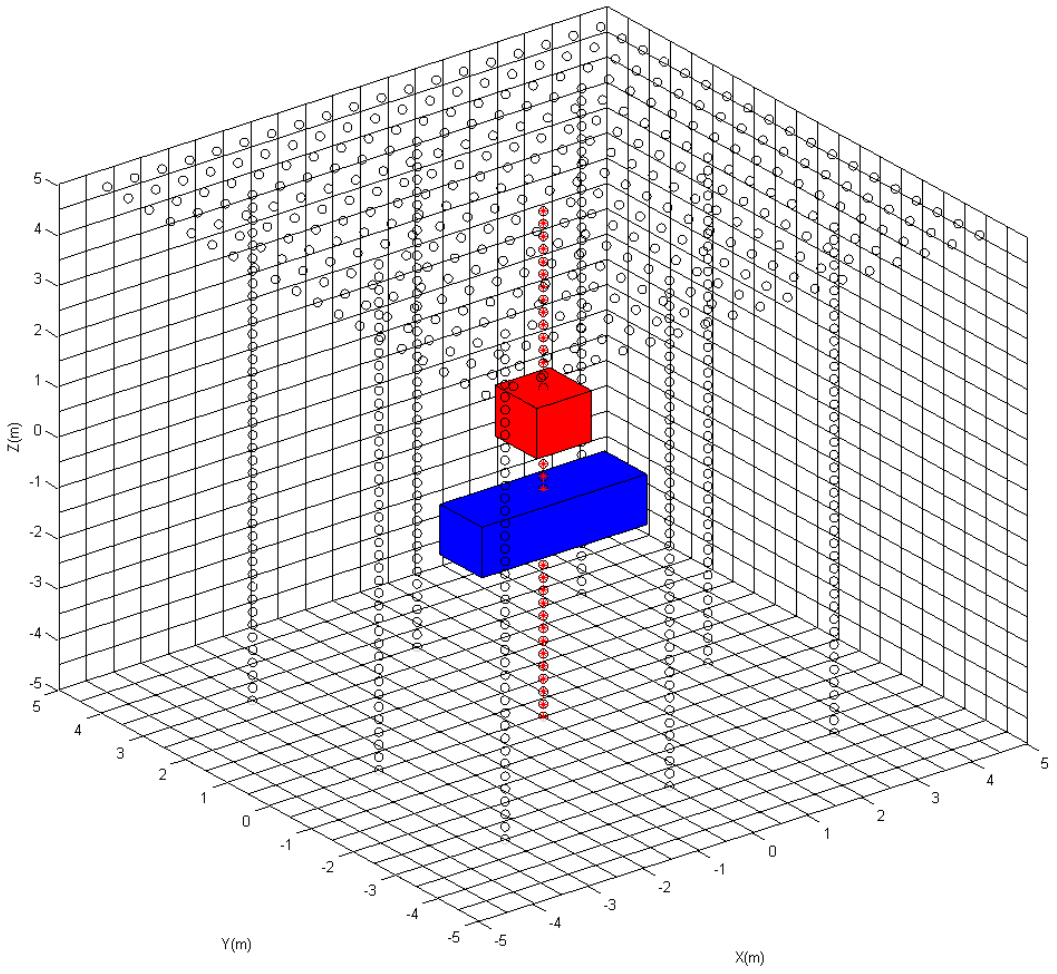

Figure 5.1 3D model showing two anomalies embedded within a homogeneous half-space. Black circles denote receiver locations and red x-markers denote transmitter locations

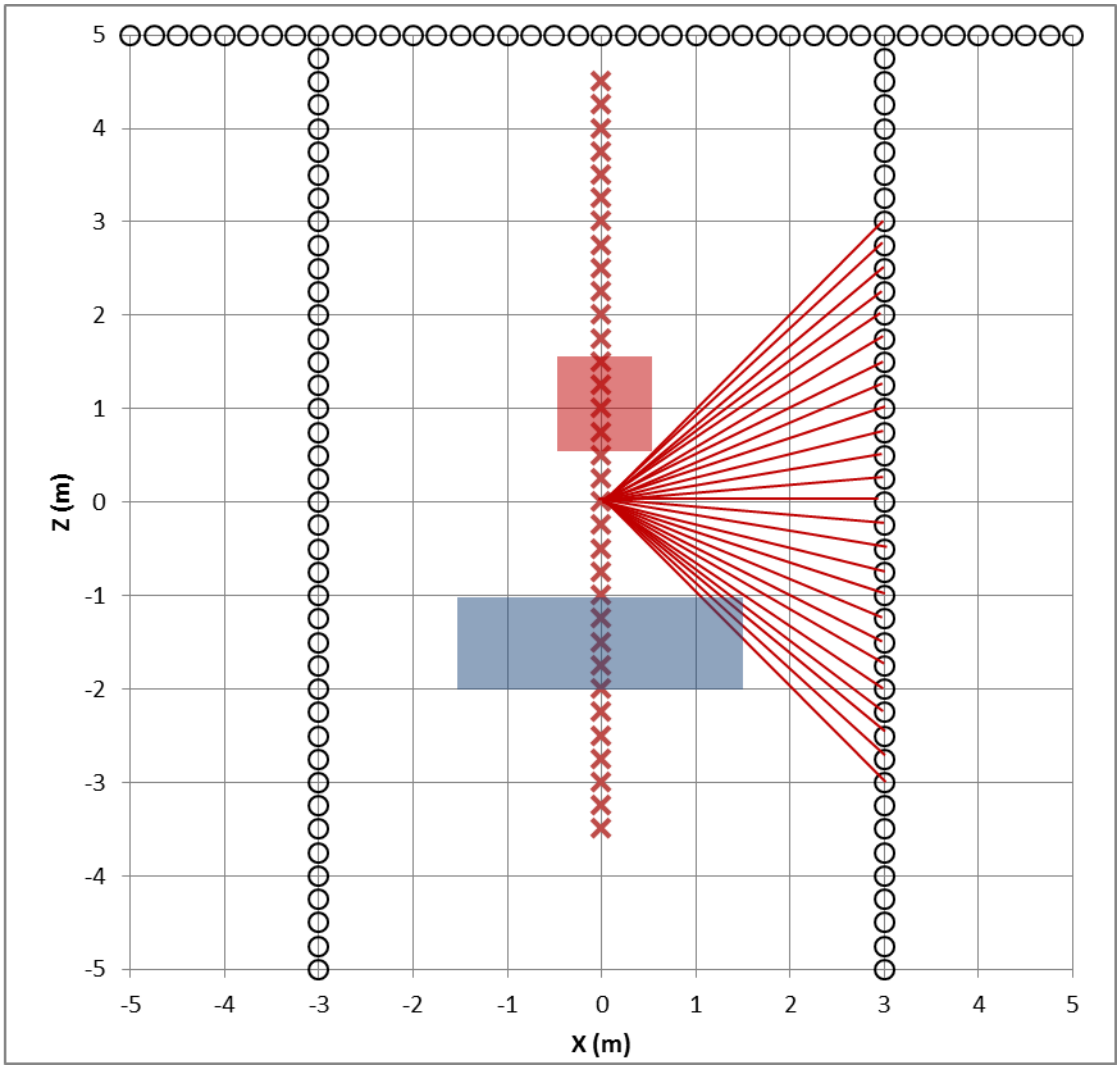

Figure 5.2 Cross section of the model doamin through the y=0m plane and the data used in the inversion. Black circles denote receiver locations and red x-markers denote transmitter locations

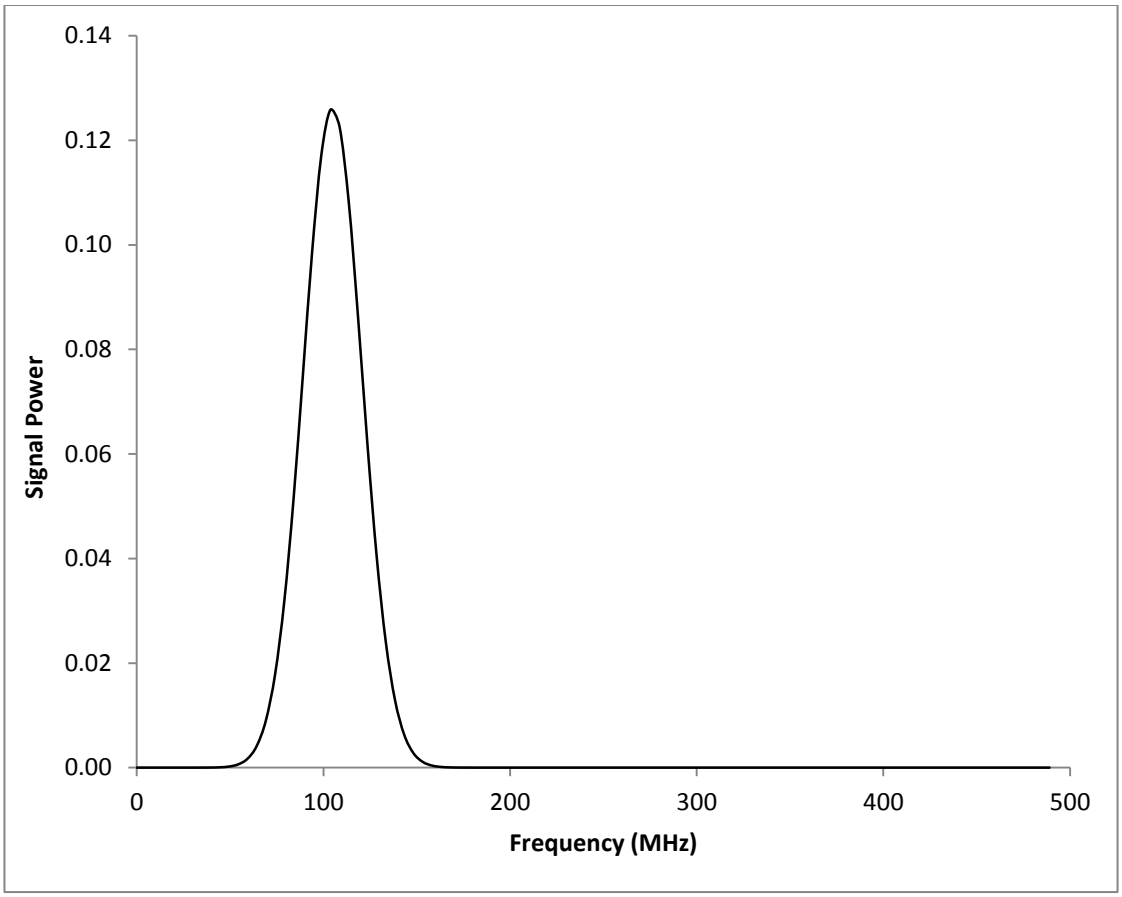

Figure 5.3 Power spectrum for the EM source used in the inversions

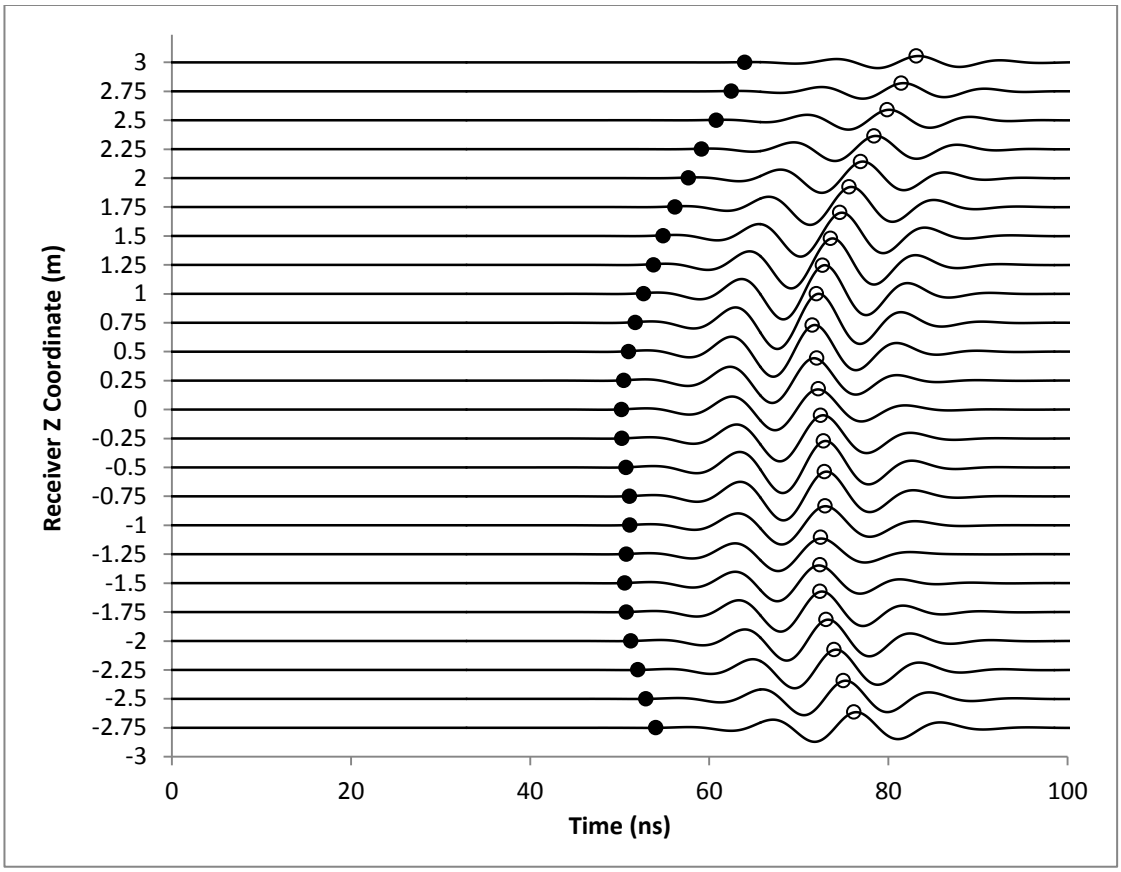

Figure 5.4 Waveform data for one fan with transmitter at (x, y, z) = (0, 0, 0) and receiver locations spanning (3, 0, -3) to (3, 0, 3)

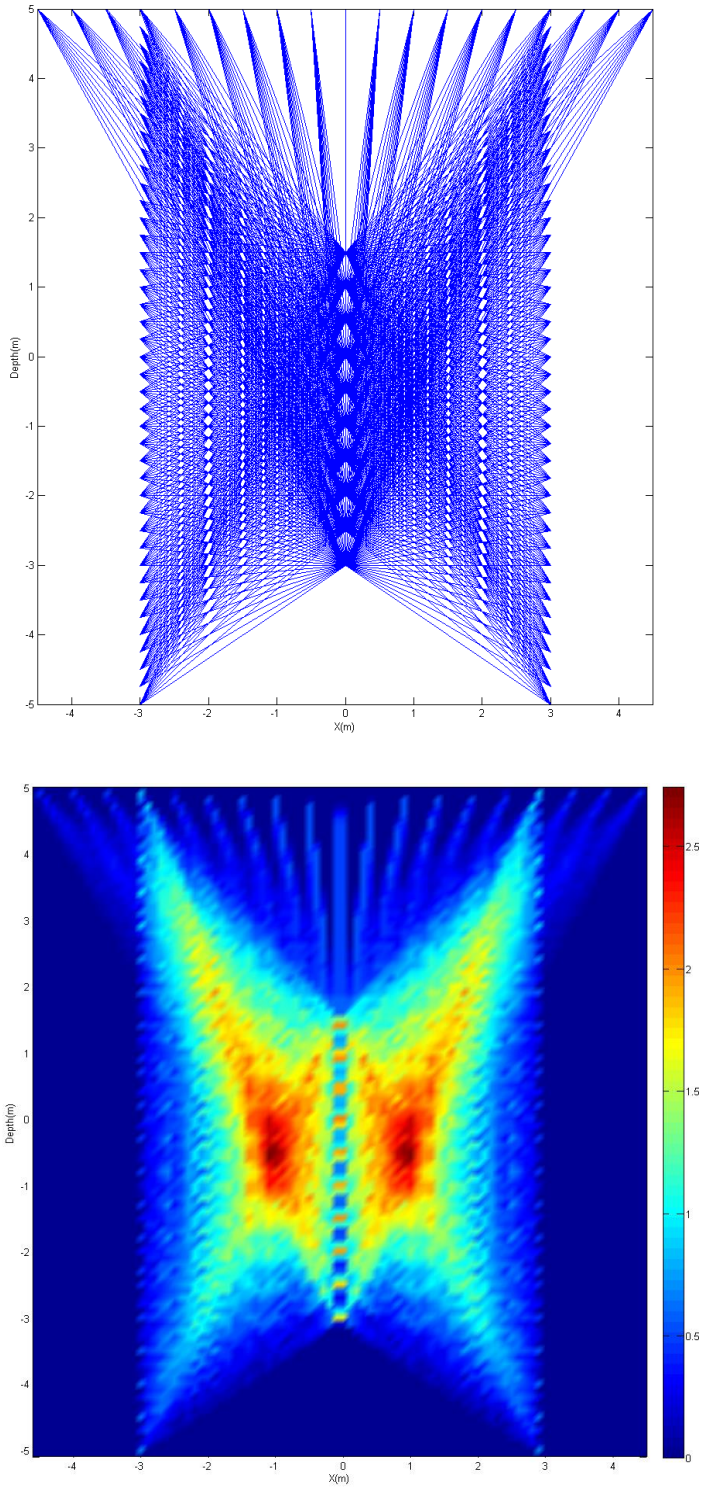

Figure 5.5 Ray coverage (upper) and ray density plot (lower) for all the data used in the inversions

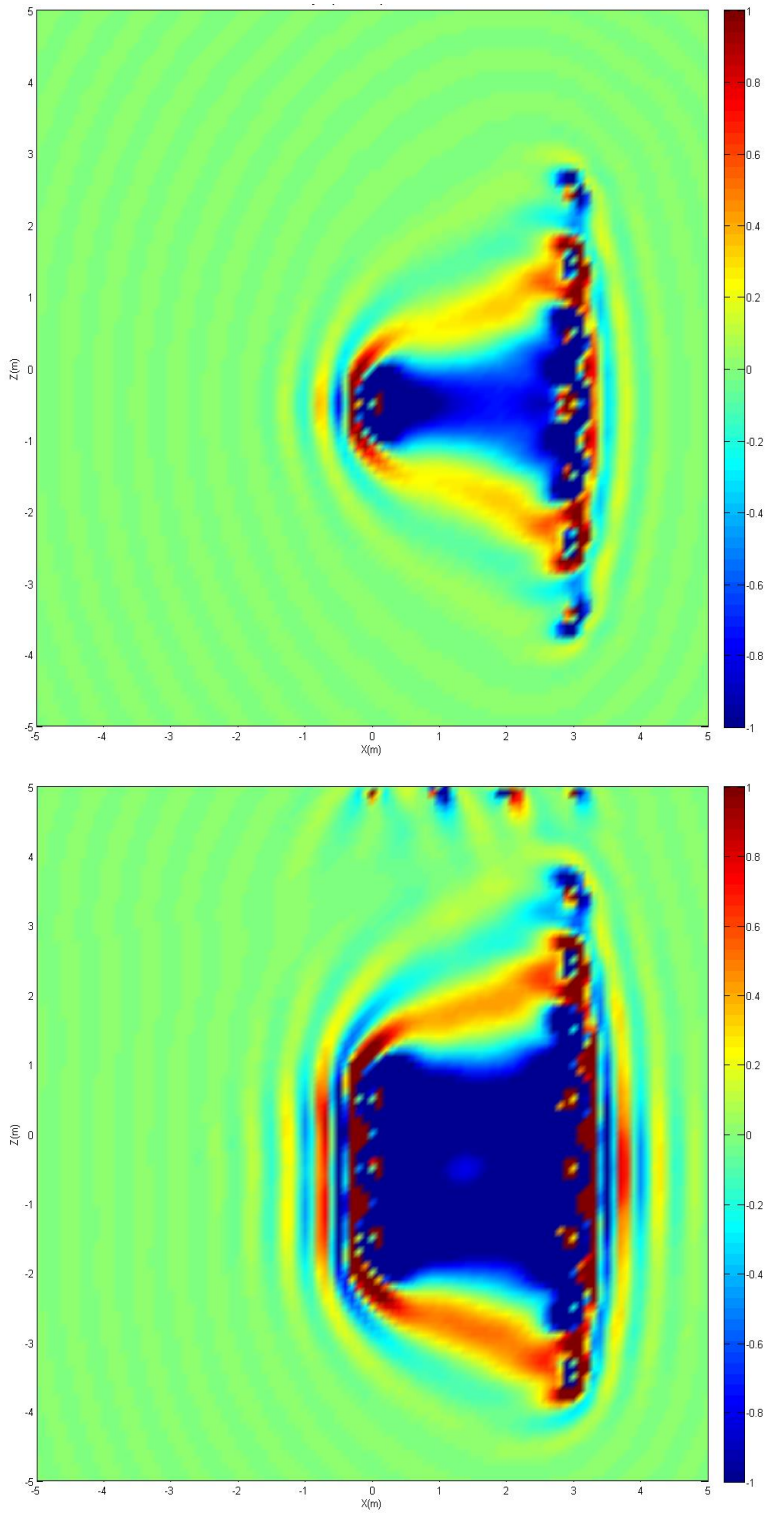

Figure 5.6 Full waveform imaginary component cumulative sensitivities at 100 MHz. Cumulative sensitivity for a single fan is shown in the upper plot and the sensitivity for a combined set of three fans is shown in the lower plot.

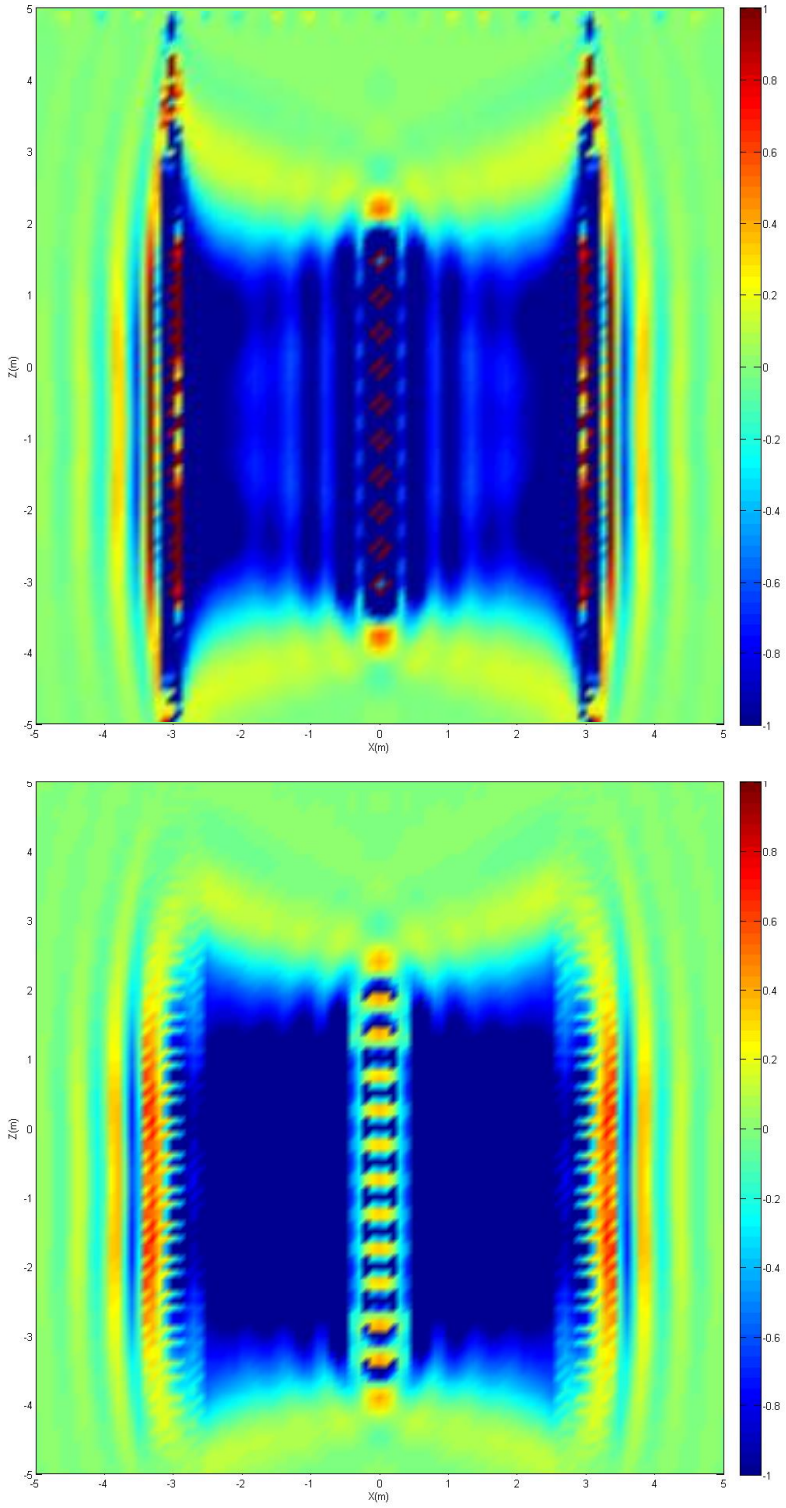

Figure 5.7 Full waveform cumulative sensitivities for the complete imaginary component dataset at 100 MHz. The upper plot shows the sensitivity without any source-receiver region filtering and the lower plot illustrates the cumulative sensitivity using the source/receiver filtering scheme described in the text.

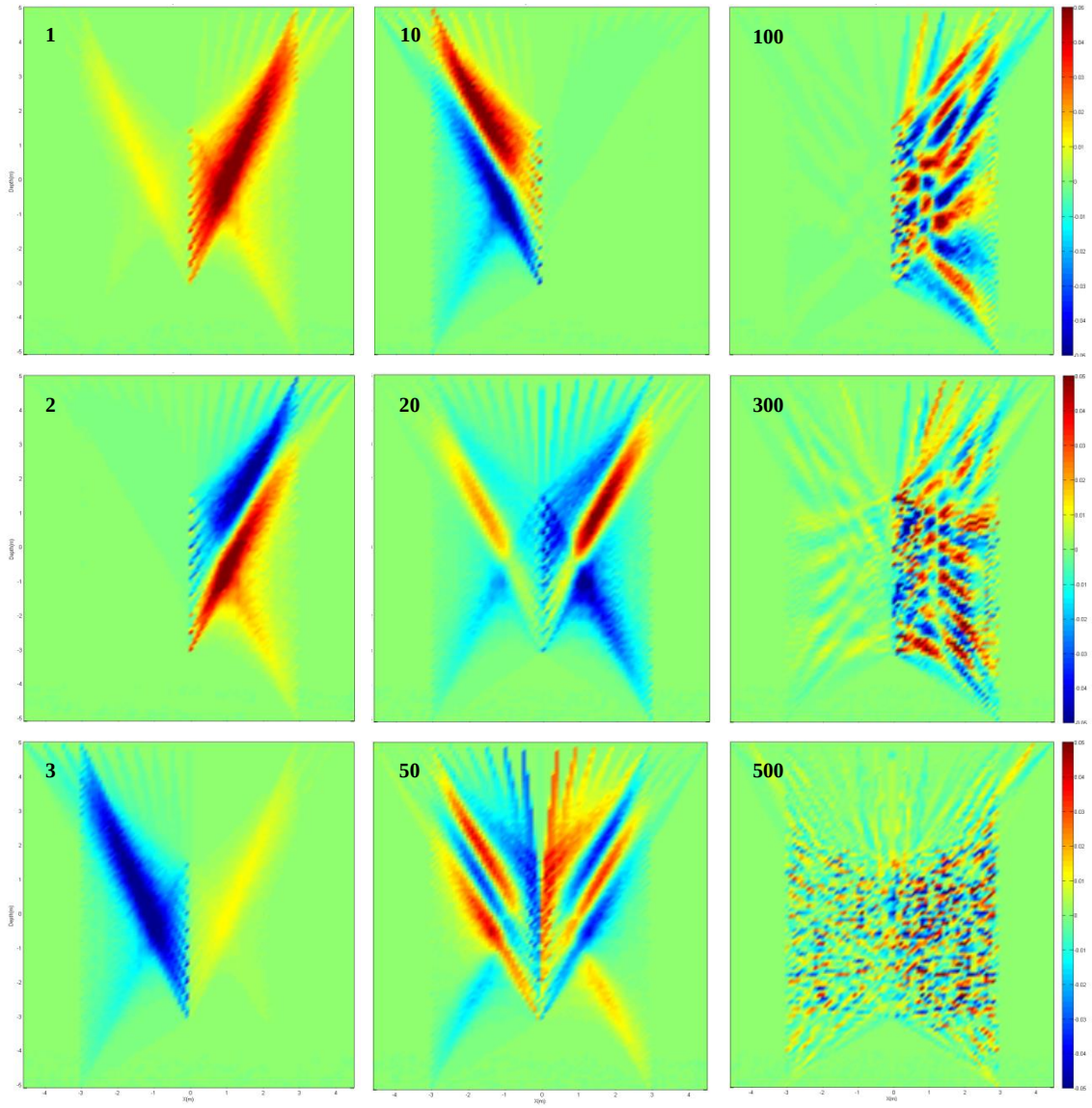

Figure 5.8 Ray theoretic model basis functions for a range of singular values truncation indices. Singular value truncation indices are shown in the upper left of each subplot.

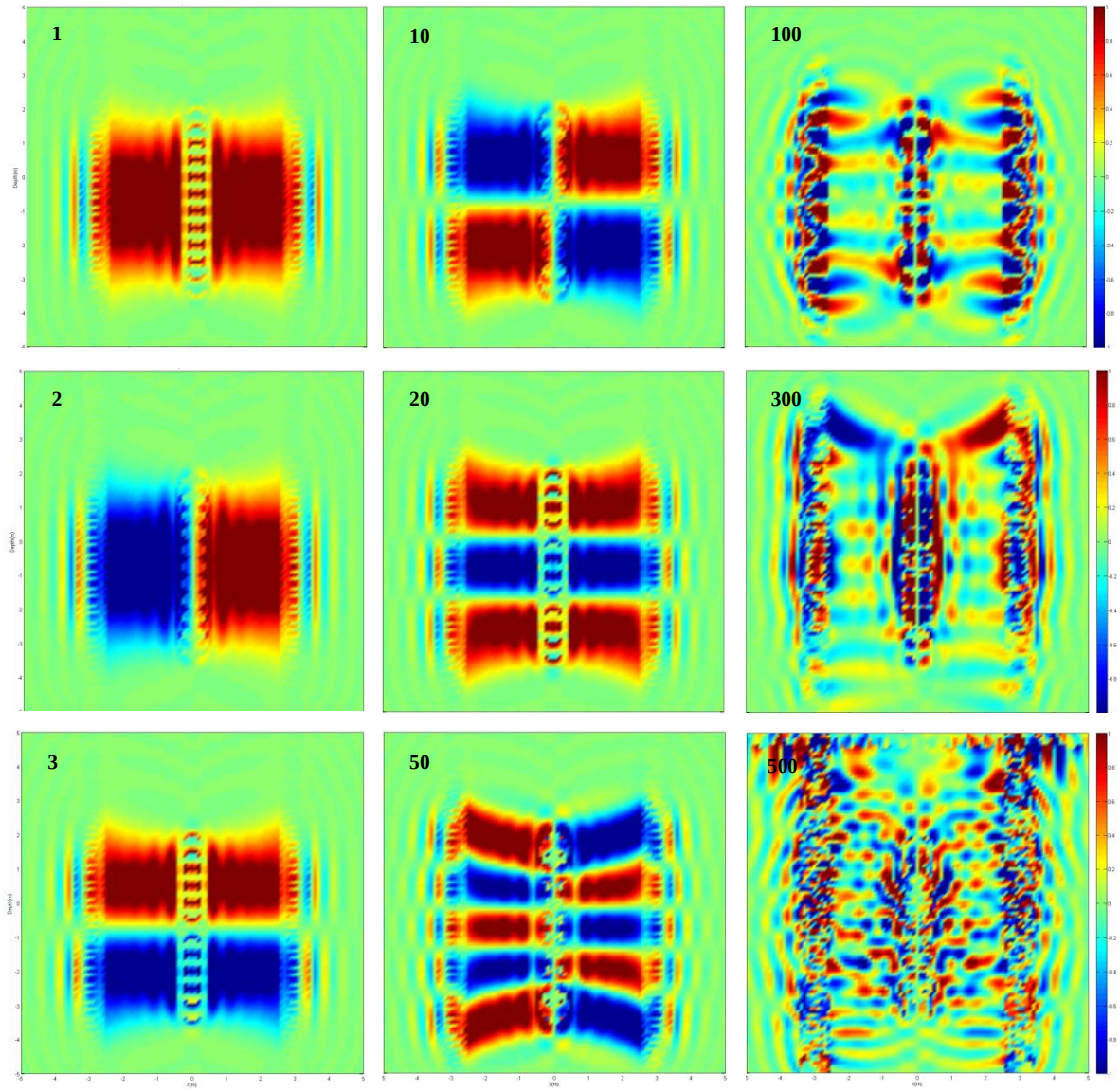

Figure 5.9 Full waveform model basis functions for a range of singular values truncation indices. Singular value truncation indices are shown in the upper left of each subplot.

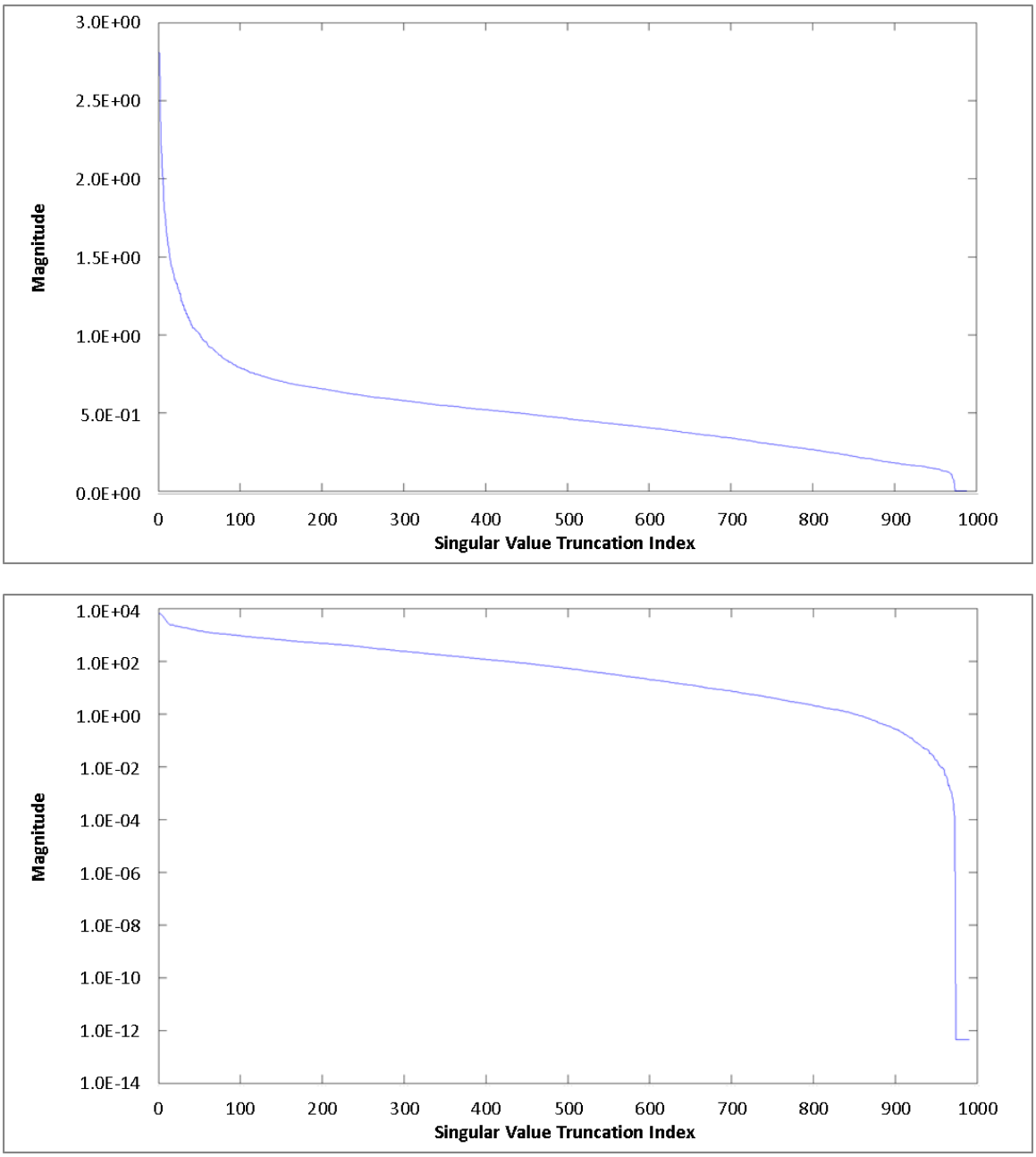

Figure 5.10 Singular values for both ray theoretic (upper) and full waveform methods (lower)

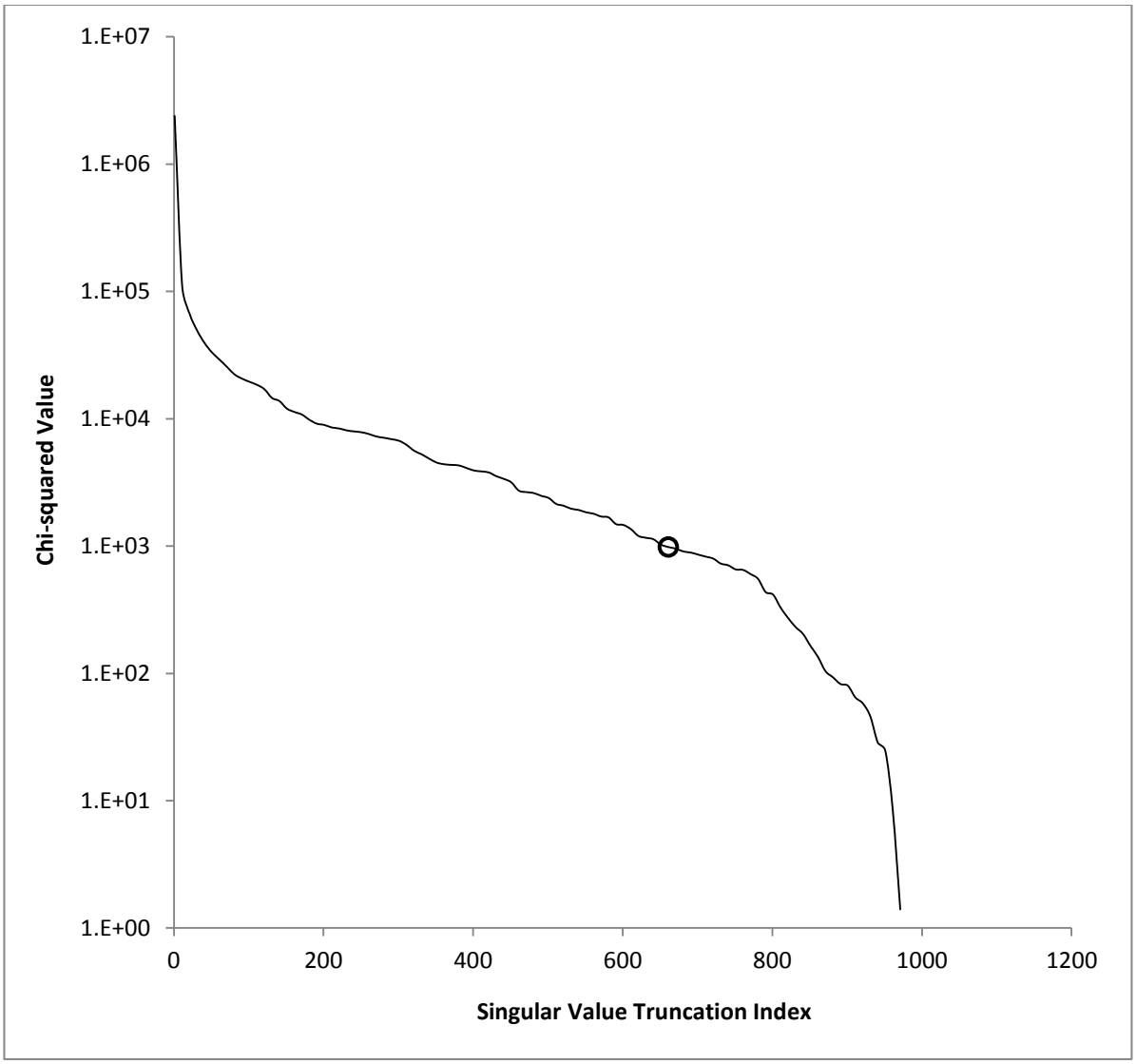

Figure 5.11 Ray theoretic chi-squared values as a function of truncation index. Black circle denote where the chi-squared is equal to the number of degrees of freedom

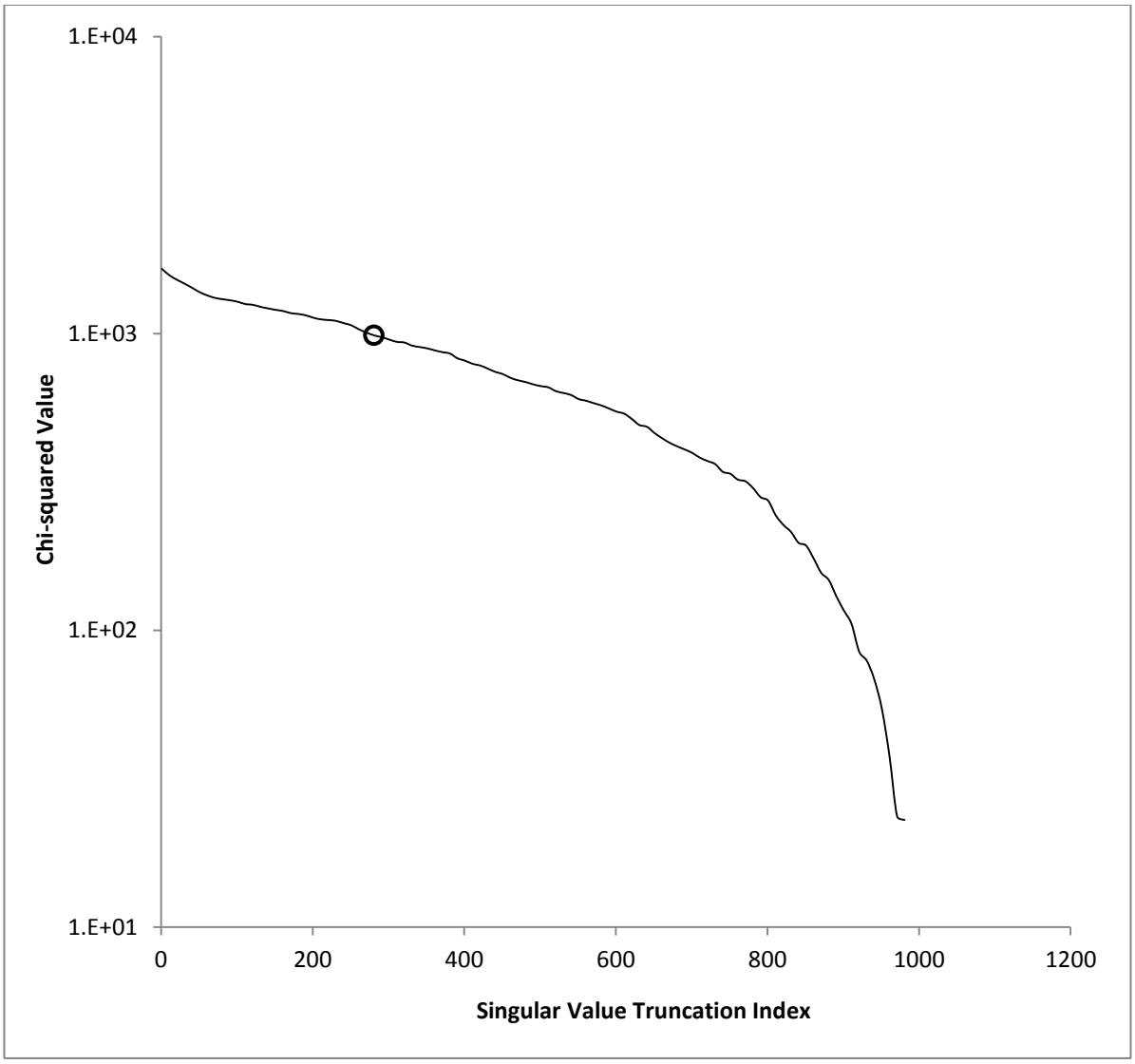

Figure 5.12 Full waveform chi-squared values as a function of truncation index. Black circle denote where the chi-squared is equal to the number of degrees of freedom

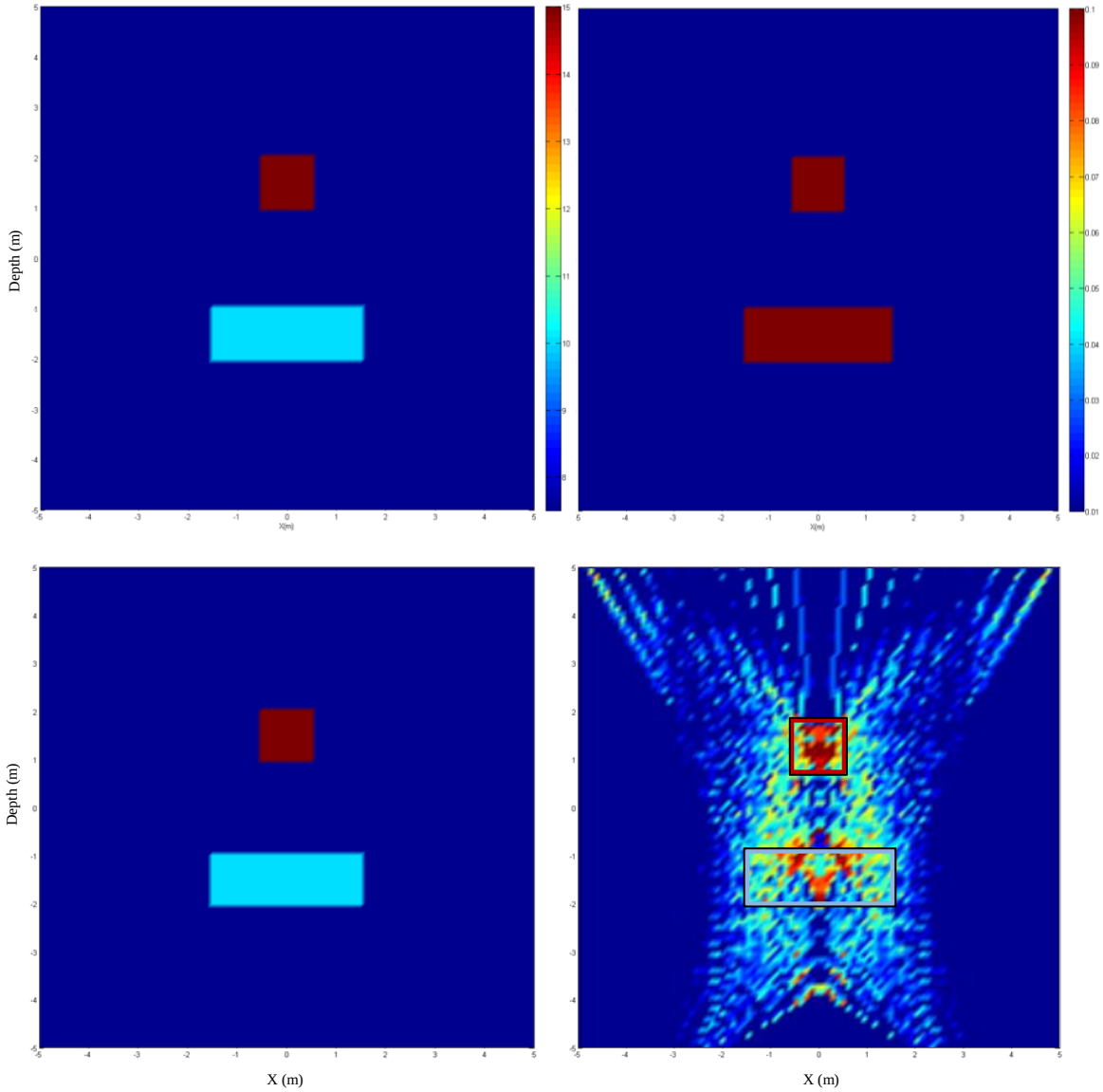

Figure 5.13 True model used in the inversion (left and upper right plots) and the results of the ray theoretic inversion for electrical permittivity (lower right)

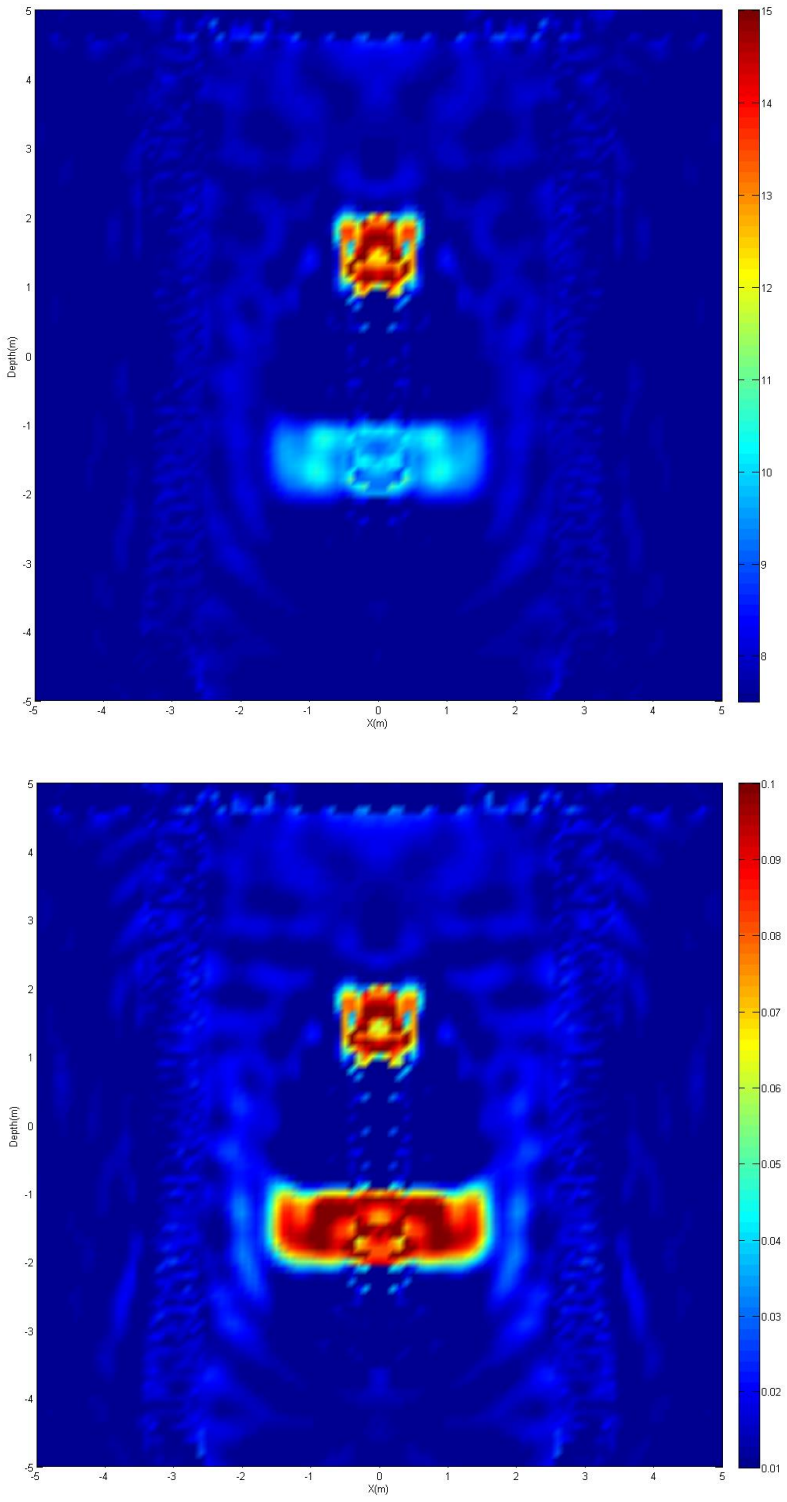

Figure 5.14 Full waveform inversion results for electrical permittivity (upper) and electrical conductivity (lower)

6 ELASTIC AND ACOUSTIC WAVE PROPAGATION

In this chapter, the basic elements of elastodynamic theory are first presented followed by a description of the volume integral equation method to simulate elastic and acoustic wave propagation. Elastic and acoustic wave propagation problems can be numerically modeled and inverted using a fast algorithm similar to those described in chapters 4 and 5 for electromagnetic problems that exploits the circulant symmetry of the underlying governing equations. Also, for the acoustic case the inversion Jacobian matrix is simple circulant and SVD can be performed in O(M*NlogN) operations where N is the number of grid cells and M the number of source locations used in the inversion.

Elastodynamic theory is generally grouped as a branch of continuum mechanics and studies the deformation and motion of material bodies without directly considering their discrete molecular properties. Central to elastic problems are the concepts of stress, deformation, strain, and motion. Material bodies can be divided into regions or elements that can be described by their location within the body. The displacement vector, **u**(**r**), describes the position of each element within the medium relative to a reference state and the body undergoes deformation, or strain **ε**, when there is a change in the relative position of the elements. When the deformations are small, the strain tensor is related to the displacement by

$$\varepsilon_{kl} = \frac{1}{2}\left(\frac{\partial}{\partial x_l} u_k + \frac{\partial}{\partial x_k} u_l \right) \tag{6.1}$$

In dyadic form as

$$\varepsilon = \frac{1}{2}\left(\mathbf{u}\nabla + \nabla\mathbf{u} \right) \tag{6.2}$$

Materials are also subject to forces and can be described using two basic types: body forces and surface forces (tractions). Body forces act within the entire volume of each element and tractions act upon the surface bounding the volume element. The total force on an element is a composite of both the volume and surface forces acting on that element. The traction, **T**, acting on a particular surface depends both on the orientation of the surface, **n**, and the stress tensor (with units of force/area), **τ**, and in 3D is given by

$$\mathbf{T} = \boldsymbol{\tau} \cdot \hat{\mathbf{n}}$$
$$T_i = \sum_{j=1}^{3} \tau_{ji} \hat{n}_j \tag{6.3}$$

The stress tensor can be shown to be symmetric, $\tau_{ij} = \tau_{ji}$, from the requirement that angular momentum is conserved (Malvern 1969).

The total force due to the stress acting on the volume element is given as a surface integral of the tractions over the bounding surface. Using Gauss's theorem, this surface integral can be converted to an equivalent volume integral. The acceleration within the material is related to the forces through Newton's law which when combined with the surface and body forces gives

$$\int_S \boldsymbol{\tau} \cdot \hat{\mathbf{n}}\, dS + \int_V \rho \mathbf{m}\, dV = \int_V \left(\nabla \cdot \boldsymbol{\tau} + \rho \mathbf{m} \right) dV = \int_V \rho \ddot{\mathbf{u}}\, dV \tag{6.4}$$

Where **m** is a body force per unit mass so that $\rho\mathbf{m} = \mathbf{f}$ is a force per unit volume. Since equation (6.4) holds for any arbitrary volume the quantities within the integrals must be equal and the equation of motion in the frequency-domain is

$$-\rho\omega^2 \mathbf{u} = \nabla \cdot \boldsymbol{\tau} + \mathbf{f} \tag{6.5}$$

It should be noted that in a continuous medium the acceleration also contains an advective term; however, when the material velocity is much smaller than the velocity of the wave, the advective term can be effectively ignored (Snieder 2001).

Finally, to apply the equation of motion to specific medium it is necessary to establish a relationship between stress and strain and is known as a constitutive equation. If the deformation is small such that the medium returns to its initial state after the force has been removed then the deformation is said to be elastic and the stress is linearly related to the strain.

$$\tau_{ij} = c_{ijkl} \varepsilon_{kl} = c_{ijkl} \frac{\partial}{\partial x_k} u_l \tag{6.6}$$

Elasticity is a generalization of Hooke's law and the fourth order elasticity tensor, c_{ijkl}, generalizes the concept the spring constant of a simple spring to three-dimensional media. The elasticity tensor possess a number of symmetries when certain indices are exchanged and have been used to simplify equation (6.6). It can be shown that the number of independent parameters in the elasticity tensor is 21; however, when the medium is isotropic there are only two: the Lamé parameters λ and μ

$$c_{ijkl} = \lambda \delta_{ij} \delta_{kl} + \mu \left(\delta_{ik} \delta_{jl} + \delta_{il} \delta_{jk} \right) \tag{6.7}$$

The elastodynamic wave equation is then obtained by substituting the constitutive equation (6.6) into the equation of motion (6.5)

$$\rho\omega^2 u_i + \frac{\partial}{\partial x_j}\left(c_{ijkl}\frac{\partial}{\partial x_k} u_l \right) = -f_i \tag{6.8}$$

In operator notation

$$\mathbf{Lu} = -\mathbf{f}$$
$$L_{ij} = \rho\omega^2\delta_{ij} + \frac{\partial}{\partial x_k}\left(c_{iklj}\frac{\partial}{\partial x_l} \right) \tag{6.9}$$

6.1 Elastodynamic Representation Theorem

In order to derive the representation theorem for elastic waves consider two solutions, $u^{(1)}$ and $u^{(2)}$ to equation (6.9) that are generated by separate body forces $f^{(1)}$ and $f^{(2)}$

$$\mathbf{Lu}^{(1)} = -\mathbf{f}^{(1)}$$
$$\mathbf{Lu}^{(2)} = -\mathbf{f}^{(2)} \tag{6.10}$$

Substituting (6.10) into the representation theorem for a general linear differential operator (2.22) gives

$$\int_V \left[u_i^{(2)}\frac{\partial}{\partial x_j}\left(c_{ijkl}\frac{\partial}{\partial x_k} u_l^{(1)} \right) - u_i^{(1)}\frac{\partial}{\partial x_j}\left(c_{ijkl}\frac{\partial}{\partial x_k} u_l^{(2)} \right) \right] dV = -\int_V \left[f_i^{(1)} u_i^{(2)} - f_i^{(2)} u_i^{(1)} \right] dV \tag{6.11}$$

The volume integrals on the left-hand side of (6.11) can be transformed into surface integrals using Gauss's theorem and simplified using symmetry properties of the elasticity tensor so that the representation theorem becomes

$$\int_S \left[n_j u_i^{(2)}\left(c_{ijkl}\frac{\partial}{\partial x_k} u_l^{(1)} \right) - n_j u_i^{(1)}\left(c_{ijkl}\frac{\partial}{\partial x_k} u_l^{(2)} \right) \right] dS = -\int_V \left[f_i^{(1)} u_i^{(2)} - f_i^{(2)} u_i^{(1)} \right] dV \tag{6.12}$$

When the forces in (6.12) correspond to concentrated point forces located at $\mathbf{r}^{(1)}$ and $\mathbf{r}^{(2)}$ and acting in the i^{th} and j_{th} direction respectively than the solutions are elastodynamic Green's functions. From equation (6.12), if the Green's function or it's traction are zero on the bounding surface then the left-hand side vanishes and gives the reciprocity theorem

$$G_{ij}(\mathbf{r}^{(1)},\mathbf{r}^{(2)}) = G_{ji}(\mathbf{r}^{(2)},\mathbf{r}^{(1)}) \tag{6.13}$$

If now only one of the forces correspond to a point force, and the Green's function satisfies homogeneous boundary conditions, then the representation theorem gives the integral solution

$$\begin{aligned} u_i(\mathbf{r}) &= \int_V G_{in}(\mathbf{r},\mathbf{r}')\, f_n(\mathbf{r}')\, dV' \\ &+ \int_S \left[G_{in}(\mathbf{r},\mathbf{r}') n_j c_{ijkl} \frac{\partial}{\partial x_k'} u_l(\mathbf{r}') - u_n(\mathbf{r}') n_j c_{ijkl} \frac{\partial}{\partial x_k'} G_{il}(\mathbf{r},\mathbf{r}') \right] dS' \end{aligned} \tag{6.14}$$

6.2 Volume Integral Equation for Elastic Waves

To develop the volume integral equation for elastic waves, the elasticity tensor and density parameters that describe the medium must first be divided into a reference and perturbation

$$\begin{aligned} \mathbf{c}(\mathbf{r}) &= \mathbf{c}^{ref}(\mathbf{r}) + \mathbf{c}^{p}(\mathbf{r}) \\ \rho(\mathbf{r}) &= \rho^{ref}(\mathbf{r}) + \rho^{p}(\mathbf{r}) \end{aligned} \tag{6.15}$$

Substituting the medium decomposition into the elastodynamic wave equation (6.9) gives

$$\begin{aligned} \left(\mathbf{L}^{ref} + \mathbf{L}^{p}\right)\mathbf{u}(\mathbf{r}) &= -\mathbf{f}(\mathbf{r}) \\ \mathbf{L}^{ref}\mathbf{u}(\mathbf{r}) &= -\left(\mathbf{f}(\mathbf{r}) + \mathbf{L}^{p}\mathbf{u}\right) \end{aligned} \tag{6.16}$$

$$\begin{aligned} L_{ij}^{ref} &= \rho^{ref}\omega^2\delta_{ij} + \frac{\partial}{\partial x_k}\left(c_{iklj}^{ref} \frac{\partial}{\partial x_l} \right) \\ L_{ij}^{p} &= \rho^{p}\omega^2\delta_{ij} + \frac{\partial}{\partial x_k}\left(c_{iklj}^{p} \frac{\partial}{\partial x_l} \right) \end{aligned} \tag{6.17}$$

Equation (6.16) shows that the full solution is equivalent to the wave-field generated in the reference medium by an effective force that is given by the right-hand side of the lower equation. The Green's function in the reference medium and the effective force can then be used in (6.14) to give the volume integral equation for elastic waves

$$\begin{aligned} u_i(\mathbf{r}) &= \int_V G_{in}^{ref}(\mathbf{r},\mathbf{r}')\, f_n(\mathbf{r}')\, dV' + \int_V G_{in}^{ref}(\mathbf{r},\mathbf{r}') L_{nj}^{p}(\mathbf{r}')\, u_j(\mathbf{r}')\, dV' \\ &+ \int_S \left[G_{in}^{ref}(\mathbf{r},\mathbf{r}') n_j c_{njkl}^{ref} \frac{\partial}{\partial x_k'} u_l(\mathbf{r}') - u_n(\mathbf{r}') n_j c_{njkl}^{ref} \frac{\partial}{\partial x_k'} G_{il}(\mathbf{r},\mathbf{r}') \right] dS' \end{aligned} \tag{6.18}$$

In developing equation (6.14) the Green's function in the reference medium was assumed to satisfy homogeneous boundary conditions. This can happen when the Green's function, the associated traction, or both vanish at the bounding surface. The least restrictive condition is that the traction must vanish at the boundary, which will be assumed here, and the volume integral equation can then be reformulated as

$$\begin{aligned} u_i(\mathbf{r}) = u_i^{ref}(\mathbf{r}) + \omega^2 \int_V G_{in}^{ref}(\mathbf{r},\mathbf{r}')\rho^p(\mathbf{r}')u_j(\mathbf{r}')\,dV' \\ - \int_V \frac{\partial}{\partial x_k'} G_{in}^{ref}(\mathbf{r},\mathbf{r}')c_{nkli}^p(\mathbf{r}')\frac{\partial}{\partial x_l'}u_j(\mathbf{r}')\,dV' \end{aligned} \tag{6.19}$$

6.3 TENSOR GREEN'S FUNCTION

The decomposition of the medium in (6.15) is completely arbitrary; however the reference medium should be chosen to make the problem easier to solve. A homogeneous, isotropic reference medium will be used in the volume integral equation to compute the elastic wave-field and is given as

$$\begin{aligned} G_{pq} = (C_{NF}^{\alpha} + C_{IF}^{\alpha})\left(\frac{3x_p x_q}{\left(|\mathbf{r}-\mathbf{r}'|\right)^2} - \delta_{pq}\right) + C_{FF}^{\alpha}\left(\frac{x_p x_q}{\left(|\mathbf{r}-\mathbf{r}'|\right)^2}\right) \\ - (C_{NF}^{\beta} + C_{IF}^{\beta})\left(\frac{3x_p x_q}{\left(|\mathbf{r}-\mathbf{r}'|\right)^2} - \delta_{pq}\right) - C_{FF}^{\beta}\left(\frac{x_p x_q}{\left(|\mathbf{r}-\mathbf{r}'|\right)^2} - \delta_{pq}\right) \end{aligned} \tag{6.20}$$

$$x_p = \left(r_p - r_p'\right);\ p,q = 1,\ 2,\ or\ 3(x,\ y,\ or\ z)$$

$$C_{NF}^{v} = \frac{-1}{4\pi\rho v^2 \kappa_v}\left[\frac{1}{\kappa_v\,|\mathbf{r}-\mathbf{r}'|^3}\right]e^{-i\kappa_v|\mathbf{r}-\mathbf{r}'|}$$

$$C_{IF}^{v} = \frac{-1}{4\pi\rho v^2 \kappa_v}\left[\frac{-1}{i\,|\mathbf{r}-\mathbf{r}'|^2}\right]e^{-i\kappa_v|\mathbf{r}-\mathbf{r}'|} \tag{6.21}$$

$$C_{FF}^{v} = \frac{-1}{4\pi\rho v^2 \kappa_v}\left[\frac{-\kappa_v}{|\mathbf{r}-\mathbf{r}'|}\right]e^{-i\kappa_v|\mathbf{r}-\mathbf{r}'|}$$

$$
\begin{aligned}
&\nu = \alpha, \beta \\
&\kappa_\alpha = \frac{\omega}{\alpha}; \quad \kappa_\beta = \frac{\omega}{\beta} \\
&\alpha = \left[\frac{\lambda + 2\mu}{\rho} \right]^{\frac{1}{2}} \\
&\beta = \left[\frac{\mu}{\rho} \right]^{\frac{1}{2}}
\end{aligned}
\tag{6.22}
$$

Several properties of the wave-field can be identified from the tensor Green's function. First, the type of motion can be determined from the polarization of the wave and is expressed in the vectorial factors containing $x_i x_j$. The Green's function gives the wave-field corresponding to a point force in the j^{th} direction therefore x_j is fixed and the product $x_i x_j$ is simply a multiple of x_i (Pujol 2003). This expression then corresponds to motion along the direction from the source to the receiver (P-wave motion) and occurs alone in the second term of equation (6.20) associated with the far-field component with velocity α. The factor $x_i x_j/|r\text{-}r'|^2\text{-}\delta_{ij}$ (S-wave motion) found in the fourth term with velocity β, corresponds to motion perpendicular to $x_i x_j$, and can be determined by taking their scalar product which is equal to zero. The final factor $(3x_i x_j/|r\text{-}r'|^2\text{-}\delta_{ij})$ that occurs in the first and third terms, is actually a combination of P-wave and S-wave motion and illustrates that the near- and intermediate-field motion is more complex than in the far-field.

Next, by comparing (6.20) and (4.20) it is clear that the elastodynamic Green's function is quite similar to the electromagnetic case. In fact, the terms with velocity β have precisely the same form as the EM Green's function. Finally, like the EM case, the Green's function only depends on the relative source and receiver locations and when discretized results in circulant matrices. This can be exploited in a similar fashion as for the EM problem to efficiently solve the volume integral equation for elastic waves.

6.4 Acoustic Wave Equation

Simplifications to the more general elastic case occur when the medium is a non-viscous fluid and results in acoustic waves. In this case, shear stresses (off-diagonal components) are

zero and the remaining stress is isotropic. It is convenient then to use the scalar valued pressure field P which is related to the stress tensor by

$$\tau_{ij} = -P\delta_{ij} \tag{6.23}$$

In a fluid, the pressure is proportional to the relative change in the volume of a fluid element which is equivalent to the divergence of the displacement at that location

$$P = -\kappa \nabla \cdot \mathbf{u} = -\kappa \sum_i \frac{\partial u_i}{\partial x_i} \tag{6.24}$$

Substituting equations (6.23) and (6.24) into the equations of motion and taking the divergence gives

$$\frac{1}{\kappa}\frac{\partial^2 P}{\partial t^2} = \sum_i \frac{\partial}{\partial x_i}\left(\frac{1}{\rho}\frac{\partial P}{\partial x_i}\right) - \sum_i \frac{\partial}{\partial x_i}\left(\frac{f_i}{\rho}\right) \tag{6.25}$$

In a medium where the density gradients are everywhere much smaller than the density itself, the derivative terms on the right-hand side of the equation of motion simplify and (6.25) can be written as the scalar wave equation with velocity $c=\sqrt{\kappa/\rho}$

$$\begin{aligned} &\nabla^2 P + \frac{\omega^2}{c^2} P = h \\ &h = \nabla \cdot f \end{aligned} \tag{6.26}$$

To develop the volume integral equation for acoustic wave propagation, the medium will be decomposed into a homogeneous reference and a medium perturbation similar to the EM and elastic cases. Rather than using the velocity directly, the medium will be specified using the inverse of velocity or slowness, s = 1/c. The integral equation solution is then given in the frequency-domain as

$$P(\mathbf{r},\omega) = P^{ref}(\mathbf{r},\omega) + \int_V g_0(\mathbf{r},\mathbf{r}',\omega)\delta s(\mathbf{r}',\omega)P(\mathbf{r}',\omega)dV' \tag{6.27}$$

$$P^{ref}(\mathbf{r},\omega) = \int_V g_0(\mathbf{r},\mathbf{r}',\omega)\delta s(\mathbf{r}',\omega)dV' \tag{6.28}$$

$$s(\mathbf{r},\omega) = s_0(\mathbf{r},\omega) + \delta s(\mathbf{r},\omega)$$

$$g_0(\mathbf{r},\mathbf{r}',\omega)=\frac{1}{4\pi}\left[\frac{e^{-i\omega s_0|\mathbf{r}-\mathbf{r}'|}}{|\mathbf{r}-\mathbf{r}'|}\right]$$

Like the EM and elastic cases, after discretization the acoustic Green's function matrix is circulant and can be incorporated into a fast FFT based solution method. One important difference is that unlike the EM and elastic problems that have tensor Green's functions and block circulant matrices, the acoustic Green's function is scalar valued producing a simple circulant matrix that can be rapidly inverted. The result is that given both the observed pressure field and the simulated pressure field in the reference medium, equation (6.27) can be rapidly inverted to estimate the medium perturbation. As discussed in chapter 2, rather than requiring $O((MN)^3)$ to determine the inverse using a direct method, the inverse of a simple circulant matrix can be obtained in O(M*NlogN) where N is the number of grid cells and M the number of source locations used in the inversion.

$$\mathbf{p}=\mathbf{p}^{ref}+\mathbf{G}_0\mathbf{S}\mathbf{p} \tag{6.29}$$

$$\mathbf{S}=\begin{pmatrix} diag(\delta\mathbf{s}) & 0 & 0 & \cdots & 0 \\ 0 & diag(\delta\mathbf{s}) & 0 & \cdots & 0 \\ 0 & 0 & diag(\delta\mathbf{s}) & \cdots & 0 \\ \vdots & \vdots & \vdots & \ddots & \vdots \\ 0 & 0 & 0 & \cdots & diag(\delta\mathbf{s}) \end{pmatrix}$$

$$\mathbf{p}=\begin{pmatrix} \mathbf{p}_1 \\ \mathbf{p}_2 \\ \mathbf{p}_3 \\ \vdots \\ \mathbf{p}_M \end{pmatrix}; \qquad \mathbf{p}^{ref}=\begin{pmatrix} \mathbf{p}_1^{ref} \\ \mathbf{p}_2^{ref} \\ \mathbf{p}_3^{ref} \\ \vdots \\ \mathbf{p}_M^{ref} \end{pmatrix}$$

Equation (6.29) can also be written as

$$\mathbf{p}=\mathbf{p}^{ref}+\mathbf{G}_0\mathbf{P}\mathbf{s} \tag{6.30}$$

$$\mathbf{P} = \begin{pmatrix} diag(\mathbf{p}_1) & 0 & 0 & \cdots & 0 \\ 0 & diag(\mathbf{p}_2) & 0 & \cdots & 0 \\ 0 & 0 & diag(\mathbf{p}_3) & \cdots & 0 \\ \vdots & \vdots & \vdots & \ddots & \vdots \\ 0 & 0 & 0 & \cdots & diag(\mathbf{p}_M) \end{pmatrix}$$

$$\mathbf{s} = \begin{pmatrix} \delta\mathbf{s} \\ \delta\mathbf{s} \\ \delta\mathbf{s} \\ \vdots \\ \delta\mathbf{s} \end{pmatrix} = \begin{pmatrix} \mathbf{I} \\ \mathbf{I} \\ \mathbf{I} \\ \vdots \\ \mathbf{I} \end{pmatrix} \cdot \delta\mathbf{s} = \mathbf{I}_M \cdot \delta\mathbf{s} \tag{6.31}$$

The inverse solution to the acoustic volume integral equation for the slowness perturbation can be determined from

$$\delta\mathbf{s} = \mathbf{I}_M^{-1}\mathbf{P}^{-1}\mathbf{G}_0^{-1}\delta\mathbf{p} \tag{6.32}$$

$$\delta\mathbf{p} = \begin{pmatrix} \mathbf{p}_1 \\ \mathbf{p}_2 \\ \mathbf{p}_3 \\ \vdots \\ \mathbf{p}_M \end{pmatrix} - \begin{pmatrix} \mathbf{p}_1^{ref} \\ \mathbf{p}_2^{ref} \\ \mathbf{p}_3^{ref} \\ \vdots \\ \mathbf{p}_M^{ref} \end{pmatrix}$$

All of the quantities in equation (6.32) can be efficiently calculated to produce the inverse solution. **P** is a diagonal matrix whose elements are the modeled wave field in the reference medium, $\mathbf{I_M}$ has a simple left inverse and matrix $\mathbf{G_0}$ is simple circulant. In this case the pseudo-inverse and SVD can be rapidly computed using the FFT providing a means to compute the inverse solution in O(M*NlogN) operations. Regularization can be performed by truncation of the singular values obtained from the SVD of the Green's function matrix.

It should be noted that the background medium in equation (6.32) was chosen to be the same as that used for the Green's function. When the background medium used to model the wavefield is different from the Green's function medium (as would occur in a non-linear iterative inversion approach), the equation must be modified following equation (2.105) with an additional term

containing the difference in slowness between the reference medium and the medium used for the Green's function, $\mathbf{S}^{\text{ref}}$

$$\delta\mathbf{s} = \mathbf{I}_M^{-1}\mathbf{P}^{-1}\left(\mathbf{G}_0^{-1} + \mathbf{S}^{ref}\right)\delta\mathbf{p} \tag{6.33}$$

7 CONCLUSIONS AND OUTLOOK

Full waveform inverse methods have the potential to overcome the limitations inherent to ray theoretical methods. A 3D frequency domain full waveform inversion (FDFWI) has been developed and demonstrated on synthetic data. The FDFWI method has been shown to provide high resolution images compared to ray theoretic methods. Due to the high computational requirements, application of the FDFWI method to 3D field applications will require parallelization of the present code. The method requires one forward simulation for each transmitter and three simulations for each receiver included in the dataset. Each of the forward simulations can be performed in parallel to reduce the time required to complete each iteration. Implementation in the frequency domain provides additional parallelization since the forward simulations for individual frequencies can also be performed in parallel. Source parameters are also expected to have a major impact on the results of the inversion. Here point source transmitters were used; however, for realistic applications 3D finite source antenna characteristics should be included. The source wavelet can influence the received signals and should also be characterized and implemented as part of the inversion. The various improvements to the current FDFWI method are planned in the near future with the hope that full waveform inversion of real-world datasets will routinely provide high resolution imaging of the subsurface.

APPENDIX SUMMARY

Appendix A and B have been included to illustrate the application of ray based methods to near-surface characterization and monitoring. The usefulness of georadar techniques for determining subsurface structures and monitoring changes in fluid contents over time are demonstrated and illustrates the utility and limitations of ray based inversion. Primary funding for the research in this dissertation was provided by the U.S. Department of Energy, Office of Groundwater and Soil Remediation, Richland Operations Office, and the Pacific Northwest National Laboratory associated with the projects described in the Appendices.

APPENDIX A

A. MONITORING VADOSE ZONE DESICCATION WITH GEOPHYSICAL METHODS

M.J. Truex, T.C. Johnson, **C.E. Strickland**, J.E. Petersen, and S.S. Hubbard
Published in: Vadose Zone Journal, **12(**2**)**, 2013, doi:10.2136/vzj2012.0147

Summary

Soil desiccation was recently field tested as a potential vadose zone (unsaturated zone) remediation technology. Desiccation removes water from the vadose zone and significantly decreases the aqueous-phase permeability of the desiccated zone, thereby decreasing movement of moisture and contaminants. The 2-D and 3-D distribution of moisture content reduction over time provides valuable information for desiccation operations and for determining when treatment goals have been reached. This type of information can be obtained through use of geophysical methods. Neutron moisture logging, cross-hole electrical resistivity tomography, and cross-hole ground penetrating radar approaches were evaluated with respect to their ability to provide effective spatial and temporal monitoring of desiccation during a treatability study conducted in the vadose zone of the DOE Hanford Site in WA.

A.1 INTRODUCTION

In situ remediation is a potential approach to address contaminants located in the vadose zone at depths below the limit of direct exposure where remediation is focused on protection of groundwater (Dresel et al. 2011). Although a vast body of research has been performed to investigate in-situ remediation of groundwater systems, significantly fewer studies have been dedicated to remediation of contaminated vadose zone regions. Concurrent with development of remediation approaches, successful vadose zone remediation will also require effective methods of remedy performance monitoring. In 2008, the Department of Energy (DOE) initiated a treatability test program to evaluate the potential of several deep vadose zone remedies for protection of groundwater (DOE 2008) with assessment of approaches that mitigate the transport of inorganic and radionuclide contaminants from the vadose zone to the groundwater. Soil desiccation was investigated as a potential vadose zone remediation technology, including laboratory studies (Ward et al. 2008; Oostrom et al. 2009 2012a,b; Truex et al. 2011), modeling studies (Ward et al. 2008; Truex et al. 2011), and field testing (Truex et al. 2012a, b) conducted as part of the treatability test efforts at the DOE Hanford Site.

Desiccation of a portion of the vadose zone, in conjunction with a surface infiltration barrier, has the potential of minimizing migration of deep vadose zone contaminants towards the water table (Truex et al. 2011). To apply desiccation, a dry gas is injected into the subsurface. The dry gas evaporates water from the porous medium until the gas reaches 100% relative humidity and can no longer evaporate water. Evaporation can remove pore water and result in very low moisture content in the desiccated zone (Ward et al. 2008; Oostrom et al. 2009; Truex et al. 2011). The desiccation process removes previously disposed and native water from the vadose zone and significantly decreases the water relative permeability of the desiccated zone. Due to these desiccation-induced changes, the future rate of movement of moisture and contaminants through this zone is decreased.

The performance of desiccation in terms of mitigating future moisture movement is related to the extent of moisture content reduction and the location and thickness of the desiccated zone (Truex et al. 2011, 2012a, b). Reducing the moisture content below the residual moisture content value for the sediment is a target for desiccation because the of the low resulting water relative permeability (Truex et al. 2012a, b). Information about the distribution of moisture content

reduction over time is needed for performance monitoring during desiccation implementation. These data are important for determining when desiccation has met treatment goals and thus when the process can be stopped. Monitoring data can also be used to guide operational decisions, such as adjustments in system flow rates and injection gas properties. While nominal values for these injection parameters can be selected based on initial site characterization data, the impact of subsurface heterogeneities cannot be fully predicted. As such, monitoring is needed to assess the impact of these heterogeneities on desiccation performance. The objective of this study was to evaluate the effectiveness of several different technologies for monitoring desiccation under field conditions. Several geophysical approaches were tested for monitoring desiccation-induced changes in moisture and temperature at the Hanford Site desiccation field test, including neutron moisture logging, temperature logging, cross-hole ground-penetrating radar and cross-hole electrical resistivity tomography.

Geophysical methods have been used extensively in the last decade to characterize and monitor subsurface hydrological processes (e.g., Rubin and Hubbard, 2005; Vereecken et al., 2006). Because geophysical data can be collected from many different platforms (e.g., from satellites and aircraft, at the ground surface of the earth, and at or between wellbores), the geophysical data can provide remote subsurface characterization or monitoring information over a variety of spatial scales and resolutions. The main advantage of using geophysical data over conventional measurements is that geophysical methods can provide spatially extensive information about the subsurface in a minimally invasive manner at a comparatively high resolution. The greatest disadvantage is that the geophysical methods only provide indirect proxy information about subsurface hydrological properties or processes.

Soil moisture content determination in the vicinity of a wellbore using neutron scattering probes has become a standard method over the past several decades (Hignett and Evett 2002). A neutron probe consists of a high energy neutron source, a low energy or thermal neutron detector, and the electronics required for counting and storing the measured response. A fast neutron source manually placed within moist soil develops a dense cloud of thermal neutrons around it and a thermal neutron detector placed near the source samples the density of the generated cloud. The concentration of thermalized neutrons is affected by both soil density and elemental composition. Elements that absorb neutrons are often in low concentration in the soil solid phase and when clay content is also low, the neutron probe response is mainly affected by

changes in moisture content (Greacen et al. 1981; Hignett and Evett 2002). Neutron moisture logging data can typically be collected with high vertical resolution and can be converted to volumetric moisture content (VMC) using published or site-specific relationships. Interpolation of neutron moisture logging data between multiple measurement wellbores can be used to generate an estimated 2-D or 3-D moisture content distribution.

Ground Penetrating Radar (GPR) methods are also commonly used to characterize or monitor subsurface moisture content. GPR methods use electromagnetic energy at frequencies of ~10 MHz to 1GHz to probe the subsurface. At these frequencies, the dielectric polarization within a material that has been subjected to an external electric field dominates the electrical response. GPR systems consist of an impulse generator which repeatedly sends a particular voltage and frequency signal to a transmitting antenna. Cross-hole GPR methods involve lowering a transmitter into a wellbore and measuring the vertical electric field with a receiving antenna that is lowered down another wellbore. The transmitting and receiving antennas are manually relocated to different positions in the wellbores to facilitate transmission of the energy through a large fraction of the area between the measurement boreholes.

Together, the electrical properties of the host material and the frequency of the GPR signal primarily control the sampling volume and the depth of penetration of the signal. The electromagnetic velocity (V) is dependent on the permittivity (ε), conductivity (σ), frequency (ω) and magnetic permittivity (μ, assumed to be equal to free space) of the subsurface material through which the signal travels as:

$$V = \left\{ \frac{\mu\varepsilon}{2} \left[\sqrt{1 + \left(\frac{\sigma}{\omega\varepsilon} \right)^2} + 1 \right] \right\}^{-\frac{1}{2}} \qquad \text{(A.1)}$$

The loss tangent is a useful metric for determining low-loss conditions and is defined as the electrical conductivity divided by the product of the dielectric permittivity and the angular frequency. In general, GPR performs better in low-loss environments, such as unsaturated coarse or moderately coarse textured soils. GPR signal strength is strongly attenuated in electrically conductive environments (such as systems dominated by the presence of clays or high ionic strength pore fluids). When low-loss conditions prevail, the velocity depends primarily on the permittivity, which can be expressed as (Davis and Annan, 1989):

$$\varepsilon \approx \left(\frac{c}{v}\right)^2 \tag{A.2}$$

where c is the propagation velocity of electromagnetic waves in free space. The velocity of the GPR signal can be obtained by measuring the travel time of the signal over a known distance between the transmitter and the receiver. Using measurements acquired from antennae located at many different vertical positions within each borehole and inversion algorithms, a 2-D image of GPR velocity between boreholes can be produced through tomographic inversion (e.g., Jackson and Tweeton 1994; Peterson, 2001) and used with (2) to estimate the 2D permittivity distribution.

Soil dielectric permittivity is strongly dependent on moisture content because of the large difference between water and bulk soil permittivity. The relative permittivity (the dielectric permittivity of a material divided by the free space permittivity, ε_0) of water is approximately 80, compared to values between 3 and 7 for typical soil mineral components. As such, under low-loss and unsaturated conditions, GPR velocity is primarily influenced by moisture variability and secondarily by texture, although texture can influence moisture dynamics and thus the effective GPR response (Grote et al., 2010). Studies have demonstrated that GPR methods can effectively estimate and monitor subsurface moisture content using measured electromagnetic velocities (Hubbard et. al. 1997; Van Overmeeren et al. 1997; Huisman et al. 2001; Binley et.al 2002; Day-Lewis et al. 2002; Laloy et al. 2012). The dielectric permittivity of soils and sediments also depends on temperature (Or and Wraith, 1999). However, for this paper we considered temperature effects to be negligible based on laboratory core permittivity measurements made over the temperature range of this experiment, which varied between $-0.4\varepsilon_0$ to $0.3\varepsilon_0$ (not shown) corresponding to estimated VMC errors of less than $0.01 m^3/m^3$.

Several different petrophysical relationships have been used to translate permittivity into moisture content estimates (Huisman et al., 2001). An example is shown in Equation 7.3, where volumetric moisture content, θ, is a linear function of the square root of the soil apparent dielectric permittivity, ε_a (Ledieu et al. 1986; White et al. 1995; Topp and Ferré 2002):

$$\theta = A\sqrt{\varepsilon_a} + B \tag{A.3}$$

where A and B are fitted parameters. In this study, we use the coefficients determined by Topp and Reynolds (1998) of A=0.115and B=-0.176. The term apparent is used here to mean the dielectric permittivity value that is inferred from measurement of the velocity of an electromagnetic wave at a given frequency. In this study, water content values obtained using Equation (7.3) deviated from those derived using the polynomial Topp's equation (Topp et al, 1980; Topp and Ferré 2002) by less than $0.01 m^3\ m^{-3}$. General guidelines for GPR acquisition, processing and water content estimation are provided by Annan (2005) and Huisman et al (2001).

Electrical Resistivity Tomography (ERT) is a method of remotely imaging the electrical conductivity (C or σ) of the subsurface that has been commonly used to monitor subsurface moisture variations (e.g., Binley and Kemna, 2005; Revil et al. 2012). For cross-hole ERT applications, electrodes installed within boreholes are used to strategically inject currents and measure the resulting potentials to produce a data set that is used to reconstruct the subsurface C structure (Daily and Owen, 1991; Johnson et al., 2010). In unsaturated sediments, C can be influenced by clay content, granulometric properties, salinity, and temperature (Lesmes and Friedman, 2005) , although moisture content (Slater and Lesmes, 2002) often dominates the response. Thus, temporal changes in moisture content during desiccation can be monitored by imaging corresponding changes in C using ERT. General guidelines associated with ERT acquisition, inversion, and interpretations are provided by Binley and Kemna (2005).

In granular materials with a non-conductive solid phase, the bulk can be described according to (Revil et al., 2012),

$$C = \sigma_f \varnothing^m S_w^n + \varnothing^m S_w^{n-1} \beta_{(+)} \bar{Q}_V \qquad \text{(A.4)}$$

where σ_f is the fluid conductivity, ϕ is the porosity, S_w, is the water saturation, m is the cementation exponent, and n is the water saturation exponent. $\beta_{(+)}$ represents the mobility of the cations in the pore water, and $\bar{Q}_V$ is the charge per unit pore volume of the diffuse part of the electrical double layer. The first term of equation 7.4 is describes the component of C arising from ionic current flow within the pore water (Archie, 1942). The second term of equation 7.4 describes the component of C arising from current flow along the pore-grain interface within the electrical double layer; the so-called surface conductivity. In clean, low-clay sand with relatively small surface area, C is dominated by the first term in equation 7.4. The Hanford Formation,

where our experiment was conducted, is comprised of high energy flood deposits, consisting of coarse gravels and sands with interbedded fine sands and silt-sized materials (Brown, 1960). We assume, therefore, that the second term of equation 7.4 is insignificant, and consider only the first term of equation 7.1 (e.g. Archie's Law). Although we have no direct information supporting the validity of Archie's Law, as will be subsequently demonstrated, the comparison between changes in water content derived from C and actual changes in water content measured by neutron probe, which rely on Archie's Law, are favorable, suggesting that our assumption is reasonable. In addition to the Archie's Law assumption, the relationship between temporal changes in water saturation and the corresponding changes in C that occur during subsurface desiccation can be simplified under the following assumptions:

ϕ and *m* are constant in time. These parameters are dependent on the textural properties of the sediment and this assumption may be appropriate for many sites.

σ_f is constant in time. This assumption is not strictly valid because ionic concentrations increase as pore water is evaporated during desiccation, but may be appropriate for many sites. This assumption was validated with core-scale measurements in this case (data not shown), and also with comparison neutron probe measurements of changes in water content.

n is independent of saturation. This assumption may be appropriate for many sites, although at low water saturation values (< ~ 5%) *n* has been observed to decrease with decreasing water saturation (Waxman and Smits, 1968; Han et. al. 2009; Hamammoto et al. 2010).

If the assumptions stated above are valid, a desiccation-induced change in water saturation can be derived from equation 7.4 in terms of the corresponding change in bulk C as

$$\frac{S_t}{S_0} = 10^{\frac{1}{n} log_{10}\left(\frac{C_t}{C_0}\right)} \qquad \text{(A.5)}$$

where S_t is the water saturation at time *t*, S_0 is the pre-desiccation baseline water saturation, and C_t and C_0 are the corresponding bulk conductivity at time *t* and pre-desiccation. As we will show, errors arising from the assumptions leading to equation 7.5 exist, but are not so large as to invalidate ERT derived changes in saturation expressed through the saturation ratio. It is important to note that the same assumptions may not fare as well at other sites. Note also that the ratios of VMC and water saturation are equivalent. Because desiccation is a non-isothermal process, the effects of temperature on bulk conductivity must also be considered. The

temperature dependence of bulk conductivity in the vadose zone is dependent on moisture content, but is always monotonic (Waxman and Thomas, 1974).

Temperature sensors can also provide a means to monitor the progress and distribution of desiccation using a network of in situ sensors. Temperature decreases due to evaporative cooling until the desiccation front reaches the monitoring locations (i.e., the time when the sediment between the injection location and the monitoring location is desiccated). At that time, the temperature at the monitoring location begins to increase toward the temperature of the injected gas because evaporative cooling is no longer occurring in the sediment between the injection location and the monitoring location (Oostrom et al. 2009). There can be multiple inflection points if there are multiple layers that are being desiccated at different rates and these layers are within a region that can impact the temperature at the monitoring location.

This paper presents an assessment of selected geophysical monitoring approaches applied before and during the desiccation field test at the Hanford Site. The methods were evaluated with respect to their ability to provide effective spatial and temporal monitoring of desiccation. Benefits and limitations of the methods were considered based on the characteristics of the data collection and analysis techniques.

A.2 Geophysical Monitoring of a Field Desiccation Experiment

A.2.1 Field Test Summary

The desiccation field test was conducted in the vadose zone at the U.S. DOE Hanford Site 200-BC-1 Operable Unit as described by Truex et al. (2012a, b) and summarized below. The total thickness of the vadose zone beneath the 200-BC-1 Operable Unit is about 100 m. About 110 million liters of aqueous waste containing high concentrations of solutes was disposed at multiple engineered cribs and trenches, primarily in the 1950s. Figure 1 shows the pre-desiccation characterization data for vertical stratigraphy, C (corresponding to the contaminant distribution), and moisture distribution at the test site injection and extraction wells in relation to the well screen interval. The test was conducted within the Hanford Formation, and porous media grain-size variations in the test interval range from sand to loamy sand (which is similar to the porous media observed throughout the full depth interval). The injection well is located

between adjacent waste disposal cribs where the subsurface was impacted by lateral movement of crib discharges.

A dipole configuration was used for the field test with injection of dry nitrogen gas and extraction of soil gas through wells screened in a target depth interval from 9.1 to 15.2 m below ground surface (bgs) to favor soil gas flow within this interval and within a defined monitoring zone. The general operational and in situ monitoring strategy is depicted in Figure 2. Use of dry nitrogen gas at a controlled temperature of 20^{o}C provided a constant inlet condition with a relative humidity of zero. Injection occurred at a stable flow rate of 510 m^3/h from January 17, 2011 through June 30, 2011 (164 days) except during a 13-day interval from April 21 through May 4, 2011 when there was no injection. Extraction of soil gas was maintained for the full test duration at a stable flow rate of 170 m^3/h. The injection and extraction wells were 12-m apart. Figure 3 depicts the lateral layout of injection and extraction wells and the monitoring locations. A 30 m by 45 m gas-impermeable membrane barrier was installed at the surface centered over the well network to inhibit soil gas flow at the ground surface.

A clustered monitoring approach was used in the test whereby a sensor borehole, containing sensors for temperature and ERT electrodes, was placed nominally adjacent to a cased, unscreened logging well used to conduct manual neutron moisture logging and to acquire cross-hole GPR data. Sensor boreholes (21.3 m total depth) were constructed with alternating 0.76-m-thick zones of 100-mesh (> 0.125 and < 0.149 mm) Colorado sand (Colorado Silica, Colorado Springs, CO) and granular bentonite from 3 to 21.3 m bgs. ERT electrodes were placed within the bentonite zones (e.g., every 1.5 m) with tubing installed to enable addition of water around each electrode to locally hydrate the bentonite and maintain effective coupling between the electrode and the subsurface. Electrical connectivity was checked periodically during the test and water added when necessary to improve electrical coupling where a threshold of 10mA injected current was used to indicate suitable electrode coupling. Sensor boreholes also contained thermistors every 0.6 m from 3 to 21.3 m bgs. Logging wells extended to 21.3 m bgs with a 2-inch PVC casing (plugged at the bottom) in a 4-inch diameter borehole and 100-mesh Colorado sand in the annular space.

A.2.2 Neutron Moisture Logging

Neutron moisture logging was conducted using a CPN 503DR Hydroprobe (InstroTek Inc., Raleigh, NC). Neutron probe measurements were acquired at depth increments of approximately 7.5 cm using a count time of 30 s and then converted to count ratio (C_R) by dividing each measurement by the standard count.

Neutron probe data were converted to VMC using a site specific relationship described by Truex et al. (2012a) and summarized below. Sediment samples were collected laterally within 0.9 m of the neutron logging well L2 (6 to18 m bgs) after the active desiccation phase of the test and sediment texture ranged from medium sand to loamy sand with the exception of one sample of sandy silt. Although clay content can also affect moisture content calibration (Greacen et al. 1981), the clay content was low at the desiccation field site, ranging between 2.4% and 8%.

Samples were grouped into sand and loamy sand texture materials. Neutron moisture probe C_R data were plotted with corresponding post-desiccation laboratory-measured VMC (computed using measured gravimetric moisture content and bulk density) from samples at the same depth. Using only samples with VMC values greater than 0.05 m^3 m^{-3}, a linear calibration relationship was observed for both sand and loamy sand. Post-desiccation VMC for some of the very dry core samples within the highly desiccated zones (loamy sand and sand textures) were 0.004 +/- 0.002 m^3 m^{-3} from laboratory gravimetric analyses, with corresponding count ratios of 0.21 +/- 0.007. For the loamy sand, using the linear relationship based on only samples above 0.05 m^3 m^{-3} would predict a count ratio of 0.34 for a moisture content of 0.004 m^3 m^{-3}, substantially different from the actual observations. Linear relationships over the full range of data could be applied but provide a poor fit to the data. For this study, a non-linear neutron probe calibration relationship captures the response for both soil types and provides a better fit to the data over the full range (Figure 4). Regression of VMC (θ) and C_R data for all core samples resulted in the relationship $\theta = 0.714C_R^2 - 0.1363C_R$, with a root mean square error of 0.015 for θ and a coefficient of determination of 0.93.

VMC values from pre-desiccation and post-desiccation neutron logging events were interpolated to a finely spaced grid encompassing the logging wells using a weighted inverse-distance interpolation scheme. Due to the high vertical resolution of the data along the logging wells, the corresponding low lateral resolution, and the expected high lateral correlation in

moisture content, we chose a 5 to 1 horizontal to vertical weighting in the interpolation. This interpolation provides a smoothed 3D estimate of VMC distribution.

A.2.3 Ground Penetrating Radar

GPR data were collected with a PulseEKKO 100 using 100 MHz borehole antennas (Sensors and Software, Inc. Missasauga, ON, Canada). Multiple offset gather surveys (Peterson, 2001) were periodically collected between logging well pairs using a vertical offset increment of 0.25 m and an angular coverage of approximately 40 degrees above and below the midpoint of each gather. Wellbore deviation logs were applied to more accurately determine the antenna positions used in the surveys. Borehole pair separation was roughly 3 m and the primary transect was along the plane between the injection and extraction wells (Figure 3). The first arrival times of the energy were picked from the data, and were inverted using MIGRATOM, a curved ray inversion software (Jackson and Tweeton 1994), to yield 2-D electromagnetic velocity estimates along key transects. The data were inverted with no vertical to horizontal anisotropy and using global minimum and maximum velocity constraints of 0 and 0.25 m/ns respectively. The results from each of the inversions produced travel time residual errors less than 1.9 ns. The velocity estimates were converted to dielectric permittivity using Equation 7.2 (i.e., by assuming low-loss conditions). Equation 7.3 was used to convert GPR-derived permittivity to VMC content.

At the desiccation site, the C ranges up to 0.330 S/m and the low-loss assumption underlying Equation (7.2) is not valid at all locations. Low-loss conditions are valid when the loss-tangent is much less than one. For instance, assuming a dielectric permittivity of 10 and a frequency of 100 MHz, the loss tangent will be less than one for C values less than 0.05 S/m. Prior to desiccation, ERT-derived C were less than 0.05 S/m at depths shallower than 10 m. A comparison of baseline near-borehole VMC estimates from GPR (derived using equations 7.2 and 7.3) to those obtained from neutron moisture logging indicate a good correlation for depths less than 10 m where C is less than 0.05 S/m. This comparison is shown in Figure 5 for borehole L3 and was similar for the other boreholes at the desiccation test site. At depths greater than 10m, the C was higher than the low-loss assumption cutoff and the linear relationship between VMC estimated from neutron moisture logging and GPR was degraded. Interpretation of GPR data for conditions with higher conductivity will be impacted by violation of the low-loss assumption which can change during the desiccation process as discussed in the next section.

A.2.4 Electrical Resistivity Tomography

ERT data were collected prior to and during desiccation using 99 electrodes; 11 electrodes equally spaced from 6.25 m to 21.5 m deep in each of the 9 sensor wells. Measurements were collected using an 8-channel MPT DAS-1 impedance tomography system (www.mpt3d.com). Full forward and reciprocal measurements were collected twice per day in order to estimate data noise and quality, and each data set contained 6114 measurements after filtering. The data were collected and inverted in 3D with isotropic (i.e. equal weighting in all directions) first order spatial derivative smoothing constraints on an unstructured tetrahedral mesh with 354,544 elements. The parallel ERT inversion software described by Johnson et al. (2010) was used to invert each data set with 100 processors on parallel computing resources housed at the Pacific Northwest National Laboratory. Elements were refined around electrodes and within the imaging region in order to optimize simulation accuracy and available resolution. Each data set was individually inverted (i.e. no constraints were applied in the time-dimension) and equation 7.5 was used to compute the saturation ratio for each element at each ERT survey time.

Core-scale testing on site sediments showed the C response to be primarily governed by decreases in water saturation as opposed to increases in fluid conductivity during desiccation, validating the assumption that fluid conductivity (σ_f) may be considered constant in time (data not shown). In addition, laboratory testing on site sediments showed *n* to be ~2.0 within the saturation range indicated by neutron moisture logging data during the desiccation test and a constant value of 2.0 was used in equation 7.5. The ERT images were also corrected for temperature prior to applying equation 7.5. Laboratory testing on Hanford site sediments showed a temperature dependence of 0.00017 S/mC° at 5% VMC and 0.00023 S/mC° at 12% VMC, consistent with published values (Friedman et al. 2005; Ruijin et al. 2010). A constant value of 0.00020 S/mC° was assumed for the temperature dependence and used to correct all C results to a temperature of 20 C° based on the interpolated temperature field.

In order for a sequence of time-lapse ERT inversions to be comparable, each inverted data set must contain the same survey configuration and the same number of measurements. This requirement is problematic when data quality degrades over the course of the monitoring period. At the desiccation site, electrodes were installed within a plug of bentonite in order to facilitate electrical coupling with the host material. Some electrodes within the desiccation zone became poorly coupled to host material upon drying, likely due to bentonite shrinkage and cracking.

Measurements using these electrodes had to be removed from every survey in the entire data set in order to produce a consistent set of measurements for the time lapse inversion. This resulted in a loss of sensitivity and image resolution at depth. Figure 6 shows the squared sensitivity of the ERT measurements to the bulk conductivity distribution pre-desiccation (left) and post-desiccation (right), along a 2D transect intersecting the injection and extraction wells. The post-desiccation decrease in sensitivity in the lower section and below the injection well is caused by the loss of electrodes during desiccation, resulting in an inability to resolve changes below about 15 m depth. This is important when interpreting the forthcoming time-lapse inversion images, which do not indicate the decreases in conductivity below 15 m that are indicated by neutron logging and radar. Note that this problem can be addressed in future applications by encasing the electrodes in a material less prone to desiccation cracking such as Portland cement grout.

A.2.5 Temperature Monitoring

Thermistors (USP8242 encapsulated negative temperature coefficient thermistors, U.S. Sensor, Orange, California) were used to monitor temperature. To achieve accurate temperature measurements over the range of interest, a fifth-order polynomial was used to relate resistance to temperature for each of the thermistors used in the field test. The manufacturer's calibration relationship was verified for a subset of the thermistors in a precision water bath spanning the 0°C–40°C temperature range with measured accuracies better than 0.07°C.

Temperatures were logged continuously (10 minute intervals) at each thermistor. In addition to use for correcting the ERT-derived C to a standard temperature prior to using the ERT data for estimating VMC changes, 3-D interpolation of the temperature data were also used to evaluate desiccation progress. The 3-D temperature field was estimated at selected times using the same interpolation technique that was used for the neutron moisture data.

A.3 RESULTS AND DISCUSSION

Neutron moisture logging provides a large number of vertically-discrete data points at multiple lateral locations over time. These data are expected to provide the most accurate and high resolution information about vertical variations in moisture at the borehole locations. Cross-hole ERT and cross-hole GPR are expected to provide indirect but more spatially extensive estimates

of moisture content and associated changes over time. The ERT was collected autonomously over several boreholes and thus offers temporally dense information in 3D; the GPR was collected manually and offers high 2D spatial resolution but low temporal resolution. The temperature sensors provide a large number of vertically-discrete data points at multiple lateral locations across the test zone and for multiple time points. In this section, we describe the datasets and their associated interpretations in terms of monitoring the distribution of moisture content reduction over time to at or below a specified threshold moisture content value. We subsequently compare the different data suites and discuss their relative benefits and limitations for monitoring a desiccation treatment zone.

A.3.1 Field Test Data

Neutron moisture logging data over time show changes in VMC at monitored locations that varied with depth and the initial moisture content associated with the sediment texture (e.g., Figure 7). Neutron logging data is expected to be an accurate localized indicator of VMC because of its calibration to physical measurement of moisture content from sediment samples. Desiccation was not uniform across the injection screen depth interval. At each monitoring location, the neutron data show the vertical distribution of desiccation and zones desiccated to below selected threshold moisture content values can be identified. For instance at location L2, the depth interval between about 13 and 17 m bgs was desiccated to a VMC below 0.02 m^3 m^{-3} by the end of active desiccation. The 3-D distribution of desiccation can be estimated by interpolating the neutron moisture logging data between monitoring locations. Figure 8 shows VMC for a 2-D plane within the 3-D neutron moisture data interpolation. The distribution of moisture content over time can be used to identify where desiccation has reached a specified threshold moisture content, nominally in the 13-17 m bgs depth interval out to a radial distance of about 3 m from the injection well for a threshold of moisture content of 0.02 m^3 m^{-3} (red zone) by the end of active desiccation in the field test. Interpretation of the 2-D moisture content representation should consider that interpolation does not incorporate subsurface conditions that can impact the distribution of desiccation away from the measurement point.

The 2-D distribution of desiccation between access wells can also be estimated by cross-hole GPR. Figure 9 shows VMC over time for a series of 2-D GPR surveys between adjacent logging wells (Figure 3). This figure was created using Equations 7.2 and 7.3, recognizing that

the validity of the low-loss assumption associated with Equation 7.2 varies both spatially and temporally. Similar to the neutron moisture data, this estimate for the distribution of moisture content over time shows desiccation in the 13-17 m bgs depth interval out to a radial distance of about 3 m from the injection well for a threshold of moisture content of 0.02 m^3 m^{-3} (dark red zone) by the end of active desiccation in the field test. Interpretation of the 2-D moisture content representation should consider that conversion of GPR-derived permittivity to VMC is impacted by C. However, desiccation reduces the C, which renders GPR data acquisition more favorable, and improves the accuracy of the GPR-derived moisture content estimate. For example, Figure 10 shows the ERT-derived C distribution along the GPR survey transect prior to the start of the test (left) and at day 140 of desiccation (right). The black regions illustrate where low-loss assumptions may not be valid (C > 0.05 S/m). Prior to desiccation, the low-loss assumption is generally valid above a depth of 10 m and invalid below10 m. At the end of desiccation, low-conductivity conditions have been established within a zone from depths of approximately 13 m to 15 m. Within this depth interval, GPR derived moisture content estimates correlate well with estimates from neutron moisture logging (Figure 11). Thus, within zones where desiccation has decreased the C, GPR can be used with confidence to estimate the moisture content distribution between wells. At other locations, the estimates should be considered with caution.

The progression and distribution of moisture content changes as imaged by ERT is shown in Figure 12. The ERT data show changes in the VMC expressed as the ratio of VMC at the time of the measurement (VMC_t) to the baseline VMC from an ERT data set collected prior to desiccation (VMC_0), estimated as described in Equation 7.5 and with recognition that the ratios of VMC and water saturation are equivalent. Thus, a VMC_t/VMC_0 ratio of one designates areas that have not changed from the conditions prior to active desiccation. Ratios lower than one indicate desiccation, for instance, where a ratio of 0.5 means that the VMC is 0.5 times what it was prior to desiccation. The representations shown in Figure 12 are for a 2-D plane extracted from 3-D ERT images. Areas where the VMC_t/VMC_0 ratio becomes less than a specified value (e.g., 0.5) could be used to interpret the distribution of desiccation below a threshold of change (moisture content decreased by half), or below an absolute threshold if used in conjunction with knowledge of the starting moisture content. The resolution of the ERT data inversion is on the order of a cubic meter. Thus, the ERT images in Figure 12 do not resolve sharp contrasts in drying zones over time, but show a “smoothed” image of how the subsurface is changing. Note

that changes below approximately 15 m were not resolved by the ERT due to electrode loss as discussed previously.

Figure 13 shows temperature distribution for a 2-D plane extracted from 3-D interpolation of temperature sensor data during active desiccation. These data representations can be used to interpret the distribution of desiccation and obtaining "significant" desiccation based on the distribution of evaporative cooling and post-cooling temperature increases. The progression of cooled zones shown at days 14, 30, and 70 are indicators of desiccation activity (evaporative cooling) and the related dominant injected dry gas flow pattern. By days 140 and 164, localized warming indicates that some zones have been desiccated. Desiccation, as indicated by cooler temperatures, continues to occur at other locations at these times. Interpretation of the 2-D temperature representations should consider that interpolation may not accurately reflect the temperature distribution away from the measurement point.

A.3.2 Comparative Assessment

The geophysical methods and temperature monitoring applied in the field test utilize substantially different methods to provide data for estimating the distribution and extent of moisture content changes during desiccation. For each method, there are benefits and limitations for use of these data to monitor desiccation based on the characteristics of the data collection, analysis techniques, and sources of error. These benefits and limitations also have implications for application of desiccation treatment on a larger scale than was applied for the field test.

Neutron moisture logging and GPR data can be converted using calibration approaches to provide VMC locally at a wellbore or within a 2-D plane, respectively. ERT cannot be directly converted to VMC, but changes in ERT-measured C can be converted to corresponding changes in VMC. Temperature monitoring cannot be related to VMC, but is an indicator of desiccation based on evaporative cooling phenomena. Datasets also have different sources of error; examples here include the errors expected based on the low-loss assumption used for the GPR interpretation and the errors associated with the loss of electrode coupling on the ERT interpretation. Thus, each data set needs to be interpreted differently and carefully with respect to monitoring the distribution of desiccation and targeted threshold moisture content.

Neutron moisture logging of a borehole is a standard method for obtaining a high resolution vertical profile (~7.5 cm vertical intervals) of VMC that is accurate locally (~30 cm radius) with

calibration to sediment data. Temporal resolution of the data depends on manual survey frequency, which may lead to lower temporal resolution than for methods that can operate autonomously. Subsurface conditions would be expected to change most rapidly near a dry gas injection well with responses becoming much slower with larger radial distances. Thus, the need for frequent data associated with reaching desiccation targets is related to the scale of the targeted treatment zone. However, for desiccation operational decisions, more frequent early-term data may be needed to help guide operational adjustments that may impact overall long-term performance.

Interpolation of VMC from neutron moisture logging data can be used to generate a three-dimensional image of moisture conditions that may be most appropriate for sites with significant anisotropy leading to dominantly horizontal soil gas flow. However, as the monitoring scale becomes larger, neutron data may become sparse compared to the targeted desiccation volume, depending on the number of access locations installed. For instance, if drying has occurred at one location, but not yet at another location, interpolation cannot effectively project the extent of drying past the first location. As distances between monitoring locations grow larger, larger portions of the subsurface are essentially not monitored for a period of time by neutron data.

Cross-hole GPR provides means to monitor VMC in two dimensions based on propagation of energy through the subsurface between two logging boreholes. Thus, it provides data for interpretation of VMC distribution away from subsurface access points and does not require interpolation between access points like the neutron moisture logging data. GPR provides high resolution within the survey plane due to high vertical density of data from multiple offset surveys at the access locations. GPR borehole spacing is constrained by energy propagation and generally needs to be less than 10 m for the vadose zone and even smaller for areas with high C (about 3 m at the desiccation test site). As with the neutron logging data, temporal resolution of the data depends on manual survey frequency. High C at contaminated sites (e.g., due to high ionic contaminant concentrations in pore water such as present in the lower portion of the test site) can severely impact the accuracy of the GPR estimate. When the ground has a high C the low-loss assumption is not valid and the EM velocity is affected by both C and permittivity changes such that accurate conversion to VMC is difficult. However, in zones with significant desiccation, the C drops because moisture content decreases. In those zones, the low-loss assumption may be valid and GPR data can be used to estimate moisture content through

Equations 7.2 and 7.3. At the field site, even very high initial conductivity dropped to levels appropriate for the low-loss assumption in desiccated zones.

Cross-hole ERT provides means to monitor the change in VMC in three dimensions based on the imaged C distribution in the subsurface between multiple electrodes. Decreases in temperature and moisture content occur during desiccation, both of which cause a decrease in C. Thus, to improve the accuracy of quantitative estimates of the moisture content change using ERT, a temperature correction is necessary. This correction is moisture content dependent, but in practice, a constant temperature correction factor is applied in the data inversion. In addition, increasing fluid conductivity with decreasing moisture content may dampen the ERT response and impact moisture content change estimates. ERT data provided limited resolution such that the distribution of spatial moisture content change is depicted with lower contrast than actually exists, appearing as a smoothed or blurred representation of actual changes. This issue is applicable with any geophysical method requiring an inversion, such as GPR; however, GPR generally provides higher spatial resolution than ERT given the same access points for electrodes and antennas. With ERT, spatial resolution can be adapted by modifying the electrode distribution and proximity to the desiccation zone, and can be selected to be appropriate for the scale of the desiccation target and the resolution needed based on the monitoring goals. As shown in Figures 6 and 12, ERT imaging resolution can change over time if electrodes have to be dropped from the network because of electrical coupling issues as the porous medium is desiccated. In the field test, maintaining electrical coupling was difficult in heavily desiccated zones, likely due to bentonite contraction and subsequent separation from electrodes. Full-scale applications would need to consider improved wetting capability or non-shrinkable grout around electrodes to maintain adequate coupling (e.g., neat Portland cement).

A significant benefit of the ERT method is that the data can be collected autonomously, which can greatly improve temporal resolution over manually-collected datasets. Thus, ERT provides the potential for relatively automated imaging of desiccation progress. ERT derived changes in bulk conductivity provide qualitative information concerning when and where desiccation is occurring without interpretation. However, to be quantitative, ERT images must be interpreted to relate the ERT-derived change in VMC (e.g., VMC_t/VMC_0) at the available data resolution to the site-specific metrics for desiccation distribution and threshold moisture content targets. Potentially, using pre-desiccation measurements of initial VMC, a threshold

VMC change ratio for reducing the VMC to below a specified threshold could be set (e.g., if the target VMC is 0.02 and the initial VMC is about 0.06, a target change ratio would be about 0.3). Interpretation would need to consider that the ERT data represent average changes within the resolution control volume (e.g., for the field test a volume of about a cubic meter). Final VMC values may need to be confirmed at selected locations with another method like neutron logging or GPR. For the field test, with consideration of the ERT resolution issues at the bottom of the test zone, a VMC reduction of about 50% from the initial moisture content value corresponded to zones where other data also indicated significant desiccation.

Due to the evaporative cooling effect of desiccation, temperature data over time can also be used to interpret desiccation distribution and roughly indicate achieving a threshold of significant desiccation based on inflection of cooling to warming trends. Resolution for these determinations depend on sensor spacing and interpolation of the data are required with related issues as discussed for the neutron logging data. Temperature sensors are robust, relatively inexpensive and data can be collected autonomously. Thus, temperature monitoring appears to be useful as part of a desiccation monitoring approach.

A.4 CONCLUSIONS

Monitoring the progression of in situ remedies such as desiccation is needed to provide information to guide operational decisions. Additionally, monitoring data are needed to determine when performance requirements such as the size of the desiccated zone and the final moisture content have been met. However, monitoring options for in situ vadose zone remedies are limited and implementation can be challenging due to the subsurface properties and limited access. Geophysical monitoring methods were evaluated as part of a field-scale treatability test of desiccation at the Hanford site with an emphasis on providing spatial and temporal information about the distribution of desiccation and the extent of moisture content reduction. The study also highlighted the benefits and limitations of different borehole and crosshole methods for monitoring desiccation. Although the method evaluation objective of the study was met, future efforts using joint or coupled inversion approaches and more sophisticated petrophysical relationships (Ferré et al., 2009; Hubbard and Linde, 2011; Laloy et al. 2012) are expected to take advantage of the benefits and compensate for some of the method-specific limitations.

Traditional moisture content monitoring through neutron moisture logging is well established and provides detailed vertical profile information at discrete logging locations. Interpolation of multiple logging locations is possible, but must be applied with caution because interpolation does not account for subsurface heterogeneities away from the logging locations and becomes less representative as the distance between logging locations increases. While GPR moisture content estimates are impacted by high C, estimates in low conductivity and significantly desiccated zones appear to be similar to neutron moisture data. GPR scaling to larger applications may be limited by the need for relatively closely spaced logging access. ERT data can be collected autonomously for good temporal resolution and can provide estimates of moisture content change in three dimensions, but not estimates of absolute moisture content. However, ERT implementation is readily scalable to larger sites. Interestingly, interpolation of temperature data, due to the evaporative cooling effect of desiccation, also provided useful 3-D information about the progress of desiccation and is a robust method for vadose zone implementation.

Acknowledgements

Primary funding for this research was provided by CH2M Hill Plateau Remediation Company, Richland, WA. Additional funding related to refinement of data analysis techniques and conducting ground penetrating radar surveys was provided by the U.S. Department of Energy Office of Groundwater and Soil Remediation and Richland Operations Office as part of the Deep Vadose Zone Applied Field Research Initiative. Pacific Northwest National Laboratory is operated by the Battelle Memorial Institute for the Department of Energy (DOE) under Contract DE-AC06-76RLO 1830. Visualization software was provided by Lawrence Livermore National Laboratory using VisIt. Neutron moisture logging was conducted by the S.M. Stoller Corporation, Hanford Office, under contract to CH2M Hill Plateau Remediation Company, Richland, WA.

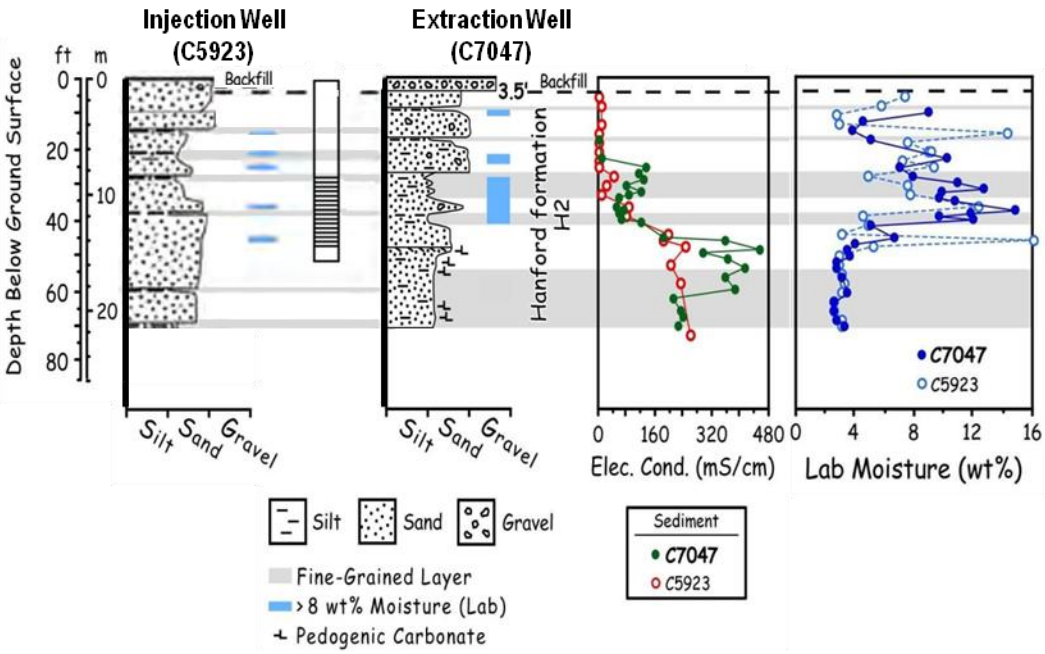

Figure A.1 Injection and extraction well borehole laboratory moisture content, extracted pore water electrical conductivity, and well screened interval (after DOE 2010; Serne et al. 2009; Um et al. 2009). Electrical conductivity was measured on pore water extracted from sediment samples.

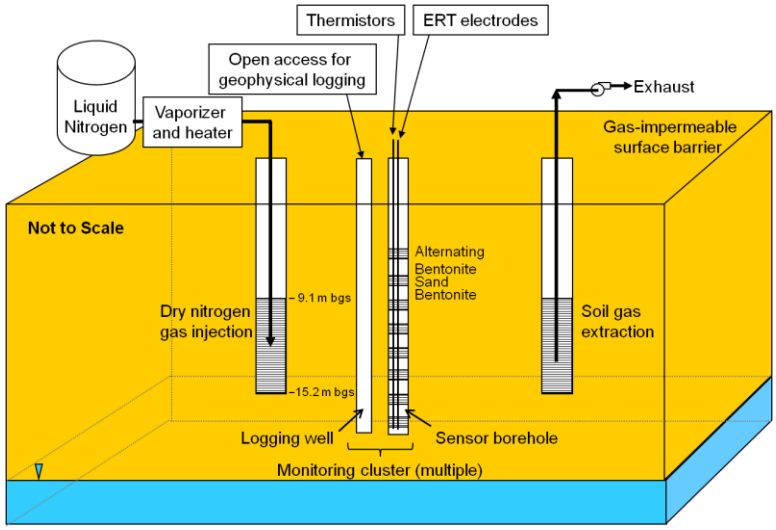

Figure A.2 Basic components of the desiccation field test system.

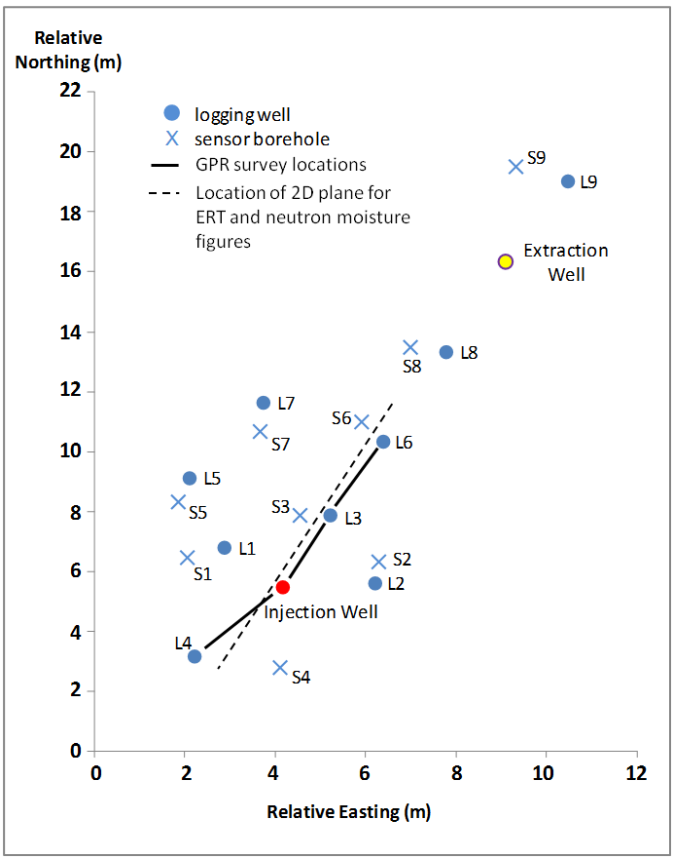

Figure A.3 Location of test site wells, where boreholes with an "S" designation contained in situ thermistors and ERT electrodes and wells with an "L" designation were cased wells for neutron logging and GPR access.

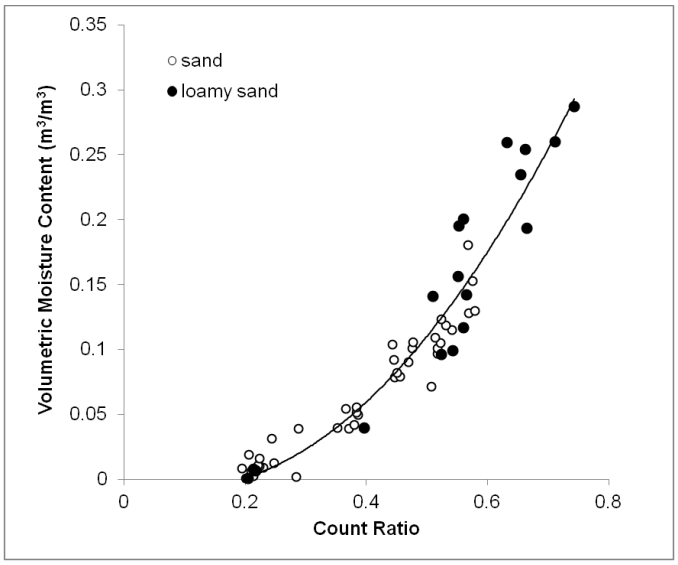

Figure A.4 Calibration relation for neutron moisture probe count ratio data and corresponding laboratory-measured volumetric moisture content (after Truex et al. 2012a).

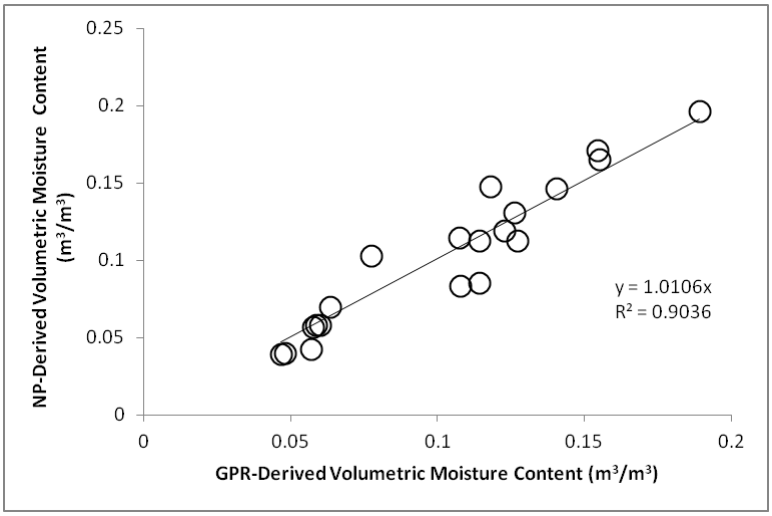

Figure A.5 Comparison of volumetric moisture content derived from GPR and neutron moisture logging (NP) for location L4 at depths less than 10 m prior to desiccation.

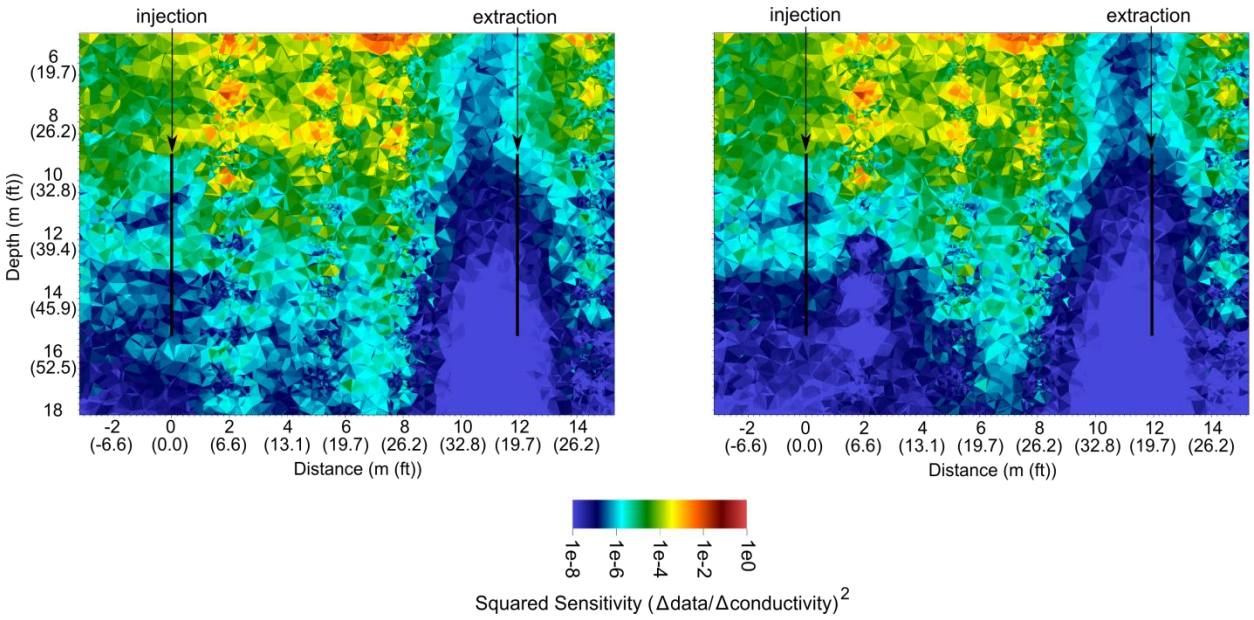

Figure A.6 ERT data sensitivity distribution for given data available before desiccation (left) and after desiccation (right). The loss in sensitivity surrounding the injection well from approximately 14 m to 16 m depth is caused by a loss of electrode coupling within the desiccation zone. The images are shown in true dimension (i.e. no smoothing between tetrahedral elements is applied).

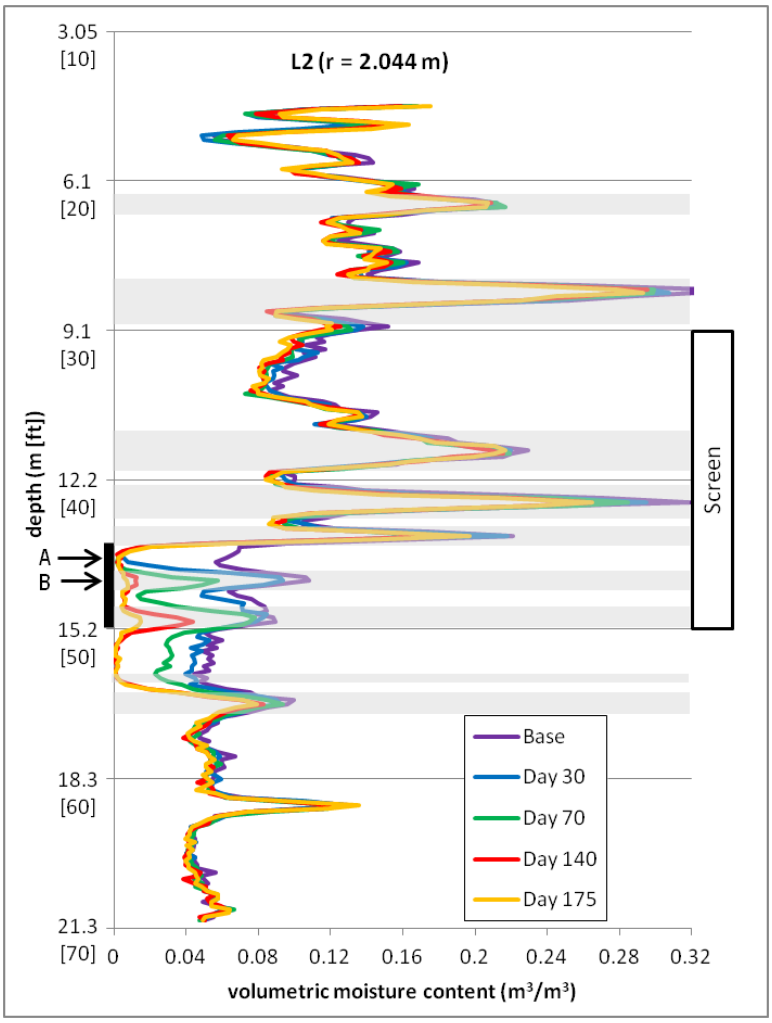

Figure A.7 Neutron moisture data at location L2 in days from start of active desiccation. Base data are pre-desiccation. Day 175 represents the end of active desiccation. Zones of loamy sand (gray) and sand (no shading) textures are shown for the depth interval 6 to 18 m bgs where samples were evaluated from a post-desiccation borehole located 0.9 m away (after Truex et al. 2012a).

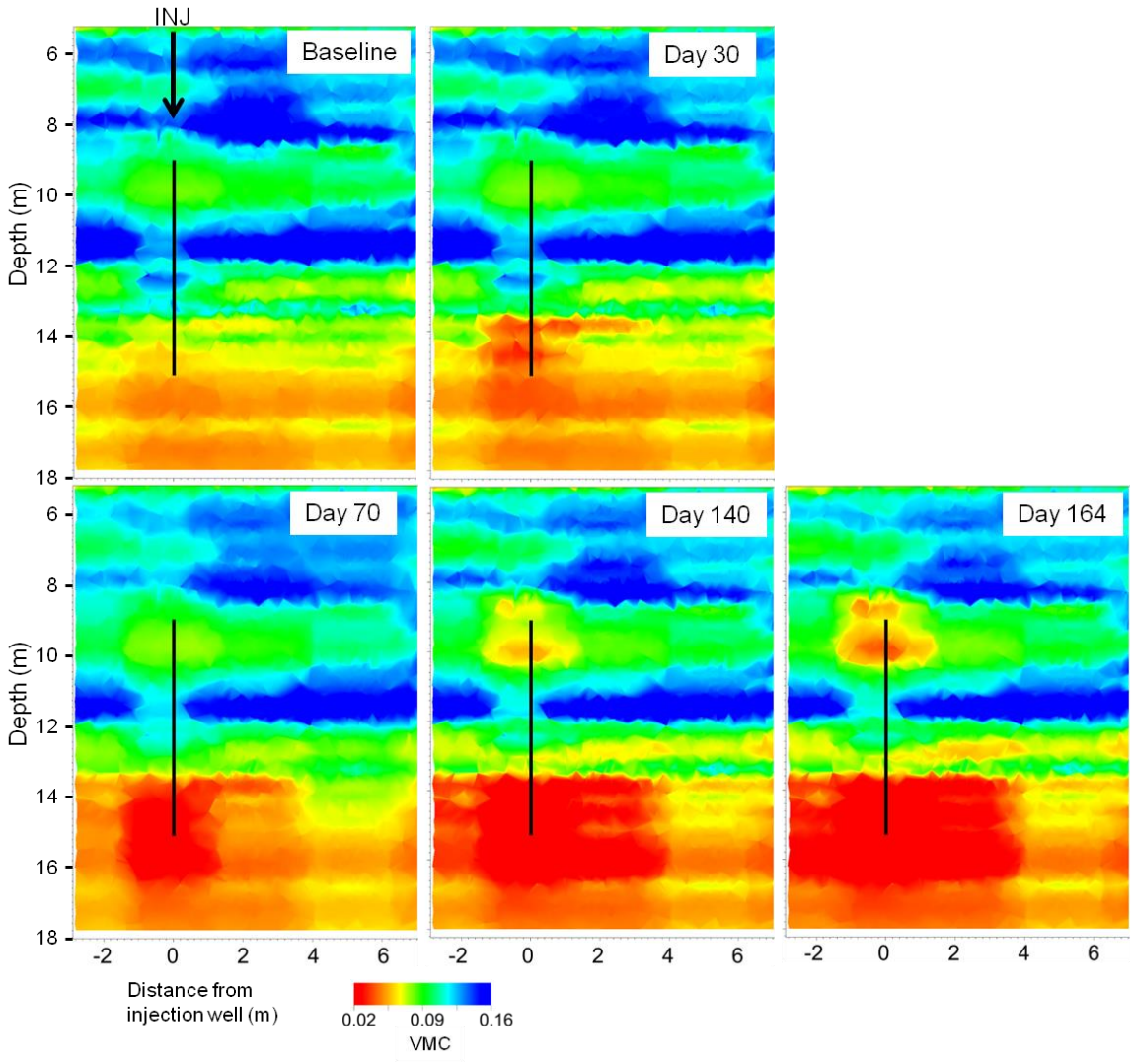

Figure A.8 Interpolation of volumetric moisture content (VMC) from neutron moisture logging data along the axis between the injection and extraction wells. Neutron moisture data from are from logging at locations L1-L7 (Figure A.3). The black line indicates the screened section of the injection well.

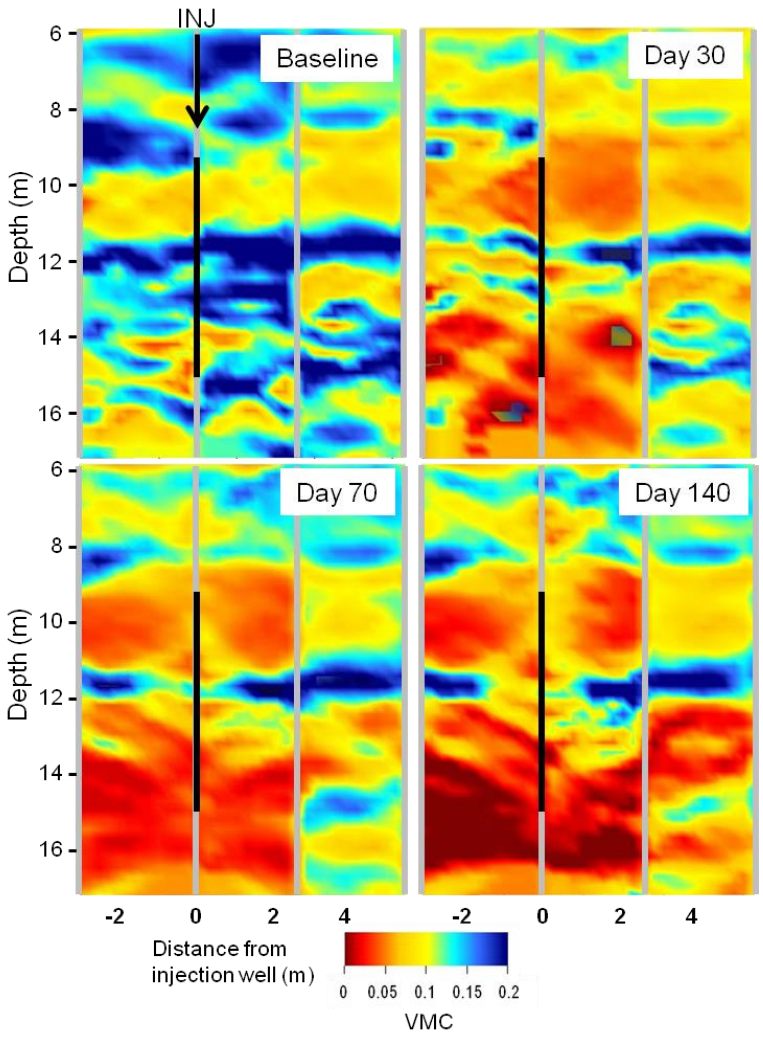

Figure A.9 2-D interpretation of volumetric moisture content (VMC) from cross-hole GPR data. See text and Figures A.10 and A.11 for interpretation of moisture content in relation to the low-loss assumption. The black line indicates the screened section of the injection well.

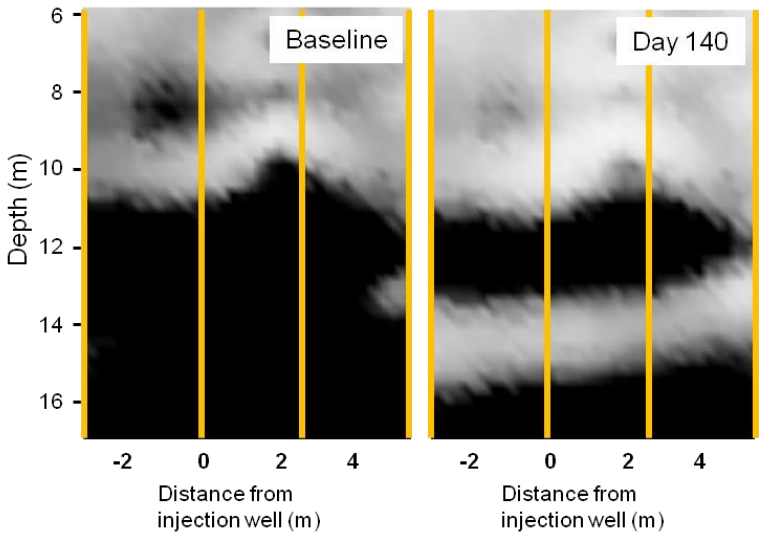

Figure A.10 Electrical conductivity distribution showing regions where the low-loss conditions can be assumed (light regions). Black regions show where the electrical conductivity is greater than 0.05 S/m and the low-loss assumption cannot be applied.

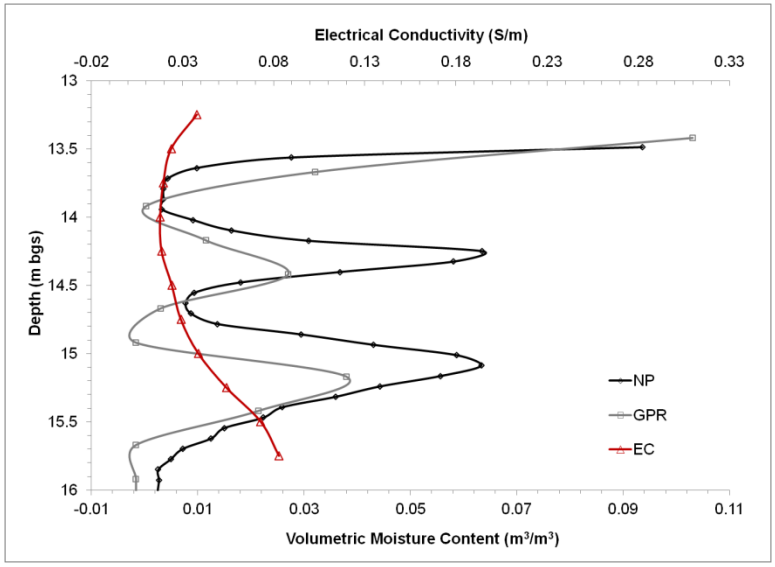

Figure A.11 Comparison of post-desiccation volumetric moisture content from GPR and neutron moisture logging (NP) for location L3 within a depth interval where electrical conductivity (C) has been decreased by desiccation (Figure A.10).

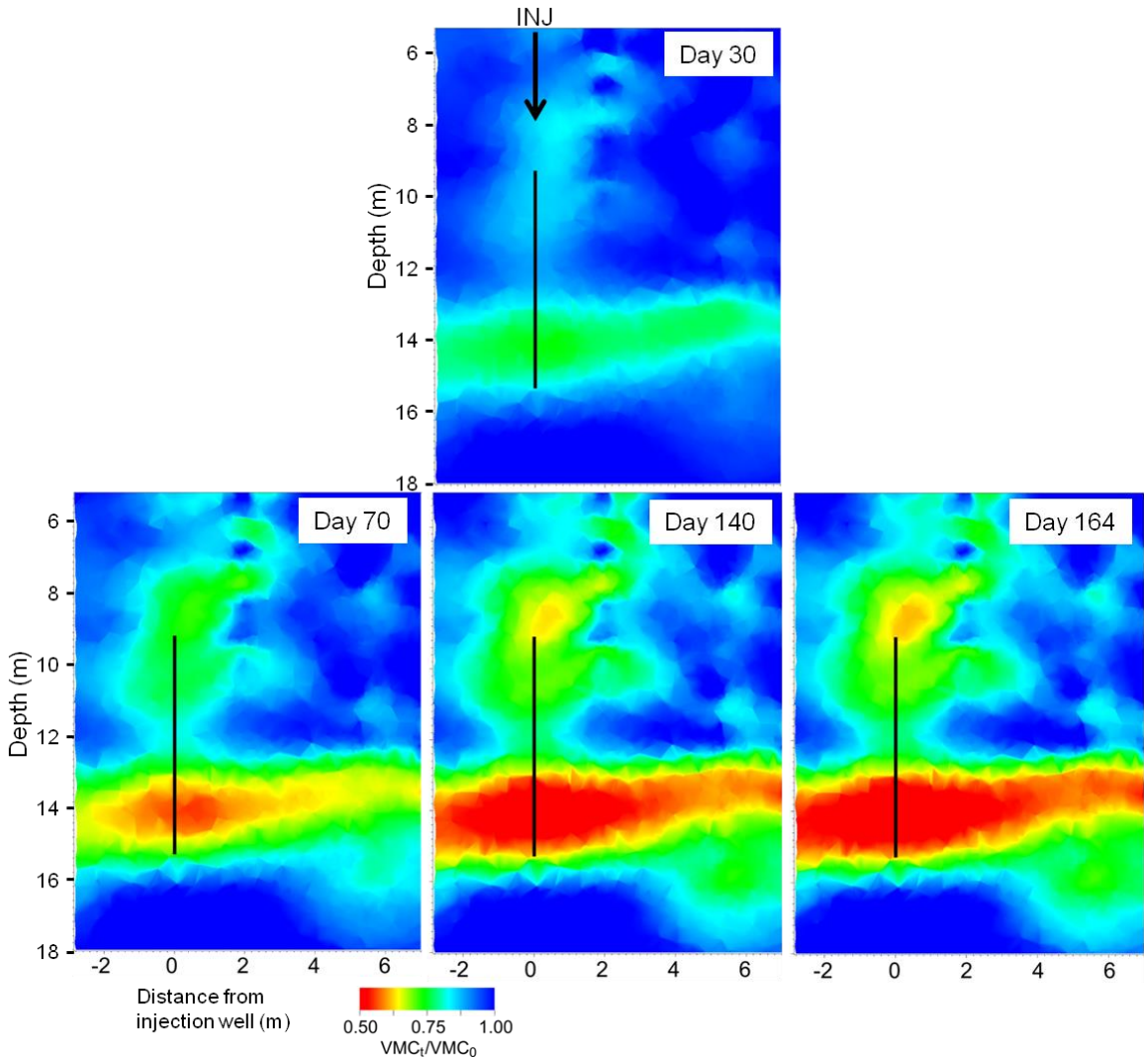

Figure A.12 Ratio of volumetric moisture content (VMC_t) to pre-desiccation volumetric moisture content (VMC_0) over time along the axis between the injection and extraction wells from cross-hole ERT. ERT data are from sensors at locations S1-S7 (Figure A.3). The black line indicates the screened section of the injection well.

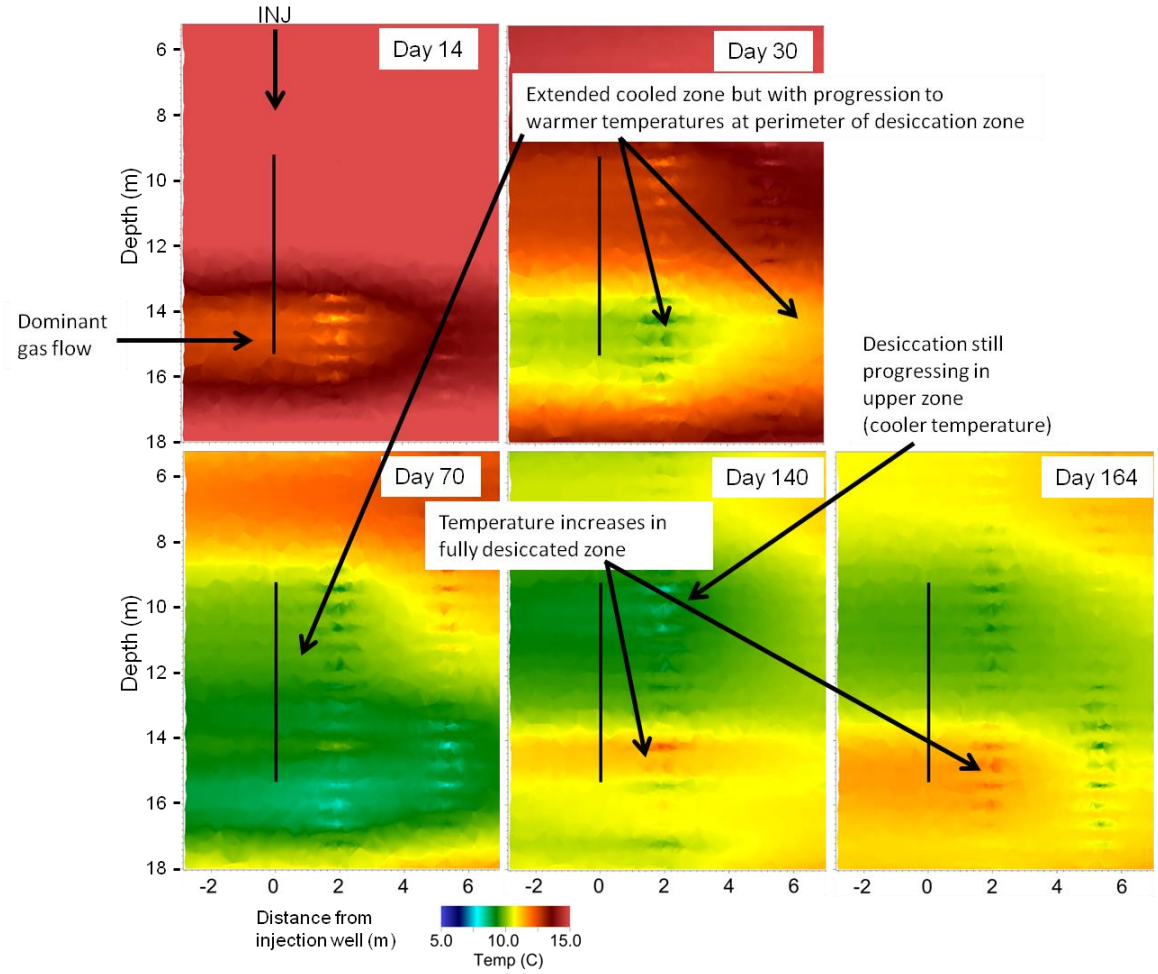

Figure A.13 Interpolated temperature response along the axis between the injection and extraction wells, indirectly showing desiccation through the evaporative cooling effect. Temperatures drop while a zone is being desiccated. Once a zone is fully desiccated, there is no more evaporative cooling and temperature rises toward the inlet temperature. Data from sensors at locations S1-S7 (Figure A.3).

APPENDIX B

B. ENGINEERED SURFACE BARRIER MONITORING USING GROUND-PENETRATING RADAR, TIME-DOMAIN REFLECTOMETRY, AND NEUTRON-SCATTERING TECHNIQUES

C.E. Strickland, A.L Ward, W.P. Clement, and K.E. Draper
Published in: Vadose Zone Journal, **9**(2):415-423, 2010. doi:10.2136/vzj2009.0008

Summary

Effective monitoring of surface barriers intended to isolate and protect waste from the accessible environment requires techniques to assess their performance. Quantifying drainage conditions at any point below the barrier is difficult because field-scale drainage measurements are not well suited for assessing spatial drainage heterogeneity. Measurements of water storage, however, can provide an indirect measure of impending drainage. We measured seasonal water content at a vegetated capillary barrier on the Hanford Site in southeastern Washington to determine effective water-storage monitoring methods. Measurements were made using ground-penetrating radar (GPR) direct ground wave methods operating at 100 MHz. Simultaneous measurements using time-domain reflectometry (TDR) and neutron-scattering probe (NP) were used to determine the sampling depth of the GPR ground wave. The ground wave sampling depth increased only slightly with decreasing moisture content, ranging from 30 to 37.5 cm. The TDR measurements were made using permanently emplaced arrays, eliminating the need for repeated ground disturbance. All three methods showed similar seasonal responses, with the highest water contents observed during the winter months and decreasing through the summer. Unlike TDR and NPs, which are local-scale measurements, GPR exhibited much greater spatial detail across the barrier surface. While measurement uncertainties exist with regard to the sampling depth and dispersive effects, our results indicate that GPR can be an effective and minimally invasive method for providing reasonable near-surface estimates of soil water content changes within an engineered barrier.

B.1 INTRODUCTION

As part of past practices related to production of nuclear materials for weapons development, radiological and chemical wastes were routinely discharged into soils at the Hanford Site in southeastern Washington State. At many sites, contaminants were transported deep into the vadose zone and, in some cases, have spread over too large an area for excavation to be a practical remedy (Ward et al., 2006). At these sites and those with low-to-intermediate levels of contaminants, remediation by in-place containment of the subsurface contaminants is viewed as a final remedy (U.S. Department of Energy, 1996). In-place containment relies heavily on engineered surface barriers and at the Hanford Site alone, an estimated 200 barriers will be needed to cover almost 1000 acres of waste sites. Yet, barrier development remains one of the top science and technology challenges within the U.S. Department of Energy (DOE) complex, primarily because of uncertainty in long-term performance.

The primary function of engineered barriers is to isolate near-surface and subsurface waste from human and biotic intrusion, thereby limiting interaction with environmental processes that could cause contaminant migration from the site for periods ranging from 500 to 1000 years (Ward and Gee, 1997; USDOE, 1999). Designing long-lived field-scale barriers is a challenging task because of the large number of variables that can influence performance. A more challenging task is that of verifying the long-term performance of barriers.

Barrier performance is controlled by unsaturated flow processes and is therefore influenced by precipitation, surface runoff, water storage, evaporation, transpiration, lateral diversion along sloped layers, and, ultimately, deep percolation. The most comprehensive approach to monitoring is therefore based on measuring components of the water balance equation (Ward and Gee, 1997; Ward et al., 2008).

Most capillary barriers are designed with a specific water-storage capacity chosen to minimize percolation under extreme precipitation conditions, and a percolation threshold to minimize the flux of contaminants to the groundwater. Deep percolation and change in soil water-storage capacity are most often selected to reflect barrier performance. Determining the effectiveness of the barrier to minimize deep percolation depends on our ability to quantify drainage conditions at any point below the barrier. While field-scale drainage measurements collect recharge over large areas, these measurements are unable to capture spatial drainage heterogeneity. Measurements of water-content can provide an indirect measure of impending

drainage conditions given the water storage capacity of a surface barrier. In addition, they provide multiple local-scale observations allowing one to build a more detailed picture of the barrier performance.

Water-content measurements can be obtained by a number of methods, including ground-penetrating radar (GPR), time-domain reflectometry (TDR), and neutron-scattering probe (NP) measurements (Gardner and Kirkham, 1952; Evett and Steiner, 1995; Huisman et.al., 2001). GPR is a non-invasive technique capable of efficiently investigating intermediate-to-large areas. The spatially continuous nature of the measurement provides information about the field-scale spatial variability of water content across the entire barrier surface. However, determining the exact sampling depth of the ground wave can be a difficult task. By using simultaneous measurements of water content at multiple depths, estimates of the ground wave sampling depth for GPR can be obtained. In addition, site-specific petrophysical relationships can improve GPR-derived estimates of water content.

Both GPR and TDR are based upon electromagnetic (EM) wave propagation, with a velocity that depends on the apparent permittivity (κ_a), or electrical permittivity, of the surrounding medium. Care must be taken when applying TDR derived relationships between apparent permittivity and water content to GPR data as each method typically operate at different frequencies. The electrical permittivity of soils generally varies with frequency and is considered a complex quantity, where both the frequency dependant magnitude and phase can be specified. Dielectric polarization and electrical conduction losses as well as frequency dependant attenuation can have a significant effect on the measured phase velocity (Schwartz et.al., 2009; Robinson et. al., 2003). The electrical permittivity of soils has also been shown to display temperature dependence which can differ significantly from pure water or dry soil (Or and Wraith, 1999; Seyfried and Grant, 2007). To obtain accurate estimates of water content, both frequency and temperature dependant effects must be accounted for.

TDR and NP are both considered local-scale methods that interrogate a small region in the vicinity of a sensing device. Determining the spatial variability at scales finer than the separation between individual point measurements is not possible using only local-scale methods. Such devices must be used in close proximity to the soil and typically require emplacement of the device itself or some form of access port. Our objective was to identify effective methods for

monitoring water content to assess drainage conditions and provide an optimum system for monitoring the long-term performance of the barrier.

B.2 METHODS AND MATERIALS

The Hanford Site has a semiarid climate with mild winter temperatures and hot summers. The average annual precipitation is 172 mm, with approximately half of the total occurring between November and February. Monthly temperatures range from 11.1 to 6.9 ºC in the winter and 17.2 to 27.9 °C in the summer (Fayer and Gee, 2006).

A Prototype Hanford Barrier (PHB) was constructed in 1994, and has been routinely monitored to evaluate its field-scale physical and hydrological performance. The PHB was designed to prevent biological intrusion into the underlying waste, minimize erosion, and eliminate water recharge all with minimal maintenance. TDR and NP measurements have been collected on the PHB in addition to seasonal GPR measurements. A cutaway view illustrates the barrier design, and thickness of various materials that compose the PHB (Figure 1). The PHB is constructed of a 1.5-m-thick silt-loam/pebble mixture at the surface positioned above layers of sand, gravel, basalt rip-rap, and finally asphalt. The outer boundary side slopes of the prototype surface barrier are basalt riprap on the north, east, and south with gravel on the west. The site is relatively flat and covered with rows of sagebrush (*Artemesia Tridenta*) and perennial grasses.

The PHB was monitored using a rectangular grid to allow for accurate spatial positioning of the measurement locations. Locations of grid points, in addition to the TDR and NP monitoring stations and GPR survey lines, are depicted in Figure 2. Three east-west and two north-south GPR lines were surveyed March 9th, May 22nd, September 18th 2001, and January 21st 2002 (Clement and Ward, 2008).

B.2.1 Ground-Penetrating Radar

Soil apparent permittivity is strongly dependent on water content owing to the large difference between water and bulk soil apparent permittivity. For both methods, the apparent permittivity is determined from the observed phase velocity of an electromagnetic pulse propagating through the soil matrix; however the frequencies employed are often quite different.

Studies have demonstrated that GPR effectively estimates subsurface water content using measured EM velocities (Du and Rummel, 1994; Van Overmeeren et al., 1997; Huisman et al., 2001). The use of petrophysical relationships to estimate water content from dielectric measurements applicable to general soils have proven quite valuable (Du and Rummel, 1994; Van Overmeeren et al., 1997).

Ground-penetrating radar surveys using two different acquisition geometries were performed to determine EM velocity of the subsurface. The first method, a commonly used variable-offset survey, is the common midpoint (CMP) method (Greaves et al., 1996). Common midpoint surveys are acquired by moving the GPR antennas away from each other around their (common) midpoint (Figure 3). The second method is denoted as wide offset reflection (WOR) and uses a common offset between the antennas that is much wider than normally used in standard GPR reflection profiles (Du and Rummel, 1994). This creates a distinct separation in arrival times of two events from which the ground velocity can be determined. This second method offers great potential to provide dense spatially sampled velocity measurements that would be very time-consuming to collect using CMP surveys.

The GPR surveys were conducted using a Sensors and Software Pulse Ekko 100 system using 100-MHz antennas. It was anticipated that water content changes would occur deeper in the soil profile. The use of lower frequency system was selected to achieve a greater signal penetration depth. The sample interval was 0.8 ns with 500 samples acquired for each trace and a recording window of 400 ns. Waveform averaging was performed to improve data quality by using a stack of at least 32 for all the surveys. A low-frequency filter was applied to the data to remove noise caused by the electronics in the radar unit. A 25-ns window automatic gain control was used for displaying the acquired traces.

Several CMP surveys were acquired at the beginning of the March field experiment to determine the EM velocity at these locations and the optimal offset at which to collect the WOR data. Antennas were initially separated by 0.1 m which was increased in 0.1 m increments by moving each antenna 0.05 m away from the midpoint. For the analysis, a 25-to-200-MHz band pass filter is applied to the data to increase the signal-to-noise ratio of the arrivals. For the WOR surveys, the antennas were initially located 1.0 m apart, and then only the receiving antenna was moved in 0.1 m increments until the final antenna separation of 3.5 m was achieved. Both antennas were then moved 0.25 m per trace, keeping the antenna separation fixed. This

acquisition geometry allowed for initial identification of the ground wave in an initial CMP-like gather, from which it could be followed throughout the WOR profile. The travel times and amplitudes were picked from unfiltered data to retain true times and amplitudes.

For the WOR surveys, the arrival times of the air and ground waves were used for calculation of the dielectric constant without having to first convert to velocity. The square root of the apparent permittivity was computed from the air and ground wave travel time picks (Huisman et al., 2001):

$$\sqrt{\kappa_a} = c(t_{ground} - t_{air}) / x + 1 \quad \text{(B.1)}$$

Where κ_a is the apparent permittivity, c is the EM velocity in a vacuum, x is the antenna separation, t_{ground} is the arrival time of the ground wave, and t_{air} the arrival time of the air wave. The apparent permittivity of the medium within the GPR sampling volume can then be converted to water content using an appropriate petro-physical relationship. While relationships applicable to general soils such as Topp's equation (Topp et al., 1980) have found widespread use, it is preferred to use a one developed for the specific soil being measured. One common method, and the method used in this study, describes the water content as a linear function of the square-root of the apparent permittivity (Evett et al., 2005)

$$\theta = a\sqrt{\kappa_a} + b \quad \text{(B.2)}$$

Equation 2 was fit to measured values of apparent permittivity for the warden silt loam/pebble admixture at various water contents. Saturation dependant electrical conductivity was also measured to partially assess the frequency dependant complex permittivity. Waveforms were acquired using a Campbell Scientific TDR100 system using a 10cm long Trifilar probe. The warden silt loam/pebble was mixed with 5 different quantities of water and packed into 10 cm diameter by 15 cm long acrylic columns. The columns were sealed and set aside to equilibrate for 1 week after which the probe was inserted vertically into the column just prior to taking readings. For each column, hourly waveforms were acquired until changes in apparent permittivity became negligible. Probe cell constants were acquired using deionized water and NaCl solutions along with the air and short circuit reflection coefficients.

B.2.2 Ground Penetrating Radar Ground Wave Sampling Depth

The ground wave samples only part of the ground between the antennas. An area immediately surrounding the antenna down to some depth comprises the sampling volume. The GPR measured travel time is a composite of any velocity variations present in the sampling volume. If it is assumed that water content is uniform parallel to the surface within the sample volume, then the GPR ground-wave measures an average of water content down to the sampling depth, representative of the soil water storage. For this paper, water storage is calculated as the fractional volume of water contained within the sampling volume and is equivalent to the water content averaged to the sampling depth.

Determining the precise sampling depth of the ground wave can be difficult; however, empirical formulations have been developed for estimating the sampling depth. The ground wave has been shown to sample a depth between one-half to one wavelength (Berktold et al., 1998). The wavelength (λ) is computed from the frequency (f) and the velocity (v) of the phase, as follows:

$$\lambda = \frac{v}{f} \tag{B.3}$$

Another approximation assumes that the sampling depth can be calculated as half the Fresnel zone (Van Overmeeren et al., 1997), where S is the antenna separation and is given by the following:

$$z = \frac{1}{2}\sqrt{\frac{vS}{f}} \tag{B.4}$$

Sperl (1999) (as cited in Huisman et al. 2003) also reported the ground wave sampling depth as ~0.145l1/2. This wide range of values reported for the ground wave sampling depth underscores the need for determining a site-specific sampling depth to provide the most realistic estimates for a particular application. Empirical methods can provide a gross approximation of the sampling depth, but a more realistic measure of the sampling depth is desirable. Correlations between GPR-determined water content values and an independent measure such as TDR or gravimetric analysis have been used to more accurately determine the sampling depth (Galagedara et al., 2003; Grote et al., 2003). Water content collected with both the TDR and NP were compared with GPR measurements at the PHB to determine the ground wave sampling depth.

B.2.3 Time-Domain Reflectometry

Time-domain reflectometry, like GPR, determines soil water content by measuring the soil apparent permittivity. TDR allows automated, local-scale measurements of soil water content making it possible to derive nearly continuous temporal data sets. Water storage is calculated by averaging water content values from the surface to the specified depth.

An automated TDR data acquisition system was used at the PHB in addition to periodic GPR and NP measurements. Water content profiles from the surface to 180 cm depth were collected at eight locations across the PHB. At each location, three segmented Environmental Systems TDR probes were placed vertically in the silt-loam layer. Individual probes are either 60 cm or 75 cm long with 4 to 5 independent sensing segments. One five segment, 75 cm probe and two four segment, 60 cm probes were installed at each spatial location. The five segment probe is located closest to the surface acquiring measurements at the 7.5 cm, 22.5 cm, 37.5 cm, 52.5 cm and 67.5 cm depths. The first 4 segment probe partially overlaps with the five segment probe producing a redundant measure at the 67.5 cm depth followed by 82.5 cm, 97.5 cm, and 112.5 cm. The final probe was positioned deepest in the profile and acquired values at 127.5 cm, 142.5 cm, 157.5 cm and finally 172.5 cm. All depths specified are for the midpoint of each segment and each segment was 15cm in length. Measurements of each segment on all TDR probes were recorded hourly during the study using a Campbell Scientific CR10 data logger interfaced to an Environmental Systems MP-917 Moisture Point Soil moisture system as well as Campbell Scientific SDMX50 coaxial multiplexers needed for sequential acquisition. The MP-917 uses a diode-shorting technique at predetermined points along the waveguide. A step voltage is generated and the algebraic sum of the incident and reflected pulses are measured from which the pulse travel time along the probe is calculated. The water content for each TDR segment was then determined from the travel time following the method of remote shorting (Hook et al., 1993).

There are two different aspects to the calibration of the TDR system, probe calibration and soil specific calibration. Probe calibration consisted of determining corrected travel times for each probe on a segment by segment basis. Probes were then inserted into air dry warden silt loam/pebble admixture and used to derive soil specific travel times for each probe segment. So that TDR and GPR measurements could be matched precisely in time, hourly water-content profiles were generated for all eight TDR locations across the PHB.

B.2.4 Neutron Probe

A single, 3.8-cm-diameter, aluminum NP access tube was located adjacent to each TDR monitoring station in addition to four intermediate locations along east–west lines at 26 and 57 m. Monthly NP measurements were obtained using a CPN International 503DR Hydroprobe (Instrotek Inc., Concord, CA). At each location, measurements were collected at 14 discrete depths starting from 195 cm below the ground surface to the 15-cm depth in 15-cm increments. Sample acquisition time was 16 s for each measurement. Before each set of measurements, c and standard count values were determined using the manufacturer's enclosure centered within a steel storage container and located away from any neutron moderators, including the operator.

A soil-specific calibration for depths from 30 to 195 cm was performed at the PHB in late October 1997. Soil sample cores were collected from the silt loam layer at the PSB to a depth of about 195 cm. Nine soil cores were taken, with each core consisting of three separate aluminum sleeves. The first two sleeves were placed inside a Giddings probe sampler tube and driven into the soil with\ an electric rotary hammer. The third sleeve was driven into the soil with the rotary hammer but without the sampler tube. After each core was taken, a neutron probe access tube was inserted in the resulting hole and readings were taken using a 1-min count time. The cores were transported to the laboratory, where they were cut into sections 15 cm long and analyzed for water content. Soil samples were weighed both before and after drying at 105°C for 24 h. To minimize the effects of compaction on water content calculation, the average bulk density of each core was assumed for each section of that core. The average bulk density was calculated using the depth of the hole, the area of the sampling tube, and the total dry weight of the soil from the core. Volumetric water content was determined by converting the mass of water to volume and multiplying by the average bulk density and finally dividing by the dry soil weight for each sample.

An assessment of the soil-air interface was also performed to determine a separate calibration for the near surface (15cm) reading (Evett et.al., 2003). A depth control stand similar to the one described in *Evett et. al. 2003* was built from 2" electrogalvanized steel pipe and plate base. The device slips over the access tube with the distance from the bottom of the gauge body to the surface set at 105 cm. Cable stops were adjusted to position the center of the detector at the ground surface and 10 cm increments above and below to 50 cm as well as the 15 cm and 45 cm below ground depths. A dry site was selected and calibration was performed similar to the one

described above except that a single access port was installed and the depth control stand used for taking readings. For the wet end, a plastic 208-L drum was packed with the silt loam mixture, a sealed access port installed and then saturated from the bottom. The water content for both the 15cm and 30-195 cm ranges were assumed to be linear functions of the count ratio, defined as the individual counts divided by the standard count.

The depth control stand was used for the calibration procedure but not for the seasonal measurements. An elevation survey of the PHB survey was performed twice during the study and showed an elevation change of <1 cm. Each access port at the PHB is set 10 cm above the ground and provided an accurate control of the NP measurement depth at each location. The remaining problem with this arrangement is that the probe housing is located too close to the soil, which may still influence the near-surface reading.

B.3 Results and Discussion

B.3.1 Wide Offset Reflection

From the CMP surveys, the optimal antenna separation for distinguishing the ground wave signal from the ground-coupled air wave was determined to be 3.5 m. If the time separation is too short, the air wave will interfere with the later arriving ground wave and potentially cause an incorrect selection for the onset of the arrival and its amplitude. An antenna separation too large will cause the amplitude to become too weak to be reliably determined. For the January and March GPR data, the ground wave is a strong, easily seen event. The May data show a less coherent ground wave. Weak ground wave signals occurred during September making reliable selection difficult, likely increasing the error in calculated water-content values (Fig. 4).

B.3.2 Ground-Wave Sampling Depth

Based on the velocities observed at the PHB, the sampling depth was predicted to be between 30 and 80 cm using equations 3 and 4. Knowledge of the ground wave sampling depth is of prime importance when using GPR to measure soil water content; however, significant variability has been observed in practice. Studies have reported ground-wave depth of penetration using 100-MHz signals from 30 cm to 85 cm (Galagedara et al., 2005a and b).

For this study, GPR survey lines were located several meters from the NP and TDR measurement stations. Individual measurements obtained from the various modalities were not collected at the same spatial location, and therefore could not be compared point for point. To overcome this difficulty, water storage at each station were spatially averaged over the barrier surface and compared to spatially averaged GPR water content values for each survey date. This was done using both NP and TDR acquired values. By using this method, it is implicitly assumed that ground-wave sampling depths do not vary significantly across the surface for a given date. The difference between the averaged GPR values and the averaged water storage from the surface to each depth was calculated (Table 1). The depth corresponding to the minimum error was chosen as sampling depth. The average, the GPR sampling depth for all measurement dates was found to be 37.5 cm using the TDR values and 30 cm using NP. The observed weak dependence of the ground-wave sampling depth on water storage supports our use of spatial averages for comparison.

Galagedara et al. 2003a performed a similar analysis by vertically installing TDR probes of different lengths at the midpoint between 100-MHz antennas and compared water-content values to estimate the ground-wave sampling depth. Correlations between GPR measurements and co-located water contents using TDR and/or gravimetric analyses have been performed by several researchers (Lesmes et al., 1999, Grote et al., 2003, Huisman et al., 2001). Collecting co-located GPR, TDR, and gravimetric water-content measurements would be the preferred method to minimize any errors caused by spatial variation. For this study, collecting co-located measurements was not used because of concerns with additional disturbance to the site. Permanent emplacement of both the TDR and NP access ports allowed for a single initial ground disturbance.

GPR-estimated water content consistently overestimated both the NP and TDR values; consequently, the highest correlation occurred at the depth with the highest water content. For the January, March, and May survey dates, a minimum error corresponding to the estimated sampling depth was readily observed. The minimum observed in September was not as obvious, likely because water content was nearly uniform for all depths. For the selected sampling depths, GPR water content overestimated the NP and TDR by 0.032 $m^3\ m^{-3}$ and 0.016 $m^3\ m^{-3}$ respectively. It should be noted that although the maximum water content that was observed increased seasonally, the general shape of the depth profile was mostly unchanged. In particular,

the depth corresponding to the maximum water content was nearly static. Slowly percolating winter precipitation followed by increased evapotranspiration in the spring and summer interact to maintain the high moisture layer at a nearly constant depth.

B.3.3 Site-Specific Petrophysical Relationship

The relationship between water content and apparent permittivity developed using TDR may not be applicable to GPR operating at 100 MHz. Electrical permittivity is a measure of a material's ability to polarize when subjected to an electric field. Materials in general do not respond instantaneously to an applied field and therefore exhibit frequency dependence. The electrical permittivity is often treated as a complex quantity, where both the frequency dependant magnitude and phase can be specified. For an isotropic material, the frequency- and temperature-dependant complex permittivity ε* is given as (Schwartz et. al., 2009)

$$\varepsilon^*(\omega,T)=\varepsilon'(\omega,T)-j\varepsilon''(\omega,T)-j\frac{\sigma_0(T)}{\omega\varepsilon_0} \tag{B.5}$$

where ε' and ε'' are the real and imaginary parts of the electrical permittivity, ω is the angular frequency, T is temperature, σ_0 is the DC electrical conductivity, ε_0 is the electrical permittivity of a vacuum, and $j = \sqrt{(-1)}$.

For transverse electromagnetic wave propagation, the apparent permittivity is

$$\kappa_a=\frac{\varepsilon'}{2}\left(1+\sqrt{\tan^2\delta+1}\right) \tag{B.6}$$

where tanδ is the loss tangent defined as the ratio of the real to imaginary components of the electrical permittivity.

Loss mechanisms associated with dielectric polarization and electrical conduction losses as well as frequency dependant attenuation can have a significant effect on the measured phase velocity. Mixtures of individual constituents with different electrical permittivity and conductivity give rise to Maxwell-Wagner polarization often resulting in enhanced bulk permittivity for low frequencies (<100 MHz) (Chen and Or, 2006). To assess the effect of from electrical conduction losses, bulk electrical conductivity of the silt loam mixture was measured at various water contents. Measured values were relatively small and spanned an order of magnitude, ranging from 0.003 S m^{-1}at a water content of 0.05 m^3 $m^{-3}$to 0.03 S m^{-1} at 0.25 m^3 m^{-}

^{3}. Seasonal electromagnetic induction surveys were also performed at the PHB and showed results similar to range defined from the TDR acquired values (Clement and Ward, 2008). The frequency dependant effects on the apparent permittivity were not directly measured but may contribute to the discrepancies between the GPR and TDR measurements.

Some insight into the temperature effects can be obtained by calculating the variation of the TDR acquired water contents that are observed over an entire day. For each GPR measurement date, the average hourly TDR water content at each depth was tabulated. Water content values were mostly scattered about the average value and showed small standard deviations (Table 2).

B.3.4 Seasonal Trends

Measurements of soil water storage obtained using GPR ground-wave velocities, TDR, and NP over the course of the experiment showed similar responses to seasonal precipitation, wettest during the winter and continually drying through the summer months The GPR surveys showed a high level of spatial detail across the site (Fig. 6). Water-content measurement depths are different for the NP and segmented TDR probes. To directly compare the measurements from both methods, adjacent TDR values were linearly interpolated to intermediate NP depths and the average absolute error for each depth was calculated. The average absolute error between the NP and TDR profiles for all eight locations and measurement dates was 0.009 m^3 m^{-3}. The depth profiles for each method compare fairly well; however, the larger sensing volume of the NP appeared to smooth the finer scale variations (Figures 7a and b).

At the PHB, the ground-wave amplitudes weakened from March to September then increased again in January. A decrease in amplitude decreases the signal-to-noise ratio, increasing errors in accurately selecting arrival times. Although the relationship can create processing difficulties, it provides a secondary means of measurement. Similar to the EM velocity, the amplitude of the ground wave is significantly affected by soil water content. The amplitude of the ground wave has been shown to increase as $\sqrt{\kappa}$ relative to the air wave amplitude (Du and Rummel, 1994). Thus, the ground wave is better observed in comparatively wetter soil. Amplitude analysis at the PHB indicates that water content decreases during the spring and summer months and is replenished in the winter months, qualitatively corroborating the results obtained by velocity analysis.

B.4 CONCLUSIONS

Both GPR and TDR have great potential to enable observation of changes in water content that occur within surface barriers. TDR can be readily used for automated measurements of water content, recording a nearly continuous temporal data set at a limited number of spatial locations. TDR also is able to effectively measure water-content depth profiles within the barrier, which could also be used to determine GPR ground-wave sampling depths. Changes in the GPR travel time and amplitude character were easily observed over the course of our experiment corresponding with seasonal water content changes. Amplitude analysis indicates that the water content changes in a manner similar to the EM velocity analysis.

Our goal was to investigate the use of GPR applied in conjunction with point measurements requiring only an initial ground disturbance to provide an improved barrier-monitoring system. GPR proved successful at imaging changes in soil water storage over the year. GPR was able to show much more spatial detail then from the fixed point measurements. In addition to the large spatial sampling density, using GPR to determine soil water storage has the advantage of being non-intrusive.

Acknowledgements

This manuscript was written primarily with funds provided by the U.S. Department of Energy Environmental Management program. Data collection and analysis were supported by the former EM-50 program and the 200-BP-1 Monitoring project managed by Fluor Hanford Inc. The authors are indebted to Dennis Dauble for his support in preparing this manuscript. Pacific Northwest National Laboratory is operated for the U.S. Department of Energy by Battelle under Contract DE-AC06-76RL01830.

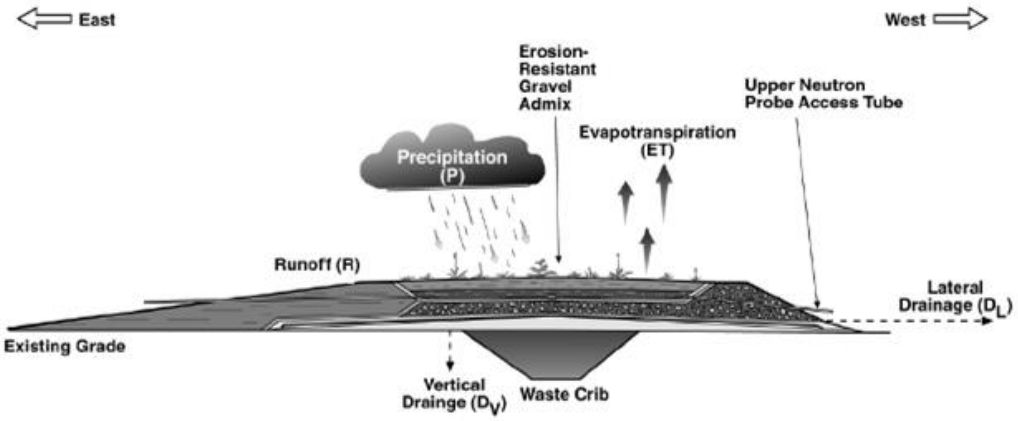

Figure B.1 Schematic cross section of the prototype Hanford barrier showing the construction detail and relative thickness of the various layers.

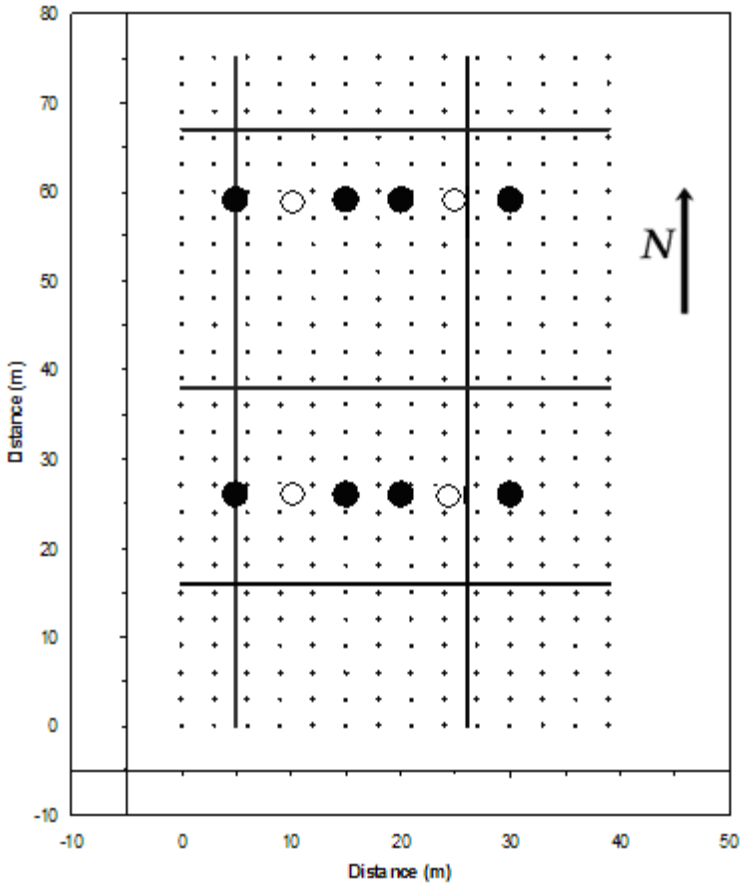

Figure B.2 Schematic showing the measurement locations used in the study. Solid lines show the GPR survey lines, large solid circles mark stations with both the TDR and NP measurements, large open circles mark where only neutron measurements were collected and the small crosses mark the survey grid.

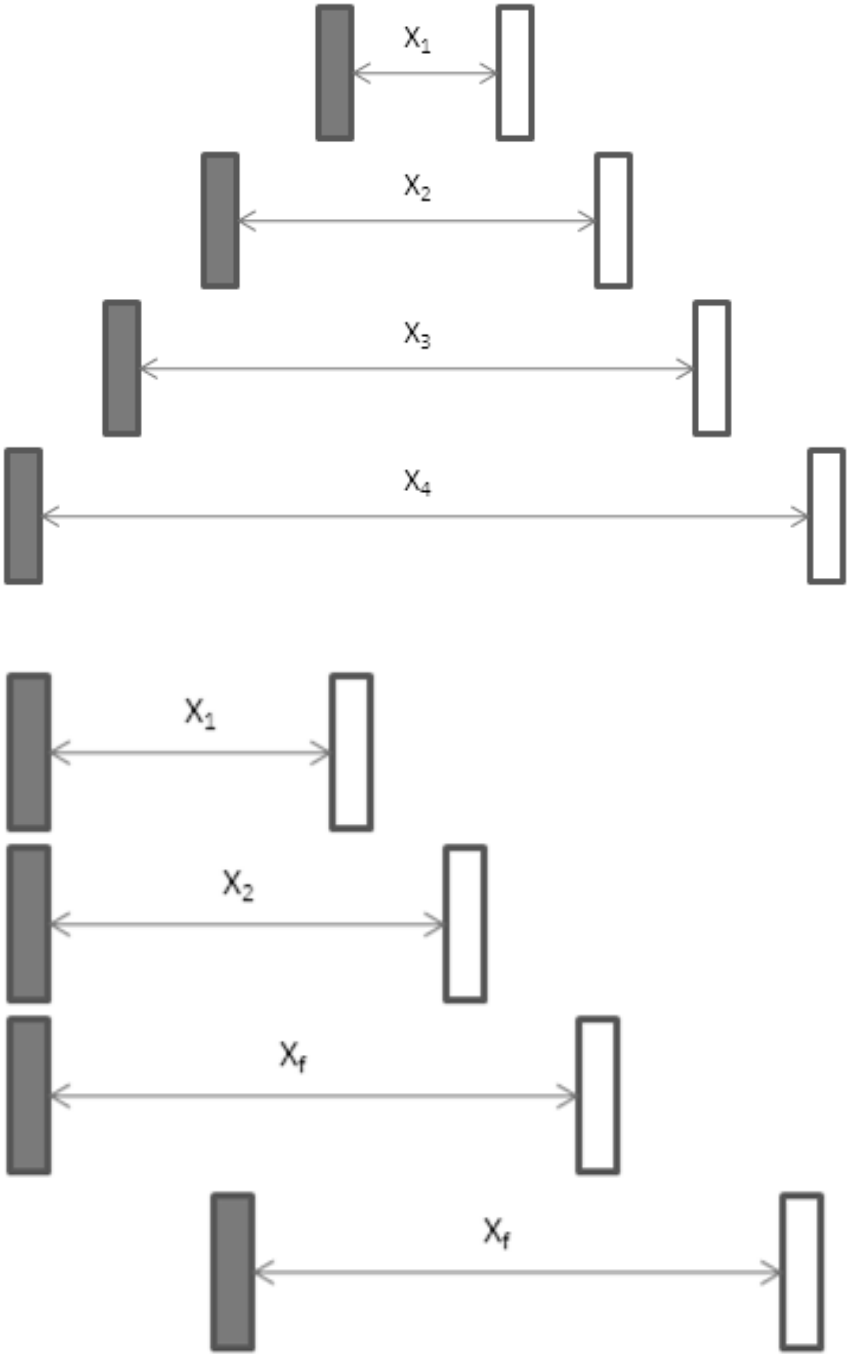

Figure B.3 Survey schematics: (a) the common midpoint (CMP) survey, where antennas were simultaneously moved away from their midpoint with traces recorded at separations *X*1, *X*2, …, etc.; and (b) the wide-offset reflection survey, where antennas were simultaneously moved together, starting with a CMP-like survey, and then continuing in the same direction but at a relatively large separation, *X*f. Dark shaded rectangles represent ground-penetrating radar transmitter antenna and lighter shaded rectangles represent receiver antenna.

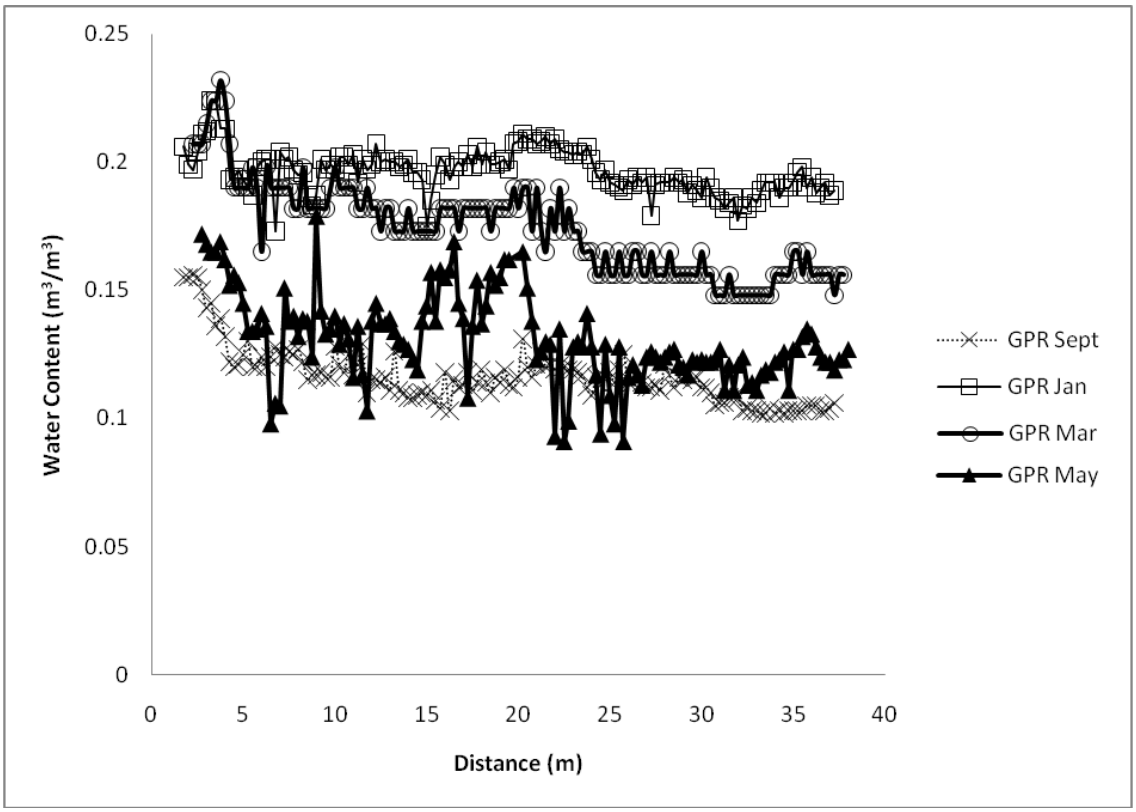

Figure B.4 Arrivals recorded in the WOR profiles. The direct ground wave and reflection can provide estimates of the EM velocity of the surface between the antennas.

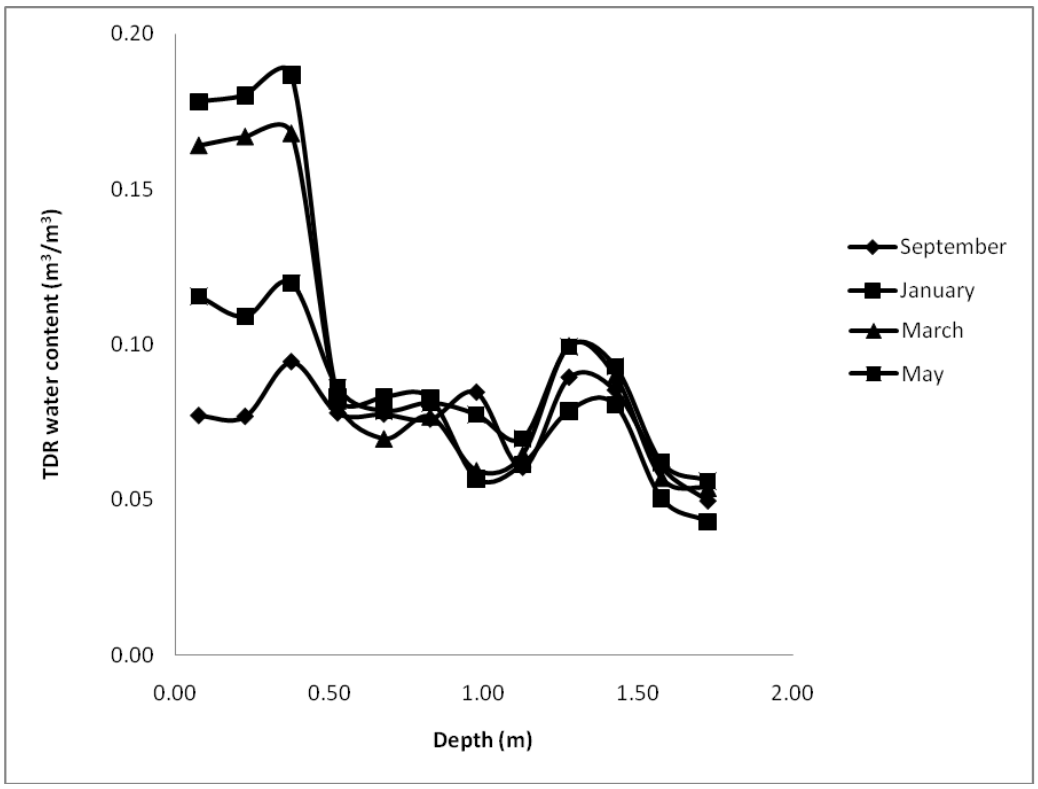

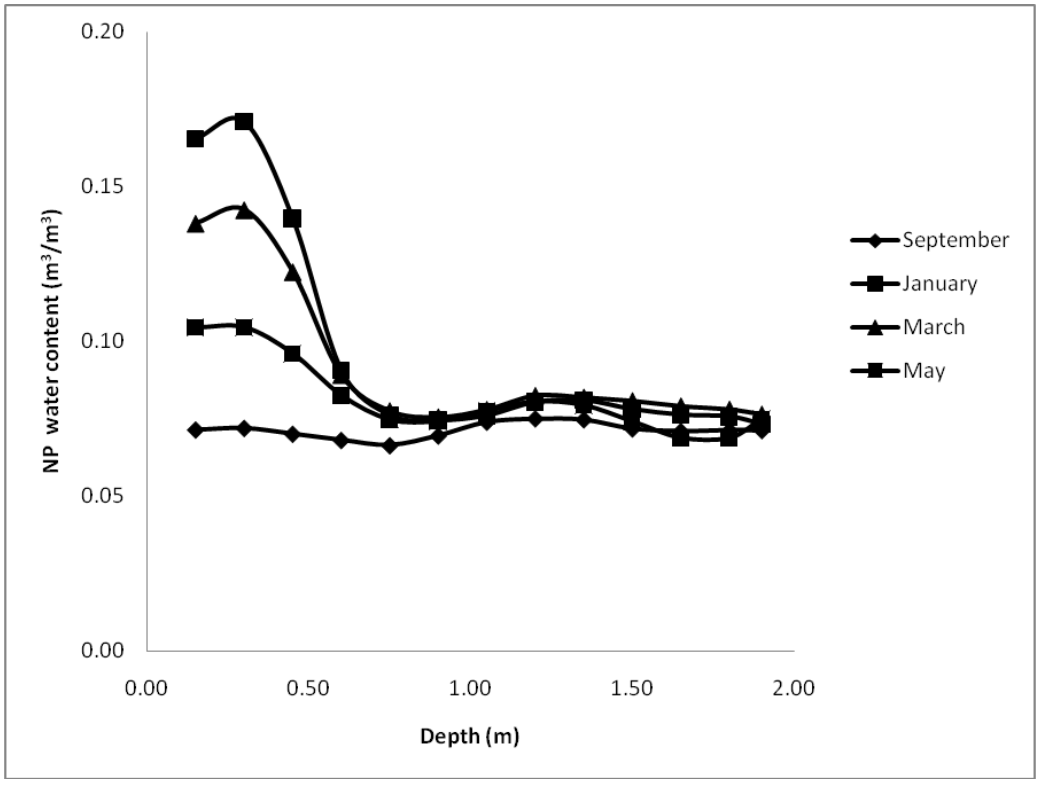

Figure B.5 Water content profiles from (a) time-domain reflectometry (TDR) and (b) neutron probe (NP).

Table B.1 Comparison of GPR water content to TDR and NP water contents average from the surfaced to each depth.

Neutron Probe				
	Average Absolute Error (m^3 m^{-3})			
Depth (m)	Sept	Jan	Mar	May
0.15	0.0428	0.0299	0.0329	0.0247
0.30	0.0426	0.0272	0.0307	0.0246
0.45	0.0431	0.0367	0.0366	0.0274
0.60	0.0439	0.0537	0.0479	0.0322
0.75	0.0447	0.0668	0.0570	0.0367
0.90	0.0447	0.0758	0.0634	0.0397
1.05	0.0441	0.0820	0.0677	0.0414
1.20	0.0434	0.0862	0.0703	0.0423
1.35	0.0430	0.0893	0.0724	0.0432
1.50	0.0430	0.0921	0.0742	0.0444
1.65	0.0430	0.0946	0.0758	0.0458
1.80	0.0430	0.0967	0.0772	0.0470
1.90	0.0430	0.0986	0.0785	0.0476
TDR				
Depth (m)	Sept	Jan	Mar	May
0.075	0.0372	0.0172	0.0068	0.0137
0.225	0.0374	0.0162	0.0054	0.0169
0.375	0.0315	0.0137	0.0046	0.0144
0.525	0.0328	0.0383	0.0257	0.0216
0.675	0.0336	0.0531	0.0409	0.0274
0.825	0.0344	0.0630	0.0498	0.0308
0.975	0.0337	0.0738	0.0586	0.0338
1.125	0.0362	0.0813	0.0646	0.0370
1.275	0.0350	0.0853	0.0653	0.0362
1.425	0.0344	0.0882	0.0669	0.0362
1.575	0.0361	0.0934	0.0712	0.0390
1.725	0.0385	0.0983	0.0750	0.0418

Table B.2 TDR water contents and daily standard deviations at each depth for GPR survey dates. Daily variations are used to assess apparent permittivity temperature effects.

Sept			Jan		Mar		May	
Depth (m)	Average($m^3 m^{-3}$)	s ($m^3 m^{-3}$)	Average($m^3 m^{-3}$)	s ($m^3 m^{-3}$)	Average($m^3 m^{-3}$)	s ($m^3 m^{-3}$)	Average($m^3 m^{-3}$)	s ($m^3 m^{-3}$)
0.075	0.0771	0.0073	0.1782	0.0071	0.1641	0.0054	0.1154	0.0068
0.225	0.0768	0.0104	0.1802	0.0093	0.1670	0.0043	0.1090	0.0042
0.375	0.0944	0.0057	0.1867	0.0076	0.1680	0.0042	0.1197	0.0053
0.525	0.0779	0.0049	0.0831	0.0254	0.0819	0.0317	0.0860	0.0171
0.675	0.0776	0.0187	0.0832	0.0185	0.0696	0.0152	0.0786	0.0159
0.825	0.0759	0.0039	0.0826	0.0058	0.0767	0.0057	0.0812	0.0059
0.975	0.0846	0.0053	0.0568	0.0246	0.0593	0.0195	0.0774	0.0148
1.125	0.0604	0.0023	0.0614	0.0068	0.0645	0.0043	0.0698	0.0061
1.275	0.0894	0.0040	0.0786	0.0062	0.0996	0.0045	0.0993	0.0056
1.425	0.0853	0.0038	0.0805	0.0074	0.0898	0.0051	0.0929	0.0046
1.575	0.0605	0.0054	0.0505	0.0066	0.0569	0.0124	0.0620	0.0101
1.725	0.0496	0.0038	0.0430	0.0044	0.0537	0.0056	0.0561	0.0078

BIBLIOGRAPHY

Aki, K., and P. G. Richards, 2002, Quantitative seismology, 2nd ed.: University Science Books.

Ammon, C. J., and J. E. Vidale, Tomography without rays, *Seism. Soc. Am. Bull.*, **83**, 509-528, 1993.

Annan, P. 2005. GPR methods for hydrogeological studies. In: Rubin Y. and Hubbard S.S. (eds), *Hydrogeophysics*,. Ser. 50, *Springer*, Dordrecht, pp. 185-214.

Archie, G.E. 1942. The electrical resistivity log as an aid in determining some reservoir characteristics. *Petroleum transactions of AIME 146*:54-62.

Aster, R. C., Thurber, C. H., & Borchers, B., 2005. *Parameter estimation and inverse problems*. Amsterdam: Elsevier Academic Press.

Barker, R.D., 1979. Signal contribution sections and their use in resistivity studies. *Geophys. J. Royal Astron. Soc.*, **59**, 123-129.

Berktold, A., K. G. Wollny, and H. Alstetter. 1998. Subsurface moisture determination with the ground wave of GPR. In Proceedings from GPR '98, 7th International Conference, May 27-30, 675-680, Univ. of Kansas, Lawrence, Kansas

Binley, A., G. Cassiani, R. Middleton, and P. Winship. 2002. Vadose zone model parameterisation using cross-borehole radar and resistivity imaging. *J. Hydrol*. 267(3 - 4):147-159.

Bleszynski, E., M. Bleszynski, and T. Jaroszewicz (1996), AIM: Adaptive integral method for solving large-scale electromagnetic scattering and radiation problems, Radio Sci., 31(5), 1225–1251, doi:10.1029/96RS02504

Binley A. and Kemna A. 2005. DC resistivity and induced polarization methods. In: Y. Rubin and S. Hubbard, eds. *Hydrogeophysics*. Chapter 5, pp 129–156. The Netherlands, Springer.

Buursink, M.L., Johnson, T.C., Routh, P.S., and Knoll, M.D., 2008, Cross-hole radar propagation velocity tomography using Fresnel volume sensitivities. *Geophys. J. Int.,* **172** (1), 1-17.

Cerveny, V.& Soares, J., 1992. Fresnel Volume ray tracing, *Geophysics*, **57**(7), 902-915.

Červený, V., 2001. Seismic Ray Method, Cambridge Univ. Press, New York.

Chavent, G., 1974. Identification of function parameters in partial differential equations, in Identification of parameter distributed systems, eds. Goodson, R.E. & Polis, New-York, ASME 1974.

Chen, P., Jordan, T.H. & Zhao, L., 2007. Full 3D waveform tomography: a comparison between the scattering-integral and adjoint-wavefield methods. *Geophys. J. Int.,* **170,** 175–181.

Chen, Y. and D. Or. 2006. Effects of Maxwell-Wagner polarization on soil complex dielectric permittivity under variable temperature and electrical conductivity. Water Resour. Res. Vol. 42 (6), W06424

Chew, W.C., 1990. Waves and Fields in Inhomogeneous Media, Van Nostrand Reinhold, New York.

Christensen, N.B., 2014 Sensitivity functions of transient electromagnetic methods, *Geophysics*, **79**(4), E167-E182.

Clement, W. P., and A. L. Ward. 2008. GPR Surveys across a Prototype Surface Barrier to Determine Temporal and Spatial Variations in Soil Moisture Content. In Chapter 23, The Handbook of Agricultural Geophysics, American Society of Agricultural Engineers, B. J. Allred, M. R. Ehsani, and J. J. Daniels (eds.), CRC Press, 305-315.

Dahlen, F.A., Hung, S.-H. & Nolet, G., 2000. Fréchet kernels for finite frequency traveltimes–I. Theory, *Geophys. J. Int.*, **141,** 157–174.

Dahlin, T. and Zhou, B., 2004. A numerical comparison of 2-D resistivity imaging with 10 electrode arrays. *Geophys. Prosp.*, **52**, 379-398.

Daily, W., and E. Owen. 1991. Cross-borehole resistivity tomography. *Geophysics. 56*:1228-1235.

Davis, P. J., Circulant Matrices, Wiley, NewYork, 1979.

Davis, J. L.and A.P. Annan. 1989. Ground penetrating radar for high resolution mapping of soil and rock stratigraphy. *Geophys. Prospect. 37* (5), 531–551.

Day-Lewis, F.D., J.M. Harris, and S.M. Gorelick. 2002. Time-lapse inversion of crosswell radar data: *Geophysics*. .67:1740-1752.

Dresel, P.E., D.M. Wellman, K.J. Cantrell, and M.J. Truex. 2011. Review: Technical and Policy Challenges in Deep Vadose Zone Remediation of Metals and Radionuclides. *Environ. Sci. Technol*. 45(10):4207-4216.

DOE. 2008. Deep Vadose Zone Treatability Test Plan for the Hanford Central Plateau. DOE/RL-2007-56, Rev. 0, U.S. Department of Energy Richland Office, Richland, WA.

Du, S., and P. Rummel.1994. Reconnaissance studies of moisture in the subsurface with GPR. In Proceedings of the fifth international conference on Ground Penetrating Radar, GPR ‘94, 1241-1248, Univ. of Waterloo, Kitchener, Ontario, Canada.

Ernst, J. R., Green, A. G., Maurer, H., and Holliger, K., 2007. Application of a new 2D time-domain full-waveform inversion scheme to crosshole radar data. *Geophysics*, **72**(5):J53–J64.

Evett, S. R., and J. L. Steiner. 1995. Precision of neutron-scattering and capacitance type soil-water content gauges from field calibration. Soil Science Society of America Journal 59:961-968.

Evett, S.R., J.A. Tolk, and T.A. Howell. 2003. A depth control stand for improved accuracy with theneutron probe. Vadose Zone Journal. Vol. 2. pp. 642–649.

Evett, S.R., J.A. Tolk, and T.A. Howell. 2005. TDR laboratory calibration in travel time, bulk electrical conductivity, and effective frequency. Vadose Zone J. 4:1020–1029

Evett, S.R. 2005. International Soil Moisture Sensor Comparison. In Irrigation Insights No. 1, Second Edition, Soil Water Monitoring, P. Charlesworth (ed.). Land & Water Australia, Braddon, Australia. pp. 68-71.

Fang, S., G. Z. Gao, and C. Torres-Verdin, 2006. Efficient 3D electromagnetic modeling in the presence of anisotropic conductive media, using integral equations, Exploration Geophysics,Vol. 37, 239-244, 2006.

Fayer, M. J. and G. W. Gee. 2006. Multiple-year water balance of soil covers in a semiarid setting. J. of Envir. Quality 35(1):366-377.

Ferré, T., L. Bentley, A. Binley, N. Linde, A. Kemna, K. Singha, K. Holliger,J. A. Huisman, and B. Minsley. 2009. Critical steps for the continuing advancement of hydrogeophysics. *Eos Trans. AGU*. 90(23):200, doi:10.1029/2009EO230004.

Friedman, S.P. 2005. Soil properties influencing apparent electrical conductivity: a review. *Comp. and Elec. in Ag. 46*:47-50.

Galagedara, L. W., G. W. Parkin, and J. D. Redman. 2003. An analysis of the GPR direct ground wave method for soil water content measurement. Hydrol.Proc. 17:3615–3628.

Galagedara, L. W., G. W. Parkin, J. D. Redman, P. von Bertoldi, and A. L. Endres.2005a. Field studies of the GPR ground wave method for estimating soilwater content during irrigation and drainage. J. Hydrol. 301:182-197.

Galagedara, L.W., J.D. Redman, G.W. Parkin, and A.P. Annan. 2005b. Numerical modeling of GPR to determine the direct ground wave sample depth. Vadose Zone J. 4:1096-1106.

Gan, H. and Chew, W. C., 1994, A discrete BCG-FFT Algorithm for Solving 3D inhomogeneous Scatterer Problems, Electromagnetic Laboratory, Department of Electrical and Computer Engineering, University of Illinois, Urbana, IL, 61801.

Gardner, W., and D. Kirkham. 1952. Determination of soil moisture by neutron scattering. Soil Science 73:391-401.

Gee, L.S. & Jordan, T.H., 1992. Generalized seismological data functionals, *Geophys. J. Int.*, **111,** 363–390.

Graves, R. W. 1996. Simulating seismic wave propagation in 3D elastic media using staggered-grid finite differences. Bulletin of the Seismological Society of America, 86(4):1091-1106

Greacen, E.L., R.L. Correll, R.B. Cunningham, O.C. Johns, and K.D. Nichols. 1981. Calibration. In Soil Water Assessment by the Neutron Method, CSIRO, Melbourne, Australia, pp. 50-78.

Greaves, R J., D. P. Lesmes, and M. N. Toksoz. 1996. Velocity variations and water content estimates from multi-offset, ground-penetrating radar. Geophysics, 61:683-695.

Grote, K., S. Hubbard, and Y. Rubin. 2003. Field-scale estimation of volumetric water content using ground-penetrating radar ground wave techniques. Water Resources Research **39**(11).

Grote, K., C. Anger, B. Kelly**,** S. Hubbard, and Y. Rubin. 2010. Characterization of soil water content variability and soil texture using GPR groundwave techniques. *J. Environmental and Engineering Geophysics.* 15(3):93-110.

Hamamoto S, P Moldup, K Kawamoto, T Komatsu. 2010. Excluded-Volume Expansion of Archie's Law for Gas and Solute Diffusivities and Electrical and Thermal Conductivities in Variably Saturated Porous Media. *Water Resources Research* 46, doi:10.1029/2099WR00842r.

Han M, S Youssef, E Rosenberg, M Fleury, P Levitz. 2009. Deviation from Archie's Law in Partially Saturated Porous Media: Wetting Film Versus Disconnectedness of the Conducting Phase. *Physical Review E*. 79,doi:10.1103/PhysRevE.79.031127.

Harrington, R. F., 1968. Field Computation by Moment Methods, R. E. Krieger, Malabar, Fla, USA.

Hayley, K., L.R. Bentley, and A. Pidlisecky. 2010. Compensating for temperature variations in time-lapse electrical resistivity difference imaging. *Geophysics. 7 (4): WA51–WA59. doi: 10.1190/1.3478208.*

Hignett, C., and S.R. Evett. 2002. Neutron Thermalization. Section 3.1.3.10 *In* Jacob H. Dane and G. Clarke Topp (eds.) Methods of Soil Analysis. Part 4 B Physical Methods. pp. 501-521.

Hook, W. R., Livingston, N. J., Sun, Z. J., Hook, P. B. 1992. Remote Diode Shorting Improves Measurement of Soil Water by Time Domain Reflectometry Soil Sci. Soc. Am. J. 56: 1384-1391

Hördt, A., 1998, Calculation of electromagnetic sensitivities in the time domain: *Geophys. J. Int.*, **133**, 713–720. Hubbard, S.S., J.E. Peterson, E.L. Majer, P.T. Zawislanski, J. Roberts, K.H. Williams, and F. Wobber. 1997. Estimation of permeable pathways and water content using tomographic radar data. *The Leading Edge of Exploration*. 16(11):1623-1628.

Hubbard, S.S. and N. Linde, 2011. Hydrogeophysics. In: Peter Wilderer (ed.) Treatise on Water Science, vol. 1. Oxford: Academic Press, pp. 401-434.

Huisman, J. A., C. Sperl, W. Bouten, and J. M. Verstraten. 2001. Soil water content measurements at different scales: accuracy of time domain reflectometry and ground-penetrating radar. *J. Hydrol*. 245:48-58.

Hung, S.-H., Dahlen, F.A. & Nolet, G. 2000. Fréchet kernels for finite frequency travel times, part II: examples, *Geophys. J. Int.*, **141,** 175–203.

Ishimaru, A., 1978. Wave Propagation and Scattering in Random Media, Academic Press, New York.

Jackson, J., 1999. Classical Electrodynamics, 3rd edn, John Wiley, New York.

Jackson, M. J., and D.R. Tweeton. *1994. MIGRATOM* - Geophysical tomography using wavefront migration and fuzzy constraints, Bureau of Mines Report of Investigations 9497, 35 pp.

Jin, J. M., 1993. The Finite Element Method in Electromagnetics. New York: John Wiley & Sons.

Jocker, J., J. Spetzler, D. Smeulders, and J. Trampert, 2006, Validation of first-order diffraction theory for the traveltimes and amplitudes of propagating waves, *Geophysics*, **71**, 167–177.

Johnson, T.C., Routh, P.S. & Knoll, M.D., 2005. Fresnel volume georadar attenuation-difference tomography, *Geophys. J. Int.*, **162**(1), 9–24.

Kravstov, Yu.A. & Orlov, Yu.I. 1980. Geometric optics of inhomogeneous media: Nauka, Moscow (in Russian), p. 750-761.

Kravtsov, Y.A., 1988. Rays and caustics as physical objects, in Progress in Optics, Vol. XXVI, pp. 227–348, ed. Wolf, E., Elsevier, Amsterdam.

Laloy, E., N. Linde, and J. A. Vrugt. 2012. Mass conservative three-dimensional water tracer distribution from Markov chain Monte Carlo inversion of time-lapse ground-penetrating radar data. *Water Resour. Res.* 48, W07510, doi:10.1029/2011WR011238.

Lanczos, C., 1996. Linear Differential Operators, Society for Industrial Mathematics.

Ledieu, J., P. De Ridder, P. De Clerck, and S. Dautrebande. 1986. A method of measuring soil moisture by time-domain reflectometry. *J. Hydrol*. 88:319-328.

Lesmes, D., R. J. Herbstzuber, and D. Wertz. 1999. Terrain permittivity mapping: GPR measurements of near-surface soil moisture. Symposium on the Application of Geophysics to Engineering and Environmental Problems, Environ. and Eng. Geophys. Soc., Oakland, Calif.

Lesmes, D. and Friedman, S., 2005. Electrical and hydrological properties, Chapter 4. In *Hydrogeophysics*; Rubin, Y., Hubbard, S., Eds.; Springer: The Netherlands, pp 87–128.

Liu Q.,Tromp J., Finite-frequency kernels based on adjoint methods. Bulletin of the Seismological Society of America 96 (6), 2383-2397

Luo, Y., and G. T. Schuster, 1991,Wave-equation traveltime inversion: *Geophysics*, **56**, 645–653.

Marfurt, K.J., 1984. Accuracy of finite-difference and finite-element modeling of the scalar and elastic wave equations, Geophysics, 49, 533–549.

Marquering, H., Dahlen, F. & Nolet, G., 1999. Three-dimensional sensitivity kernels for finite-frequency traveltimes: the banana-doughnut paradox, *Geophys. J. Int.*, **137,** 805–815.

Meles, G. A., Van der Kruk, J., Greenhalgh, S. A., Ernst, J. R., Maurer, H., and Green, A. G. 2010. A new vector waveform inversion algorithm for simultaneous updating of conductivity and permittivity parameters from combination crosshole/borehole-tosurface GPR data. IEEE Transactions on Geoscience and Remote Sensing, 48(9):3391–3407.

Meles G.A, S.A Greenhalgh, J. Kruk, A.G. Green, H. Maurer, 2012. Taming the non-linearity problem in GPR full-waveform inversion for high contrast media, *J. Appl. Geophys.*, **78**, 31–43.

Menke, W., 1984. Geophysical data analysis: Discrete inverse theory. Orlando, Fla: Academic Press.

Mora, P., 1987. Nonlinear two-dimensional elastic inversion of multioffset seismic data. Geophysics, 52(9):1211–1228.

Nolet, G., 1987. Seismic wave propagation and seismic tomography, in Seismic Tomography with Applications in Global Seismology and Exploration Geophysics, pp. 1–23, ed. Nolet, G., Reidel, Dordrecht.

Oostrom, M., T.W. Wietsma, C.E. Strickland, V.L. Freedman, and M.J. Truex. 2011. Sensor and numerical simulator evaluation for porous medium desiccation and rewetting at the intermediate laboratory scale. Accepted for publication, *Vadose Zone J.*

Oostrom, M., T.W. Wietsma, J.H. Dane, M.J. Truex, and A.L. Ward. 2009. Desiccation of Unsaturated Porous Media: Intermediate-Scale Experiments and Numerical Simulation. *Vadose Zone J*. 8:643–650.

Or, D. and J. M. Wraith. 1999. Temperature effects on soil bulk dielectric permittivity measured by time domain reflectometry: A physical model. *Water Resour. Res.* 35(2):371–383, doi:10.1029/1998WR900008.

Peterson, J. 2001. Pre-inversion corrections and analysis of radar tomographic data. *J. Environ. Eng. Geophysics* **6** (1), 1-18.

Plessix, R. E., 2006, A review of the adjoint-state method for computing the gradient of a functional with geophysical applications: *Geophys. J. Int.*, **167**(2), 495–503.

Pratt, R. G., 1999. Seismic waveform inversion in the frequency domain, part 1: Theory and verification in a physical scale model. Geophysics, 64(3):888–901.

Pujol, J., 2003. Elastic wave propagation and generation in seismology, Cambridge University Press

Revil, M., M. Karaoulis, T. Johnson, and A. Kemna. 2012. Some low-frequency electrical methods for subsurface characterization. *Hydrogeology Journal* 15(16). doi: 10.1007/s10040-011-0819-x.

Robinson, D. A., S. B. Jones, J. M. Wraith, D. Or, and S. P. Friedman. 2003. "A Review of Advances in Dielectric and Electrical Conductivity Measurement in Soils Using Time Domain Reflectometry." Vadose Zone J 2(4):444-475.

Rubin Y and Hubbard S., 2005. *Hydrogeophysics*, Water and Science Technology Library, vol 50. The Netherlands: Springer.

Ruijun, M., A. McBratney, B. Whelan, B. Minasny, and M. Short. 2011. Comparing temperature correction models for soil electrical conductivity measurement. *Prec. Ag. 12*:55-66, doi:10.1007/s11119-009-9156-7

Schwartz, R.C., S.R. Evett, M.G. Peltier and J.M. Bell. 2009. Complex permittivity model for time domain reflectometry soil water content sensing: I. Theory. Soil Sci. Soc. Am. J. 73:886-897

Seyfried, M. S. and L. E. Grant. 2007. Temperature Effects on Soil Dielectric Properties Measured at 50 MHz. Vadose Zone J 6(4):759-765.

Shen, Y., Zhang, Z., & Zhao, L., 2008. Component-dependent Fréchet sensitivity kernels and utility of three-component seismic records, *Bull. Seism. Soc. Am.*, **98(**5**),** 2517–2525.

Sheriff, R. E., and L. P. Geldart, 1982, Exploration seismology: Cambridge University Press.

Slater, L.D., and D.P. Lesmes. 2002. Electrical-hydraulic relationships observed for unconsolidated sediments. *Water Resour. Res. 38*:1213-1225.

Snieder, R. & Lomax, A., 1996. Wavefield smoothing and the effect of rough velocity perturbations on arrival times and amplitudes, *Geophys. J. Int.*, **125**, 796–812.

Snieder, R., 2002. General theory of elastic wave scattering , in Scattering and Inverse Scattering in Pure and Applied Science , Eds. Pike, R. and P. Sabatier, Academic Press, San Diego, 528-542

Strickland CE, TC Johnson, and RI Odom. 2015. "Three-Dimensional Fréchet Sensitivity Kernels for Electromagnetic Wave Propagation." Geophysical Journal International (in review)

Taflove, A. and Brodwin, M. E., 1975. Numerical-solution of steady-state electromagnetic scattering problems using time-dependent maxwells equations. IEEE Transactions on Microwave Theory and Techniques, 23(8):623–630.

Tarantola, A., 1987. Inverse Problem theory, Elsevier, Amsterdam.

Tarantola, A., 2004. Inverse Problem Theory and Methods for Model Parameter Estimation. SIAM: Society for Industrial and Applied Mathematics.

Tian, Y., R. Montelli, G. Nolet, and F. A. Dahlen, 2007, Computing traveltime and amplitude sensitivity kernels in finite-frequency tomography: *J. Comp. Phys.*, **226**, 2271–2288.

Tølbøll, R. J., and N. B. Christensen, 2007, The sensitivity functions of frequency-domain magnetic dipole-dipole systems: *Geophys.*, **72**(2), F45–F56

Topp, G. C., J. L. Davis, and A. P. Annan, 1980. Electromagnetic determination of soil water content: Measurements in coaxial transmission lines. *Water Resour. Res.* 16(3):574–582, doi:10.1029/WR016i003p00574.

Topp, G.C. and P.A. Ferré. 2002. 3.1 Water content. p. 417-545. In J.H. Dane and G.C. Topp (eds.) Methods of Soil Analysis Part 4 Physical Methods, SSSA Book Series No. 5, Soil Sci. Soc. Amer., Madison, WI.

Topp, G.C. and W.D. Reynolds. 1998. Time domain reflectometry: a seminal technique for measuring mass and energy in soil. Soil and Tillage Res. 47:125-132.

Tromp, J., Tape, C. & Liu, Q., 2005. Seismic tomography, adjoint methods, time reversal, and banana-doughnut kernels, *Geophys. J. Int.*, **160**, 195–216.

Truex, M.J., M. Oostrom, V.L. Freedman, C.E. Strickland, and A.L. Ward. 2011. Laboratory and Modeling Evaluations in Support of Field Testing for Desiccation at the Hanford Site. PNNL-20146, Pacific Northwest National Laboratory, Richland, WA.

Truex, M.J., M. Oostrom, C.E. Strickland, G.B. Chronister, M.W. Benecke, and C.D. Johnson. 2012a. Field-Scale Assessment of Desiccation Implementation for Deep Vadose Zone Contaminants. Accepted for publication, *Vadose Zone J.*

Truex, M.J., M. Oostrom, C.E. Strickland, T.C. Johnson, V.L. Freedman, C.D. Johnson, W.J. Greenwood, A.L. Ward, R.E. Clayton, M.J. Lindberg, J.E. Peterson, S.S. Hubbard, G.B. Chronister, and M.W. Benecke. 2012b. Deep Vadose Zone Treatability Test for the Hanford Central Plateau: Soil Desiccation Pilot Test Results. PNNL-21369, Pacific Northwest National Laboratory, Richland, WA.

United States Department of Energy. 1996. Focused Feasibility Study of Engineered Barriers for Waste Management Units in the 200 Areas. DOE/RL-93-33, Bechtel Hanford, Inc., Richland, WA.

United States Department of Energy. 1999. 200-BP-1 Prototype Barrier Treatability Test Report. DOE/RL-99-11, U. S. Department of Energy, Richland, WA.

Van Bladel, J., 1961. Some remarks on Green's dyadic for infinite space, *IRE Trans. Antennas Propagat.* **AP-9**, 563-566.

van der Kruk, J., C.P.A. Wapenaar, J.T. Fokkema and P.M van den Berg, 2003. Three-dimensional imaging of multicomponent ground-penetrating radar data, Geophysics, 68, 1241-1254, doi:10.1190/1.1598116

Van Overmeeren, R., S. Sariowan, and J. Geherls. 1997. Ground penetrating radar for determining volumetric soil water content: Results of comparative measurements at two test sites. *J. Hydrol*. 197:316-338.

Vasco, D. & Majer, E., 1993.Wavepath traveltime tomography, Geophys. J. Int., 115**,** 1055-1069.

Vasco, D.W., Peterson, J.E., & Majer, E., 1995. Beyond ray tomography: wavepaths and Fresnel volumes, *Geophysic*s, **60**(6)**,** 1790-1804.

Vereecken H, Binley A, Gassiani G, Revil A, and Titov K (2006) *Applied Hydrogeophysics*, NATO Science Series, Earth and Environmental Science Vol. 71, Springer, Netherlands

Vidale, J. and Clayton, R., 1986. A stable free-surface boundary condition for two-dimensional elastic finite-difference wave simulation. GEOPHYSICS, 51(12), 2247–2249. doi:10.1190/1.1442078

Wang T. and Fang S., 2001, 3-D electromagnetic anisotropy modeling using finite differences, Geophysics Vol. 66, No.5 P. 1386-1398.

Ward, S.H.&Hohmann,G.W., 1988. Electromagnetic theory for geophysical applications, in Electromagnetic Methods in Applied Geophysics, Vol. 1, pp. 131–312, ed. Nabighian, M.N., Society of Exploration Geophysicists, Tulsa, OK.

Ward, A. L., and G. W. Gee. 1997. Performance evaluation of a field scale surface barrier. J. Environ. Qual. 26:694-705.

Ward A. L., M. E. Conrad, W. D. Daily, J. B. Fink, V. L. Freedman, G. W. Gee, G. M. Hoversten, J. M. Keller, E. L. Majer, C. J. Murray, M. D. White, S. B. Yabusaki, and Z. F. Zhang. 2006. Vadose Zone Transport Field Study: Summary Report. PNNL-15443, Pacific Northwest National Laboratory, Richland, WA.

Ward A.L., M. Oostrom, and D.H. Bacon. 2008. Experimental and Numerical Investigations of Soil Desiccation for Vadose Zone Remediation: Report for Fiscal Year 2007. PNNL-17274, Pacific Northwest National Laboratory, Richland, Washington.

Ward AL, SO Link, CE Strickland, KE Draper, and RE Clayton. 2008. 200-BP-1 Prototype Hanford Barrier Annual Monitoring Report for Fiscal Years 2005 Through 2007. PNNL-17176, Pacific Northwest National Laboratory, Richland, WA.

Watanabe, T., T.Matsuoka, and Y. Ashida, 1999, Seismic traveltime tomography using Fresnel volume approach: 69thAnnual International Meeting, SEG, Expanded Abstracts, 1402–1405.

Waxman, M. H., and L.J.M. Smits. 1968. Electrical conduction in oil-bearing sands. *Society of Petroleum Engineers Journal.* 8:107-122.

Waxman, M. H., and E. C. Thomas. 1974. Electrical conductivities in shaly sands: Part 1—The relation between hydrocarbon saturation and resistivity index; Part 2—The temperature coefficient of electrical conductivity. *Journal of Petroleum Technology*. 26:213–225.

White, I., and S. J. Zegelin**.** 1995. Electric and dielectric methods for monitoring soil-water content. In *Handbook of Vadose Zone Characterization and Monitoring*, eds. L. G. Wilson, L. G. Everett, and S. Cullen, Chapter 22, A. F. Lewis, New York.

Wilt, M. J., Alumbaugh. D. L.. Morrison, H.F., Becker, A., Lee, K.H., and Deszcz-Pan, M., 1995. Cross-hole electromagnetic tomography: System design considerations and field results, *Geophysics.* **60**, 871-885.

Woodward, M.J., 1992.Wave-equation tomography, *Geophysics*, **57**(1), 15–26.

Yilmaz, O., 2001. Seismic Data Processing, Society of Exploration Geophysicists, Tulsa

Yomogida, K., 1992. Fresnel zone inversion for lateral heterogeneities in the Earth, PAGEOPH, **138**, 391–406.

Zhang, Z., & Shen, Y., 2008. Cross-dependence of finite-frequency compressional waveforms to shear seismic wave speeds, *Geophys. J. Int.*, **390**, 174, 941–948.

Zhao, L., Jordan, T.H., Olsen, K.B. & Chen, P., 2005. Fréchet Kernels for Imaging regional earth structure based on three-dimensional reference models, *Bull. Seism. Soc. Am.*, **95,** 2066–2080.

Zhdanov, M.S., 2002. Geophysical inverse theory and regularization problems: Elsevier, New York.

Zwamborn, P. and P. M. van den Berg, 1992. The three dimensional weak form of the conjugate gradient FFT method for solving scattering problems. IEEE Transactions on Microwave Theory and Techniques, vol. 40, no. 9, pp. 1757–1766.

VITA

Research interests involve the use of geophysical methods for subsurface characterization and monitoring, primarily related to the injection or extraction of fluids specifically:

- Wave propagation simulation and inversion methods
- Joint hydrological and geophysical inversion
- Field-scale seismic and electromagnetic monitoring of fluid injection and extraction.

Education

B.S. Applied and Computational Mathematical Sciences, University of Washington, 2001
M.S. Chemistry/Chemical Physics, Washington State University, 2007
Ph.D. Geophysics, Earth and Space Sciences, University of Washington, 2015

Professional Experience

Bechtel Hanford Inc., 1999-2000
Richland, WA
Scientist
Groundwater and vadose zone integration project

Pacific Northwest National Laboratory, 2001-Present
Richland, WA
Senior Research Scientist

- Vadose zone transport field study, mock tank leak detection monitoring
- Hanford barrier monitoring project
- Integrated field research challenge, Hanford 300A
- Deep vadose zone treatability test, soil desiccation and reactive gas remediation monitoring
- Pacific northwest seismic network (PNSN), eastern Washington/Hanford network
- Basalt carbon sequestration pilot test
- FutureGen 2.0 carbon sequestration project
- Subsurface technology and engineering research (SubTER)

Publications

2015

Strickland CE, TC Johnson, and RI Odom. 2015. "Three-Dimensional Fréchet Sensitivity Kernels for Electromagnetic Wave Propagation." Geophysical Journal International (in review)

2014

Strickland CE, VR Vermeul, A Bonneville, EC Sullivan, TC Johnson, FA Spane, and TJ Gilmore. 2014. "Geophysical Monitoring Methods Evaluation for the FutureGen 2.0 project." GHGT-12 (2014) 63, pp. 4394-4403. EnergyProcedia. doi:10.1016/j.egypro.2014.11.474

Vermeul VR, CE Strickland, PD Thorne, BN Bjornstad, RD Mackley, ME Kelley, EC Sullivan, MD Williams, JE Amonette, JL Downs, BG Fritz, JE Szecsody, A Bonneville, and TJ Gilmore. 2014. "FutureGen 2.0 Monitoring Program: An Overview of the Monitoring Approach and Technologies Selected for Implementation." ." GHGT-12 (2014) 63, pp. 4062-4070. EnergyProcedia. doi:10.1016/j.egypro.2014.11.438

Sullivan EC, BA Hardage, CE Strickland, A Bonneville, and TJ Gilmore. 2015. "Application of three component VSP technology at seismically difficult sites: An example from the FutureGen 2.0 site, Morgan County, Illinois, USA." GHGT-12 (2014) 63, pp. 5051-5062. EnergyProcedia. doi:10.1016/j.egypro.2014.11.535

Szecsody JE, L Zhong, JN Thomle, VR Vermeul, CE Strickland, MD Williams, J Liu, JP McKinley, ME Bowden, TJ Gilmore, EER Eisenhauer, and F Colwell. 2014. "Influence of scCO2 Injection on Precipitation and Metals Migration, and Changes in Electrical Resistivity." In International Conference on Greenhouse Gas Technologies (GHGT). PNWD-SA-10402, Battelle—Pacific Northwest Division, Richland, WA.

Vermeul VR, JE Amonette, CE Strickland, JE Szecsody, MD Williams, A Bonneville, TA Johnson, TC Johnson, M Oostrom, SL Porse, FA Spane, CF Spencer, and JN Thomle. 2014. FutureGen 2.0 Monitoring Systems Design Basis and Technology Selection: Geohydrologic, Geochemical and Geophysical Considerations . PNWD-4435, Battelle—Pacific Northwest Division, Richland, WA.

Truex MJ, CE Strickland, CD Johnson, TC Johnson, RE Clayton, and GB Chronister. 2014. Deep Vadose Zone Treatability Test for the Hanford Central Plateau: Interim Post-Desiccation Monitoring Results, Fiscal Year 2014. PNNL-23731, Pacific Northwest National Laboratory, Richland, WA.

Vermeul VR, A Bonneville, ME Kelley, RD Mackley, CE Strickland, PD Thorne, and MD Williams. 2014. FutureGen 2.0 – CO_2 Pipeline and Storage Project Testing and Monitoring Plan. PNWD-4428, Battelle—Pacific Northwest Division, Richland, WA.

2013

Bonneville A, CE Strickland, JA Dermond, Y Fang, EC Sullivan, E Heggy, and J Normand. 2013. "Geophysical Monitoring of Ground Surface Deformation Associated with a Confined Aquifer Storage and Recovery Operation." PNNL-SA-93318, Pacific Northwest National Laboratory, Richland, WA.

Liu Z, M Flury, ZF Zhang, JB Harsh, GW Gee, CE Strickland, and RE Clayton. 2013. "Transport of Europium Colloids in Vadose Zone Lysimeters at the Semiarid Hanford Site." Environmental Science & Technology 47(5):2153-2160.

Truex MJ, TC Johnson, CE Strickland, JE Peterson, and SS Hubbard. 2013. "Monitoring Vadose Zone Desiccation with Geophysical Methods." Vadose Zone Journal 12(2):, doi:10.2136/vzj2012.0147

Truex MJ, M Oostrom, CE Strickland, TC Johnson, CD Johnson, RE Clayton, and GB Chronister. 2013. Deep Vadose Zone Treatability Test for the Hanford Central Plateau: Interim Post-Desiccation Monitoring Results. PNNL-22826, Pacific Northwest National Laboratory, Richland, WA.

Ward AL, RJ Versteeg, KE Draper, CE Strickland, T Fu, and N Qafoku. 2013. Remediation and Closure Science Vadose Zone Hydrology Summary Report for Fiscal Year 2007 . PNNL-17534, Pacific Northwest National Laboratory, Richland, WA.

2012

Zhang ZF, CE Strickland, JG Field, DL Parker, and RE Clayton. 2012. "Evaluating the Performance of a Surface Barrier on Reducing Soil-Water Flow ." Vadose Zone Journal 11(3):Article No. 0117. doi:10.2136/vzj2011.0117

Oostrom M, TW Wietsma, CE Strickland, VL Freedman, and MJ Truex. 2012. "Sensor and numerical simulator evaluation for porous medium desiccation and rewetting at the intermediate laboratory scale." Vadose Zone Journal 11(1):Article No. 0089. doi:10.2136/vzj2011.0089

Truex MJ, M Oostrom, CE Strickland, GB Chronister, MW Benecke, and CD Johnson. 2012. "Field-Scale Assessment of Desiccation Implementation for Deep Vadose Zone Contaminants." Vadose Zone Journal 11(4):, doi:10.2136/vzj2011.0144

Truex MJ, M Oostrom, CE Strickland, TC Johnson, VL Freedman, CD Johnson, WJ Greenwood, AL Ward, RE Clayton, MJ Lindberg, JE Peterson, SS Hubbard, GB Chronister, and MW Benecke. 2012. Deep Vadose Zone Treatability Test for the Hanford Central Plateau: Soil Desiccation Pilot Test Results. PNNL-21369, Pacific Northwest National Laboratory, Richland, WA.

2011

Zhang ZF, CE Strickland, JG Field, and DL Parker. 2011. T-TY Tank Farm Interim Surface Barrier Demonstration - Vadose Zone Monitoring FY10 Report. PNNL-20144, Pacific Northwest National Laboratory, Richland, WA.

Truex MJ, M Oostrom, VL Freedman, CE Strickland, TW Wietsma, GD Tartakovsky, and AL Ward. 2011. Laboratory and Modeling Evaluations in Support of Field Testing for Desiccation at the Hanford Site. PNNL-20146, Pacific Northwest National Laboratory, Richland, WA.

Vermeul VR, BG Fritz, JS Fruchter, WJ Greenwood, TC Johnson, JA Horner, CE Strickland, JE Szecsody, and MD Williams. 2011. 100-NR-2 Apatite Treatability Test: Fall 2010 Tracer Infiltration Test (White Paper) . PNNL-20322, Pacific Northwest National Laboratory, Richland, WA.

2010

Zhang ZF, CE Strickland, JG Field, and DL Parker. 2010. T Tank Farm Interim Surface Barrier Demonstration - Vadose Zone Monitoring FY09 Report. PNNL-19123, Pacific Northwest National Laboratory, Richland, WA.

Zhang ZF, CE Strickland, JG Field, and DL Parker. 2010. T-TY Tank Farm Interim Surface Barrier Demonstration-Vadose Zone Monitoring Plan. PNNL-19772, Pacific Northwest National Laboratory, Richland, WA.

Slater L, D Ntarlagiannis, FD Day-Lewis, K Mwakanyamale, RJ Versteeg, AL Ward, CE Strickland, CD Johnson, and JW Lane. 2010. "Use of Electrical Imaging and Distributed Temperature Sensing Methods to Characterize Surface Water-Groundwater Exchange Regulating Uranium Transport at the Hanford 300 Area, Washington." Water Resources Research 46(10):Paper No. W10533. doi:10.1029/2010WR009110

Strickland CE, AL Ward, WP Clement, and KE Draper. 2010. "Engineered Surface Barrier Monitoring Using Ground-Penetrating Radar, Time-Domain Reflectometry, and Neutron-Scattering Techniques." Vadose Zone Journal 9(2):415-423. doi:10.2136/vzj2009.0008

2009

Zhang ZF, CE Strickland, JG Field, and DL Parker. 2009. T Tank Farm Interim Surface Barrier Demonstration - Vadose Zone Monitoring FY08 Report. PNNL-18083 FINAL, Pacific Northwest National Laboratory, Richland, WA.

Rockhold ML, DL Saunders, CE Strickland, SR Waichler, and RE Clayton. 2009. Soil Water Balance and Recharge Monitoring at the Hanford Site - FY09 Status Report. PNNL-18807, Pacific Northwest National Laboratory, Richland, WA.

2008

Zhang ZF, and CE Strickland. 2008. T Farm Interim Surface Barrier Vadose Zone Monitoring FY08 Fourth-Quarter Status Report. PNNL-17914, Pacific Northwest National Laboratory, Richland, WA.

Zhang ZF, CE Strickland, JM Keller, CD Wittreich, and HA Sydnor. 2008. T Tank Farm Interim Surface Barrier Demonstration -Vadose Zone Monitoring FY07 Report. PNNL-17306, Pacific Northwest National Laboratory, Richland, WA.

Ward AL, SO Link, CE Strickland, KE Draper, and RE Clayton. 2008. 200-BP-1 Prototype Hanford Barrier Annual Monitoring Report for Fiscal Years 2005 Through 2007 . PNNL-17176, Pacific Northwest National Laboratory, Richland, WA.

2007

Strickland, CE. 2007. "Reactive Molecular Dynamics Force Field for Simulating Hydrogenated Boron Nitrogen Compounds and Interactions with Nanoporous Silicates." M.S. Thesis. Washington State University.

Zhang ZF, JM Keller, and CE Strickland. 2007. T Tank Farm Interim Surface Barrier Demonstration--Vadose Zone Monitoring Plan. PNNL-16538, Pacific Northwest National Laboratory, Richland, WA.